1983

Theoretical And Experimental Studies In Visible Laser Spectroscopy

Akira Brian Yamashita

CANADIAN THESES ON MICROFICHE

I.S.B.N.

THESES CANADIENNES SUR MICROFICHE

National Library of Canada
Collections Development Branch

Canadian Theses on
Microfiche Service

Ottawa, Canada
K1A 0N4

Bibliothèque nationale du Canada
Direction du développement des collections

Service des thèses canadiennes
sur microfiche

NOTICE

The quality of this microfiche is heavily dependent upon the quality of the original thesis submitted for microfilming. Every effort has been made to ensure the highest quality of reproduction possible.

If pages are missing, contact the university which granted the degree.

Some pages may have indistinct print especially if the original pages were typed with a poor typewriter ribbon or if the university sent us a poor photocopy.

Previously copyrighted materials (journal articles, published tests, etc.) are not filmed.

Reproduction in full or in part of this film is governed by the Canadian Copyright Act, R.S.C. 1970, c. C-30. Please read the authorization forms which accompany this thesis.

THIS DISSERTATION
HAS BEEN MICROFILMED
EXACTLY AS RECEIVED

AVIS

La qualité de cette microfiche dépend grandement de la qualité de la thèse soumise au microfilmage. Nous avons tout fait pour assurer une qualité supérieure de reproduction.

S'il manque des pages, veuillez communiquer avec l'université qui a conféré le grade.

La qualité d'impression de certaines pages peut laisser à désirer, surtout si les pages originales ont été dactylographiées à l'aide d'un ruban usé ou si l'université nous a fait parvenir une photocopie de mauvaise qualité.

Les documents qui font déjà l'objet d'un droit d'auteur (articles de revue, examens publiés, etc.) ne sont pas microfilmés.

La reproduction, même partielle, de ce microfilm est soumise à la Loi canadienne sur le droit d'auteur, SRC 1970, c. C-30. Veuillez prendre connaissance des formules d'autorisation qui accompagnent cette thèse.

LA THÈSE A ÉTÉ
MICROFILMÉE TELLE QUE
NOUS L'AVONS REÇUE

NL-339 (r. 82/08)

Canada

THEORETICAL AND EXPERIMENTAL STUDIES IN VISIBLE LASER SPECTROSCOPY

by

Akira Brian Yamashita

Department of Chemistry

Submitted in partial fulfillment
of the requirements for the degree of
Doctor of Philosophy

Faculty of Graduate Studies
The University of Western Ontario
London, Ontario
January, 1983

ABSTRACT

In this thesis, two different aspects of the interaction of radiation with molecules are studied. First, a previously-derived exact solution to the time-dependent Schroedinger equation describing the interaction between a sinusoidally-oscillating field and an N-level atomic or molecular system is used to examine the temporal and steady-state behaviour of a five-level model molecular system. Secondly, the technique of polarization labelling spectroscopy is used to study the E 0_g^+ state of the iodine molecule.

The behaviour of the five-level system, consisting of a ground state and four "nearly degenerate" excited states, is studied for various experimental conditions, and for single- and three-photon transitions. From these calculations, it is possible to predict some aspects of the behaviour of molecules in laser radiation fields of varying intensities. When the laser intensity is strong, the excited states behave like a single band. When the laser intensity is weak, an interpretation in terms of individual two-level systems is possible. The multi-photon results show that an underlying interaction between levels persists even when the spectrum appears to consist of well-separated peaks.

The introduction of differing individual relaxation terms for the energy levels is discussed, and it is shown that the previous formalism for the undamped temporal results, with some modifications, can be used to describe the damped systems. A uniform damping model is used to demonstrate how peaks in a steady-state spectrum corresponding to transitions with differing temporal behaviour can be differentially damped. Generally, the temporal behaviour of the undamped system

is useful for predicting the results in the damped examples.

In polarization labelling spectroscopy, only "probe" laser radiation corresponding to "labelled" transitions is recorded, so the technique is very useful in simplifying otherwise complicated molecular spectra. In this work, the technique has been used in a two-photon excitation experiment to study the E state of the iodine molecule. Although iodine has been studied extensively, the ion-pair states are only now being well-characterized. The results of the polarization labelling experiments presented here are used to obtain better determinations of the molecular constants describing the E state.

ACKNOWLEDGEMENTS

I am happy to have this opportunity to express my thanks to my two supervisors, Dr. J.C.D. Brand and Dr. W.J. Meath. I am extremely grateful to them not only for their expert guidance and ever-willing assistance in this research, but also for their patience and tolerance in the face of my many mistakes.

As a half-brother in two research groups at Western, I am able to blame twice as many people for the way things have turned out - and I'm not afraid to name names. In particular, I thank Drs. Aitken Hoy, Dan Margoliash, Jerry Moloney, and Gerry Thomas for help with the computing, and Drs. Keith Cross, Niko Ernsting, and A.K. Kalkar, and Ms. Lori Parkinson for expert assistance with the polarization labelling experiments. As well, I acknowledge the other members of these research groups (who shall remain unnamed so that innocent families will not suffer needlessly) for many helpful discussions over the years.

I would also like to thank the other members of the internationally-recognized "extended spectroscopic coffee table" (with branches in West Germany, India, and Australia) for successfully keeping me out of the depression workshop. Especially, I recognize the work of Stan and Peter Markiewicz in helping me to remain in good humour. Finally, I thank Ms. Janice Miller for her typing of the thesis. Any errors are the fault of the author and not the typist.

TO MY FATHER AND

TO THE MEMORY OF MY MOTHER

It may be observed
in a general way
that life would be
better, distinctly,
if more of the people
with nothing to say
were able to say it
succinctly.

- Piet Hein

TABLE OF CONTENTS

LIST OF FIGURES

LIST OF TABLES

LIST OF PHOTOGRAPHIC PLATES

CHAPTER 1

INTRODUCTION

The recent rapid development of laser technology has opened up many new avenues of research for chemists in general, and for spectroscopists in particular. As an intense source of coherent, monochromatic radiation, the laser has been responsible not only for an improvement in conventional spectroscopic determinations, but also for the development of entirely new laser spectroscopy techniques [1,2]. As lasers and laser techniques become increasingly more sophisticated, the need arises for better theoretical models and calculational methods to describe the interaction of radiation with matter.

The first part of this thesis, Chapters 2-4, involves applications of solutions for the time-dependent Schroedinger wave equation to various aspects of the single and multi-photon spectroscopy of a model molecular system, while Chapters 5-7 describe the technique of polarization labelling spectroscopy and its application to the iodine molecule.

Solutions to the time-dependent Schroedinger equation, for the interaction of a sinusoidal applied electric field with an N-level atomic or molecular system, are discussed in Chapter 2. First, perturbation theory [3-5] and the rotating wave approximation [6-8] are briefly reviewed, primarily to point out the shortcomings of these approximate solutions, but also to determine some useful predictive formulae that can help in the interpretation of the exact results used in the spectroscopic applications. Next, the salient features of the derivation of an exact solution [9-12] are reviewed

in Section 2.4, with the emphasis on those aspects most necessary for understanding the procedures required for carrying out the calculations reported in the later chapters. The Floquet formalism [12-15] used to obtain steady-state spectral results is presented in the next section, followed by a description of the uniform collision damping model [12,16,17] in which a mean collision time is introduced to limit the time the sample interacts with the radiation field.

Chapter 3 is concerned with the temporal and steady-state behaviour of a five-level model molecular system. The model consists of a ground state which can undergo dipole allowed transitions to an excited "doorway" state [18] which is connected to three background states via static coupling terms. This five-level model was chosen to be large enough to show some of the spectroscopic effects due to interactions between excited levels (and, therefore, realistic) and small enough for reasonably economic calculations (and, therefore, feasible). The single-photon studies in Section 3.2 illustrate the changes in both the temporal and steady-state behaviour of the various states of the molecule as the laser intensity is varied. The three-photon results that follow show very complicated interactions between excited levels exist for higher-photon transitions that make the interpretation of the spectra very difficult even for weak applied fields.

Various relaxation effects are considered in Chapter 4. Individual levels in the molecule can be damped to varying degrees by adding phenomenological decay constants to the diagonal elements of the energy matrix describing the system [7,14,19]. It can then be demonstrated, see Section 4.1, that the formalism (Section 2.4)

previously used to generate the temporal spectral results can also be employed, with slight modifications, to determine the temporal behaviour of the damped system. Initial calculations are carried out on a simple two-level system, and these results are found to be useful in Section 4.3 for interpreting various relaxation effects in the five-level system of Chapter 3. The uniform collision damping model is applied to the three-photon transition and it is shown, for example, that the excitations to various excited states can be blocked by decay processes depending on the relationship between the decay constants and the temporal periods associated with the various transitions from the ground state of the molecule.

The technique of polarization labelling spectroscopy, developed in the mid-1970's [20-22], produces a spectrum that is very much simplified relative to a conventional absorption or emission spectrum. In Chapter 5, the theory of the experiment is reviewed briefly, in particular with reference to [22-24]. Since the crossed linear polarizers used in the experiment prevent radiation other than that corresponding to labelled transitions from being transmitted, the resulting spectrum has very few lines, and the assignment of these lines is aided by a knowledge of the originally pumped transitions. After early studies of the sodium dimer [21,22,25], the technique has been extended to, among others, nitrogen dioxide [22-24,26,27] and iodine [23,28]. The present work concentrates on the use of polarization spectroscopy for a rotational analysis of the E state of iodine. The experimental arrangements used in this work are described in Section 5.2, followed by some examples of results of polarization labelling experiments.

In Chapter 6, the molecular states of iodine are discussed [29]. Although the molecule has been studied extensively, the high-energy ion-pair states are only now being fully investigated. The recent flurry of research activity has included closer examination of the known ion-pair states of iodine [30,31], as well as the observation of new molecular states [31-35].

Chapter 7 contains the results of the polarization labelling experiment for the E ← B ← X system of the iodine molecule. A vibrational analysis of the E state has already been done on the emission spectrum of iodine pressured with an inert gas [36], and rotational analyses have been done on two-photon excitation spectra [37-40]. The present study was undertaken with an eye to obtaining improved values for the constants describing the E state.

Atomic units are used throughout the first part of the thesis, while in the second part, cgs or MKS units are usually employed. The "spectroscopic" units of energy are defined in S.I. units [41] as

$$1\ cm^{-1} = 1.9865 \times 10^{-23}\ J$$

$$1\ eV = 1.6022 \times 10^{-19}\ J.$$

The conversion factors for a number of atomic units are given [41] in Table (1-1).

Table (1-1). Conversion factors for atomic units to S.I. units

Atomic unit	Value in S.I. units
Charge (e)	1.6022×10^{-19} C
Length (a_0)	5.2918×10^{-11} M
Mass (m_e)	9.1095×10^{-31} kg
Angular momentum ($\hbar$)	1.0546×10^{-34} J.s.
Time	2.4189×10^{-17} s
Frequency	4.1341×10^{-16} s^{-1}
Energy (hartree)	4.3598×10^{-18} J
Electric dipole moment ($\mu = ea_0$)	8.4784×10^{-30} C. m.
Electric field amplitude ($\varepsilon = ea_0^{-2}$)	5.1423×10^{11} V. m^{-1}

CHAPTER 2

SOLUTIONS TO THE TIME-DEPENDENT SCHROEDINGER EQUATION

2. Solutions to the time-dependent Schroedinger equation

This chapter provides the basic theoretical background material needed for the sets of calculations carried out in the following two chapters. It begins with a very brief overview of two well-known methods that have often been used to approximate solutions to the time-dependent Schroedinger equation for the interaction of atoms or molecules with a radiation field. The previously-derived formalism for an exact solution [9,11,12,14] is then reviewed, with the emphasis here on those results most pertinent to the calculations of the next chapters. While this serves to provide a good working understanding of the treatment, some of the fine points of the earlier derivation are suppressed for the sake of brevity. For further details, the reader is directed to the original publications referred to in the text of this chapter.

2.1 The time-dependent Schroedinger equation

The behaviour of an atomic or molecular system in a time-dependent radiation field can be described by the time-dependent Schroedinger equation

$$H(r,t)\ \Psi(r,t) = i\frac{\partial}{\partial t}\Psi(r,t) \qquad (2.1\text{-}1)$$

where r and t signify dependence on spatial and temporal coordinates, respectively. The total Hamiltonian, H, in the above equation can be separated into two parts - the time-independent Hamiltonian, $H^{(0)}(r)$, and the time-dependent perturbation, $V(r,t)$ [3,5,42]. The stationary state problem defined by the time-independent Hamiltonian has the general form

$$H^{(0)}(r)\ \Psi^{(0)}(r,t) = i\frac{\partial}{\partial t}\Psi^{(0)}(r,t) \qquad (2.1\text{-}2)$$

The wavefunction may be written in terms of a complete spectrum of orthonormal basis functions, ϕ_k, and corresponding energies, E_k, as [43]

$$\Psi^{(0)}(r,t) = \sum_k b_k\ \phi_k(r)\ \exp\{-iE_k t\} \qquad (2.1\text{-}3)$$

where the b_k are independent of time and the individual basis functions satisfy the equation

$$H^{(0)}(r)\ \phi_k(r) = E_k\ \phi_k(r) \qquad (2.1\text{-}4)$$

The analogous solution for the time-dependent problem is of the form [3,5,44]

$$\Psi(r,t) = \sum_k b_k(t)\ \phi_k(r)\ \exp\{-iE_k t\} \qquad (2.1\text{-}5)$$

with the normalization condition

$$\langle\Psi(r,t)|\Psi(r,t)\rangle = \sum_k |b_k(t)|^2 = 1 \qquad (2.1\text{-}6)$$

When (2.1-5) is substituted into (2.1-1), the result, after a few manipulations, is a set of coupled equations for the time-dependent expansion coefficients occurring in (2.1-5) [3-5]:

$$i\frac{\partial}{\partial t} b_j(t) = \sum_k V_{jk}(t)\, b_k(t) \exp\{i(E_j-E_k)t\} \qquad (2.1\text{-}7)$$

where

$$V_{jk}(t) = \langle\phi_j(r)|V(r,t)|\phi_k(r)\rangle \qquad (2.1\text{-}8)$$

The temporal behaviour of the coefficients, $b_k(t)$, gives the change in state amplitudes due to the perturbation while the absolute value squared, $|b_k(t)|^2$, is proportional to the population of the k-th state at time t. The induced temporal transition probability, $P_{kk}(t)$, is then defined as

$$P_{kk}(t) = |b_k(t)|^2 \qquad (2.1\text{-}9)$$

The accurate determination of $P_{kk}(t)$ is the ultimate goal of the treatments outlined below.

2.2 Time-dependent perturbation theory

Time-dependent perturbation theory provides an approximate solution to equation (2.1-1) or (2.1-7) that is valid for a small perturbation

taken over a short period of time [3]. The total Hamiltonian is written as

$$H(r,t) = H^{(0)}(r,t) + \lambda V(r,t) \qquad (2.2\text{-}1)$$

where λ is a dimensionless parameter used to describe the order of the perturbation calculation and is set equal to 1 in the final result [3,5]. The total wavefunction can be expanded in terms of the parameter λ to yield

$$\Psi(r,t) = \sum_{s=0}^{\infty} \lambda^s \Psi^{(s)}(r,t) \qquad (2.2\text{-}2).$$

Equation (2.2-1) and (2.2-2) can be used to rewrite (2.1-1) in terms of powers of λ. Collecting the terms of equal order in λ then yields the following set of equations [4,5]

$$\begin{aligned}
&[H^{(0)}(r) - i\frac{\partial}{\partial t}]\Psi^{(0)}(r,t) = 0 \\
&[H^{(0)}(r) - i\frac{\partial}{\partial t}]\Psi^{(1)}(r,t) + V(r,t)\Psi^{(0)}(r,t) = 0 \\
&\qquad\vdots \\
&[H^{(0)}(r) - i\frac{\partial}{\partial t}]\Psi^{(s)}(r,t) + V(r,t)\Psi^{(s-1)}(r,t) = 0 \qquad (2.2\text{-}3)
\end{aligned}$$

The first equation is simply the stationary state problem of (2.1-2). The solution, $\Psi^{(0)}$, can be used to generate the first order correction term, $\Psi^{(1)}(r,t)$. The procedure may be repeated to obtain higher order corrections in terms of previous results. The s-th order result, when written in the same form as (2.1-5), becomes

$$\psi^{(s)}(r,t) = \sum_k b_k^{(s)}(t)\, \phi_k(r)\, \exp\{-iE_k t\} \qquad (2.2\text{-}4)$$

with (taking $\lambda = 1$)

$$b_k(t) = \sum_s b_k^{(s)}(t) \qquad (2.2\text{-}5)$$

Equation (2.2-4) substituted into (2.2-3) yields the following equation for $b_k^{(s)}(t)$ in terms of the (s-1)-th order terms [3,4]

$$\frac{\partial}{\partial t} b_k^{(s)}(t) = -i \sum_{m=0}^{\infty} \langle \phi_k(r) | V(r,t) | \phi_m(r) \rangle\, b_m^{(s-1)}(t)$$
$$\exp\{i(E_k - E_m)t\} \qquad (2.2\text{-}6)$$

When the perturbation represents a classical monochromatic radiation field, $V(r,t)$ can be written as

$$V(r,t) = -\underline{\mu}\cdot\underline{\varepsilon}\, \cos(\nu t+\delta) \qquad (2.2\text{-}7)$$

where $\underline{\mu}$ is the electric dipole moment operator, $\underline{\varepsilon}$ is the electric field amplitude, ν is the field frequency, and δ is an arbitrary phase factor. In exponential form, the perturbation term becomes

$$V(r,t) = -\frac{\mu_z \varepsilon}{2} \{\exp[i(\nu t+\delta)] + \exp[-i(\nu t+\delta)]\} \qquad (2.2\text{-}8)$$

for a field defining the z-axis. For the resonant absorption from state 1 to state n, the initial conditions

$$b_k^{(0)} = \delta_{1,k}$$

$$b_k^{(s)} = 0, \; s > 0 \tag{2.2-9}$$

and the normalization conditions [5]

$$\langle \Psi^{(0)}(r,t) | \Psi^{(0)}(r,t) \rangle = 1$$

$$\sum_{n=0}^{\infty} \langle \Psi^{(n)}(r,t) | \Psi^{(s-n)}(r,t) \rangle = 0, \; s > 0 \tag{2.2-10}$$

produce for $b_n^{(1)}(t)$

$$b_n^{(1)}(t) = -\frac{\mu_{n1}\varepsilon}{2} \{ (\exp[i(\omega_{n1} + \nu)t] - 1) \frac{\exp(i\delta)}{(\omega_{n1} + \nu)}$$

$$+ (\exp[i(\omega_{n1} - \nu)t] - 1) \frac{\exp(i\delta)}{(\omega_{n1} - \nu)} \} \tag{2.2-11}$$

where

$$\omega_{n1} = E_n - E_1$$

$$\mu_{n1} = \langle \phi_n(r) | \mu_z | \phi_1(r) \rangle \tag{2.2-12}$$

In absorption, the conventional perturbation theory result is obtained by neglecting the term with the larger denominator [45]. The approximate first order transition probability is then given by [3]

$$P_{nn}^{(1)}(t) = |b_n^{(1)}(t)|^2 \approx |\mu_{n1}|^2 \varepsilon^2 \frac{1}{(\omega_{n1} - \nu)^2} \{ \sin^2 (\frac{[\omega_{n1} - \nu]t}{2}) \}$$

(2.2-13)

Of note here is the fact that when $\frac{|\mu_{n1}|^2\varepsilon^2}{(\omega_{n1} - \nu)^2}$ is large, the temporal induced transition probability can have unrealistic values exceeding unity. This is an example of the secular divergences [5,46] plaguing the time-dependent perturbation theory results, restricting the treatment to very short times. When a very short time period or a frequency very close to resonance is considered, the sine term may be replaced by its argument to yield a further simplification:

$$P_{nn}^{(1)}(t) \approx |\mu_{n1}|^2\varepsilon^2 \frac{t^2}{4} \qquad (2.2\text{-}14)$$

Equation (2.2-13) shows that the single photon transition probability is dependent upon the first power of the laser intensity, $I(\alpha\varepsilon^2)$. The generalization to m-photon transitions results in an induced transition probability that is proportional to the m-th power of the laser intensity, and occurs at a frequency of $\frac{\omega_{n1}}{m}$ [3,4,13].

2.3 The rotating wave approximation

The Rabi rotating wave approximation (RWA) [6-8] produces a solution to the time-dependent Schroedinger equation that remains valid for much longer times and greater field strengths than does the perturbation theory solution. As well, the RWA solution eliminates the secular divergences pointed out for the perturbation theory results.

The sinusoidal electromagnetic wave is separated into two "oppositely rotating halves" by writing it as the sum of two exponential terms with arguments of opposite sign (see (2.2-8)). The coupled differential equations describing the time evolution of a two-level system in the interaction representation are given by (δ=0)

$$i\frac{\partial}{\partial t} b_1(t) = -\frac{\mu_{12}\varepsilon}{2}\{\exp[-i(\omega_{21}-\nu)t] + \exp[-i(\omega_{21}+\nu)t]\}b_2(t)$$

$$i\frac{\partial}{\partial t} b_2(t) = -\frac{\mu_{12}\varepsilon}{2}\{\exp[i(\omega_{21}+\nu)t] + \exp[i(\omega_{21}-\nu)t]\}b_1(t) \qquad (2.3\text{-}1)$$

where

$$\omega_{21} = E_2 - E_1 > 0 \qquad (2.3\text{-}2).$$

Near resonance,

$$\omega_{21} - \nu \approx 0$$

$$\omega_{21} + \nu \approx 2\nu \qquad (2.3\text{-}3)$$

The terms in (2.3-1) with $\sim 2\nu$ in the argument of the exponential will be rapidly oscillatory. Since these terms will be minor contributors to the time development of the two states, they are dropped in the rotating wave approximation. This points out the "on resonance" nature of this method. As the frequency gets further from resonance, the terms to be neglected have a more significant effect on the

temporal behaviour. Invoking the RWA transforms (2.3-1) to the following:

$$i\frac{\partial}{\partial t} b_1(t) = -\frac{\mu_{12}\varepsilon}{2} \exp\{-i(\omega_{21} - \nu)t\} b_2(t)$$

$$i\frac{\partial}{\partial t} b_2(t) = -\frac{\mu_{12}\varepsilon}{2} \exp\{i(\omega_{21} - \nu)t\} b_1(t) \qquad (2.3\text{-}4)$$

A further transformation of the form

$$b_k(t) = C_k(t) \exp\{i\alpha_k t\} \qquad (2.3\text{-}5)$$

removes the time dependence in the coefficients of (2.3-4) [19,47-50] to yield the well-known result in matrix form

$$i\frac{\partial}{\partial t}\begin{bmatrix} C_1(t) \\ C_2(t) \end{bmatrix} = \begin{bmatrix} 0 & -\frac{\mu_{12}\varepsilon}{2} \\ -\frac{\mu_{12}\varepsilon}{2} & \Delta \end{bmatrix}\begin{bmatrix} C_1(t) \\ C_2(t) \end{bmatrix} \qquad (2.3\text{-}6)$$

where $\Delta = \omega_{21} - \nu$ is a measure of how far the frequency is from being on resonance. The resulting induced transition probability for the transition from state 1 to state 2 is given by

$$P_{22}(t) = |C_2(t)|^2 = \frac{|\mu_{12}\varepsilon|^2}{(\omega_{21}-\nu)^2 + |\mu_{12}\varepsilon|^2} \sin^2\{\tfrac{1}{2}\sqrt{(\omega_{21}-\nu)^2 + |\mu_{12}\varepsilon|^2}\, t\} \qquad (2.3\text{-}7)$$

Inspection of this expression reveals that the induced transition probability will not exceed unity at any time, in contrast to (2:2-13). When the frequency is exactly on resonance, (2.3-7) simplifies to

$$P_{22}(t) = \sin^2\{\frac{|\mu_{12}\varepsilon|t}{2}\} \qquad (2.3\text{-}8).$$

In this case, the transition probability oscillates between the values of 0 and 1 with an overall Rabi period of $\frac{2\pi}{|\mu\varepsilon|}$.

The long-time-average of equation (2.3-7) may be used to generate the spectrum produced by continuous wave (cw) laser excitation. This requires only the replacement of the $\sin^2$ term with its long-time-average value of $\frac{1}{2}$ to yield

$$P_{22} = \frac{|\mu_{12}\varepsilon|^2}{2[(\nu-\omega_{21})^2 + |\mu_{12}\varepsilon|^2]} \qquad (2.3\text{-}9)$$

This describes a Lorentzian lineshape with a peak value of 0.5 at $\nu = \omega_{21}$ and a half-width at half-maximum (HWHM) of $|\mu_{12}\varepsilon|$.

It may also be pointed out that (2.3-7) will reduce to (2.3-13) when $|\mu_{12}\varepsilon| \ll (\omega_{21}-\nu)$. This serves to underline the fact that the perturbation theory treatment is restricted to cases in which the laser intensities are very weak.

The multi-photon analogue of (2.3-7) is given by [13,47]

$$P_{22}(t) = \frac{|u|^2}{(\omega_{21}-n\nu)^2 + |u|^2} \sin^2\{\frac{t}{2}\sqrt{(\omega_{21}-n\nu)^2 + |u|^2}\} \qquad (2.3\text{-}10)$$

where n is the number of photons involved in the transition (n odd) and u is given by

$$u = (\mu\varepsilon)^n[2^{4p}(p!)^2\,\nu^{2p}]^{-1} \qquad (2.3\text{-}11a)$$

with

$$p = \frac{n-1}{2} \qquad (2.3\text{-}11b)$$

The Rabi period at the resonance frequency is now given by

$$\Delta t^R = \frac{2\pi}{|u|} \qquad (2.3\text{-}12)$$

The HWHM of the peak in the spectrum can be determined from (2.3-10) by first writing

$$(\omega_{21} - n\nu) = n(\frac{\omega_{21}}{n} - \nu) \qquad (2.3\text{-}13)$$

The HWHM is then given by

$$\text{HWHM} = \frac{|u|}{n} \qquad (2.3\text{-}14)$$

The counter-rotating terms which are discarded in the RWA were shown by Bloch and Siegert [51] to contribute to a shift in the peak position to higher frequency than that predicted by the two-level energy level diagram (ie. the zero-field limit). The first term in the expansion for the Bloch-Siegert shift is given by [8,13,51-59]

$$\delta\nu = \nu - \omega_{12} = \frac{|\mu_{12}\varepsilon|^2}{4\omega_{12}} \qquad (2.3\text{-}15)$$

where ω_{12} is the predicted unshifted resonance frequency. In fact, higher order terms have been determined in a number of cases, with

agreement up to terms of the order of $(\mu\varepsilon)^6$ [13,54-58]. According to (2.3-15), the square of the coupling strength determines the size of the frequency shift, so the Bloch-Siegert shift will be more pronounced as the laser intensity ($I\alpha\varepsilon^2$) is increased.

At this point, the dimensionless coupling strength parameter, β, given by

$$\beta_{12} = \frac{|\mu_{12}\varepsilon|}{\omega_{12}} \qquad (2.3\text{-}16)$$

is introduced. The β parameter relates the coupling strength to the energy of the transition and provides a useful means of comparing systems as $\mu_{12}\varepsilon$ or ω_{12} are scaled up or down. The Bloch-Siegert shift, relative to the zero-field resonance frequency, can be rewritten as a power series in β [13,51-59]. The first term, corresponding to (2.3-15), is given by

$$\frac{\delta\nu}{\omega_{12}} = \frac{1}{4}\beta^2 \qquad (2.3\text{-}17)$$

The shift in the frequency of the transition as a fraction of the zero-field energy of the transition is, to a first approximation, a quadratic function of β.

The multi-photon Bloch-Siegert shift has been derived for a two-level system. For the three-photon transition there is agreement among various authors [13,52,53,58b,59] that the shift in frequency is given to a first approximation by

$$\delta\nu = \nu - \frac{\omega_{12}}{3} = \frac{(\mu\varepsilon)^2}{8\nu} \qquad (2.3\text{-}18)$$

Hioe [58b] has calculated the shift to terms of order $(\mu\varepsilon)^8$:

$$\delta\nu = \nu - \frac{\omega_{12}}{3} = \frac{(\mu\varepsilon)^2}{8\nu} + \frac{3(\mu\varepsilon)^4}{512\nu^3} - \frac{65(\mu\varepsilon)^6}{147456\nu^5} - 2.51823003 \times 10^{-4} \frac{(\mu\varepsilon)^8}{\nu^7} \qquad (2.3\text{-}19)$$

The shifted resonance frequency, ν, can be obtained by inverting (2.3-19), or by iterating (2.3-19).

Although the treatment outlined above deals with a two-level system, the RWA has been applied to many-level systems [47,49,60,61]. The Bloch-Siegert shift given here has been derived only for a two-level system, but can be applied, with reservations, to multi-level systems (see below and [62]).

2.4 An exact power series solution

As the previous sections indicate, the perturbation theory result is only reliable for very short times and very weak fields. The Rabi rotating wave approximation, on the other hand, is valid over a much greater range of time and laser intensity, and successfully avoids the secular divergences that restrict the perturbation theory results. However, disregarding the "counter-rotating" terms in the coupled differential equation (compare (2.3-1) and (2.3-4)) can seriously compromise the results when the terms to be neglected begin to make a significant contribution to the temporal behaviour of the system. Clearly, the introduction of any approximations means that there will be conditions under which the solution is no longer valid. An exact solution to the Schroedinger equation, applicable for all values of the field strength and time [9,11,12,14] will be outlined

below.

The treatment described in this section uses a power series solution to solve the coupled differential equations (2.1-7). With the recurrence relations that are produced, the solution can be determined to any degree of accuracy by varying the number of terms retained in the converging series sums. With a sinusoidal perturbation (see (2.2-7)), the periodicity of the resulting Hamiltonian may be exploited, so that the solution at arbitrary times can be determined once the solution over the first period of the perturbation is known [10,11]. Re-casting the results in Floquet form [13,14] makes it relatively easy to calculate phase- and long-time-averaged transition probabilities. The brief description given below stresses the computational steps that are to be taken in actually carrying out the calculation. For further details of the development of the method of solution, the reader is directed to references [9,11,12,14].

The time-dependent wavefunction in the Schroedinger representation is given by

$$\Psi(r,t) = \underline{\phi}^{T}(r)\,\underline{a}(t) \tag{2.4-1}$$

with the normalization condition

$$\underline{a}^{\dagger}(t)\,\underline{a}(t) = 1 \tag{2.4-2}$$

The column vector $\underline{a}(t)$ and the row vector $\underline{\phi}^{T}(r)$ are defined by

$$(\underline{a}(t))_j = a_j(t)$$

$$(\underline{\phi}(r))_j = \phi_j(r) \tag{2.4-3}$$

The Hamiltonian for the system may be written

$$H(r,t) = H^{(0)}(r) + V(r,t) = H^{(0)}(r) - \mu\varepsilon \cos(\nu t + \delta) \quad (2.4\text{-}4)$$

for a sinusoidal monochromatic external perturbation. In the dipole approximation, the time-dependent coefficients, $a_j(t)$, satisfy the matrix equation

$$i\frac{\partial}{\partial t}\underline{a}(t) = -\underline{\underline{\mu}}\varepsilon \cos(\nu t + \delta)\underline{a}(t) + \underline{\underline{E}}'\underline{a}(t) \quad (2.4\text{-}5)$$

where the matrices $\underline{\underline{\mu}}$ and $\underline{\underline{E}}'$ are defined by

$$(\underline{\underline{\mu}})_{ij} = \mu_{ij} \; ; \quad (\underline{\underline{E}}')_{ij} = E_i\delta_{ij} - \mu_{ij}\varepsilon^{\circ} \quad (2.4\text{-}6)$$

The ε° terms can represent internal couplings between levels or the application of static external fields [17].

The solution for $\theta = \nu t + \delta$ on the $[0,2\pi]$ interval is given by

$$\underline{a}(\theta) = \underline{\underline{F}}(\theta)\underline{C}_0(\delta) \quad (2.4\text{-}7)$$

where the column vector $\underline{C}_0(\delta)$ is determined from the initial condition

$$\underline{a}(t=0) = \underline{a}(\delta) = \underline{A} \quad (2.4\text{-}8)$$

and the equation

$$\underline{C}_0(\delta) = \underline{\underline{F}}^{-1}(\delta)\underline{A} \quad (2.4\text{-}9)$$

The matrix $\underline{\underline{F}}$ is obtained from the power series expansion outlined in [11]. For $\theta = \gamma + n\pi$, $n = 0,1$, and $0 \leq \gamma \leq \pi$, the solution is

$$\underline{\underline{F}}(\gamma) = \sum_{\ell=0}^{\infty} \underline{\underline{Q}}_{\ell} \gamma^{\ell} \qquad (2.4\text{-}10)$$

The recurrence relation for the determination of $\underline{\underline{Q}}$ is

$$\underline{\underline{Q}}_{\ell+1} = \frac{1}{i\nu(\ell+1)} \{ \underline{\underline{E}}' \underline{\underline{Q}}_{\ell} + (-1)^{n+1} \sum_{m=0}^{\infty} \frac{(-1)^m}{(2m)!} \underline{\underline{\mu}} \epsilon \underline{\underline{Q}}_{\ell-2m} \} ,$$

$$\ell - 2m \geq 0 \qquad (2.4\text{-}11)$$

with

$$(\underline{\underline{Q}}_0)_{ij} = \delta_{ij} \qquad (2.4\text{-}12)$$

Although the sums in (2.4-10) and (2.4-11) are formally written to include an infinite number of terms, computationally, good convergence is obtainable with the retention of a reasonably small number of terms [11]. In order to keep the terms down to a manageable number, it may be required, in some cases, to break the γ-interval into lengths smaller than π[17] (see below).

When θ is greater than 2π, the following equations hold

$$\underline{\underline{F}}(\beta+2s\pi) = \underline{\underline{F}}(\beta)\underline{\underline{F}}(2s\pi), \quad 0 \leq \beta \leq 2\pi \qquad (2.4\text{-}13)$$

$$\underline{\underline{F}}(2s\pi) = [\underline{\underline{F}}(2\pi)]^s \qquad (2.4\text{-}14)$$

Thus, once the solution over the initial $[0,2\pi]$ interval has been generated, the result at arbitrary time can be generated from the general equation [14]

$$\underline{a}(\beta + 2s\pi) = \underline{\underline{F}}(\beta)[\underline{\underline{F}}(2\pi)]^s \underline{C}_0(\delta) \qquad (2.4\text{-}15)$$

Equation (2.4-14) is very important when the temporal behaviour at very long times is being investigated. However, if the matrix $\underline{\underline{F}}(2\pi)$ is multiplied by itself a number of times, the computed result quickly loses significant figures. A much better way to evaluate (2.4-14) for very large values of s begins with the diagonalization of $\underline{\underline{F}}(2\pi)$:

$$\underline{\underline{F}}(2\pi) = \underline{\underline{S}}[\underline{\underline{D}}]\underline{\underline{S}}^{-1} \qquad (2.4\text{-}16)$$

where $\underline{\underline{D}}$ is a diagonal matrix. Since $\underline{\underline{S}}^{-1}$ is the inverse of $\underline{\underline{S}}$, raising $\underline{\underline{F}}(2\pi)$ to the s-th power reduces to

$$[\underline{\underline{F}}(2\pi)]^s = \underline{\underline{S}}[\underline{\underline{D}}]^s \underline{\underline{S}}^{-1} \qquad (2.4\text{-}17)$$

The individual complex elements of the matrix $\underline{\underline{D}}$ can be re-written in polar form [63] as

$$z = a + bi = r(\cos \Omega + i \sin \Omega) = r \exp(i\Omega) \qquad (2.4\text{-}18)$$

where

$$r = \sqrt{a^2 + b^2}$$

$$\tan \Omega = \frac{b}{a} \qquad (2.4\text{-}19)$$

It then follows that

$$z^n = r^n(\cos n\Omega + i \sin n\Omega) = r^n \exp(in\Omega) \qquad (2.4\text{-}20)$$

Computationally, the diagonalization may be carried out quite efficiently through the use of standard computer library routines [64]. Subsequent use of equations (2.4-17) and (2.4-20) then allows for the evaluation of the right hand side of (2.4-14) for large values of the exponent s.

When the laser intensity is especially strong, the power series solution may require a great many terms before it converges on the first (or second) $[0,\pi]$ interval. In these cases, the $[0,2\pi]$ interval can be broken up into a number of sub-intervals in which fewer terms are required for convergence. To do this, the recurrence relation (2.4-11) is re-written as [17]

$$\underline{\underline{Q}}_{\ell+1} = \frac{1}{i\nu(\ell+1)} \{\underline{\underline{E}}' \underline{\underline{Q}}_\ell - [\cos\alpha \sum_{m=0}^{\infty} \frac{(-1)^m}{(2m)!} \underline{\underline{\mu\varepsilon}}\, \underline{\underline{Q}}_{\ell-2m} + \sin\alpha \sum_{m=0}^{\infty} \frac{(-1)^m}{(2m+1)!} \underline{\underline{\mu\varepsilon}}\, \underline{\underline{Q}}_{\ell-2m-1}]\} \qquad (2.4\text{-}21)$$

The phase factor α insures that the correct expansion coefficients in (2.4-10) are obtained when γ is re-set to zero at the beginning of each sub-interval. For example, if a $\frac{\pi}{2}$ sub-interval size is to be

used for the $[0,2\pi]$ calculation, the γ value ranges from 0 to $\frac{\pi}{2}$ for each of $\alpha = 0, \frac{\pi}{2}, \pi$, and $\frac{3\pi}{2}$.

The calculation for different values of the phase factor δ (see (2.2-7)) can be accomplished once the $\underline{\underline{F}}(\theta)$ have been determined over the initial $[0,2\pi]$ theta-interval for $\delta = 0$; when $\delta = 0$, $t = 0$ corresponds to $\theta = 0$, while when $\delta \neq 0$, $t = 0$ corresponds to $\theta = \delta$. For $\delta \neq 0$, the initial $\underline{C}_0(\delta)$ vector must be determined from (2.4-9). This is easily accomplished if $\underline{\underline{F}}(\delta)$ has already been calculated as part of the $\delta = 0$ set of results. For example, when $\delta = \pi$ and $t = 0$ one has

$$\underline{\underline{F}}(\nu t = 0, \delta = \pi) = \underline{\underline{F}}(\nu t = \pi, \delta = 0) = \underline{\underline{F}}(\pi) \qquad (2.4\text{-}22)$$

That is, the matrix $\underline{\underline{F}}(\delta)$ required to initialize $\underline{C}_0$ for a value of $\delta \neq 0$ will already be present from an initial $\delta = 0$ calculation on the $[0,2\pi]$ interval. Using (2.4-7), the values of $\underline{a}(\theta)$ on the $[0,2\pi]$ interval for $\delta \neq 0$ can be determined directly from the previously computed $\underline{\underline{F}}(\theta)$ values for $\delta = 0$ and the $\underline{C}_0(\delta)$ just determined. This procedure is especially useful when a number of calculations are contemplated, for example as are necessary to produce the phase-averaged result for the temporal behaviour of the transition probabilities.

In summary, the procedure to be used to determine the temporal behaviour of transition probabilities is as follows:

(1) Determine the $\underline{\underline{F}}(\theta)$ values on the $[0,2\pi]$ interval using (2.4-21) and (2.4-10) for the initial conditions given by $\underline{A}$, $\underline{\underline{E}}$, and $\underline{\mu\varepsilon}$, and ν, with $\delta = 0$. The size of the sub-interval to be used in (2.4-21) depends upon the magnitude of the coupling, $\mu\varepsilon$, relative

to the energy of the transition. As $\mu\varepsilon$ increases, a smaller sub-interval must be used if the same degree of accuracy is to be attained with the same number of terms in the sum occurring in (2.4-10).

(2) Calculate $\underline{C}_0(\delta)$ from (2.4-9), using the appropriate $\underline{\underline{F}}(\delta)$ matrix determined in step (1).

(3) Generate $\underline{a}(\theta)$ on the $[0,2\pi]$ interval from (2.4-7) using the $\underline{\underline{F}}(\theta)$ and $\underline{C}_0(\delta)$ values already determined.

(4) Continue the calculations to arbitrarily long times by using (2.4-15).

2.5 The exact solution in Floquet form

The transformation of the results of the previous section into Floquet form [13,14] provides no significant improvement for the determination of the temporal behaviour of the transition probabilities. The real advantage of the Floquet formalism lies in the ease with which phase- and time-averaged results can be generated. Phase- and time-averaging of the temporal transition-probabilities makes it possible to generate cw laser-excited frequency-sweep spectra [13,14,16, 65].

The solution to (2.4-5) can be written in Floquet form [66-68]

$$\underline{\underline{G}}(\theta) = \underline{\underline{Z}}(\theta)\exp(i\underline{\underline{\Delta}}\theta) \qquad (2.5\text{-}1)$$

where $\underline{\underline{Z}}$ is a periodic square matrix such that

$$\underline{\underline{Z}}(\theta + 2\pi) = \underline{\underline{Z}}(\theta) \qquad (2.5\text{-}2)$$

The matrix $\underline{\underline{\Delta}}$ is a real constant diagonal matrix whose elements are the characteristic exponents of the solution.

The matrix $\underline{\underline{F}}(2\pi)$ can be diagonalized (see (2.4-16)) as

$$\underline{\underline{F}}(2\pi) = \underline{\underline{S}}\,\underline{\underline{D}}\,\underline{\underline{S}}^{-1} \tag{2.5-3}$$

The complex eigenvalues of $\underline{\underline{F}}(2\pi)$, λ_j, are the elements of the diagonal matrix, $\underline{\underline{D}}$. Since $\underline{\underline{F}}(2\pi)$ is a unitary matrix, the eigenvalues become [13,14,63] in polar form (see also (2.4-18) and (2.4-19)),

$$\lambda_j = \exp(i\,\Delta_j\,2\pi) \tag{2.5-4}$$

with [69]

$$2\pi\Delta_j = \tan^{-1}(\mathrm{Im}\,\lambda_j/\mathrm{Re}\,\lambda_j) \tag{2.5-5}$$

Equation (2.5-3) then becomes

$$\underline{\underline{F}}(2\pi) = \underline{\underline{S}}\,\exp(i\,\underline{\underline{\Delta}}\,2\pi)\underline{\underline{S}}^{-1} \tag{2.5-6}$$

and for $\theta = \nu t + \delta = 2n\pi$, using (2.4-14) and (2.4-20),

$$\underline{\underline{F}}(2n\pi) = \underline{\underline{S}}\,\exp(i\,\underline{\underline{\Delta}}\,2n\pi)\underline{\underline{S}}^{-1} \tag{2.5-7}$$

Multiplying from the right by $\underline{\underline{S}}$ produces the Floquet form of the solution to (2.4-5)

$$\underline{\underline{G}}(2n\pi) = \underline{\underline{F}}(2n\pi)\underline{\underline{S}} = \underline{\underline{S}}\,\exp(i\,\underline{\underline{\Delta}}\,2n\pi) \tag{2.5-8}$$

Comparison with (2.5-1) shows

$$\underline{\underline{Z}}(2n\pi) = \underline{\underline{F}}(2n\pi)\underline{\underline{S}}\,\exp(-i\,\underline{\underline{\Delta}}\,2n\pi) = \underline{\underline{S}} \tag{2.5-9}$$

For arbitrary values of θ [14],

$$\underline{\underline{Z}}(\theta) = \underline{\underline{F}}(\theta)\underline{\underline{S}}\,\exp(-i\,\underline{\underline{\Delta}}\,\theta) \tag{2.5-10}$$

The solution to (2.4-5) given by (2.4-7) can now be written in terms of the Floquet results

$$\underline{a}(\theta) = \underline{\underline{Z}}(\theta) \exp(i \underline{\underline{\Delta}} \theta) \underline{b}_0(\delta) \qquad (2.5\text{-}11)$$

where

$$\underline{b}_0(\delta) = \underline{\underline{S}}^{-1} \underline{C}_0(\delta) \qquad (2.5\text{-}12)$$

Thus, once the $\underline{\underline{F}}$ matrix has been determined on the original $[0,2\pi]$ interval, the calculation may proceed either along the lines of the previous section or with the transformation to the Floquet formalism. The procedure for the latter would be as follows:

(1) Diagonalize $\underline{\underline{F}}(2\pi)$ in order to obtain $\underline{\underline{S}}$, $\underline{\underline{S}}^{-1}$, and the λ_j.

(2) Use the λ_j in (2.5-5) to obtain the characteristic exponent matrix, $\underline{\underline{\Delta}}$. Characteristic exponent plots may be used to predict resonance peak positions and widths in the frequency-sweep spectrum. As well, the characteristic exponents are very easily related to dressed-atom energies [13,17,70,71].

(3) Determine $\underline{b}_0(\delta)$ from (2.5-12) and $\underline{\underline{Z}}(\theta)$ from (2.5-10).

(4) Generate $\underline{a}(\theta)$ from (2.5-11).

The phase- and/or time-averages of the temporal transition probabilities can be calculated readily from the Floquet results derived above [14]. Phase-averaging takes into account the effects of various values of the phase factor, δ (see (2.2-7)), while time-averaging produces the steady-state results that can be observed with a long-timescale irradiation.

The phase-averaged temporal result is written [14]

$$\overline{P}_{jj}(t) = \frac{1}{\pi} \int_0^{\pi} |a_j(t)|^2 \, d\delta \qquad (2.5\text{-}13)$$

Writing terms out explicitly, (2.5-13) becomes

$$\overline{P}_{jj}(t) = \sum_{gg'} \exp[i(\Delta_g - \Delta_{g'})\nu t]\beta_{gg'}{}^{jj}(\nu t) \qquad (2.5\text{-}14)$$

where

$$\beta_{gg'}{}^{jj}(\nu t) = \frac{1}{\pi}\int_0^{\pi} [Z_{jg}(\nu t+\delta)Z_{jg'}{}^{*}(\nu t+\delta)b_{og}(\delta)b_{og'}{}^{*}(\delta) \exp[i(\Delta_g - \Delta_{g'})\delta]]d\delta \qquad (2.5\text{-}15)$$

The periodicity of $\underline{\underline{Z}}(\theta)$ (see (2.5-2)) means that $\beta_{gg'}{}^{jj}(\nu t)$ is also periodic:

$$\beta_{gg'}{}^{jj}(\nu t) = \beta_{gg'}{}^{jj}(\nu t + 2\pi) \qquad (2.5\text{-}16)$$

The time-averaged result for a single phase, δ, is given by (with $\theta' = \nu t$) [34]

$$\overline{P}_{jj}(\delta) = \frac{1}{2\pi}\int_0^{2\pi} \sum_k |Z_{jk}(\theta')|^2 \, d\theta' \, |b_k(\delta)|^2 \qquad (2.5\text{-}17)$$

Finally, the phase- and long-time-averaged induced transition probability is given by

$$\overline{P}_{jj} = \lim_{\tau\to\infty} \frac{1}{\tau}\int_0^{\tau} \overline{P}_{jj}(t)\, dt \qquad (2.5\text{-}18)$$

This can be reduced to the very simple form [14]

$$\overline{P}_{jj} = \sum_g \frac{1}{2\pi}\int_0^{2\pi} \beta_{gg}{}^{jj}(\theta')\, d\theta' \qquad (2.5\text{-}19)$$

where $\beta_{gg}{}^{jj}(\theta')$ is given by (see 2.5-16)).

$$\beta_{gg}{}^{jj}(\theta') = \frac{1}{\pi}\int_0^{\pi} |Z_{jg}(\theta' + \delta)|^2 \, |b_g(\delta)|^2 \, d\delta \qquad (2.5\text{-}20)$$

All of the results of this section still require only that the $\underline{\underline{F}}(\theta)$ matrix be determined on a $[0,2\pi]$ interval. These initial determinations are used to generate all values of the integrands necessary for numerical integration of (2.5-13), (2.5-17), and (2.5-19). The integrands appearing in these phase- and time-averaging integrals are so well-behaved that a Simpson's $\frac{2}{3}$ rule [72] calculation can be used to evaluate the integrals to 5-10 figure accuracy [12,17]. To produce a smooth frequency-sweep spectrum, a cubic spline interpolation routine [73,74] is used to fit a curve to the individual discrete points.

In the examples of the following chapters, the solutions on the $[0,2\pi]$ interval are determined to 12 figure accuracy with a maximum of 45 terms in the sums of (2.4-10) and (2.4-11). This requires that the $[0,2\pi]$ interval be broken up into smaller sub-intervals (see (2.4-21)), but the coupling strengths considered below are weak enough ($\beta < 0.1$) that sub-intervals of $\frac{\pi}{2}$ or $\frac{\pi}{4}$ are sufficiently small for this purpose. The integrations over phase and time are performed with interval sizes of $\frac{\pi}{16}$ in the Simpson's rule calculations. The cubic spline interpolation requires that a great many individual points be determined in the region of a peak in the spectrum, but the flatter portions of the curve are easily handled with very few points.

2.6 Damping

The semiclassical approach being used here cannot account for the spontaneous decay of the states of the system. Phenomenological decay terms can be introduced into the formalism [7,14,19] by replacing the energy terms, E_j, with the "damped" energies, $E_j - \frac{i\Gamma_j}{2}$. The

decay term is chosen to be of this form so that in the absence of an applied field the state will decay exponentially. That is, if the wavefunction for the state j is written in the interaction representation

$$\psi_j(r,t) = \phi_j(r) \exp[-i(E_j - \frac{i\Gamma_j}{2})t] \qquad (2.6\text{-}1)$$

then in the absence of an external field, the state amplitude, $b_j(t)$, will decay according to

$$b_j(t) = \exp[-\frac{\Gamma_j}{2} t] \qquad (2.6\text{-}2)$$

The transition probability, $P_{jj}(t)$ (see (2.1-9)), will then decay exponentially:

$$P_{jj}(t) = |b_j(t)|^2 = \exp(-\Gamma_j t) \qquad (2.6\text{-}3)$$

The problem with introducing relaxation effects in this manner is that it precludes the use of the Floquet formalism described in the previous section since the $\underline{\underline{F}}(2\pi)$ matrix will no longer be unitary [14,63] (see (2.4-18) and 2.5-4)). The temporal behaviour of these "damped" systems may still be studied, using methods completely analogous to those in section 2.4, and this aspect of the work will be dealt with in more detail, with examples, in Chapter 4.

Phase- and time-averaged results can be obtained from the Floquet formalism when a collision damping model is employed [17]. When this method is employed, the atoms or molecules under study are assumed to

undergo "collisions" that will interrupt their interaction with the radiation field. The mean collision time, τ, may refer, for example, to the time between molecular collisions in a gas sample, or the transit time of a beam of molecules through a laser beam. The probability that an atom or molecule has survived in the field at time t is given by [16,65]

$$\frac{1}{\tau} \exp[-(t-t_0)/\tau] \, dt_0 \tag{2.6-4}$$

where τ is the mean collision time, t is the time of measurement, and t_0 is the initial time of the interaction with the field. The damped induced transition probability becomes

$$\langle |a_j|^2 \rangle_\tau = \frac{1}{\tau} \int_{-\infty}^{t} |a_j(t-t_0)|^2 \exp[-(t-t_0)/\tau] \, dt_0 \tag{2.6-5}$$

The final phase-averaged result is (with $\theta' = \nu t$) [17]

$$\overline{P}^{\tau}_{jj} = \sum_{gg'} \{ \int_0^{2\pi} \beta_{gg'}{}^{jj}(\theta') \exp[i\Gamma_{gg'} t] d\theta' \} [\nu\tau(1-\exp[i\Gamma_{gg'}\tfrac{2\pi}{\nu}])]^{-1} \tag{2.6-6}$$

with

$$\Gamma_{gg'} = (\Delta_g - \Delta_{g'})\nu + \frac{i}{\tau} \tag{2.6-7}$$

and all other terms as previously defined (see (2.5-16)).

The exact power series solution to the time-dependent Schroedinger equation, with the extensions to Floquet formalism and the collision

damping model, as outlined above, provides an efficient and economical means of treating thoroughly the problem of multi-level systems interacting with arbitrarily strong sinusoidal radiation fields. Once the solutions over initial $[0,2\pi]$ intervals have been determined, temporal, phase- and/or time-averaged, and damped transition probabilities can all be generated.

CHAPTER 3

THE FIVE-LEVEL SYSTEM

The power series and Floquet formalism described in Chapter 2 will be applied here to a five-level model molecular system. It should be borne in mind that although this chapter concerns itself with a five-level system and some moderately strong laser intensities, the extension to more levels and stronger laser sources poses no problem in principle [11,14]. The solution in matrix form ((2.4-15), for example) requires only that the dimensions of the matrices be changed to accommodate the number of levels to be included in the calculation [75], while arbitrarily strong coupling strengths can be handled with the retention of a reasonably small number of terms in the power series sums (see (2.4-10)) by breaking the $[0,2\pi]$ interval of the calculation into smaller sub-intervals (see (2.4-21)) [17]. That said, it must be pointed out that, in fact, larger calculations can quickly become expensive. The five-level model was chosen because it provides a reasonably realistic model for investigating interesting features of single- and multi-photon spectroscopy while maintaining economic feasibility.

3.1 The five-level energy level diagram

The energy level diagram for the model five-level molecular system is shown in figure (3-1). This model consists of an original two-level system in which the excited state is coupled through static matrix elements to three nearly isoenergetic "secondary" levels. Transitions from the ground state to these secondary levels are forbidden, so it

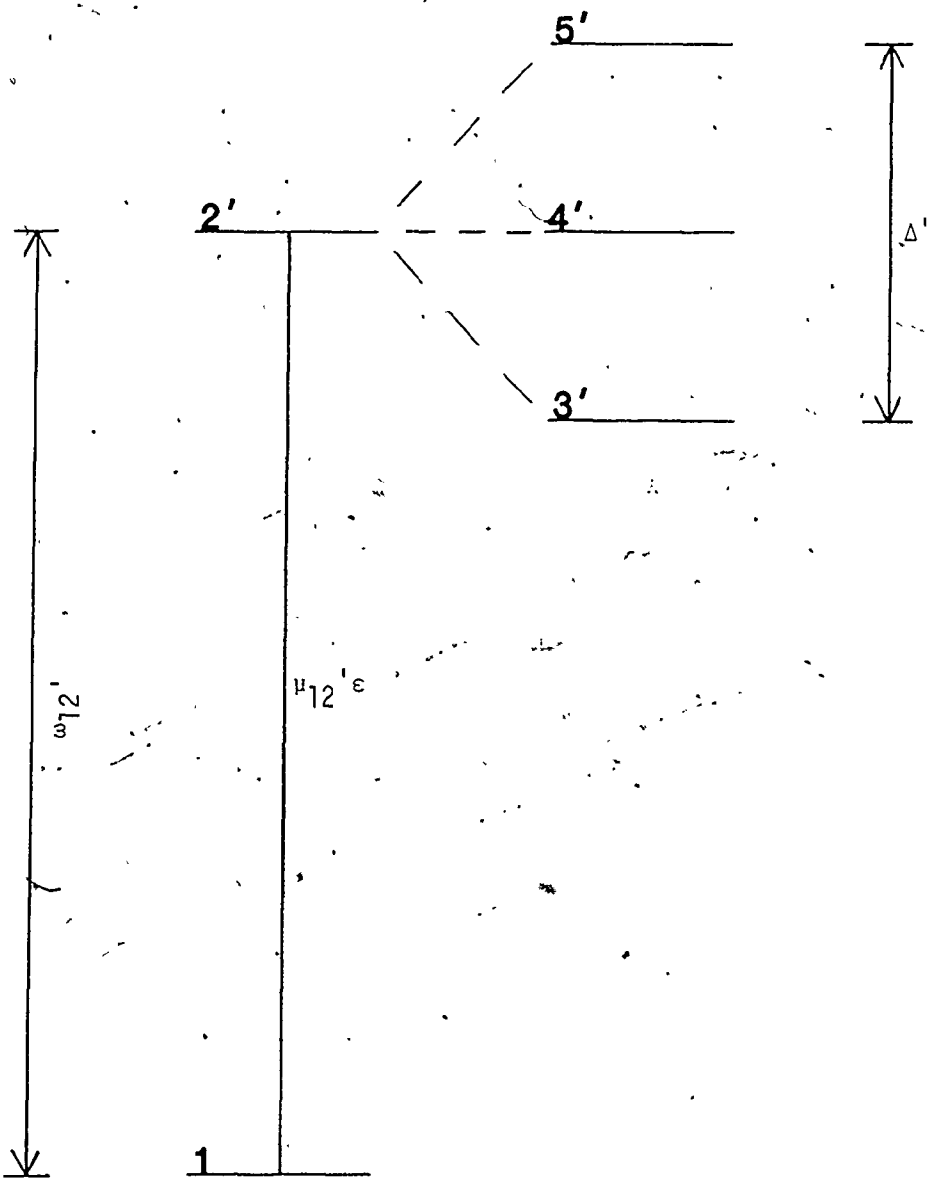

Figure (3-1). Energy level diagram for the undiagonalized five-level system. The transition from level 1 to level 2' is allowed. Level 2' is coupled through static terms, V, to "background" states 3', 4', and 5'. $E_1 = -7.12 \times 10^{-2}$, $E_{2'} = 0$, $E_{3'} = -1.50 \times 10^{-4}$, $E_{4'} = 0$, $E_{5'} = 1.50 \times 10^{-4}$. $E_{2'} - E_1 = \omega_{12'} = 7.12 \times 10^{-2}$ ($\sim$15,630 cm^{-1}), $\Delta' = E_{5'} - E_{3'} = 3.00 \times 10^{-4}$ ($\sim$65 cm^{-1}), $V = 5.00 \times 10^{-5}$ ($\sim$11 cm^{-1}). The value of the coupling strength, $\mu_{12'}\varepsilon$, varies in the applications that follow.

is only through the static coupling, V, that molecules make their way into these "background" states.

The energy of the allowed transition in the original two-level system lies in the visible region of the electromagnetic spectrum ($E_{2'} - E_1 = \omega_{12'} \sim 15630\ cm^{-1}$) and is on the order of a transition in, for example, the B ← X system of the iodine molecule [76]. The energy spacings between the background levels are taken to be equal, as are the couplings between the background levels and the excited state of the two-level system. These are chosen in this manner mainly for simplicity; the formalism can just as easily handle unequal spacings and couplings. The $\mu\varepsilon^\circ$ matrix elements (see (2.4-6)) that couple the secondary levels to the two-level system are relatively large [77], but this serves to emphasize the effects of the coupling.

Although the calculations may be carried out with the representation of figure (3-1), more easily physically interpretable results are obtained by taking the static perturbation into account before the laser radiation is applied. The static coupling terms, which can correspond to internal couplings between levels (e.g. spin-orbit coupling) or to the application of an external static field [17], have the effect of mixing the four upper levels and "splitting" their energies [43,78]. This is accounted for by first diagonalizing the upper levels of the system to produce the energy level diagram of figure (3-2). Each of the diagonalized energy levels now has some of the original excited state 2' character and, therefore, some of the oscillator strength of the allowed transition. None of the excited states are coupled to each other.

Figure (3-2). Energy level diagram for the diagonalized (in V) five-level system. Transitions from level 1 to all four upper levels are allowed. $E_1 = -7.12 \times 10^{-2}$, $E_2 = -1.6730 \times 10^{-4}$, $E_3 = -4.4829 \times 10^{-5}$, $E_4 = 4.4829 \times 10^{-5}$, $E_5 = 1.6730 \times 10^{-4}$, $\Delta = E_5 - E_2 = 3.3460 \times 10^{-4}$ ($\sim 75\ cm^{-1}$), $\omega^{\circ}_{12} = E_2 - E_1 = 7.1033 \times 10^{-2}$ ($\sim 15{,}590\ cm^{-1}$), $\omega^{\circ}_{13} = 7.1155 \times 10^{-2}$ ($\sim 15{,}620\ cm^{-1}$), $\omega^{\circ}_{14} = 7.1245 \times 10^{-2}$ ($\sim 15{,}635\ cm^{-1}$), $\omega^{\circ}_{15} = 7.1367 \times 10^{-2}$ ($\sim 15{,}665\ cm^{-1}$). The diagonalized upper levels can be expressed in terms of the excited states of the undiagonalized representation as

$$\psi_2 = 0.32506\,\phi_2 - 0.93930\,\phi_3 - 0.097146\,\phi_4 - 0.051222\,\phi_5$$

$$\psi_3 = -0.62796\,\phi_2 - 0.29854\,\phi_3 + 0.70040\,\phi_4 + 0.16116\,\phi_5$$

$$\psi_4 = -0.62796\,\phi_2 - 0.16116\,\phi_3 - 0.70040\,\phi_4 + 0.29854\,\phi_5$$

$$\psi_5 = 0.32506\,\phi_2 + 0.051222\,\phi_3 + 0.097146\,\phi_4 + 0.93930\,\phi_5$$

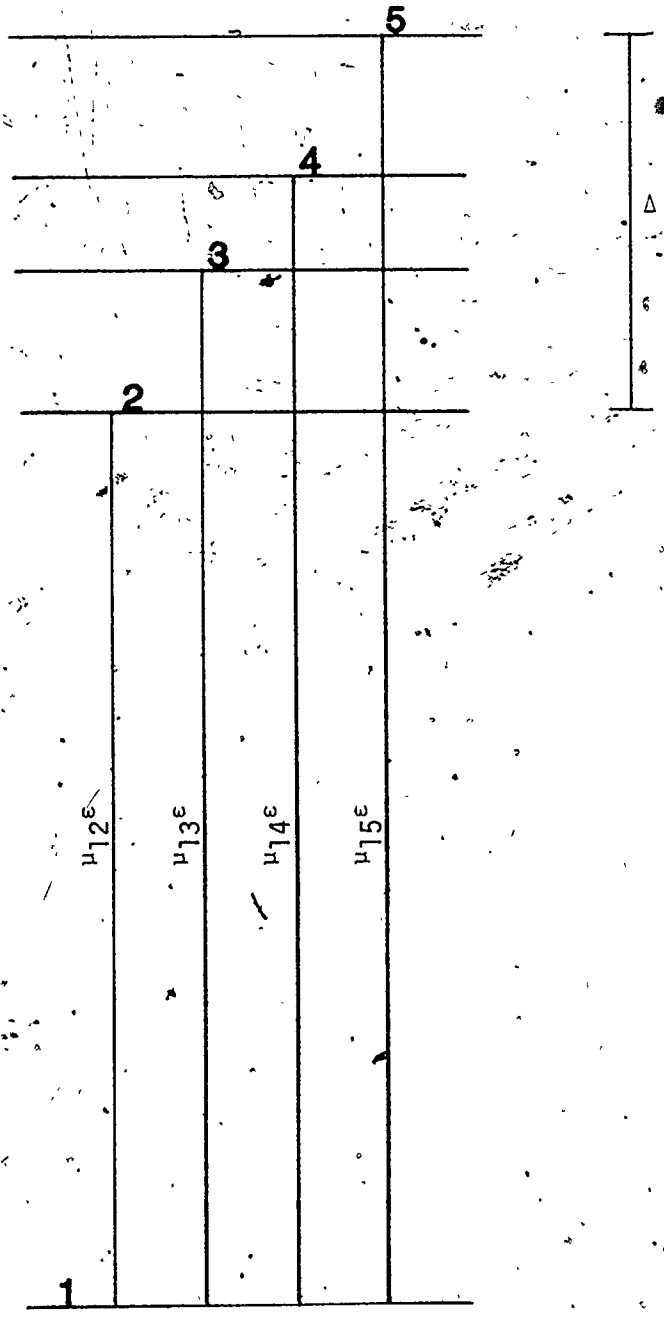
5
4
3
2
1
Δ
$\mu_{12\varepsilon}$
$\mu_{13\varepsilon}$
$\mu_{14\varepsilon}$
$\mu_{15\varepsilon}$

3.2 Single-photon results

Conventional absorption spectroscopy consists of scanning the wavelength of the laser radiation in the region where the frequency is approximately equal to the energy difference between the ground and excited states, and monitoring the absorption of radiation. This is in contrast to multi-photon spectroscopy in which more than one photon is involved, and the laser frequency is some fraction of the total transition energy [3,13,79]. This section concerns itself only with the single-photon transitions in the five-level model system.

3.2.1 Steady-state spectra

The phase- and long-time-averaged induced transition probability $(1 - \overline{P}_{11})$, calculated from (2.5-19), corresponds to the steady-state absorption spectrum. In figure (3-3) the spectrum for the diagonalized energy level diagram of figure (3-2) with $\mu_{12}\varepsilon = \mu_{15}\varepsilon = 9.199 \times 10^{-4}$ and $\mu_{13}\varepsilon = \mu_{14}\varepsilon = -1.777 \times 10^{-3}$ is shown. These values of the coupling strengths correspond to the value of $\mu_{12},\varepsilon = 2.83 \times 10^{-3}$ in the undiagonalized energy level diagram of figure (3-1). The spectrum consists of a single broad peak that shows no discernible structure from the four individual upper levels. This is not surprising given the width of the peak (half-width at half-maximum (HWHM) $\sim$ 2.85×10^{-3}) and the fact that the four excited levels reside within a very narrow frequency band ($E_5 - E_2 = 3.34 \times 10^{-4}$).

Of note is the fact that the spectrum very much resembles the result that would be predicted for the original two-level system. The single peak has a maximum value of approximately 0.5 and a HWHM approximately equal to the original μ_{12},ε value, in agreement with

Figure (3-3). The phase- and long-time-averaged induced transition probability, $(1 - \overline{P}_{11})$, for the five-level energy level diagram of figure (3-2) with $\mu_{12}\varepsilon = \mu_{15}\varepsilon = 9.199 \times 10^{-4}$ and $\mu_{13}\varepsilon = \mu_{14}\varepsilon = -1.777 \times 10^{-3}$ ($\mu_{12}'\varepsilon = 2.83 \times 10^{-3}$). The single peak centred around $\nu \sim 7.125 \times 10^{-2}$ has a maximum peak height of $\sim$0.503 and a half-width at half-maximum (HWHM) of $\sim 2.85 \times 10^{-3}$.

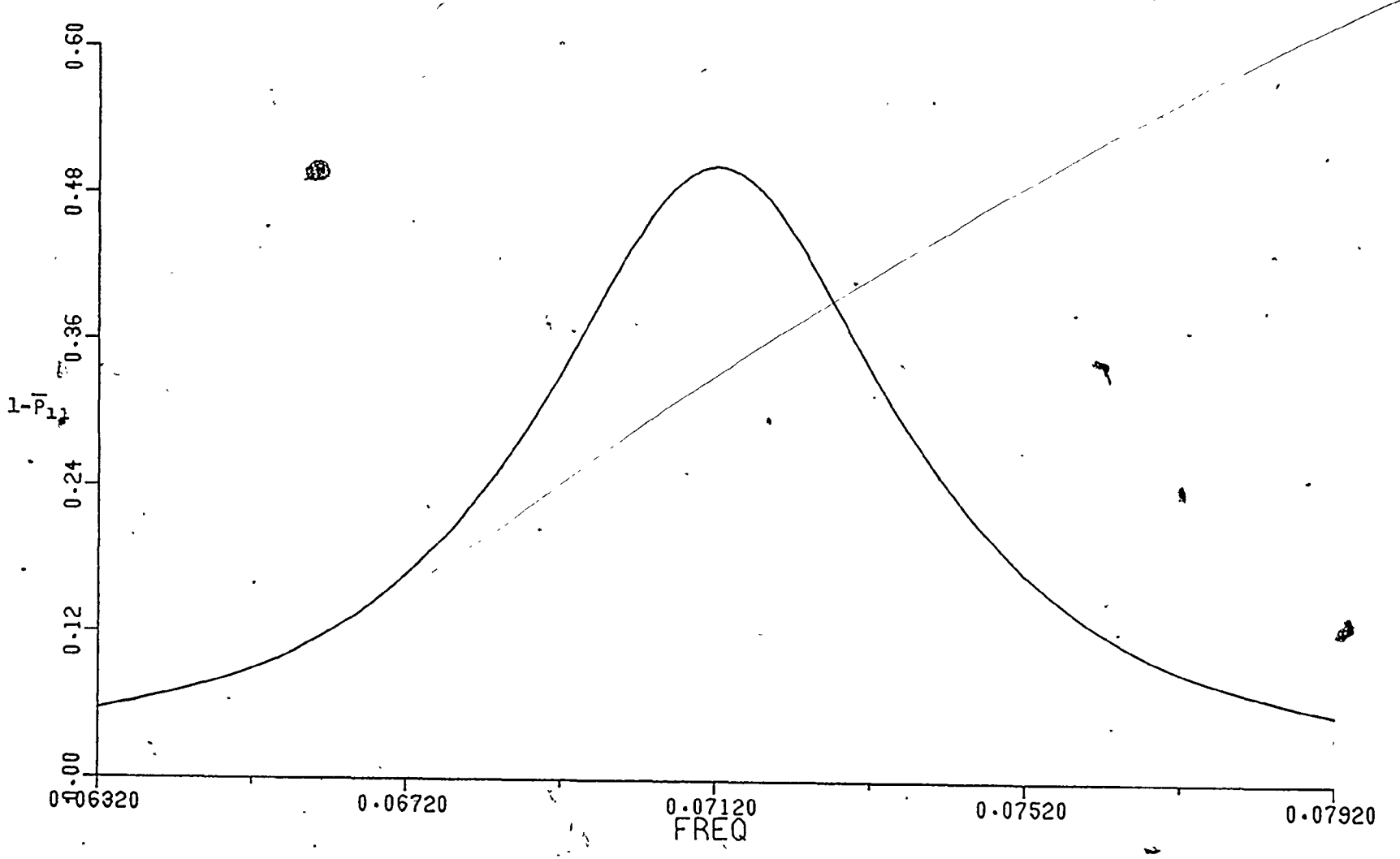
0.60
0.48
0.36
0.24
0.12
0.00
$1-\bar{P}_{11}$
0.06320
0.06720
0.07120
0.07520
0.07920
FREQ

the approximate result given by (2.3-9). The excited states of this system, then, appear to be acting like a single level rather than as four individual states.

In this strong coupling case, the four excited levels act like a single level since the width of the peak completely overwhelms the energy level spacings ($\frac{\Delta}{HWHM} << 1$, where $\Delta = E_5 - E_2$). The correlation with the undiagonalized $\mu_{12'\varepsilon}$ is also in agreement with the fact that the static coupling terms are very small in comparison to the coupling of the original two levels through the radiation field (ie. $\frac{V}{\mu_{12'\varepsilon}} < 1.8 \times 10^{-2}$). Indeed, if the static coupling terms were further reduced, eventually, as they approach zero, the original two-level system would be produced.

The single peak of figure (3-3) has been decomposed into the contributions from the individual upper levels in figure (3-4). Although the matrix elements coupling the excited states to the ground state are not all equal, the widths of the individual peaks are almost the same ($HWHM_2 \sim HWHM_5 \sim 3.20 \times 10^{-3}$, $HWHM_3 \sim HWHM_4 \sim 2.80 \times 10^{-3}$) and are approximately equal to $\mu_{12'\varepsilon}$. No link can be made between the widths of these individual levels and their diagonalized coupling strengths. The differing $\mu\varepsilon$ values are manifested in the different peak maxima for $\overline{P}_{22}$ and $\overline{P}_{55}$ ($\sim$0.057) as opposed to $\overline{P}_{33}$ and $\overline{P}_{44}$ ($\sim$0.197). That is, the larger matrix elements coupling levels 3 and 4 to the ground state do not result in a greater width for their peaks, but do correlate with a greater overall averaged transition probability.

Finally, it is pointed out that the peak maxima in figure (3-4) do not correlate with the energy level positions of figure (3-2). Since

Figure (3-4). The phase- and long-time-averaged (steady-state) induced transition probabilities for the four individual upper levels of figure (3-3). Approximate peak positions and peak (heights) are given by $\omega_{12} \sim 7.15 \times 10^{-2}$, height ~ 0.057; $\omega_{13} \sim 7.13 \times 10^{-2}$, height ~ 0.197; $\omega_{14} \sim 7.11 \times 10^{-2}$, height ~ 0.197; $\omega_{15} \sim 7.09 \times 10^{-2}$, height ~ 0.057. (a) $\overline{P}_{22}$ (b) $\overline{P}_{33}$ (c) $\overline{P}_{44}$ (d) $\overline{P}_{55}$

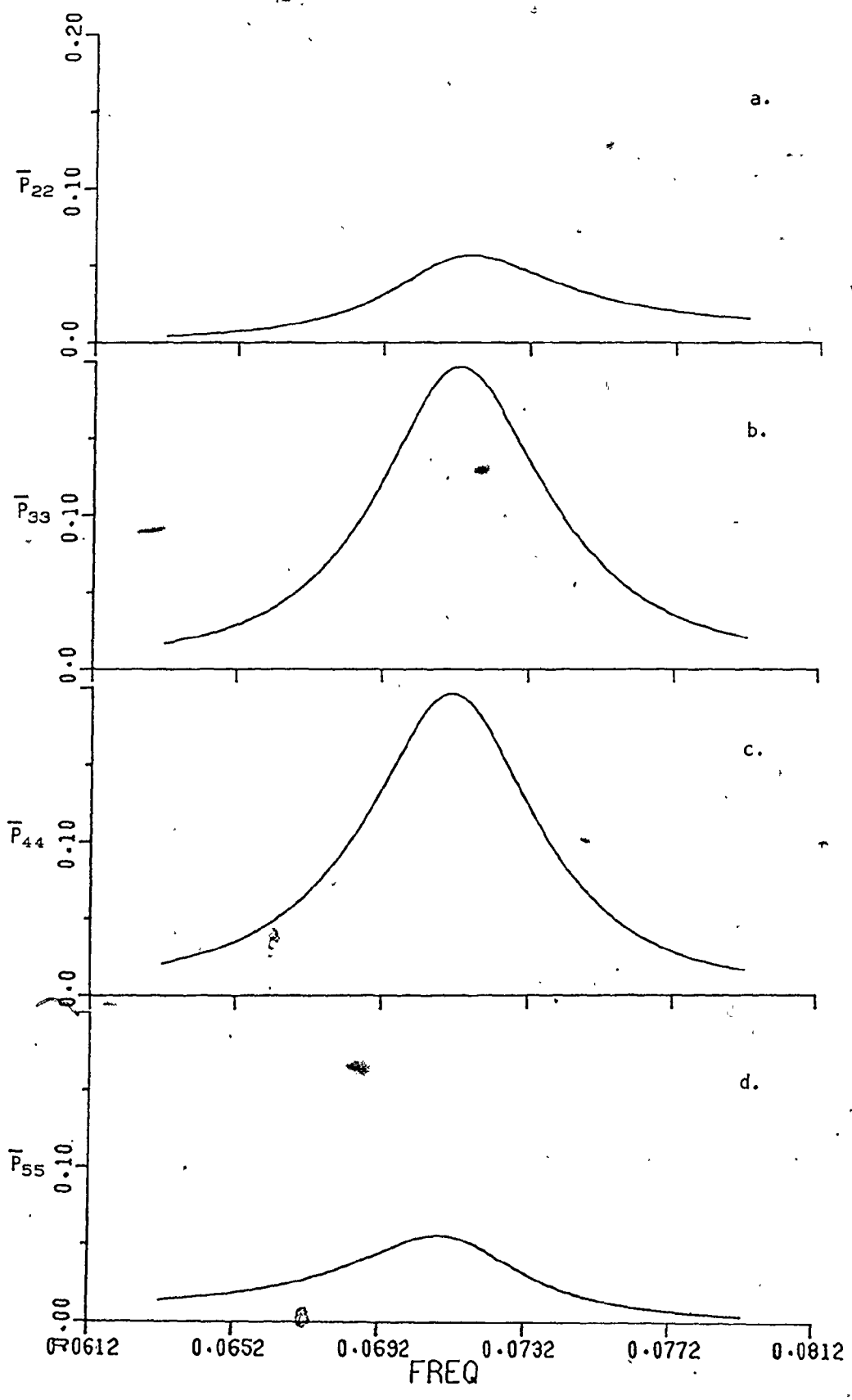
0.20
0.10
0.0
$\bar{P}_{22}$
a.
$\bar{P}_{33}$
b.
$\bar{P}_{44}$
c.
$\bar{P}_{55}$
d.
0.00
0.0612
0.0652
0.0692
0.0732
0.0772
0.0812
FREQ

the peaks are so wide, it is not unexpected that the individual peaks lie on top of one another. However, the unusual positions of the peak values in the curves ($\omega_{12} \sim 0.0715$, $\omega_{13} \sim 0.0713$, $\omega_{14} \sim 0.0711$, $\omega_{15} \sim 0.0709$) relative to the zero field predictions ($E_2 - E_1 = \omega_{12}^{\circ} \sim 0.071033$, $\omega_{13}^{\circ} \sim 0.071155$, $\omega_{14}^{\circ} \sim 0.071245$, $\omega_{15}^{\circ} \sim 0.071367$) imply that the individual levels are "stealing" intensity from one another in a very complicated manner. This aspect of the behaviour will be dealt with more thoroughly below.

Figure (3-3) indicates that when the coupling strengths are large, the four upper states give the appearance of a single level. In order to resolve the individual peaks in the absorption spectrum, the coupling strengths must be reduced. A weak field calculation for the five-level model is illustrated by figure (3-5). In this example, the coupling strengths are given by $\mu_{12'\varepsilon} = 2.83 \times 10^{-5}$, $\mu_{12\varepsilon} = \mu_{15\varepsilon} = 9.199 \times 10^{-6}$ and $\mu_{13\varepsilon} = \mu_{14\varepsilon} = -1.777 \times 10^{-5}$. Now the spectrum consists of four very distinct peaks corresponding to the four excited levels. In marked contrast to the previous spectrum (figure (3-3)), the system here behaves like four separate levels coupling independently to the ground state.

The steady-state contributions from each of the four upper levels to the overall spectrum of figure (3-5) are shown in figure (3-6). The individual levels are each acting like the excited state of a simple two-level system. The peak height for each is approaching 0.5, and the width ($HWHM_2 \sim HWHM_5 \sim 1.0 \times 10^{-5}$, $HWHM_3 \sim HWHM_4 \sim 2.0 \times 10^{-5}$) is approximately equal to the diagonalized $\mu\varepsilon$ value. The peak positions are located very near the resonance frequencies predicted by figure (3-2).

Figure (3-5). The steady-state induced transition probability, $(1 - \overline{P}_{11})$, for the five-level energy level diagram of figure (3-2) with $\mu_{12}\varepsilon = \mu_{15}\varepsilon = 9.199 \times 10^{-6}$ and $\mu_{13}\varepsilon = \mu_{14}\varepsilon = -1.777 \times 10^{-5}$ ($\mu_{12}, \varepsilon = 2.83 \times 10^{-5}$). The spectrum consists of four peaks (peak heights $\sim$ 0.503, 0.512, 0.512, 0.503) located at the expected resonance frequencies, $\omega_{12} = 7.1033 \times 10^{-2}$, $\omega_{13} = 7.1155 \times 10^{-2}$, $\omega_{14} = 7.1245 \times 10^{-2}$, $\omega_{15} = 7.1367 \times 10^{-2}$.

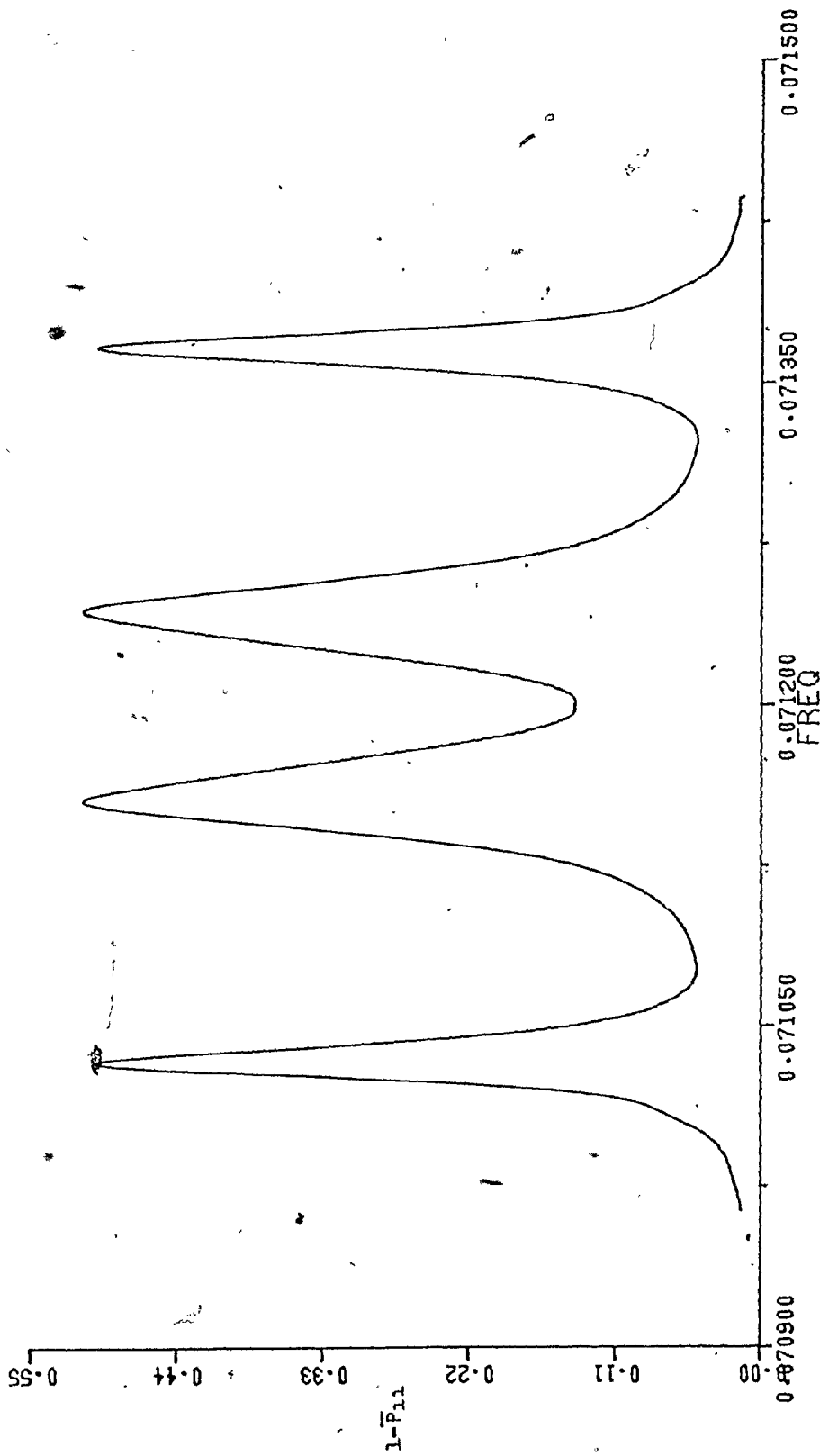
0.071500
0.071350
0.071200
FREQ
0.071050
0.070900
0.00
0.11
0.22
0.33
0.44
0.55
$1-\bar{P}_{11}$

Figure (3-6). Steady-state induced transition probabilities for the four individual upper levels of figure (3-2) for the coupling strengths given in figure (3-5). The widths of the individual peaks ($HWHM_2 \sim HWHM_5 \sim 1.0 \times 10^{-5}$, $HWHM_3 \sim HWHM_4 \sim 2.0 \times 10^{-5}$) are on the order of the coupling strengths given in figure (3-5). The peak heights are given by $\overline{P}_{22} \sim \overline{P}_{55} \sim 0.492$ and $\overline{P}_{33} \sim \overline{P}_{44} \sim 0.495$. (a) $\overline{P}_{22}$ (b) $\overline{P}_{33}$ (c) $\overline{P}_{44}$ (d) $\overline{P}_{55}$

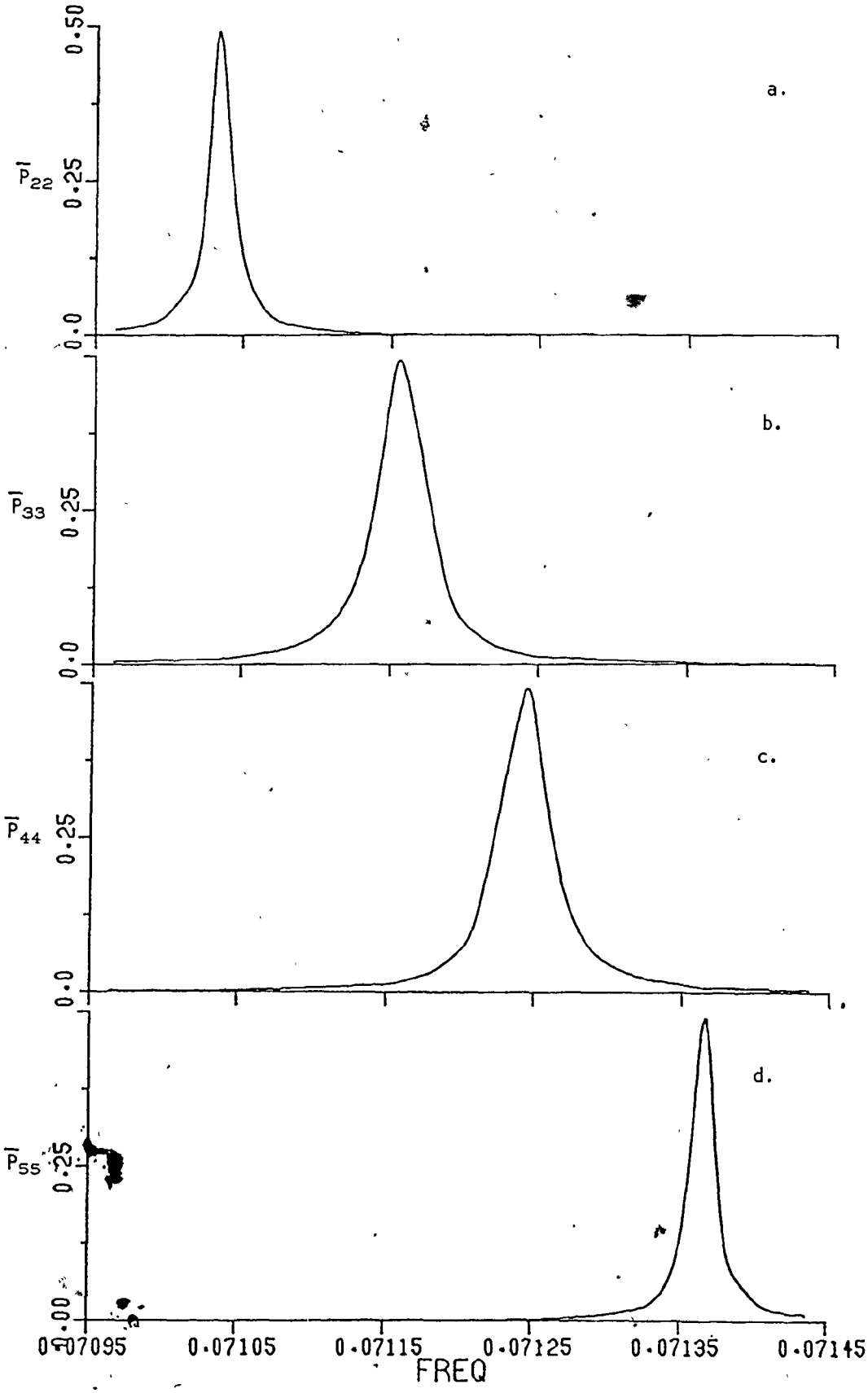
a.
b.
c.
d.
$\bar{P}_{22}$
$\bar{P}_{33}$
$\bar{P}_{44}$
$\bar{P}_{55}$
0.50
0.25
0.0
0.00
0.07095
0.07105
0.07115
0.07125
0.07135
0.07145
FREQ

In the limiting case in which the four levels act completely independently, the absorption spectrum should consist of four peaks of 0.5 maximum height. Figure (3-5) shows that there is still some overlapping of peaks such that the total probability exceeds 0.5 at the peaks. Strictly speaking, the weak field limit requires a laser intensity that is weaker still, if there is to be no overlapping of the peaks. Similarly, the strong field case of figure (3-3) approaches a two-level result, but has a maximum in the steady-state spectrum that is just over 0.5. As mentioned in the discussion of figure (3-3), an exact two-level result is obtained only if the static perturbation terms are allowed to disappear completely.

Figure (3-7) shows the steady-state spectrum for the case in which $\mu_{12}\varepsilon = 7.14 \times 10^{-5}$, $\mu_{12}\varepsilon = \mu_{15}\varepsilon = 2.32 \times 10^{-5}$ and $\mu_{13}\varepsilon = \mu_{14}\varepsilon = -4.483 \times 10^{-5}$. As the laser intensity is increased from the previous case, the peaks corresponding to the individual upper levels have broadened and now overlap considerably, especially the peaks for levels 3 and 4. This overlapping in the middle of the spectrum produces overall transition probabilities significantly greater than 0.5.

The individual level steady-state contributions are shown in figure (3-8). The peak positions ($\mu_{12} \sim 0.07104$, $\mu_{13} \sim 0.07116$, $\mu_{14} \sim 0.07124$, $\mu_{15} \sim 0.07136$) and widths ($HWHM_2 \sim HWHM_5 \sim 2.7 \times 10^{-5}$, $HWHM_3 \sim HWHM_4 \sim 4.7 \times 10^{-5}$) are close to the two-level Rabi predictions. The overlapping of the individual peaks pointed out above in the overall steady-state spectrum can be clearly seen by comparing the four single-level spectra. Also, although the overlapping of peaks causes the total spectrum to exceed 0.5 at the peak maxima, the significant amounts of population in the neighbouring levels acts to

Figure (3-7), The steady-state induced transition probability, $(1 - \overline{P}_{11})$, for the five-level energy level diagram of figure (3-2) with $\mu_{12}\varepsilon = \mu_{15}\varepsilon = 2.321 \times 10^{-5}$ and $\mu_{13}\varepsilon = \mu_{14}\varepsilon = -4.483 \times 10^{-5}$ ($\mu_{12}\varepsilon = 7.14 \times 10^{-5}$). The four peaks overlap considerably, so all four peak maxima exceed 0.5. The peak heights are $\sim$ 0.510, 0.570, 0.570, 0.510.

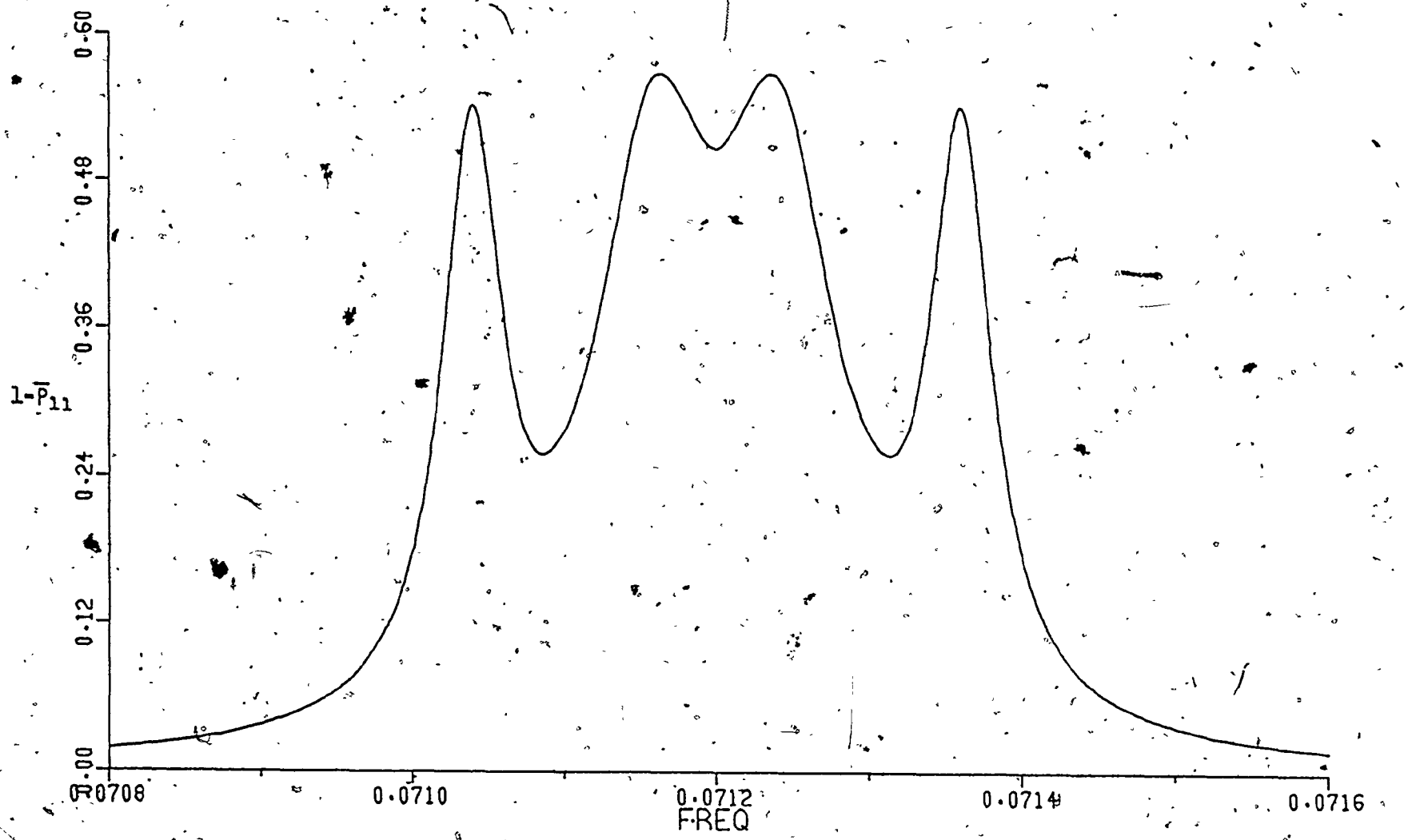
0.60
0.48
0.36
0.24
0.12
0.00
$1-\bar{P}_{11}$
0.0708
0.0710
0.0712
0.0714
0.0716
FREQ

Figure (3-8). Steady-state induced transition probabilities for the four individual upper levels of figure (3-2) for the coupling strengths given in figure (3-7). Although the overall spectrum in figure (3-7) shows the peaks exceeding 0.5, the individual level contributions are all ~ 0.46, less than 0.5 (a) $\overline{P}_{22}$, HWHM $\sim 2.7 \times 10^{-5}$ (b) $\overline{P}_{33}$, HWHM $\sim 4.7 \times 10^{-5}$ (c) $\overline{P}_{44}$, HWHM $\sim 4.7 \times 10^{-5}$ (d) $\overline{P}_{55}$, HWHM $\sim 2.7 \times 10^{-5}$.

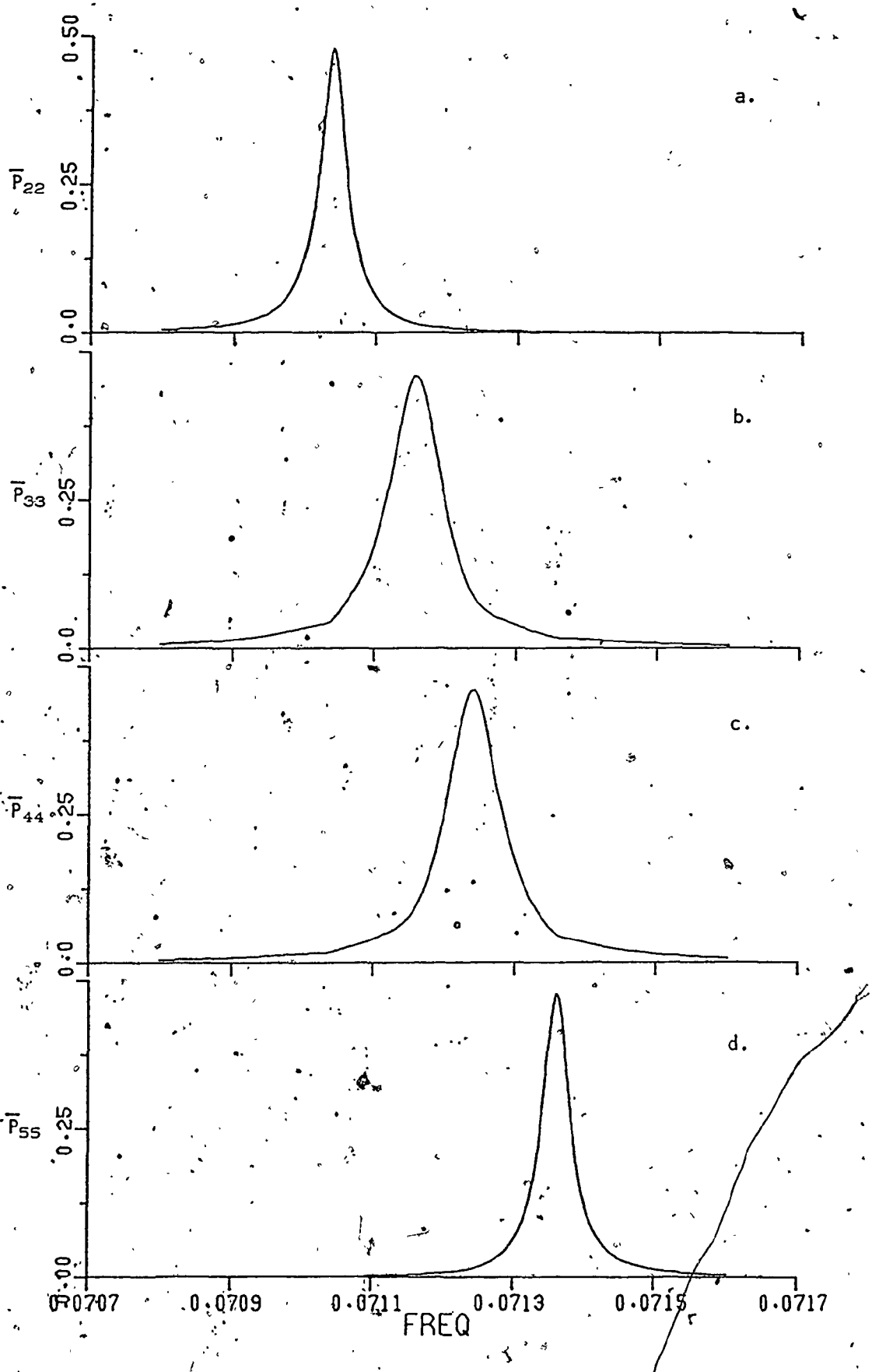
a.
b.
c.
d.
$\bar{P}_{22}$
$\bar{P}_{33}$
$\bar{P}_{44}$
$\bar{P}_{55}$
0.50
0.25
0.0
0.0707
0.0709
0.0711
0.0713
0.0715
0.0717
FREQ

prevent the individual averaged transition probabilities from attaining a maximum value of 0.5.

A further increase in laser intensity produced the spectrum shown in figure (3-9). In this example, $\mu_{12}\varepsilon = 2.83 \times 10^{-4}$, $\mu_{12}\varepsilon = \mu_{15}\varepsilon = 9.199 \times 10^{-5}$ and $\mu_{13}\varepsilon = \mu_{14}\varepsilon = -1.777 \times 10^{-4}$. The widths of the individual levels are now such that the steady-state spectrum for the system consists of a single peak with no apparent structure due to the four upper levels. Continuing the trend from the previous spectra, the overlapping of peaks means that the maximum height in the peak is well above 0.5 (eventually, the five-level system will approach a two-level limit with a maximum steady-state absorption peak of 0.5 as $\frac{V}{\mu_{12}\varepsilon} \to 0$; see figure (3-3) and its discussion).

The decomposition of figure (3-9) into the contributions from the individual levels is shown in figure (3-10). Figures (3-9) and (3-10) offer a unique way to discuss the trends in the spectra in going from the extreme cases of figure (3-3) to figure (3-5). Although figure (3-8) resembles the single peak spectrum of figure (3-3), the individual results are very different from those of figure (3-4). Unlike the strong coupling case in which the individual contributions consisted of peaks of similar width covering the same frequency range, the individual peaks in figure (3-10) have differing half-widths ($HWHM_2 \sim HWHM_5 \sim 1.2 \times 10^{-4}$, $HWHM_3 \sim HWHM_4 \sim 3.0 \times 10^{-4}$) and peak positions. While these values of the half-widths do not correlate with the Rabi predictions as well as the peaks in figure (3-6) do, the trend to greater widths for greater coupling strengths is present.

The overlapping of peaks in figure (3-10) illustrates that the individual levels can steal intensity from one another. The peaks

Figure (3-9). The steady-state induced transition probability $(1 - \overline{P}_{11})$, for the five-level energy level diagram of figure (3-2) with $\mu_{12}\varepsilon = \mu_{15}\varepsilon = 9.199 \times 10^{-5}$ and $\mu_{13}\varepsilon = \mu_{14}\varepsilon = -1.777 \times 10^{-4}$ ($\mu_{12'}\varepsilon = 2.83 \times 10^{-4}$). The single peak has a maximum value of ~ 0.78 and a HWHM $\sim 2.4 \times 10^{-4}$.

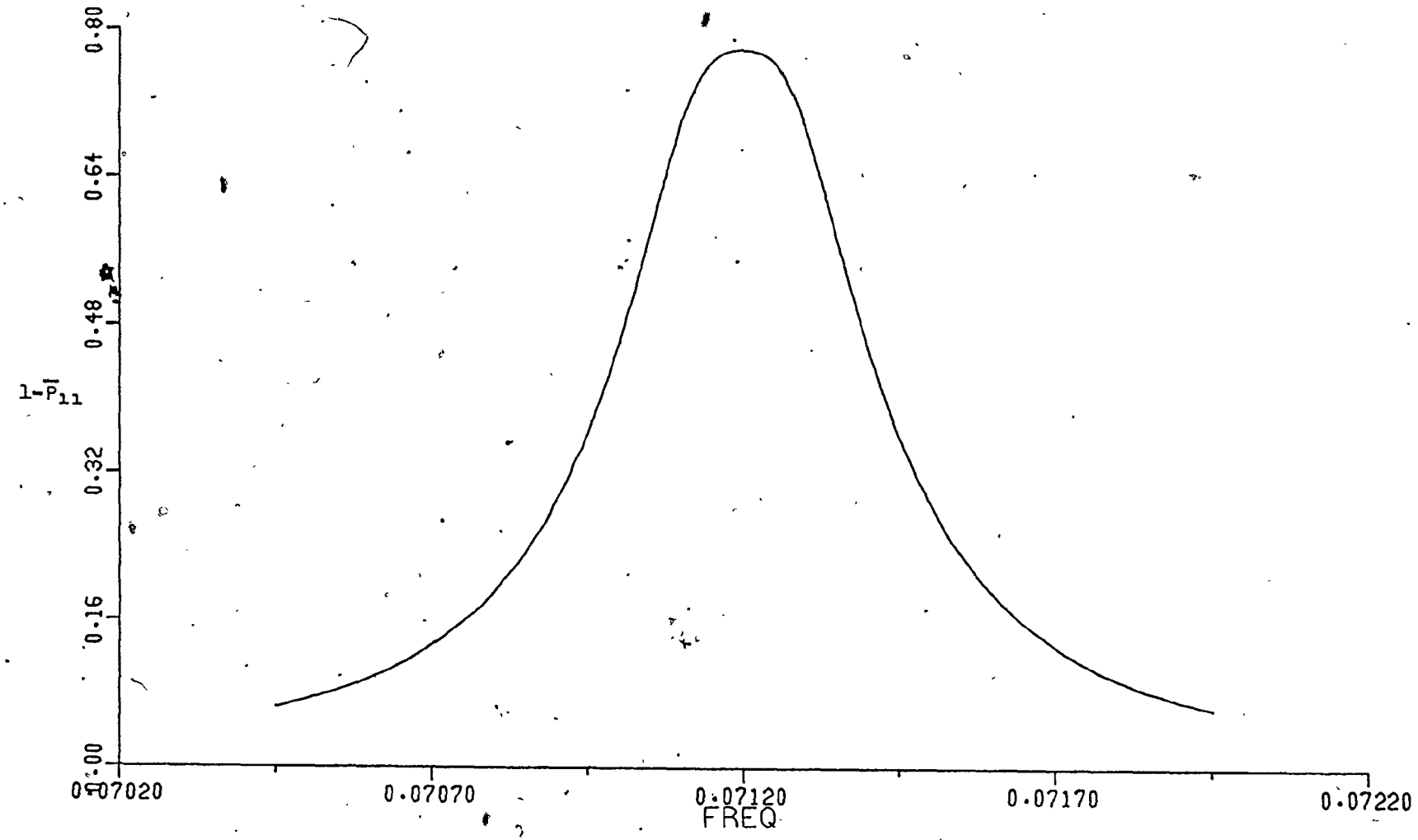
0.80
0.64
0.48
0.32
0.16
0.00
$1-\bar{P}_{11}$
0.07020
0.07070
0.07120
0.07170
0.07220
FREQ

Figure (3-10). Steady-state induced transition probabilities for the four individual upper levels of figure (3-2) for the coupling strengths given in figure (3-9). These plots show unexpected resonance frequencies and "shoulders" for some peaks. (a) $\overline{P}_{22}$, $\omega_{12} \sim 7.113 \times 10^{-2}$, height ~ 0.29, HWHM $\sim 1.2 \times 10^{-4}$, (b) $\overline{P}_{33}$, shoulder $\sim 7.111 \times 10^{-2}$, $\omega_{13} \sim 7.123 \times 10^{-2}$, height ~ 0.20, (c) $\overline{P}_{44}$, shoulder $\sim 7.132 \times 10^{-2}$, $\omega_{14} \sim 7.117 \times 10^{-2}$, height ~ 0.20, (d) $\overline{P}_{55}$, $\omega_{15} \sim 7.127 \times 10^{-2}$, height ~ 0.29, HWHM $\sim 1.2 \times 10^{-4}$.

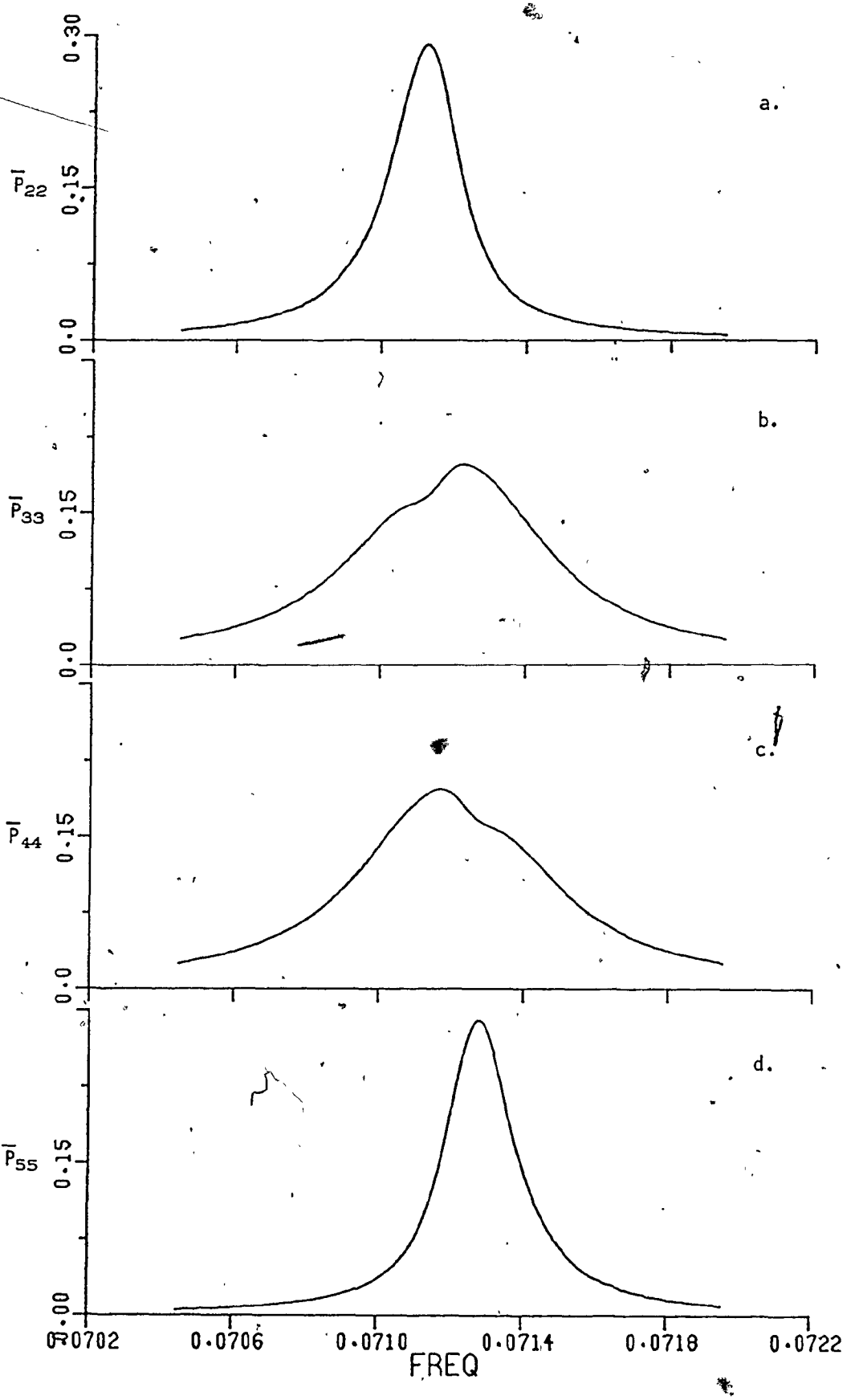
0.30
0.15
0.0
$\bar{P}_{22}$
a.
$\bar{P}_{33}$
b.
$\bar{P}_{44}$
c.
$\bar{P}_{55}$
d.
0.00
0.0702
0.0706
0.0710
0.0714
0.0718
0.0722
FREQ

corresponding to levels 3 and 4 (figures (3-10b) and 3-10c)) have their resonance (ie. peak maximum) frequency positions "reversed" in that the peak in $\overline{P}_{33}$ (located at $\omega_{13} \sim 0.07123$) is nearer to the expected resonance frequency for level 4 ($\omega_{14}^{\circ} \sim 0.071245$) than that for level 3 ($\omega_{13}^{\circ} \sim 0.071155$), and vice versa. Near the frequency of the expected resonance, the steady state transition probability has a shoulder ($\omega_{13} \sim 0.07111$) that has an intensity ($\overline{P}_{33} \sim 0.16$) near that of the peak maximum ($\overline{P}_{33} \sim 0.20$). This somewhat unusual intensity distribution is explained in part by examining the trend illustrated by figures (3-5), (3-7), and (3-9). As the laser intensity is increased, the widths of the peaks broaden and overlap until in (3-9) they have the appearance of a single peak. The widths of the individual levels 3 and 4 (figure (3-10)), relative to their energy spacing, are such that considerable average transition probability would be anticipated for level 3 at the expected resonance frequency of level 4, and vice versa. Given this, an interpretation for the unusual peak positions is that the already-expected high steady-state transition probability for, say, level 3 at the level 4 resonance frequency is apparently further enhanced by the efficiency with which level 4 returns population to the rest of the system through the ground state. The shoulders on the peaks are very close to the expected resonance frequencies, and apparently represent what remains of the expected resonance peaks. The same stealing phenomenon has been pointed out earlier in the discussion of figure (3-4). Arguments similar to those just outlined can be used in the strong coupling case to explain the unusual peak positions and the "reversed intensities" in the wings of the peaks in figure (3-4); see also section 3.2.2.

Finally, it should be remembered that the Bloch-Seigert shift (see (2.3-15) and 2.3-17)) predicts that the position of the peak in a two-level spectrum will not be at the exact frequency of the energy level diagram, but rather will be displaced toward higher frequency. Since the solution used above is exact, it takes into account the shifts in frequencies so no corrections of the results are necessary; the Bloch-Seigert shifts are already present in the spectra presented above. Because the shift depends on the square of the coupling strength, it would be expected that the most significant effect will be in the strong coupling case of figure (3-3). In fact, assuming the five-level systems to behave like a two-level system with $\mu\varepsilon = 2.83 \times 10^{-3}$ ($\beta < 0.04$) leads to a prediction of a shift of only 2.81×10^{-5}. Compared to the width of the peak (HWHM $\sim 2.85 \times 10^{-3}$) a shift of this size is too small to be observed graphically. Examination of the numerical results used to generate figure (3-3) indicates that a small shift ($<3 \times 10^{-5}$) is present. The weaker coupling cases ($\beta < 0.004$) have correspondingly smaller shifts associated with them, and none are significant enough to effect the qualitative interpretations of the plots presented above.

3.2.2 Temporal results

The time-dependent behaviour of the systems described above can be determined from the power series solution results [11] (see (2.4-15) for example) or from the Floquet formalism [14] (see 2.5-11)). When the coupling strengths are large, or for multi-photon spectra, the initial phase of the sinusoidal field (see (2.2-7)) can have a significant effect on the curves that are generated [14]. To avoid

difficulties of this type, the phase-averaged treatment given by (2.5-14) can be used to generate temporal transition probabilities that are more readily compared to the spectra of section 3.2.1. The resulting temporal plots can be used in concert with the steady-state results to better understand the behaviour of the systems under study. The ordering of the discussion below follows that for the steady-state discussion of the last section, namely $\mu_{12},\varepsilon = 2.83 \times 10^{-3}$, 2.83×10^{-5}, 7.14×10^{-5}, 2.83×10^{-4}.

Figure (3-11) shows the temporal behaviour of the upper levels of the five-level system of figures (3-3) and (3-4) as a function of both time and radiation frequency. The maximum peak heights as a function of frequency reflect the steady-state results of figure (3-4). As pointed out in the discussion of that figure, the upper states do not act so much as individual levels as they do parts of a single broad level. This is especially in evidence when the steady-state or temporal results are examined near the resonance peak ($\nu = 0.0712$) in the total steady-state spectrum of figure (3-3). In the temporal plots, the ground state will at times be completely de-populated (figure 3-12)), and will approach a steady-state value of 0.5 in the phase- and time-averaged spectrum. However, none of the excited states receives a majority of the excited population. Instead, the excited levels overlap so much that all four will show appreciable transition probability, with the amount in each level dictated by the fraction of the original excited state residing in it [80]. Further, the period for the de-population and re-population of the ground state ($\Delta t \sim 2200$ at $\nu = 0.0712$, see figure (3-12)) is approximately equal to the Rabi two-level prediction, $\frac{2\pi}{\mu\varepsilon}$ (see (2.3-8)), where the $\mu\varepsilon$ value

Figure (3-11). The phase-averaged temporal behaviour of the upper levels of the five-level system of figures (3-3) and (3-4). Frequencies were chosen to include some of the expected resonance frequencies (see figure (3-2)) and some of the approximate observed resonance frequencies (see figures (3-3) and (3-4)). (a) $\overline{P}_{22}(t)$ (b) $\overline{P}_{33}(t)$ (c) $\overline{P}_{44}(t)$ (d) $\overline{P}_{55}(t)$.

a.

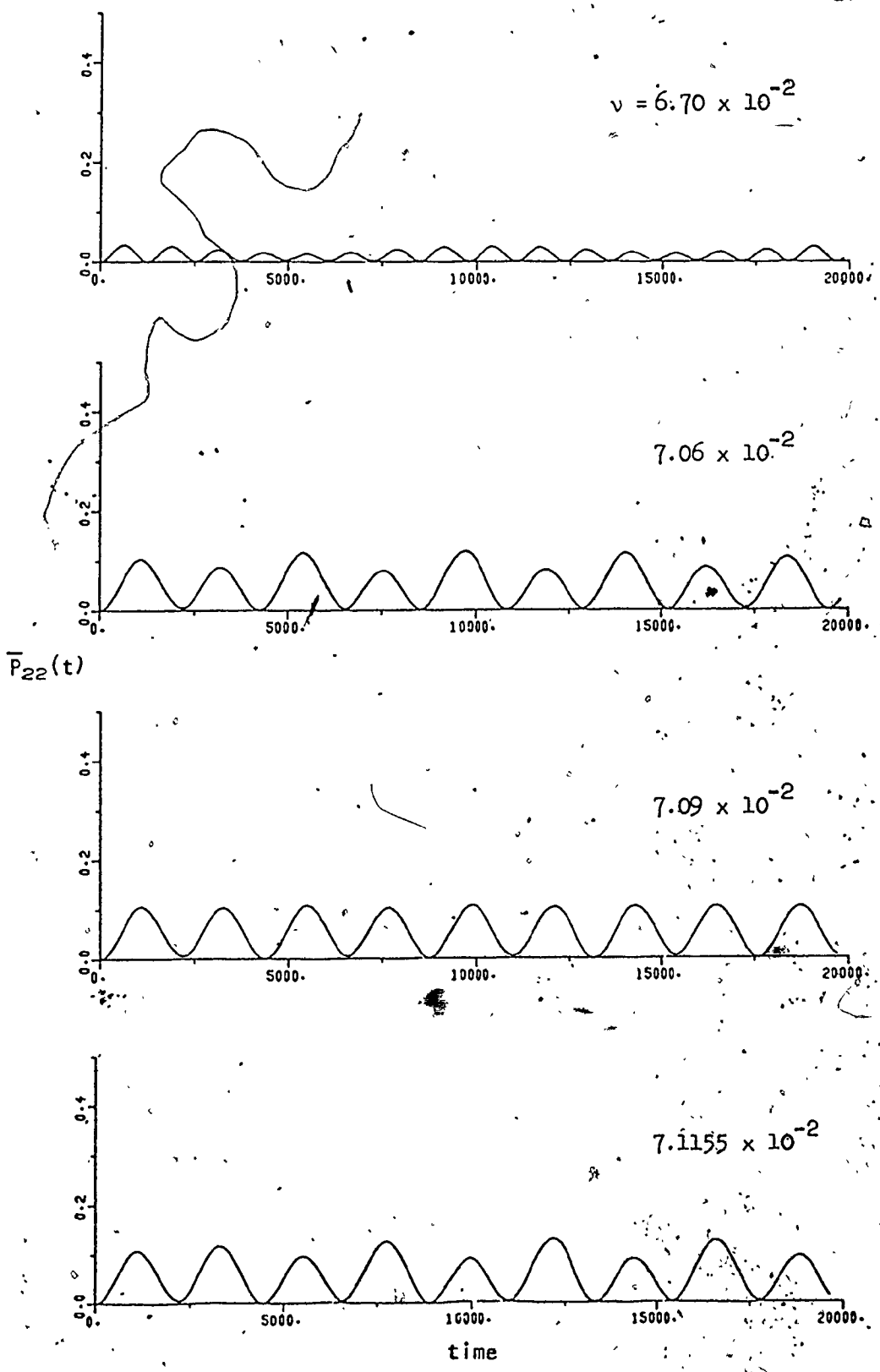
$\nu = 6.70 \times 10^{-2}$
7.06×10^{-2}
7.09×10^{-2}
7.1155×10^{-2}
$\overline{P}_{22}(t)$
time
0.0
0.2
0.4
0.
5000.
10000.
15000.
20000.

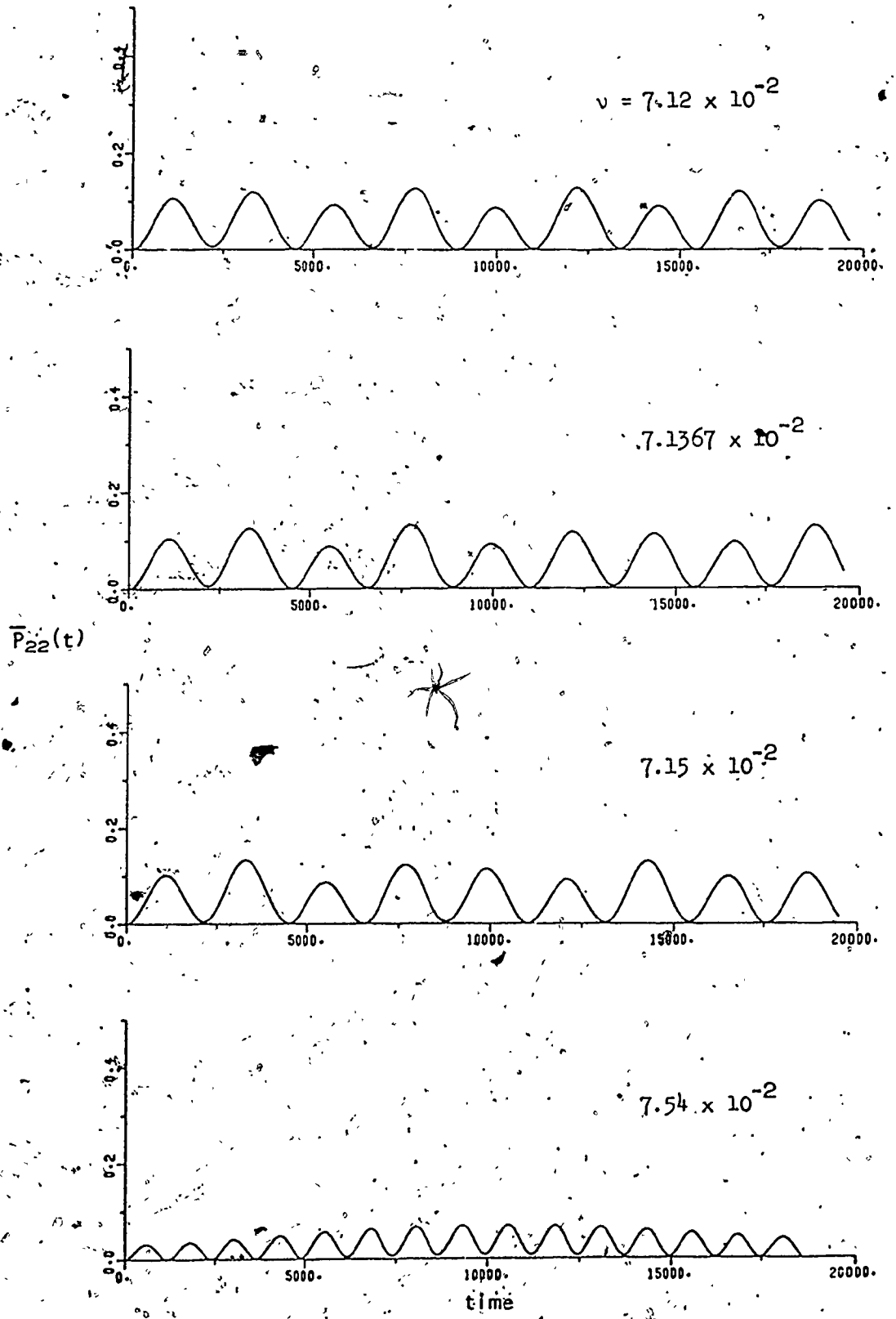
ν = 7.12 x 10^-2
7.1367 x 10^-2
7.15 x 10^-2
7.54 x 10^-2
P̄22(t)
0.0
0.2
0.4
0.
5000.
10000.
15000.
20000.
time

b.

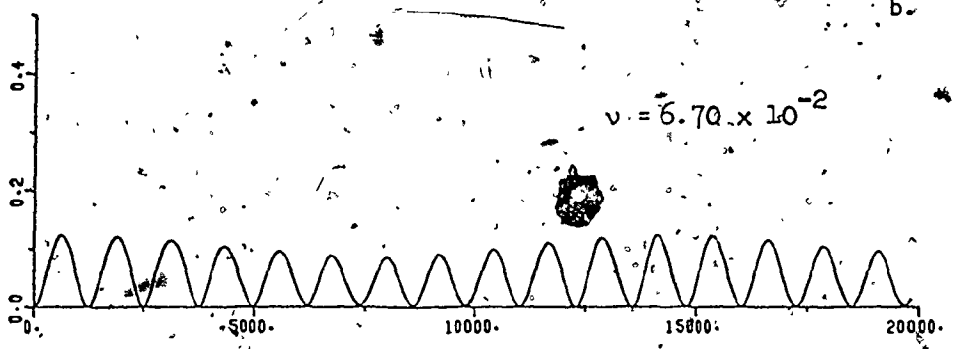

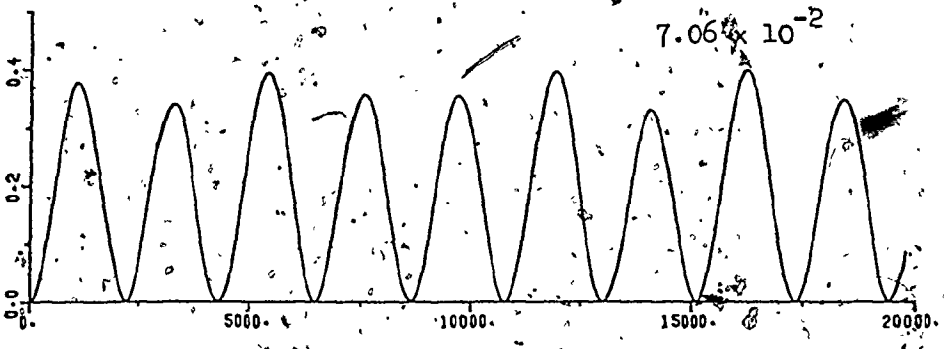

$\bar{P}_{33}(t)$

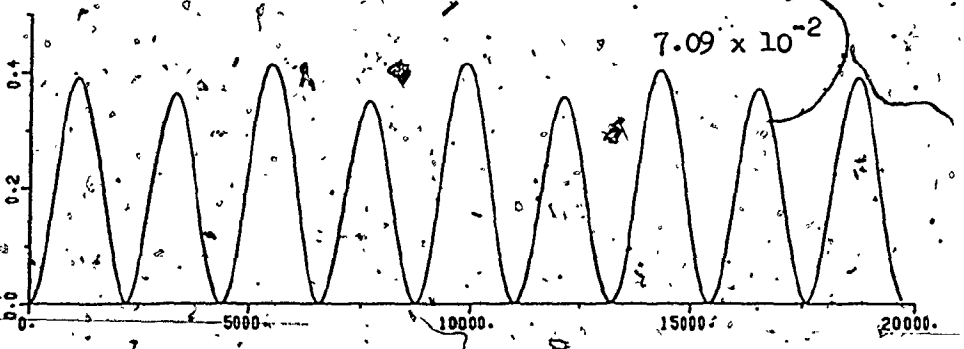

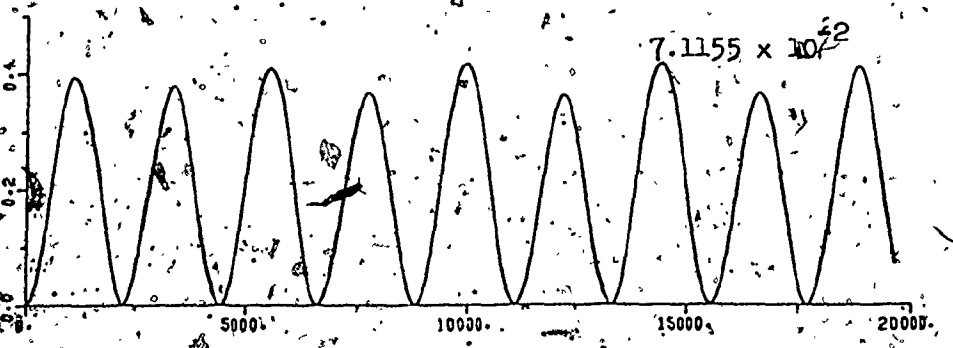

time

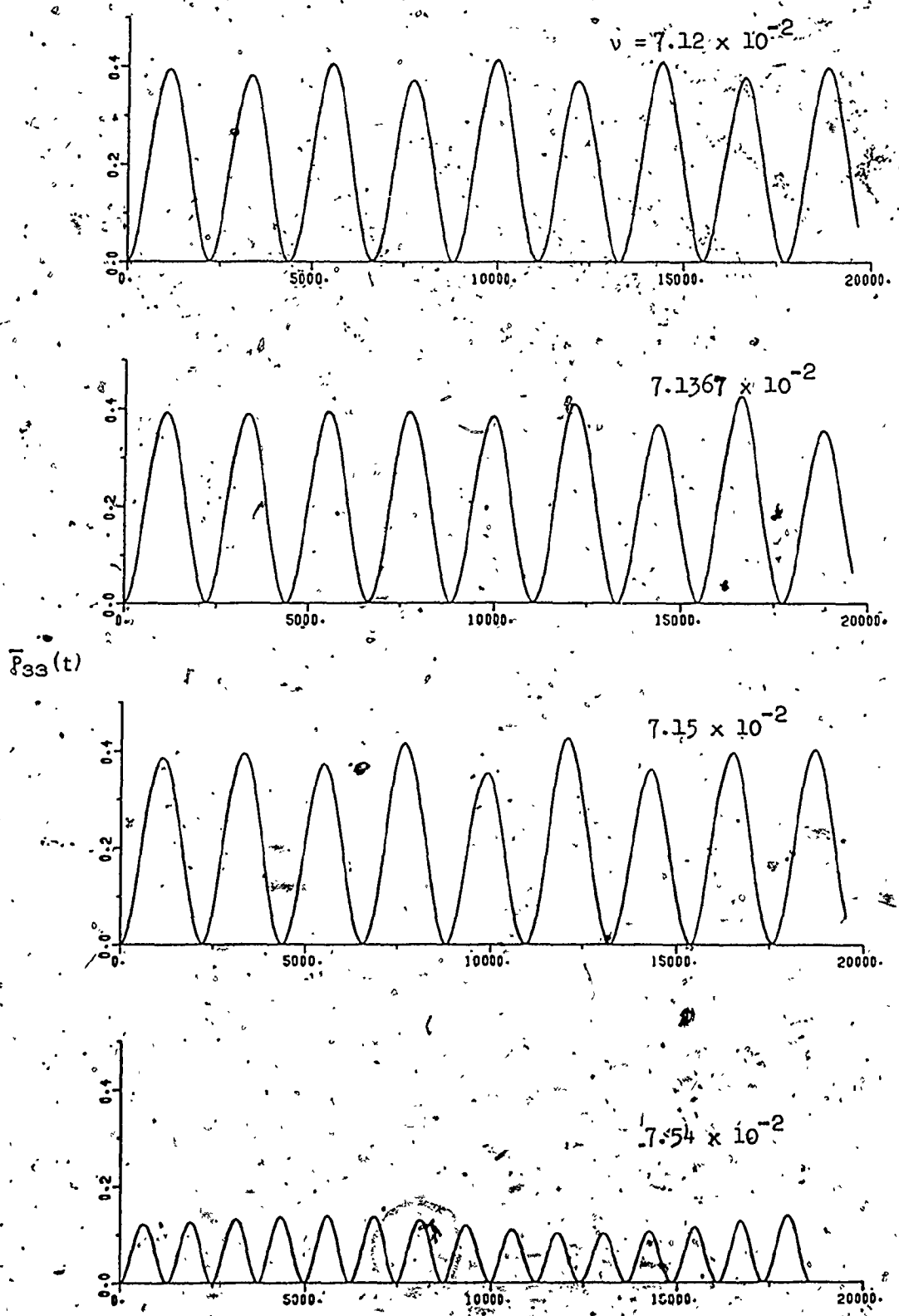
ν = 7.12 x 10^-2
7.1367 x 10^-2
7.15 x 10^-2
7.54 x 10^-2
P̄33(t)
0.0
0.2
0.4
0.
5000.
10000.
15000.
20000.
time

c.

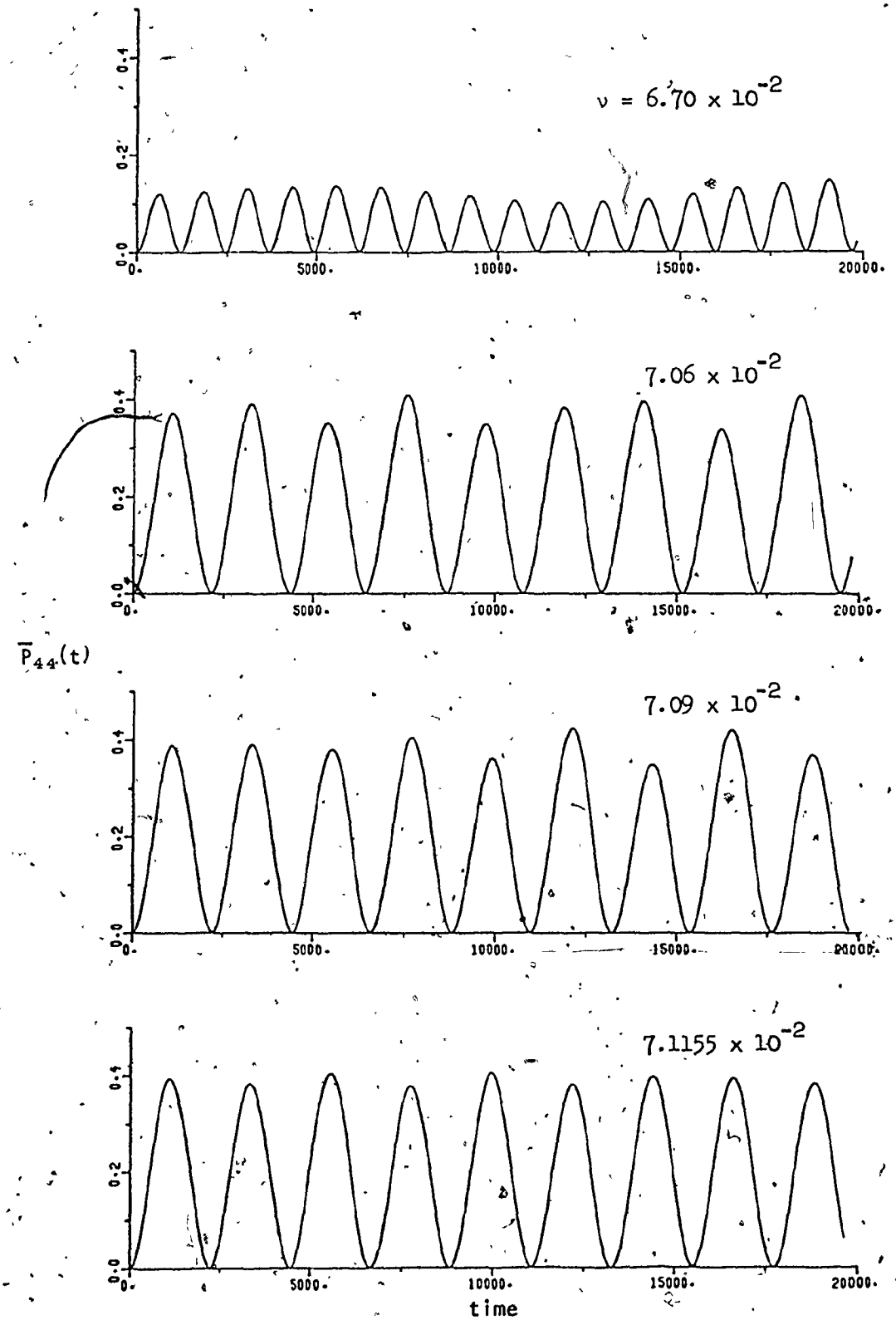
$\nu = 6.70 \times 10^{-2}$
7.06×10^{-2}
7.09×10^{-2}
7.1155×10^{-2}
$\overline{P}_{44}(t)$
0.0
0.2
0.4
0.
5000.
10000.
15000.
20000.
time

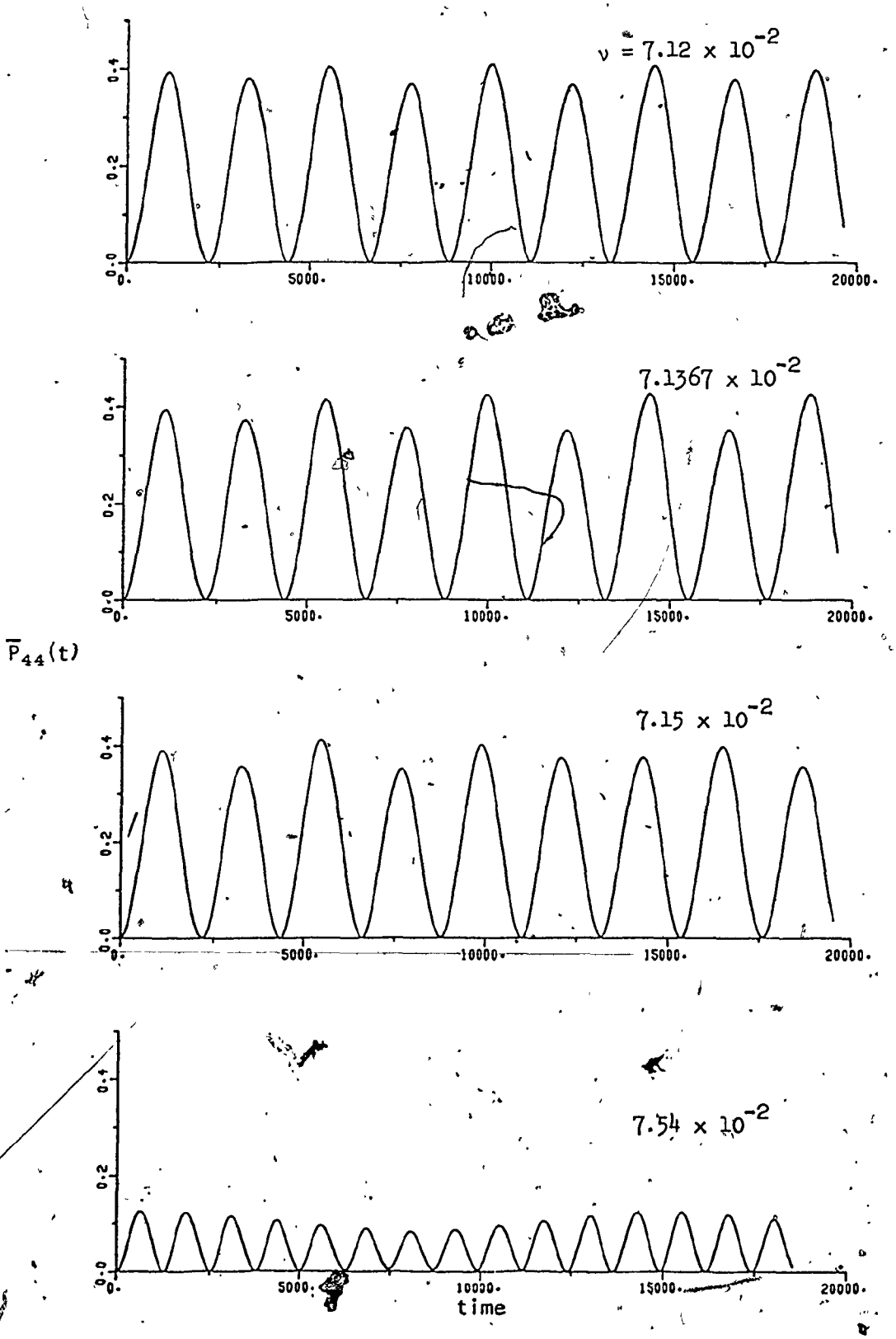
$\nu = 7.12 \times 10^{-2}$
7.1367×10^{-2}
$\bar{P}_{44}(t)$
7.15×10^{-2}
7.54×10^{-2}
0.0
0.2
0.4
0.
5000.
10000.
15000.
20000.
time

d.

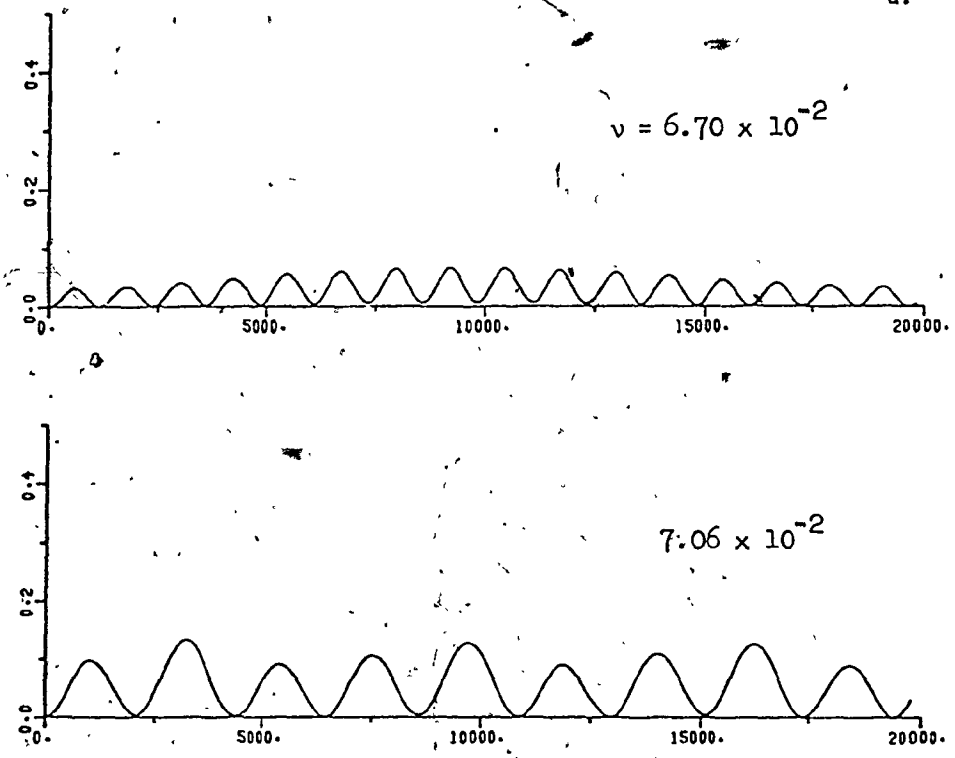
$\nu = 6.70 \times 10^{-2}$
7.06×10^{-2}
7.09×10^{-2}
7.1155×10^{-2}
$\bar{P}_{ss}(t)$
0.0
0.2
0.4
0.
5000.
10000.
15000.
20000.
time

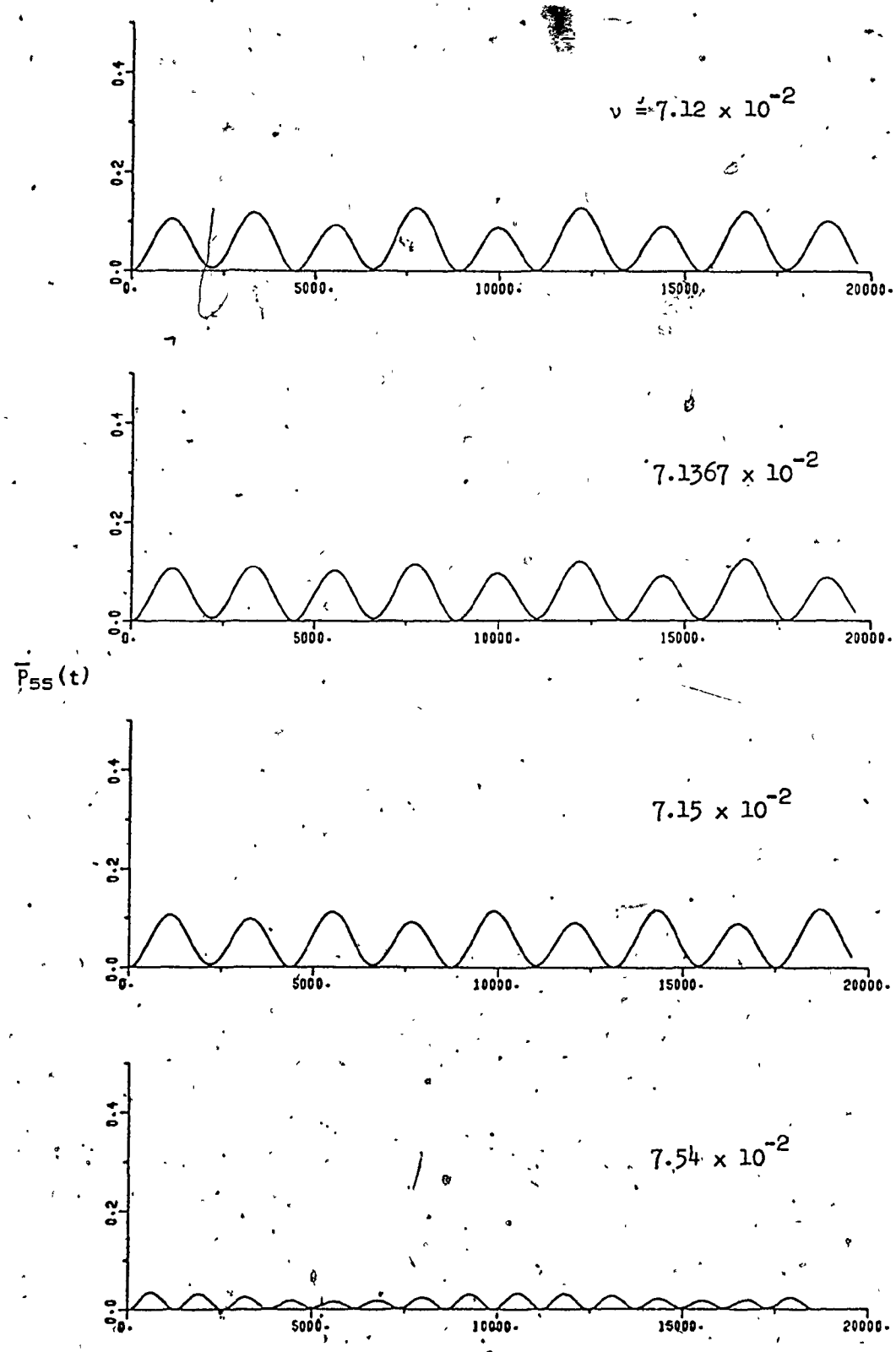
$\nu = 7.12 \times 10^{-2}$
7.1367×10^{-2}
7.15×10^{-2}
7.54×10^{-2}
$\bar{P}_{55}(t)$
0.0
0.2
0.4
0.
5000.
10000.
15000.
20000.
time

Figure (3-12). Phase-averaged temporal behaviour of the ground state, $\overline{P}_{11}(t)$, corresponding to figure (3-11) at $\nu = 7.12 \times 10^{-2}$. The period for the oscillatory behaviour is $\Delta t \sim 2200$.

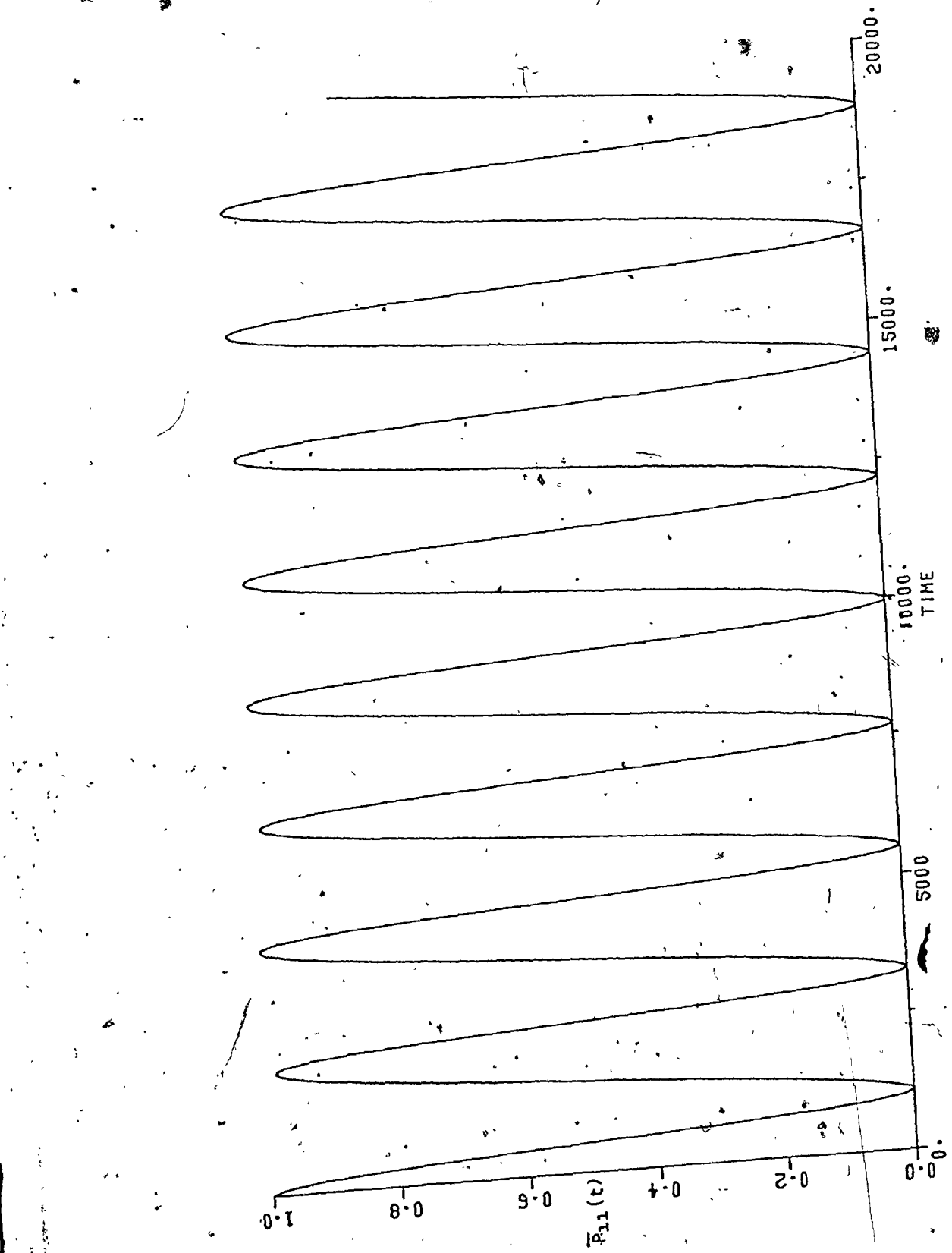
20000.
15000.
10000.
TIME
5000
0.0
0.2
0.4
0.6
0.8
1.0
$\bar{R}_{11}(t)$

is that for the undiagonalized energy level diagram of figure (3-1) ($\frac{2\pi}{\mu_{12}+\varepsilon}$ = 2220). Similarly, each of the excited states, regardless of the magnitude of the oscillator strength produced by the diagonalization of the levels, oscillates with approximately this same period.

The temporal plots also illustrate the significant amount of stealing of intensity from levels closer to the laser frequency by levels that are further from the exciting laser line. Near the single resonance frequency (0.0712) of the five-level system of figure (3-3), the overlapping of individual level peaks means that intensity is shared by all four levels. The more interesting point is that in the "wings" of the peaks the intensities of the transition probabilities are reversed from those predicted from the zero field energy level diagram of figure (3-2). For example, the transitions to levels 2 and 5 in figures (3-11a) and (3-11d) (see also figure 3-4)) may be examined. At the high frequency end of the spectrum, level 5 does initially have the greater transition probability, as expected. However, level 2, although further from the laser line, "steals" enough intensity to have a greater averaged transition probability (see figure (3-4) and compare figures (3-11a) and (3-11d) for ν = 0.0754). Level 2 is likely aided in this "thievery" by levels 3 and 4 which have larger coupling strengths and transition probabilities (see figures (3-11b) and (3-11c)).

Temporal plots corresponding to figures (3-5) and (3-6) are shown in figure (3-13). As pointed out earlier, the five-level system can now be considered to act like four separate two-level systems. That is, the individual levels interact with the ground state almost independently of each other, and figures (3-5), (3-6), and (3-13) are all easily

Figure (3-13). The phase-averaged temporal behaviour of the upper levels of the five-level system of figures (3-5) and (3-6). Frequencies were chosen to correspond to some of the peak maxima at the resonance frequencies, or to the "troughs" between the peaks. (a) $\overline{P}_{22}(t)$ - (b) $\overline{P}_{33}(t)$ (c) $\overline{P}_{44}(t)$ (d) $\overline{P}_{55}(t)$.

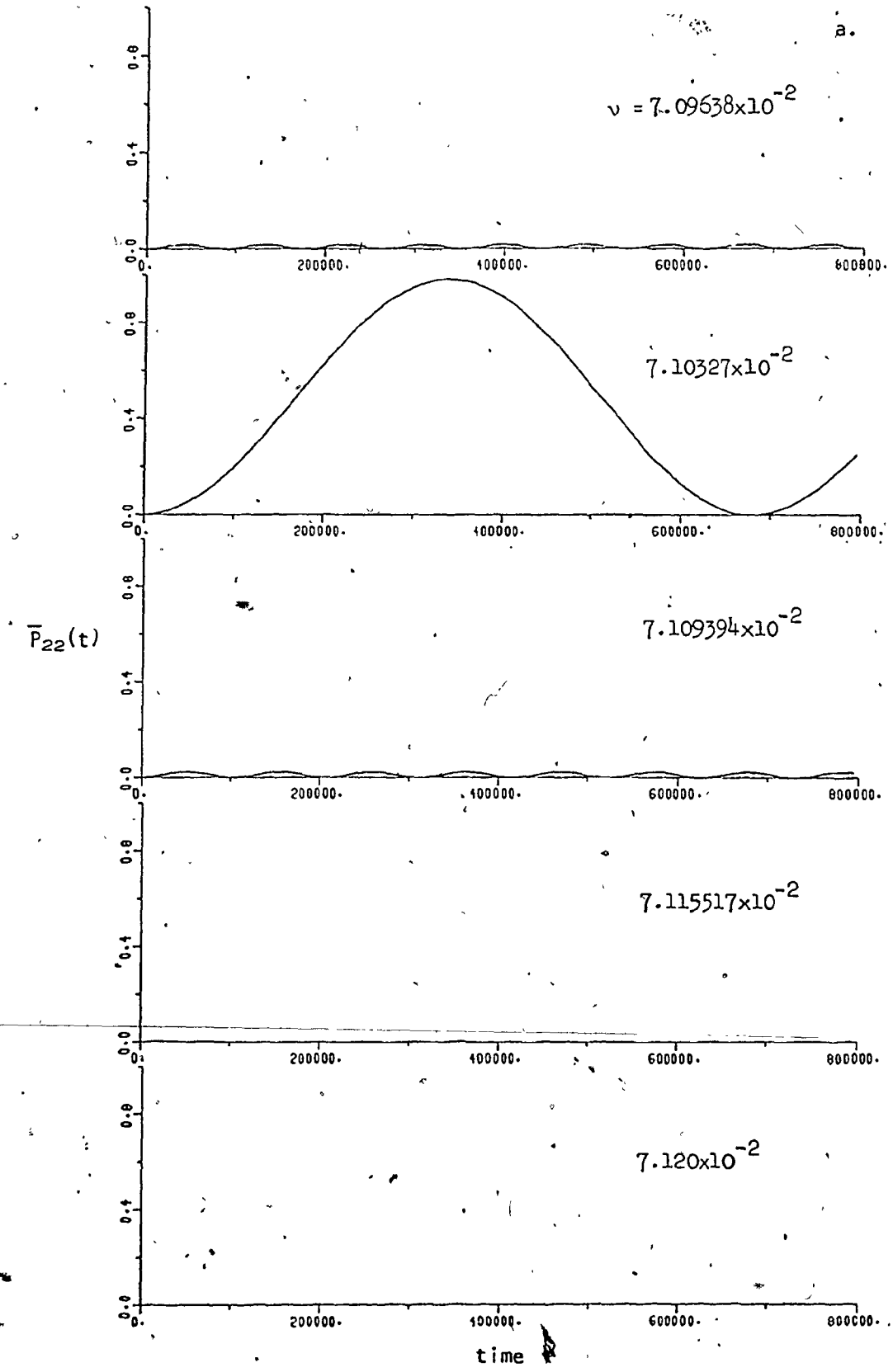
a.
$\nu = 7.09638 \times 10^{-2}$
7.10327×10^{-2}
7.109394×10^{-2}
7.115517×10^{-2}
7.120×10^{-2}
$\bar{P}_{22}(t)$
0.0
0.4
0.8
0.
200000.
400000.
600000.
800000.
time

b.

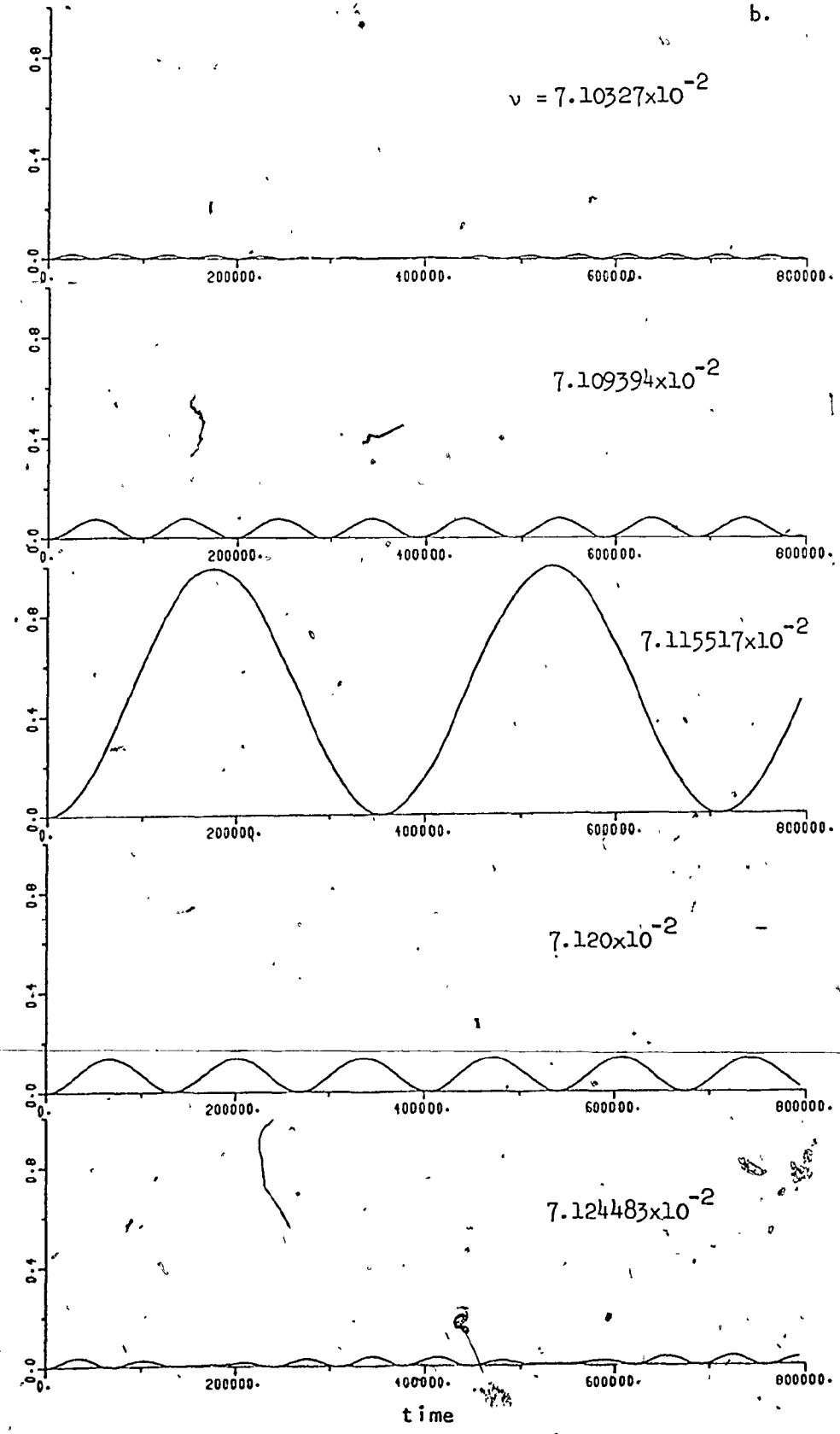
$\nu = 7.10327 \times 10^{-2}$
7.109394×10^{-2}
7.115517×10^{-2}
7.120×10^{-2}
7.124483×10^{-2}
$\bar{P}_{33}(t)$
0.0
0.4
0.8
0.
200000.
400000.
600000.
800000.
time

c.

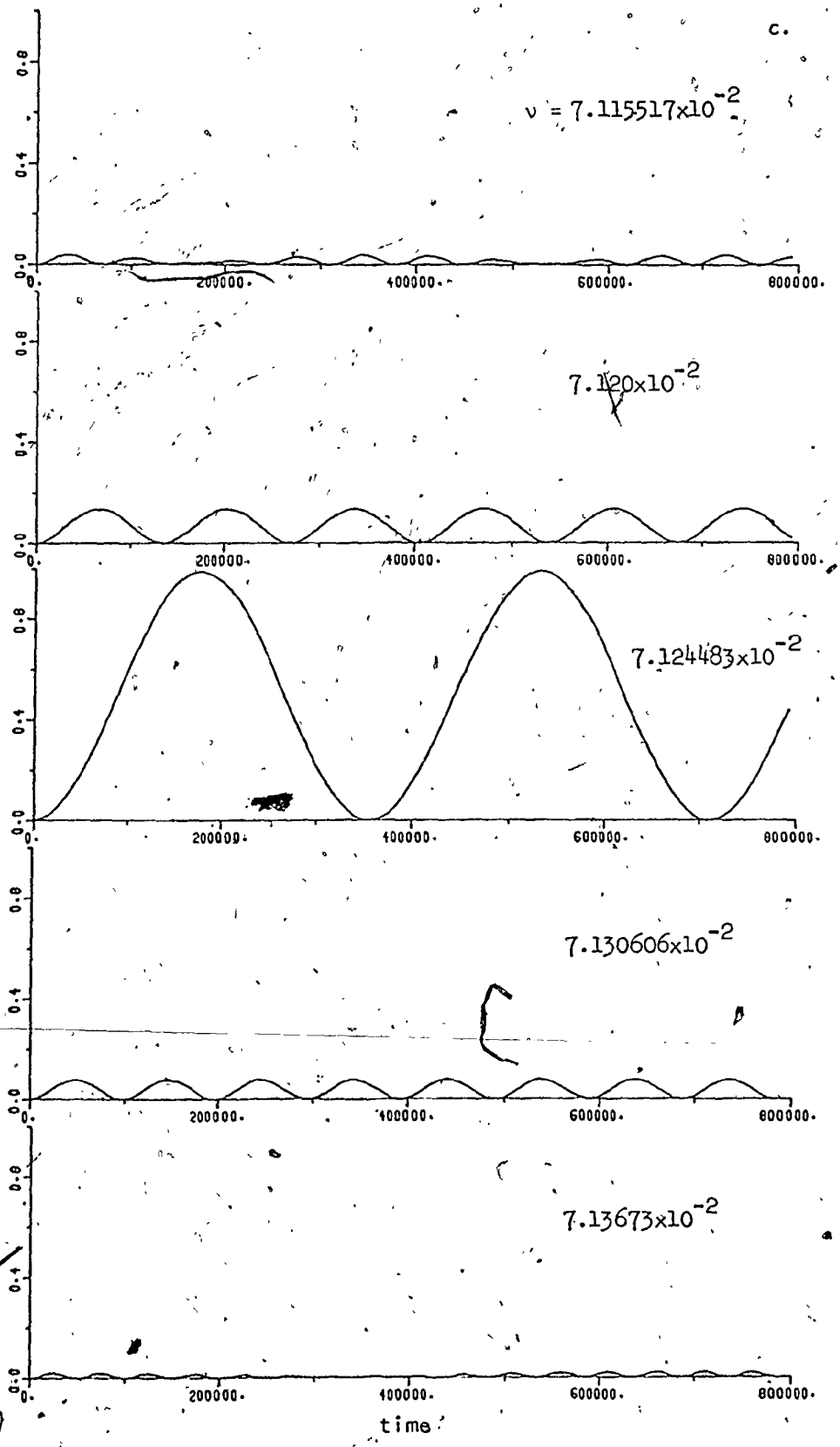
$\nu = 7.115517 \times 10^{-2}$
7.120×10^{-2}
7.124483×10^{-2}
7.130606×10^{-2}
7.13673×10^{-2}
$\bar{P}_{44}(t)$
0.0
0.4
0.8
0.
200000.
400000.
600000.
800000.
time

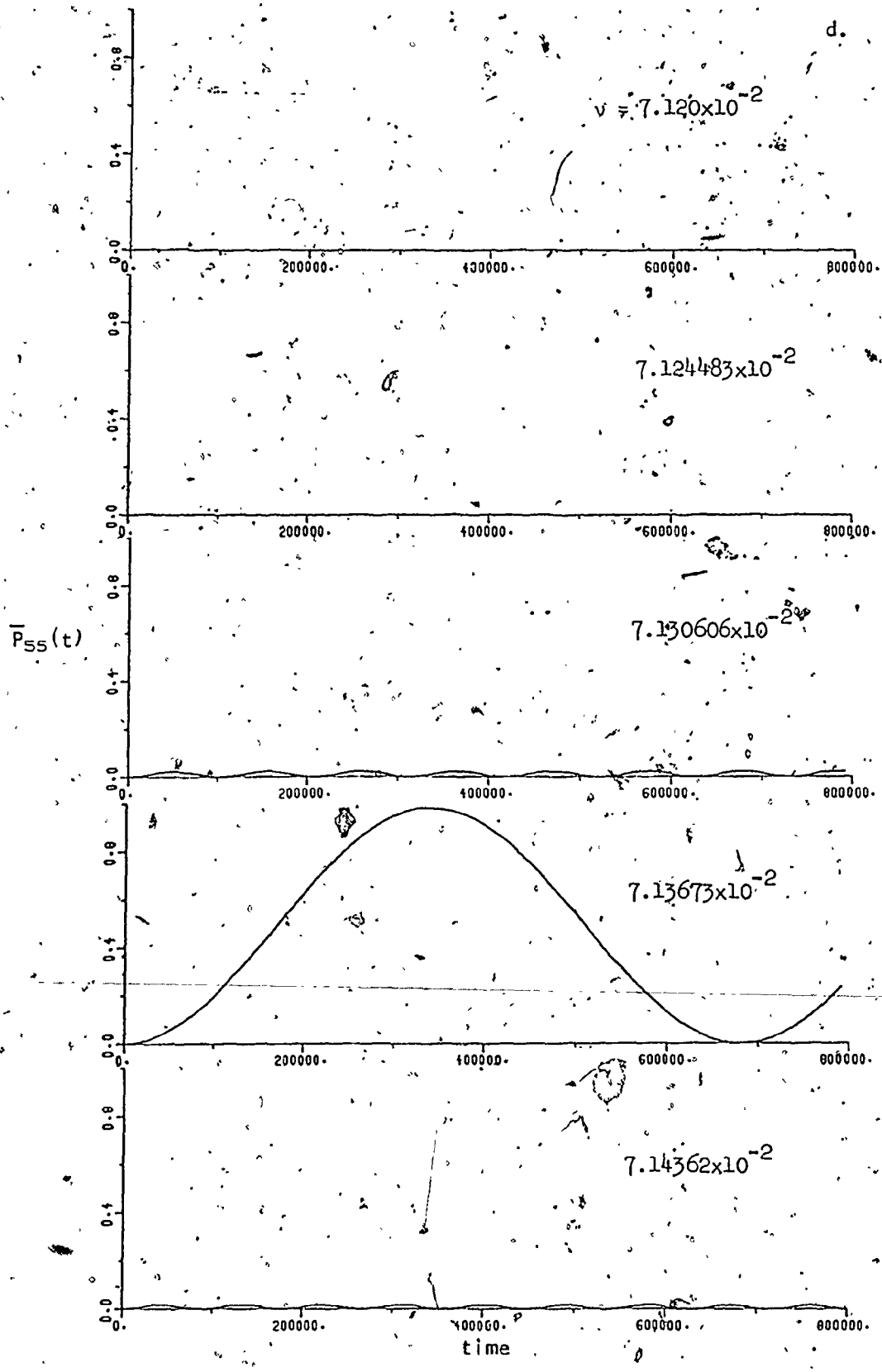
d.
$\nu = 7.120\times10^{-2}$
7.124483×10^{-2}
7.130606×10^{-2}
7.13673×10^{-2}
7.14362×10^{-2}
$\bar{P}_{55}(t)$
0.0
0.4
0.8
0.
200000.
400000.
600000.
800000.
time

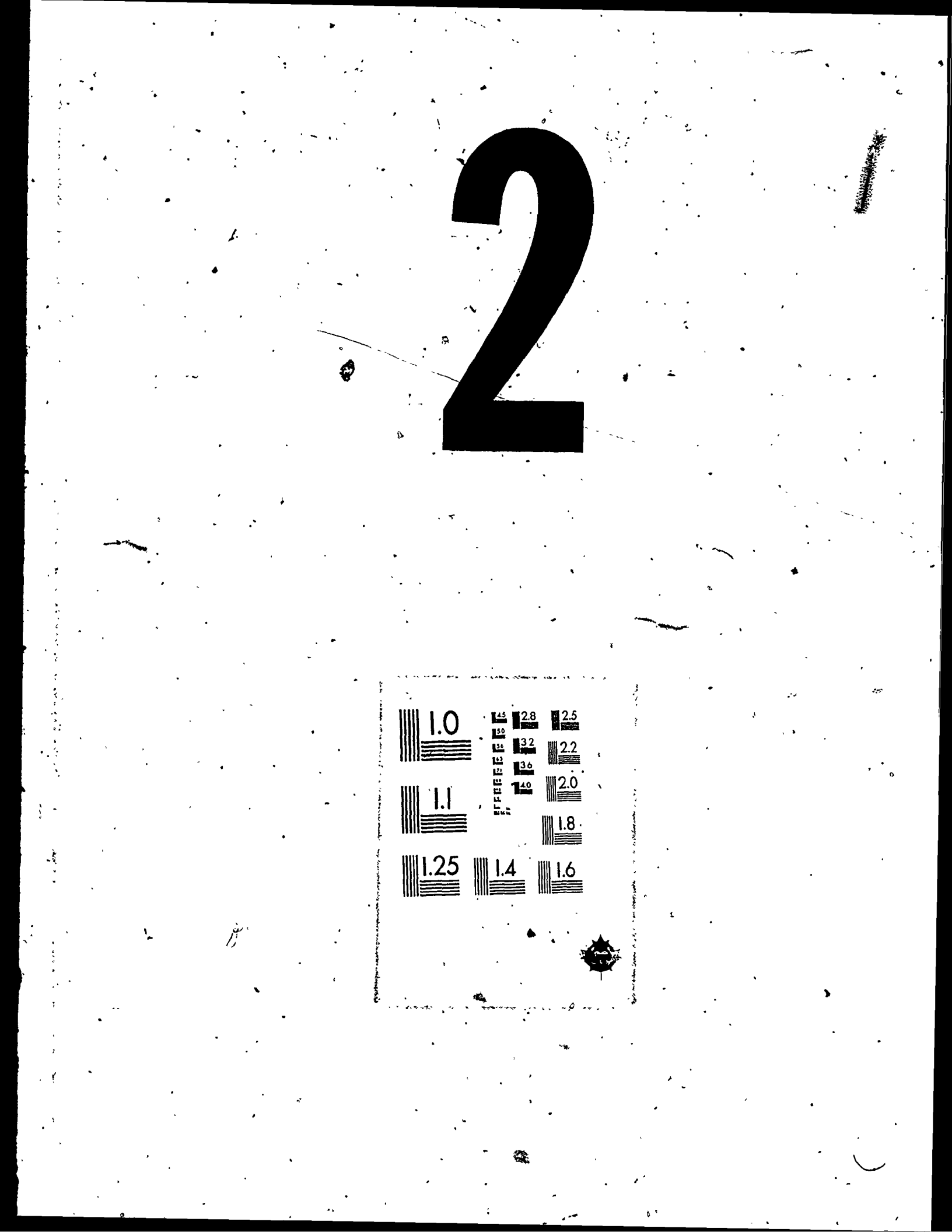
2
1.0
1.1
1.25
1.4
1.6
1.8
2.0
2.2
2.5
2.8
3.2
3.6
4.0
4.5
5.0
5.6

described in terms of simple two-level arguments. On resonance, the population in the excited level oscillates between 0 and ~1 with the period predicted by the coupling strength and the Rabi formula ($\Delta t_{2,5} \sim 6.8 \times 10^5$, $\Delta t_{3,4} \sim 3.6 \times 10^5$, $\Delta t_{2,5}^R = 6.83 \times 10^5$, $\Delta t_{3,4}^R = 3.54 \times 10^5$, see (2.3-8)). It should be recalled that the widths of the peaks in the steady-state calculation (see figure (3-6)) are also correctly related to the diagonalized coupling strengths and the Rabi formula.

The time-dependent plots corresponding to figures (3-7) and (3-8) are shown in figure (3-14). As in the previous case, the simple two-level Rabi formula gives a good approximation for the period with which the excited states oscillate on resonance ($\Delta t_{2,5} \sim 2.65 \times 10^5$, $\Delta t_{3,4} \sim 1.45 \times 10^5$, $\Delta t_{2,5}^R = 2.71 \times 10^5$, $\Delta t_{3,4}^R = 1.40 \times 10^5$). Now, however, the maximum value for the transition probability is not as close to 1.0 as in the weaker coupling strength case, since significantly more population goes into the neighbouring levels. This is in correspondence with the overlapping of peaks in figure (3-7) and the peak maxima being less than 0.5 in figure (3-8).

The time-dependent plots corresponding to figures (3-9) and (3-10) are shown in figure (3-15). In this case, complicated combinations of various periods conspire to give the plots the appearance of only very approximate periodicity. As a resonance is neared as a function of frequency, the "period" of the induced transition probability increases (compare $\nu = 0.0709$ and $\nu = 0.07113$ in figure (3-15a)), as predicted by (2.3-7) in the RWA (see also, for example, figure (3-14)).

The complicated behaviour of these temporal results illustrates the simplification in interpretation that is produced when the Floquet

Figure (3-14). The phase-averaged temporal behaviour of the upper levels of the five-level system of figures (3-7) and (3-8). Frequencies were chosen to include some of the peak maxima at the resonance frequencies, or the troughs between the peaks (a) $\overline{P}_{22}(t)$ (b) $\overline{P}_{33}(t)$ (c) $\overline{P}_{44}(t)$ (d) $\overline{P}_{55}(t)$.

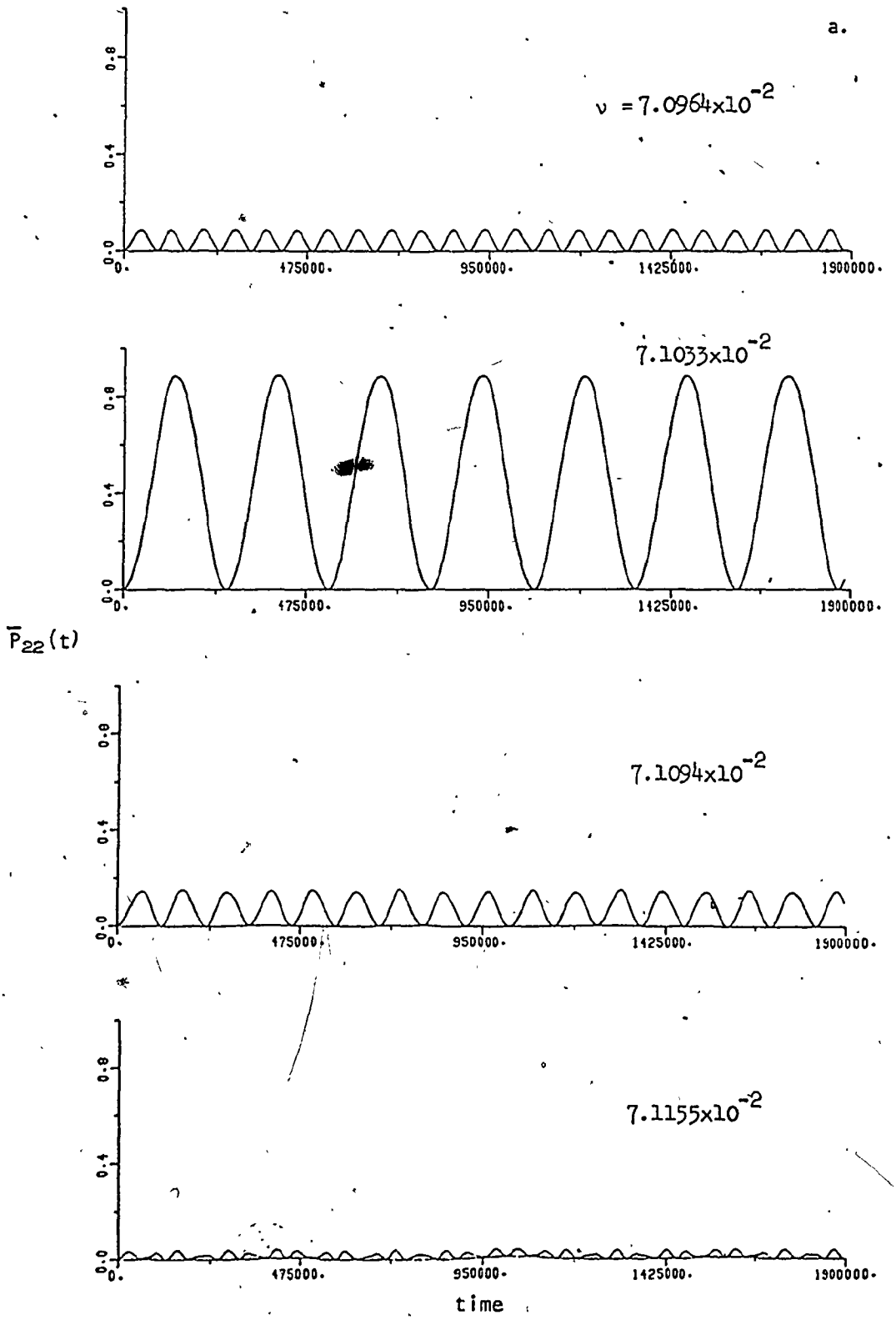
a.
$\nu = 7.0964 \times 10^{-2}$
7.1033×10^{-2}
$\bar{P}_{22}(t)$
7.1094×10^{-2}
7.1155×10^{-2}
0.0
0.4
0.8
0.
475000.
950000.
1425000.
1900000.
time

b.

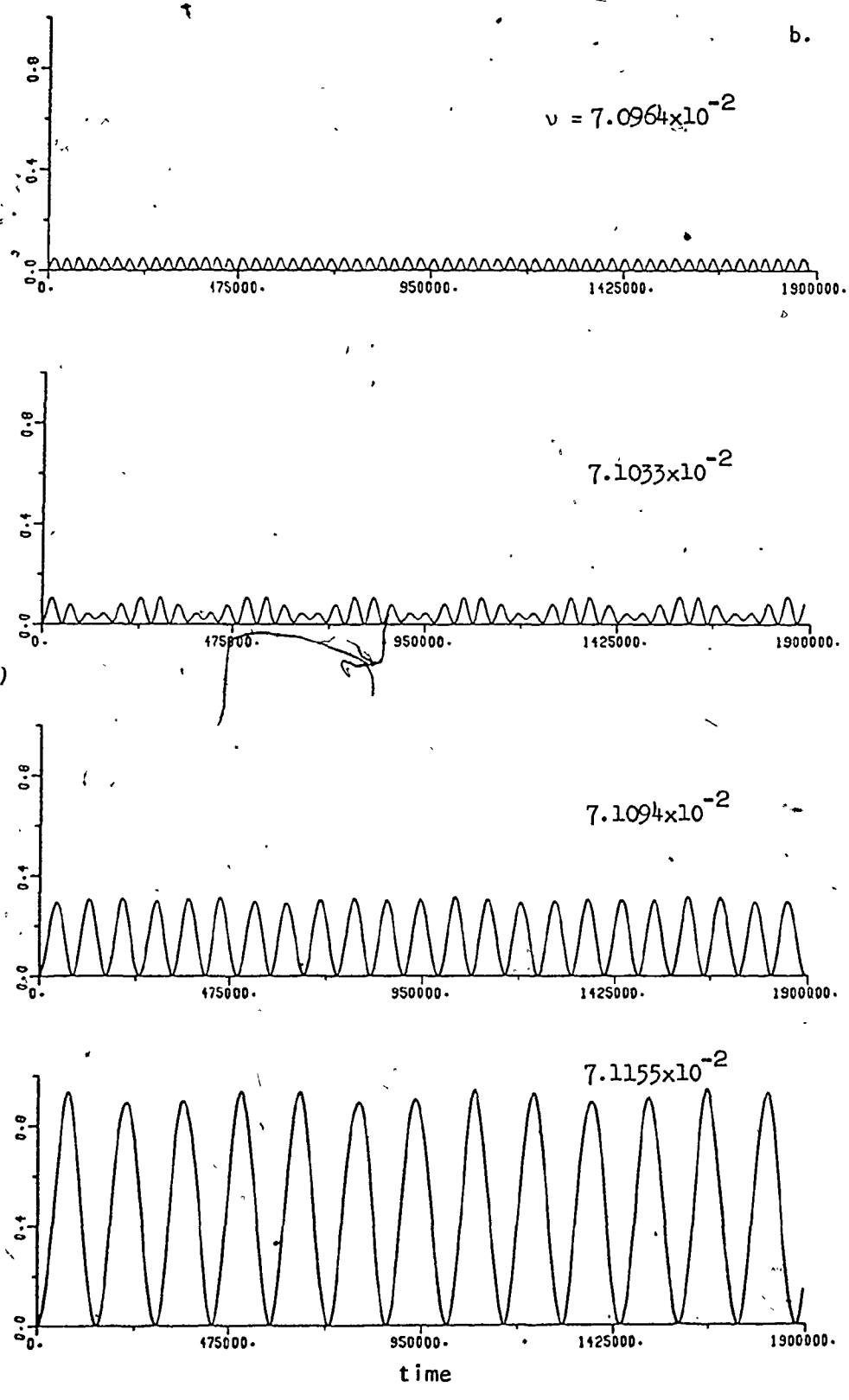
$\nu = 7.0964 \times 10^{-2}$
7.1033×10^{-2}
7.1094×10^{-2}
7.1155×10^{-2}
$\bar{P}_{33}(t)$
0.8
0.4
0.0
0.
475000.
950000.
1425000.
1900000.
time

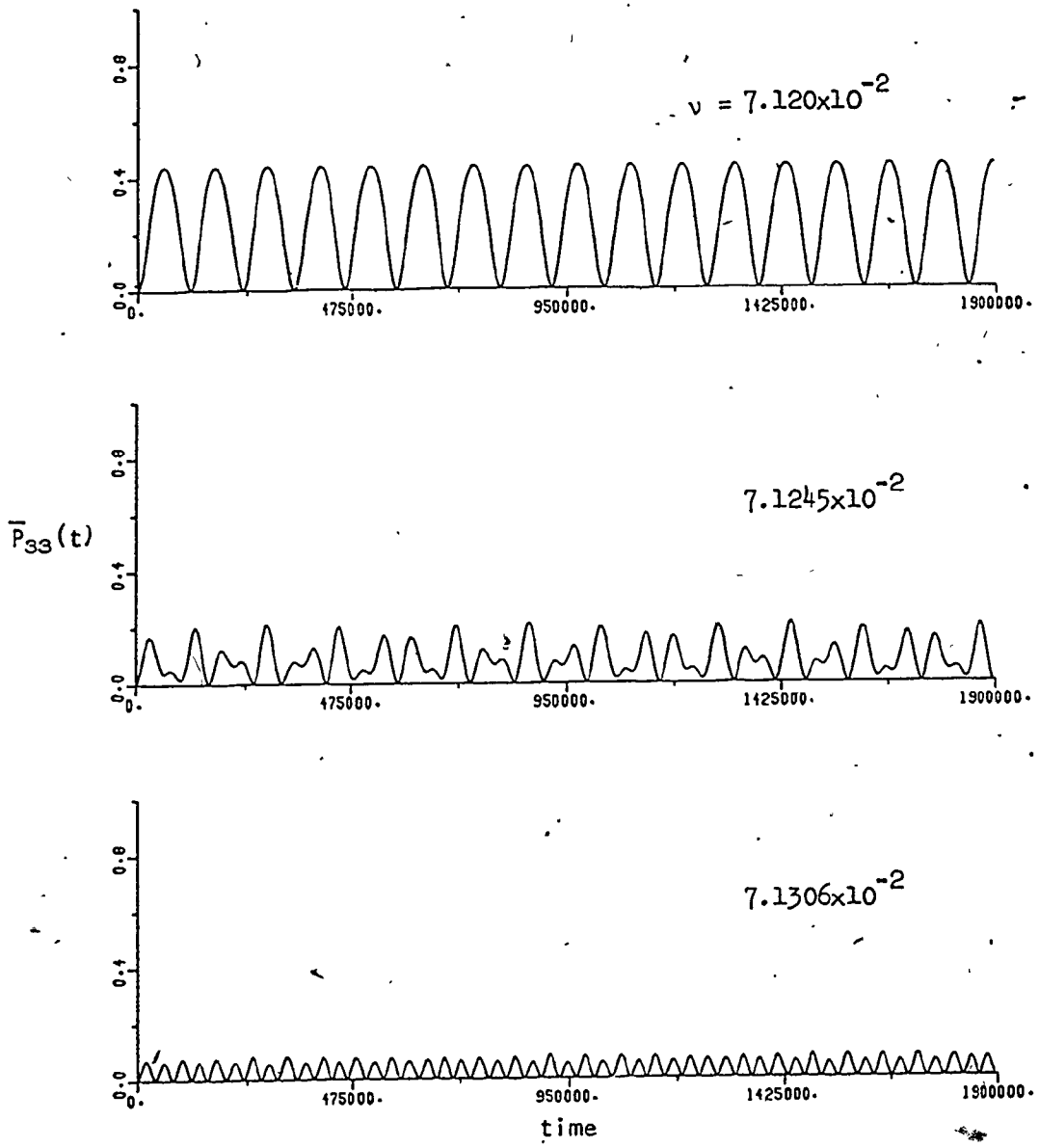
$\nu = 7.120 \times 10^{-2}$
7.1245×10^{-2}
7.1306×10^{-2}
$\bar{P}_{33}(t)$
0.0
0.4
0.8
0.
475000.
950000.
1425000.
1900000.
time

c.

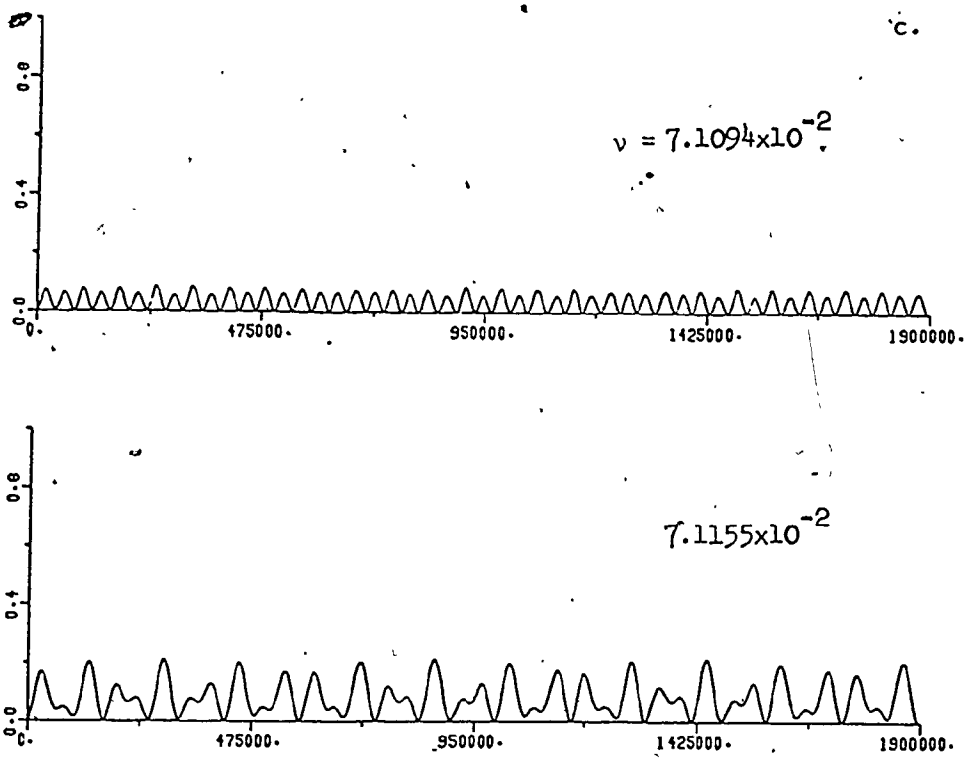
$\nu = 7.1094 \times 10^{-2}$
7.1155×10^{-2}
7.120×10^{-2}
7.1245×10^{-2}
$\overline{P}_{44}(t)$
0.0
0.4
0.8
0.
475000.
950000.
1425000.
1900000.
time

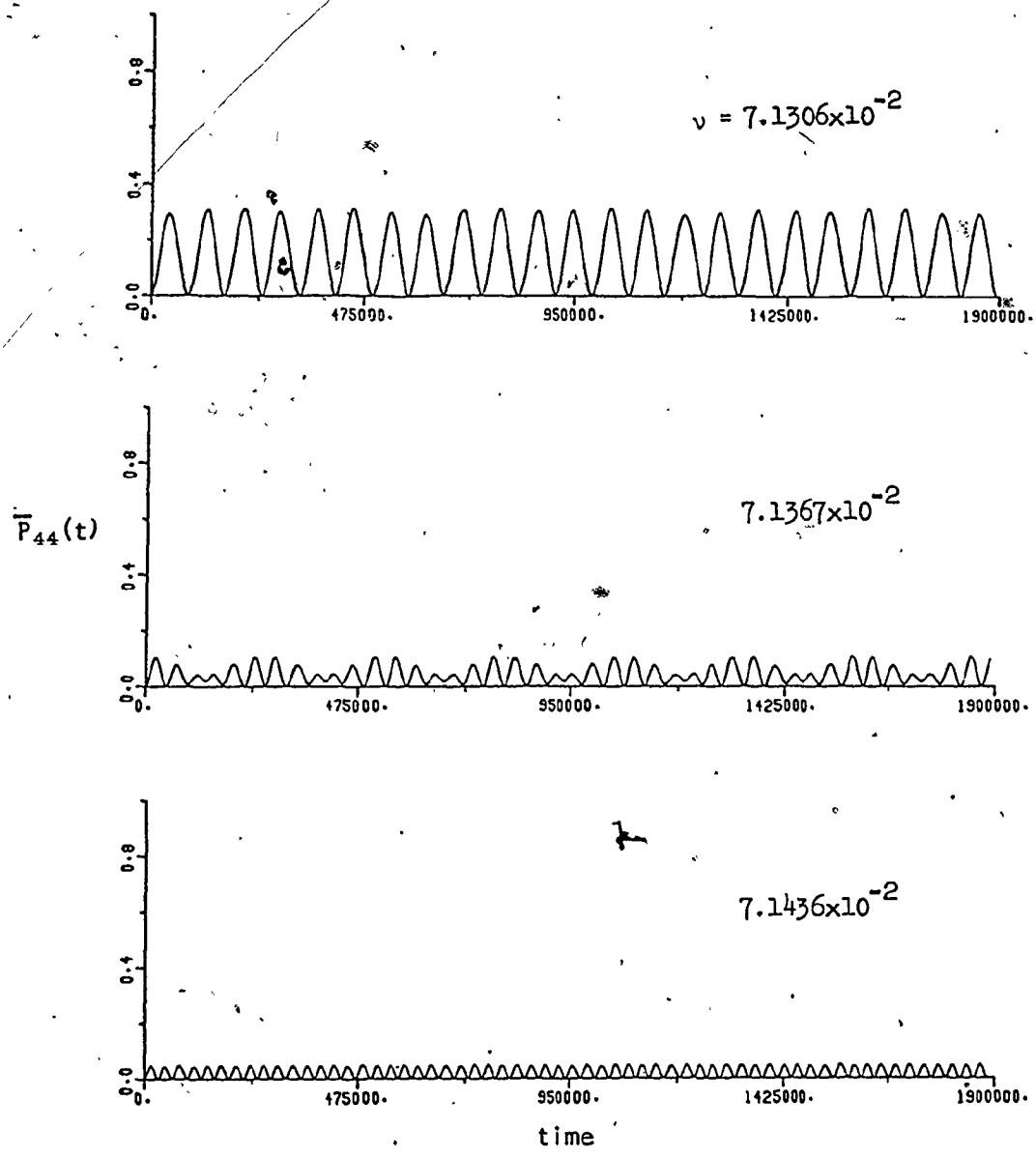
$\nu = 7.1306 \times 10^{-2}$
7.1367×10^{-2}
7.1436×10^{-2}
$\bar{P}_{44}(t)$
0.0
0.4
0.8
0.
475000.
950000.
1425000.
1900000.
time

d.

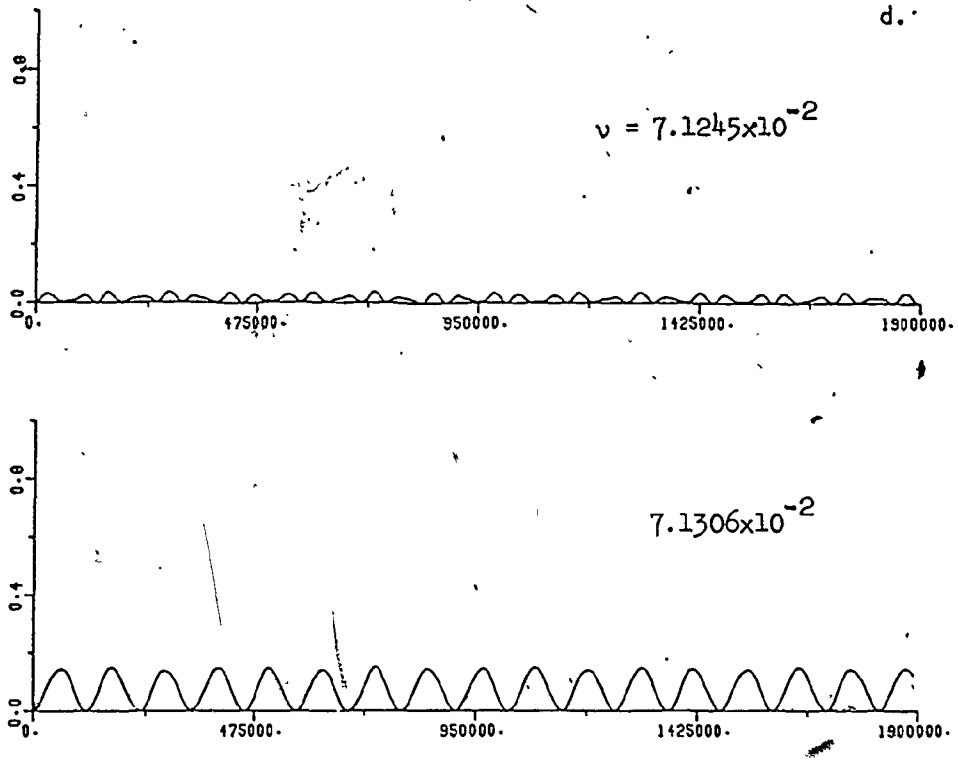
$\nu = 7.1245 \times 10^{-2}$
7.1306×10^{-2}
7.1367×10^{-2}
7.1436×10^{-2}
$\bar{P}_{55}(t)$
0.0
0.4
0.8
0.
475000.
950000.
1425000.
1900000.
time

Figure (3-15). The phase-averaged temporal behaviour of the upper levels of the five-level system of figures (3-9) and (3-10). Frequencies were chosen to include some of the observed resonance peaks and shoulders (see figure (3-10)) and some of the expected resonance frequencies (see figure (3-2)). (a) $\overline{P}_{22}(t)$ (b) $\overline{P}_{33}(t)$ (c) $\overline{P}_{44}(t)$ (d) $\overline{P}_{55}(t)$.

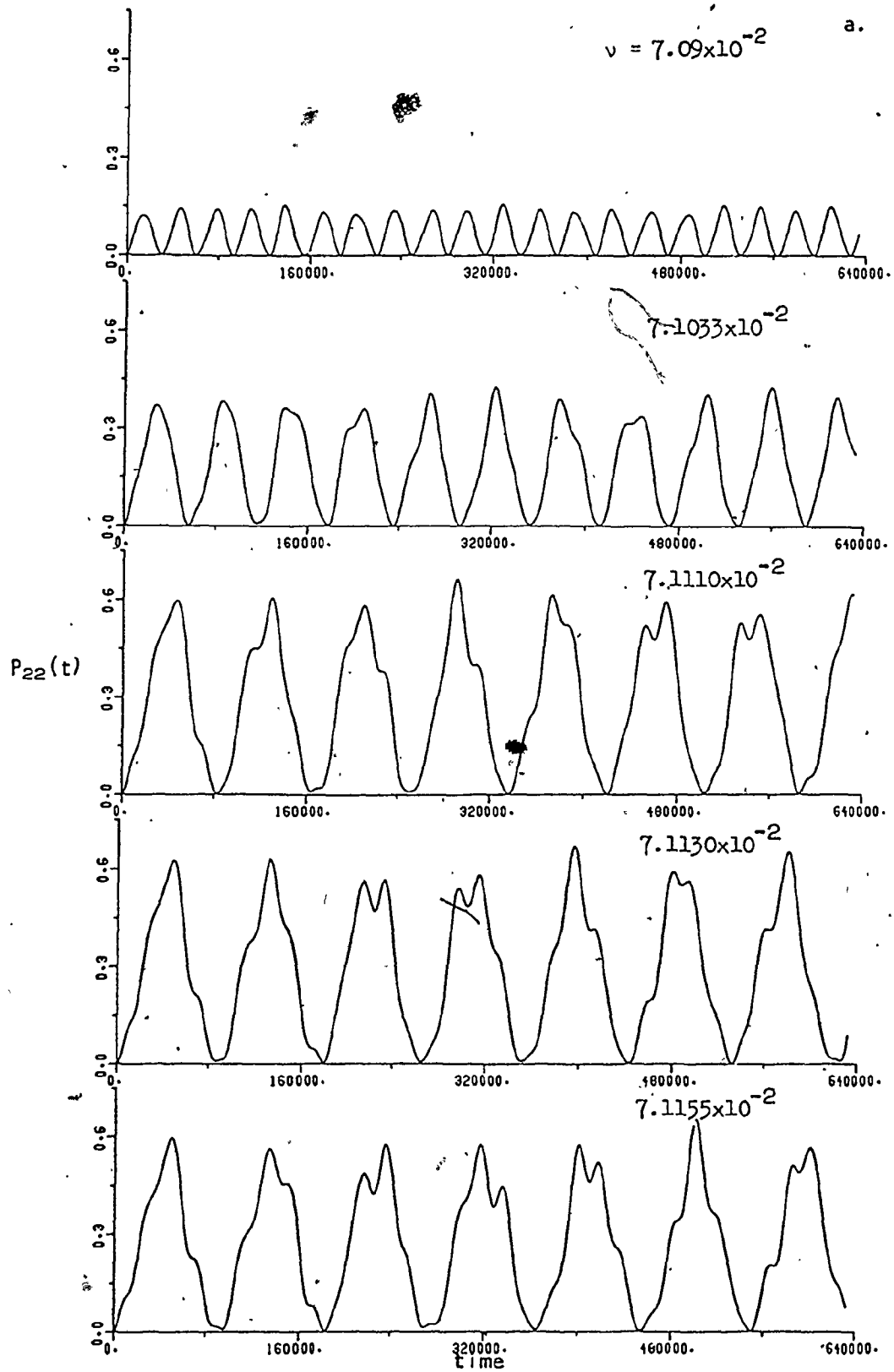
a.
ν = 7.09x10^-2
7.1033x10^-2
7.1110x10^-2
7.1130x10^-2
7.1155x10^-2
P22(t)
time
0.0
0.3
0.6
0.
160000.
320000.
480000.
640000.

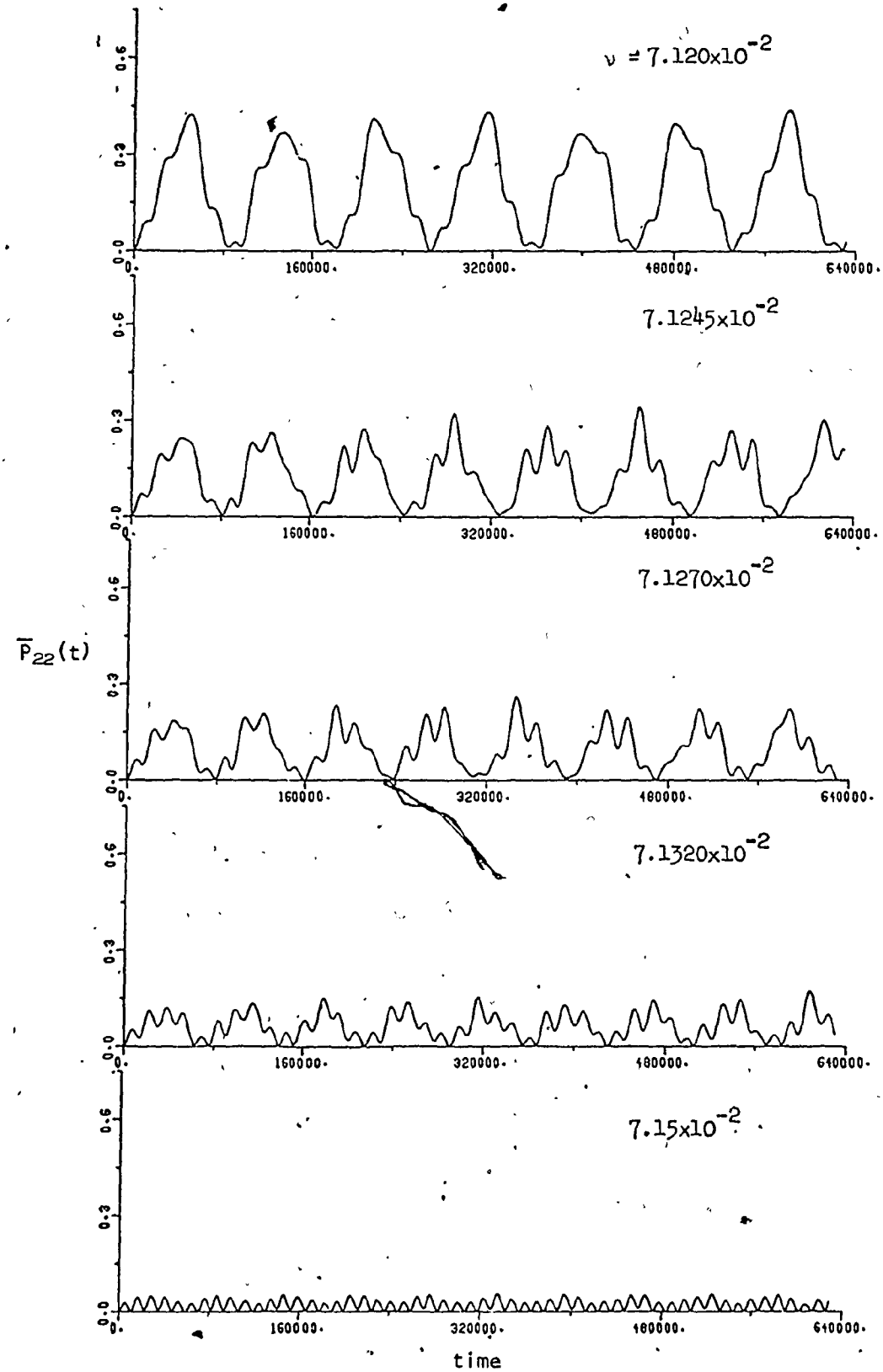
$\nu = 7.120\times10^{-2}$
7.1245×10^{-2}
7.1270×10^{-2}
7.1320×10^{-2}
7.15×10^{-2}
$\bar{P}_{22}(t)$
0.0
0.3
0.6
0.
160000.
320000.
480000.
640000.
time

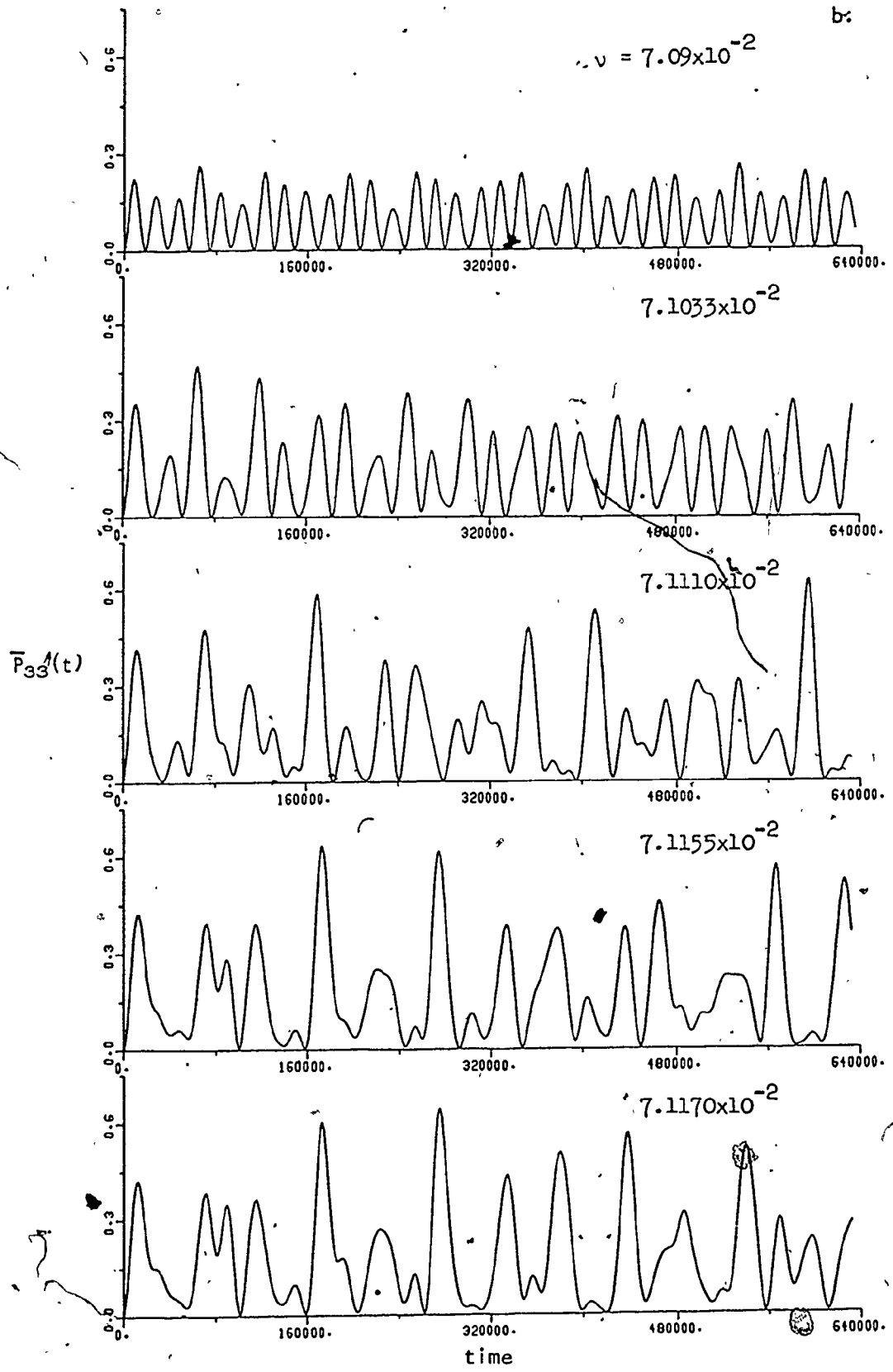
b:
ν = 7.09x10^-2
7.1033x10^-2
7.1110x10^-2
7.1155x10^-2
7.1170x10^-2
0.6
0.3
0.0
0.
160000.
320000.
480000.
640000.
P̄33(t)
time

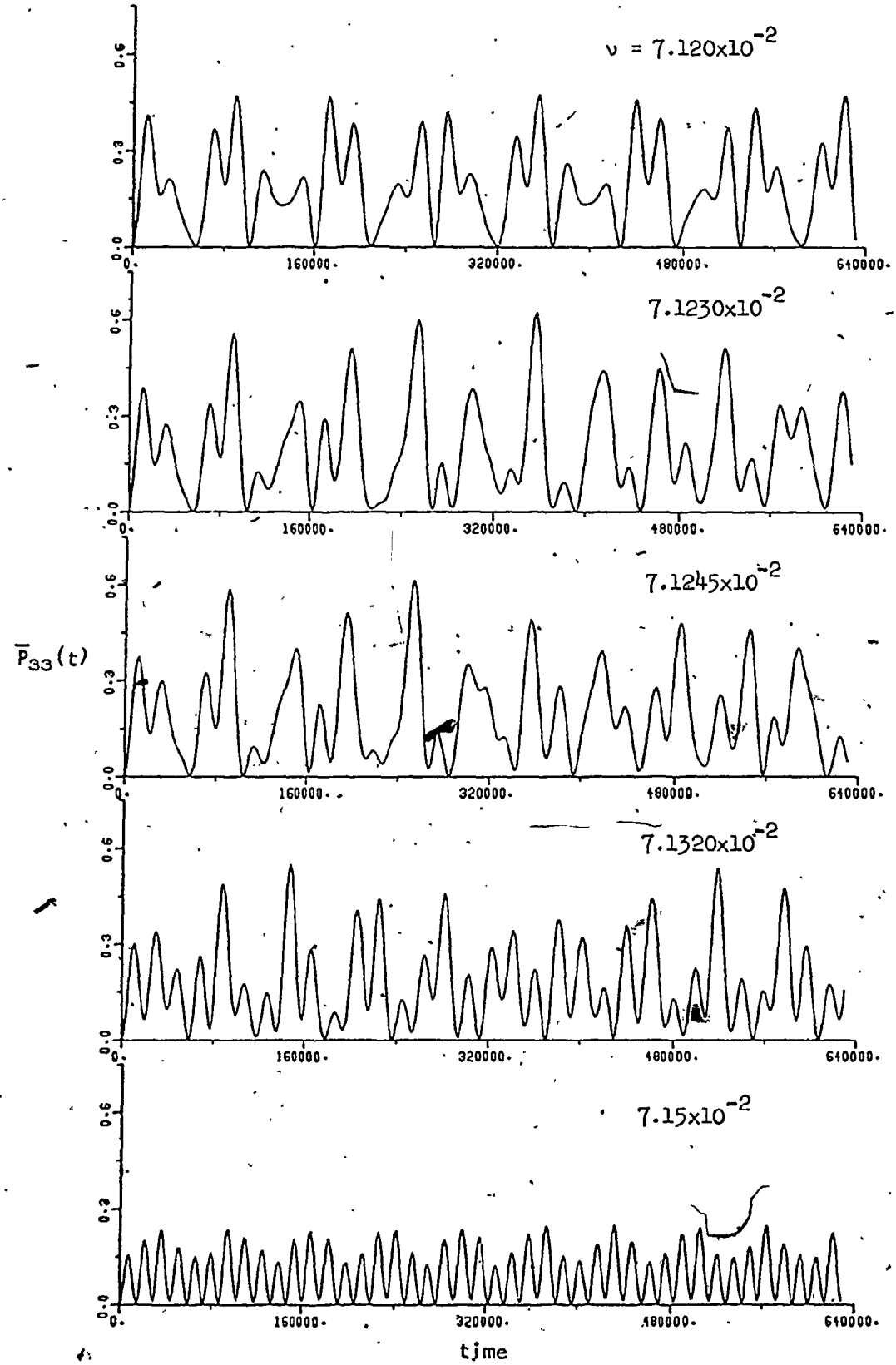
ν = 7.120x10^-2
7.1230x10^-2
7.1245x10^-2
7.1320x10^-2
7.15x10^-2
P̄33(t)
0.0
0.3
0.6
0.
160000.
320000.
480000.
640000.
time

c.

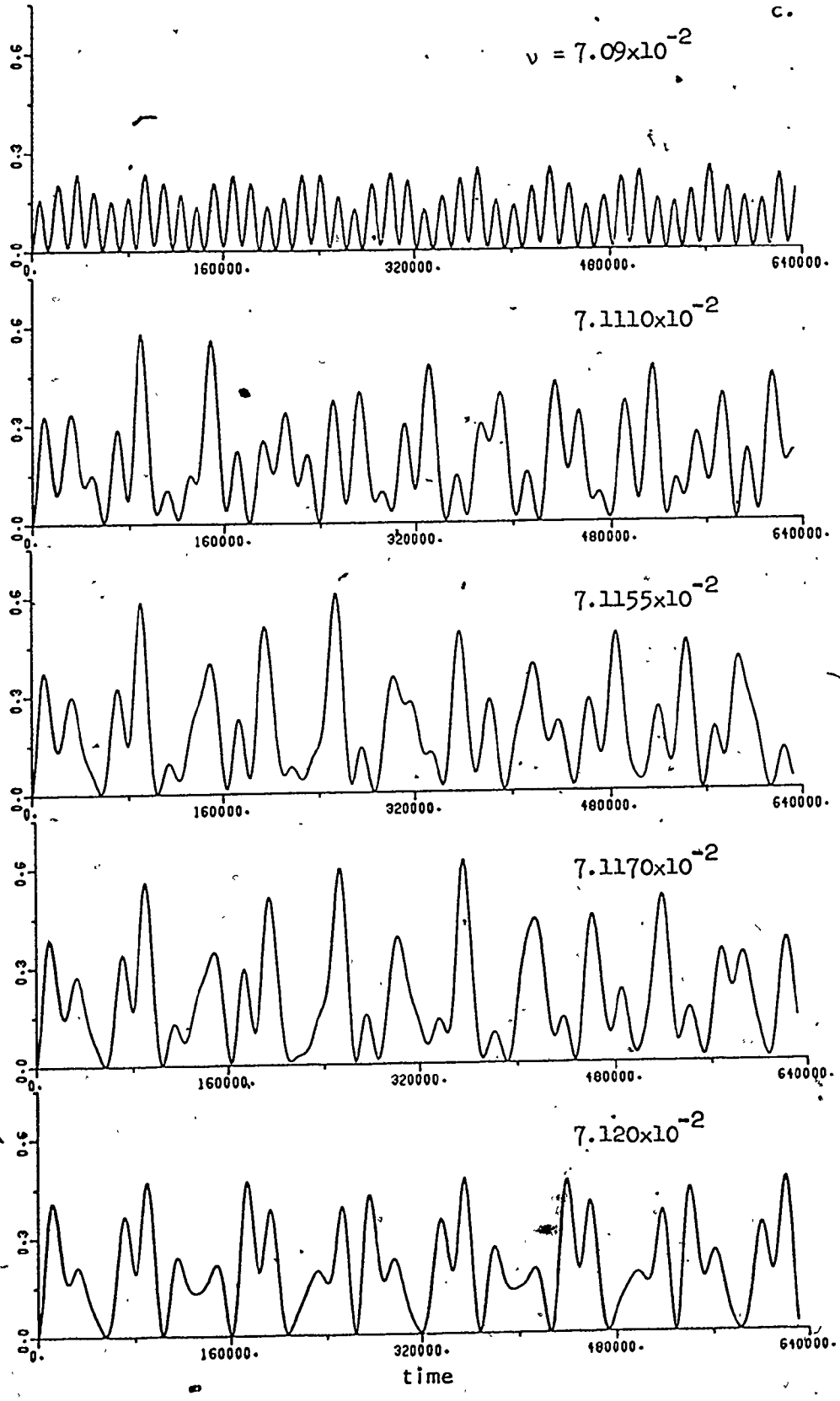
$\nu = 7.09\times10^{-2}$
7.1110×10^{-2}
7.1155×10^{-2}
7.1170×10^{-2}
7.120×10^{-2}
$\overline{P}_{44}(t)$
0.0
0.3
0.6
0.
160000.
320000.
480000.
640000.
time

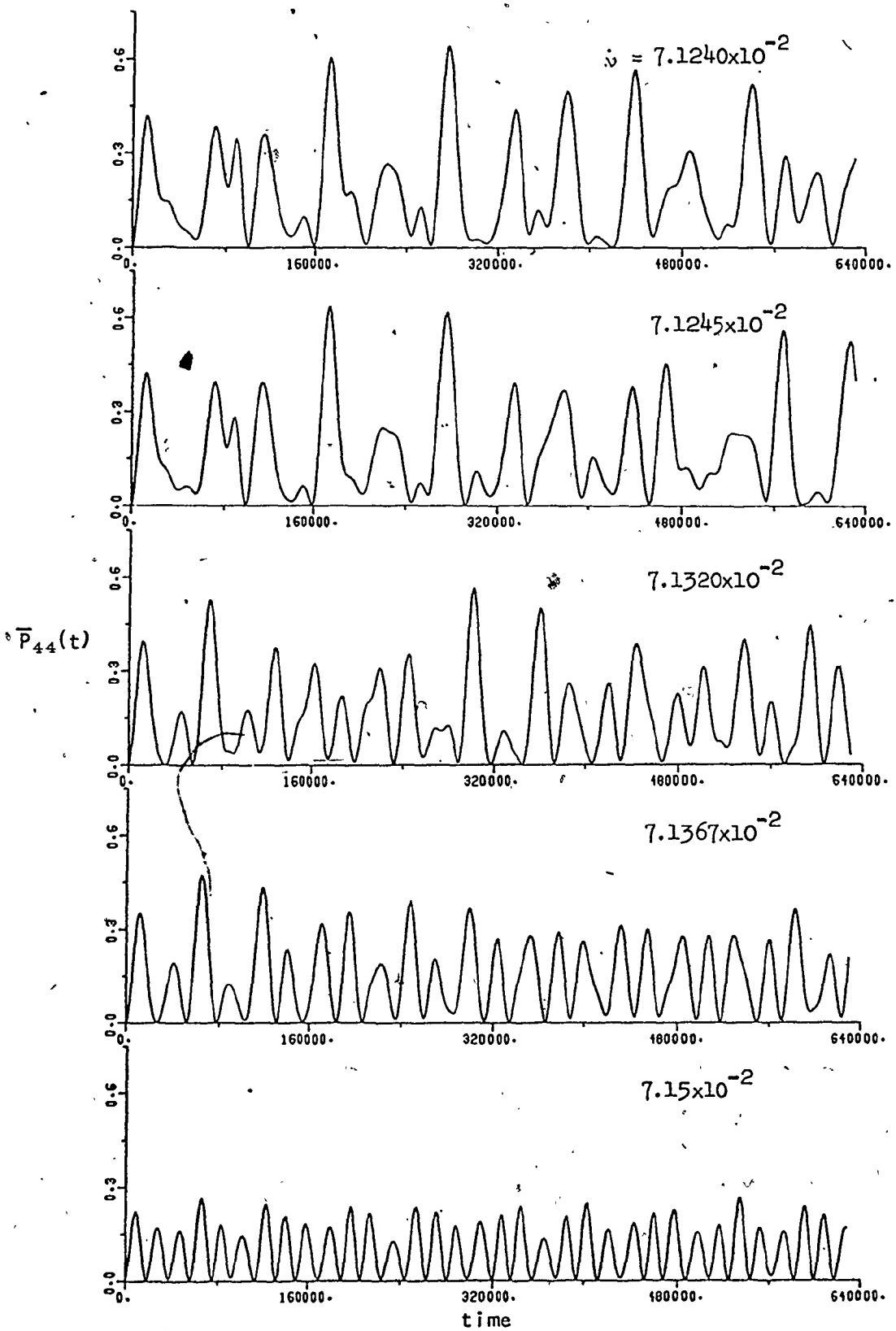
$\dot{\nu}$ = 7.1240x10^{-2}
7.1245x10^{-2}
7.1320x10^{-2}
7.1367x10^{-2}
7.15x10^{-2}
$\overline{P}_{44}(t)$
0.0
0.3
0.6
0.
160000.
320000.
480000.
640000.
time

d.

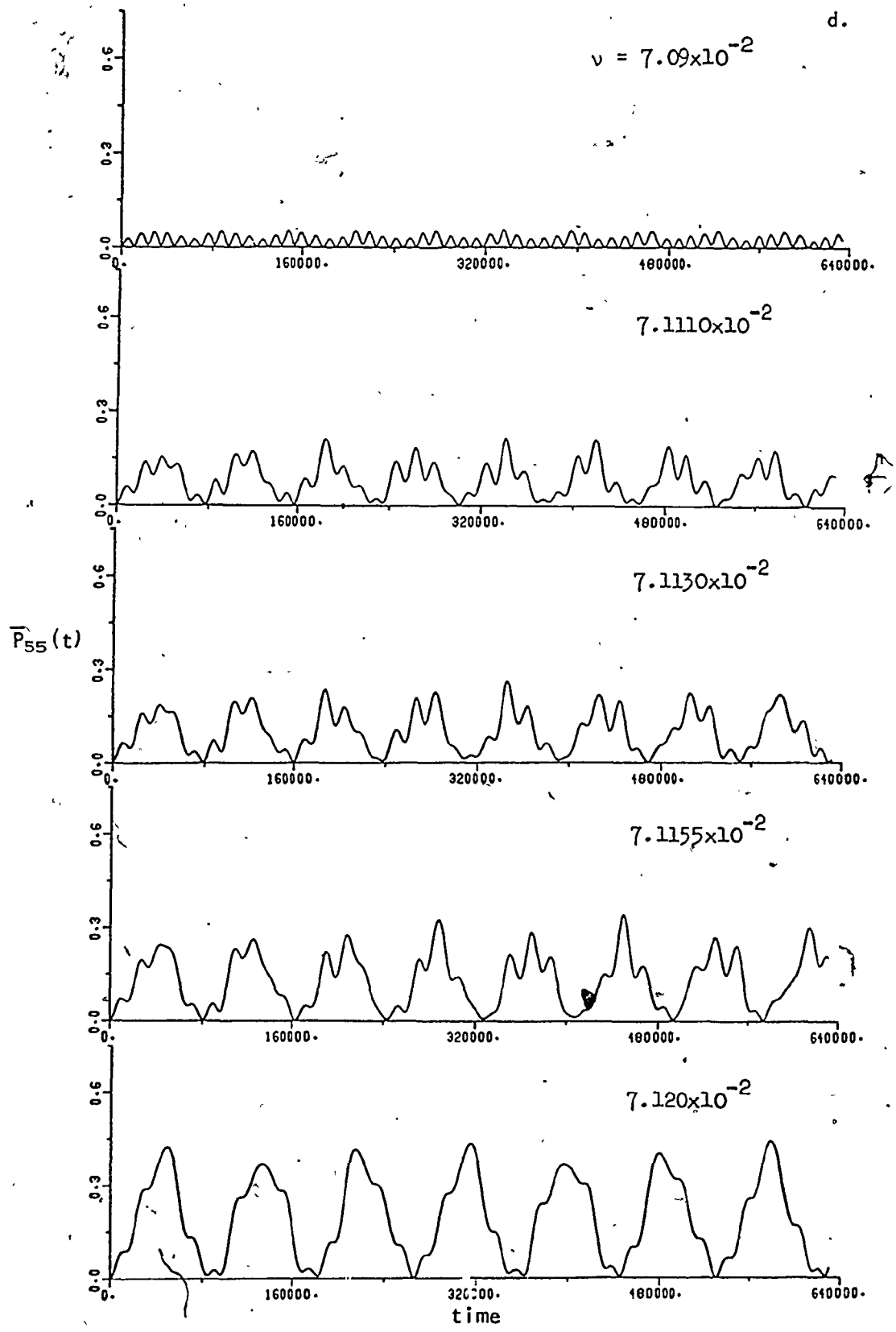
$\nu = 7.09\times10^{-2}$
7.1110×10^{-2}
7.1130×10^{-2}
7.1155×10^{-2}
7.120×10^{-2}
$\overline{P}_{55}(t)$
0.0
0.3
0.6
0.
160000.
320000.
480000.
640000.
time

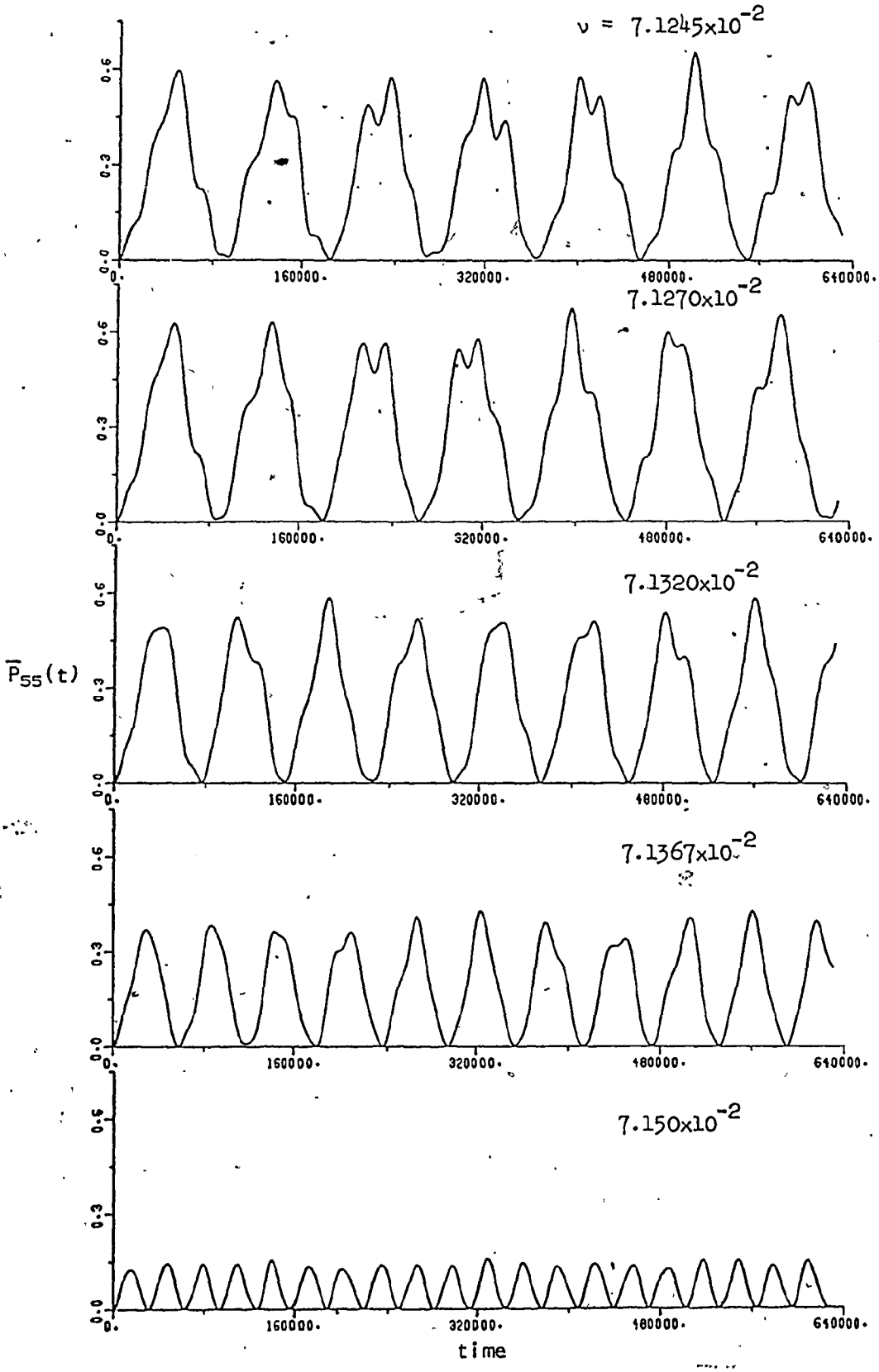
ν = 7.1245x10^-2
7.1270x10^-2
7.1320x10^-2
7.1367x10^-2
7.150x10^-2
P̄55(t)
0.0
0.3
0.6
0.
160000.
320000.
480000.
640000.
time

formalism is used to produce steady-state spectra. The irregularity of the transition probabilities as a function of time gives little indication that the phase- and time-averaged results will be as smooth as figures (3-9) and (3-10) indicate. The irregular behaviour of the curves in figure (3-15) shows that the determination of the "resonant" frequencies for the different levels from the temporal results is not easy. Examination of the time-dependent transition probabilities for levels 3 and 4 (figures (3-15b) and (3-15c)), for example, illustrate that it is virtually impossible to predict the steady-state behaviour in the region of a resonance, in particular, the reversal of the peak positions in figure (3-10) from those expected from the zero field predictions.

These steady-state and time-dependent calculations on a simple five-level system serve to illustrate the behaviour that can be expected for single-photon interactions of a molecular system with lasers of varying intensities. Many of the ideas outlined above may be extended to multi-photon calculations as well (see below).

3.3 Three-photon results

In a two-level system involving even and odd parity states, dipole selection rules forbid even multi-photon transitions between the two levels. However, three-photon (and higher order odd-photon transitions) will be allowed [11,13,14,52,53], with the two levels acting alternately as virtual levels through which the transition proceeds [81]. The intensity will be expected to be very weak since it requires three photons to hit the molecule simultaneously and the transitions are really very far off resonance [13]. The three-photon

resonance peaks will generally be much narrower than their single-photon analogues (see (2.3-9) and (2.3-14)), so that the separation of peaks seen in figure (3-5) should be accomplished more easily in multi-photon spectra.

As mentioned in section 2.2, multi-photon induced transition probabilities are dependent on higher orders of the laser intensity [3,4,13], so that multi-photon spectra can be enhanced relative to single-photon results by increasing the laser strength. The three-photon signal may increase when there are real states at the intermediate energies of the virtual levels, but the understanding of the spectrum will be complicated by the fact that there can be sequential single-photon transitions occurring as well as multi-photon transitions [19,82]. The three-photon spectra in this section proceed through (essentially) virtual levels rather than through real intermediate levels.

3.3.1 Steady-state results

The phase- and long-time-averaged transition probability, $(1-\overline{P}_{11})$, for the five-level system of figure (3-2) and the strong coupling case of figures (3-3) and (3-4) is shown in figures (3-16) for the three-photon transition ($\mu_{12}\varepsilon = 2.83 \times 10^{-3}$, $\mu_{12}\varepsilon = 9.199 \times 10^{-4}$, $\mu_{13}\varepsilon = \mu_{14}\varepsilon = -1.777 \times 10^{-3}$). Interesting differences with the single-photon result of figure (3-3) are immediately noticeable.

The most striking features of the three-photon spectrum are the narrowness of the peaks (recall (2.3-14)) and their apparent complete separation from one another. Whereas the single-photon result for the same system showed a single broad peak (figure 3-3)), the

Figure (3-16). The steady-state induced transition probability, $(1 - \overline{P}_{11})$, for the five-level energy level diagram of figure (3-2) for three-photon transitions. Coupling strengths are given by $\mu_{12}\varepsilon = \mu_{15}\varepsilon = 9.199 \times 10^{-4}$ and $\mu_{13}\varepsilon = \mu_{14}\varepsilon = -1.777 \times 10^{-3}$ ($\mu_{12'}\varepsilon = 2.83 \times 10^{-3}$). The resonance frequencies are given by $\nu_2 \sim 2.37003 \times 10^{-2}$, $\nu_3 \sim 2.37457 \times 10^{-2}$, $\nu_4 \sim 2.37793 \times 10^{-2}$, $\nu_5 \sim 2.38134 \times 10^{-2}$. The frequencies corresponding to the peak positions are verified using the numerical data used to generate the figure.

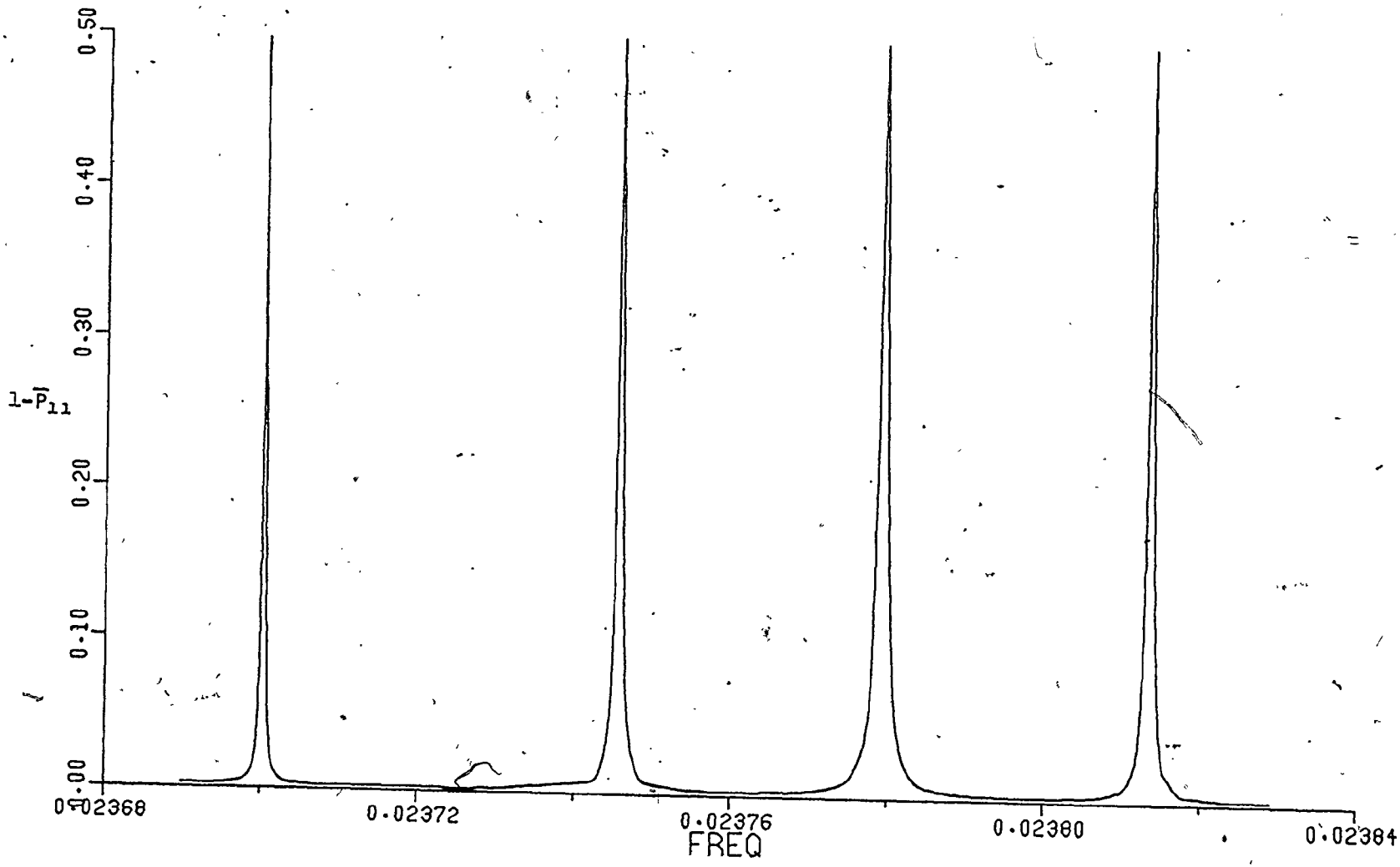
0.50
0.40
0.30
0.20
0.10
0.00
$1-\bar{P}_{11}$
0.02368
0.02372
0.02376
0.02380
0.02384
FREQ

three-photon spectrum consists of four very narrow and distinct peaks. In fact, even for these relatively large values of the coupling strengths, the individual peaks are better separated than were those for the weak coupling case in the single-photon results (figure (3-5)). Interestingly, then, the same energy levels and coupling strengths that give rise to the appearance of a single transition in the one-photon frequency range appear to act very much like individual levels when excited in the three-photon frequency region.

The contributions from the individual levels to the total spectrum are shown in figure (3-17). In contrast to what might be predicted from the weak field results for the single-photon spectrum (see figures (3-5) and (3-6)), the individual peaks do not reach a maximum value of 0.5 ($\overline{P}_{22} \sim 0.494$, $\overline{P}_{33} \sim 0.463$, $\overline{P}_{44} \sim 0.457$, $\overline{P}_{55} \sim 0.484$). The final peak heights of $\sim$0.5 in the overall spectrum (figure (3-16)) are attained thanks to the additional small contributions from the off-resonance levels. That is, the peak in figure (3-16) corresponding to the level 3 resonance, for example, is mainly due to level 3 (see figure (3-17)), but also has contributions from the other three levels. These appear in figure (3-17) as small secondary peaks at the level 3 three-photon resonance frequency.

The secondary peaks appear as a result of the fact that the three-photon transitions proceed via virtual levels. At the frequency of a resonance, the three-photon excitation to a particular level may proceed with any of the excited states acting as a virtual level, the transitions to all four upper levels being allowed. Figure (3-18) illustrates how the level 3 transition, for example, can also proceed through the virtual levels of states 2, 4, and 5. The secondary peaks

Figure (3-17). The three-photon steady-state induced transition probabilities for the four individual upper levels of figure (3-2) for the coupling strengths given in figure (3-16). The secondary peaks in the spectra are located at the resonance frequencies for the other levels. (a) $\overline{P}_{22}$, peak height $\sim$ 0.494, HWHM $\sim$ 1.9×10^{-7}; secondary peaks (left to right) $\sim$ 0.0023, $\sim$ 0.0020, $\sim$ 0.00052. (b) $\overline{P}_{33}$, peak height $\sim$ 0.463, HWHM $\sim$ 4.0×10^{-7}; secondary peaks $\sim$ 0.0038, $\sim$ 0.029, $\sim$ 0.0040 (c) $\overline{P}_{44}$, peak height $\sim$ 0.457, HWHM $\sim$ 6.0×10^{-7}; secondary peaks $\sim$ 0.0018, $\sim$ 0.033, $\sim$ 0.011 (d) $\overline{P}_{55}$, peak height $\sim$ 0.484, HWHM $\sim$ 3.8×10^{-7}; secondary peaks $\sim$ 0.00043, $\sim$ 0.0015, $\sim$ 0.013.

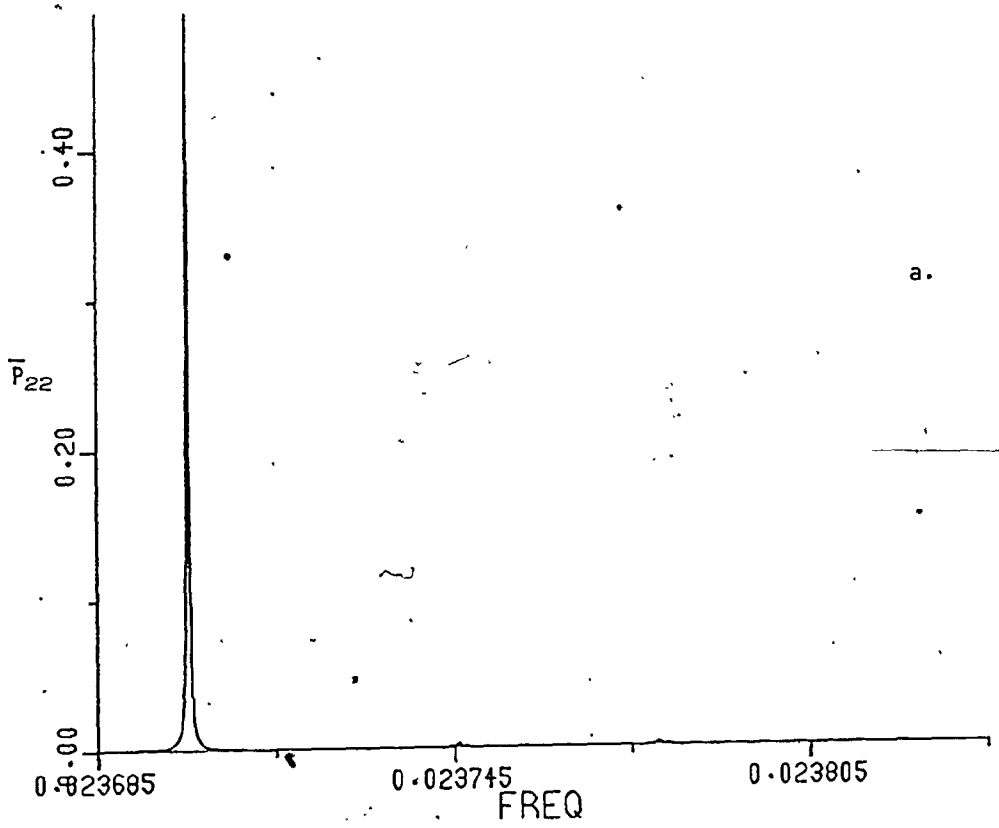
0.40
0.20
0.00
$\overline{P}_{22}$
0.023685
0.023745
0.023805
FREQ

a.

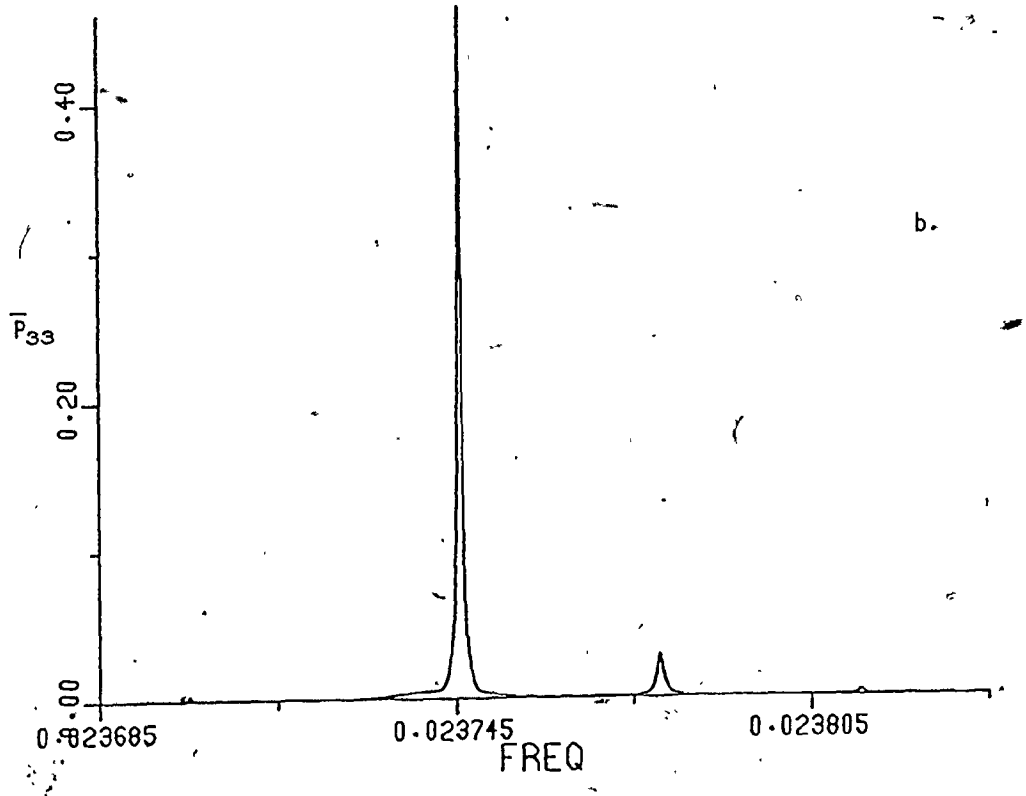
0.40
0.20
0.00
$\overline{P}_{33}$
0.023685
0.023745
0.023805
FREQ

b.

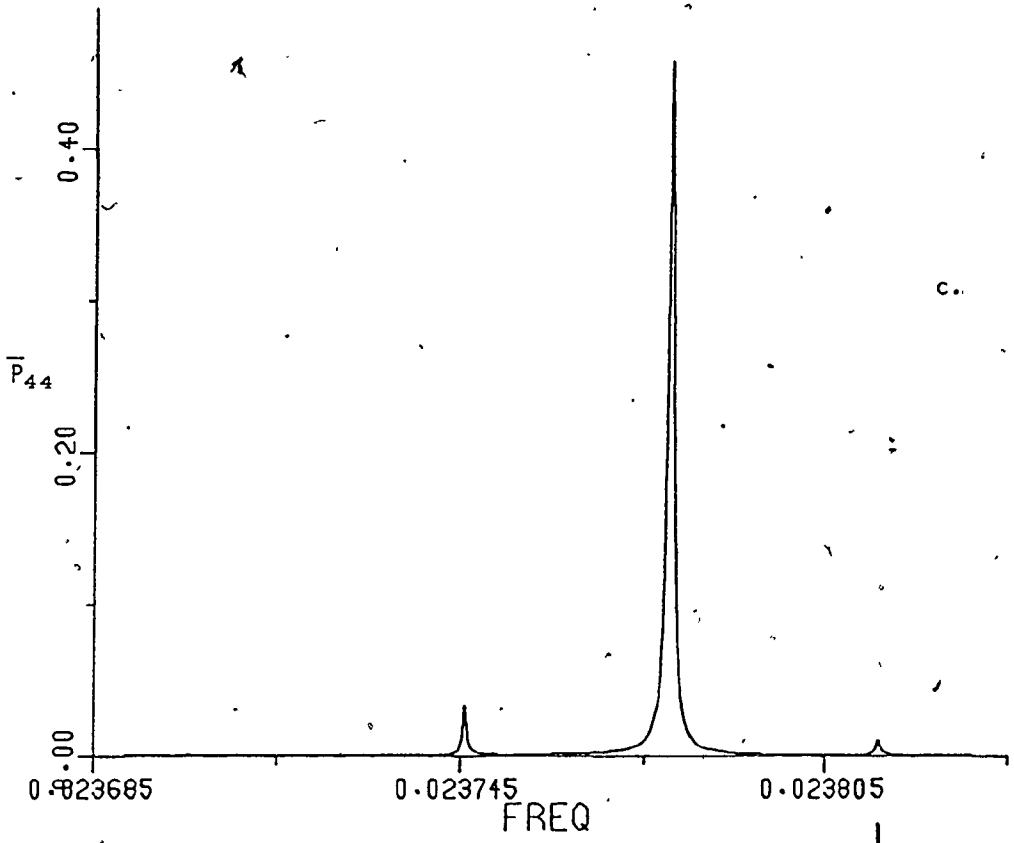
0.40
0.20
0.00
$\bar{P}_{44}$
0.023685
0.023745
0.023805
FREQ

c.

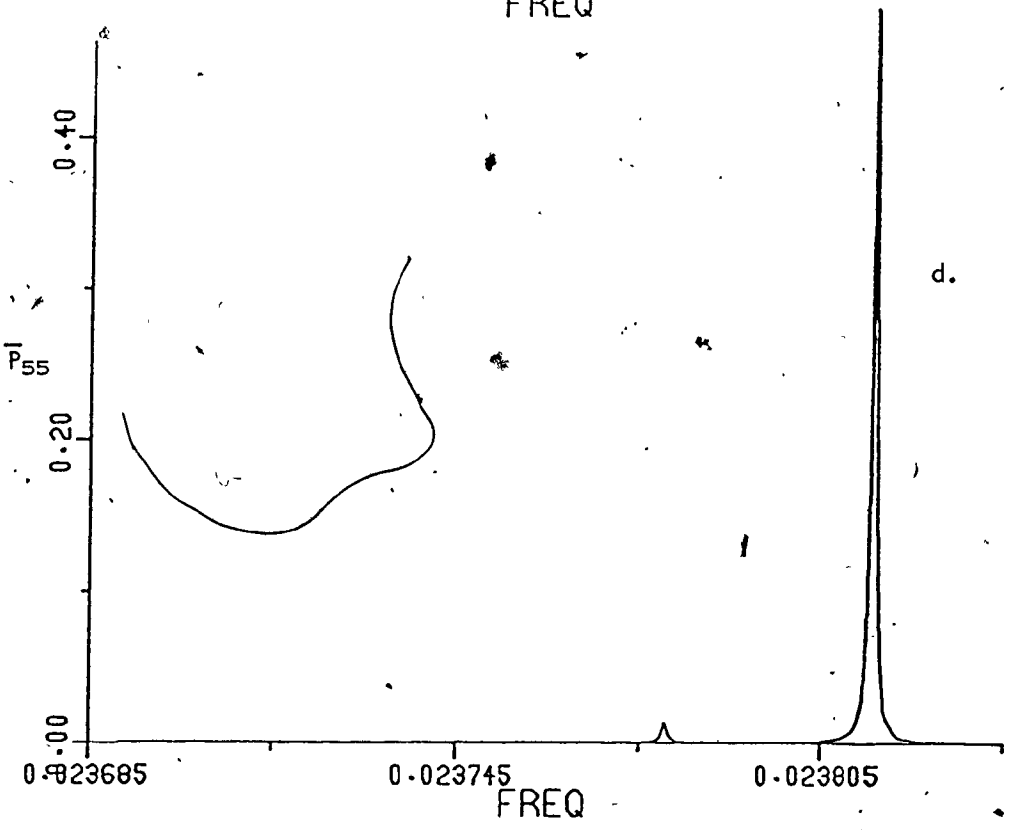
0.40
0.20
0.00
$\bar{P}_{55}$
0.023685
0.023745
0.023805
FREQ

d.

Figure (3-18). Various excitation schemes by which the three-photon transition to level 3 may proceed. (a) On resonance, the three-photon excitation may proceed through states 3 and 1 acting alternately as virtual levels. (b) - (d) At the same three-photon resonance frequency the transition may proceed in slightly off-resonant stages through virtual levels of states 2, 4, and 5. This illustrates how off-resonance levels may become involved in a resonant transition, giving rise to the small secondary peaks in figure (3-17).

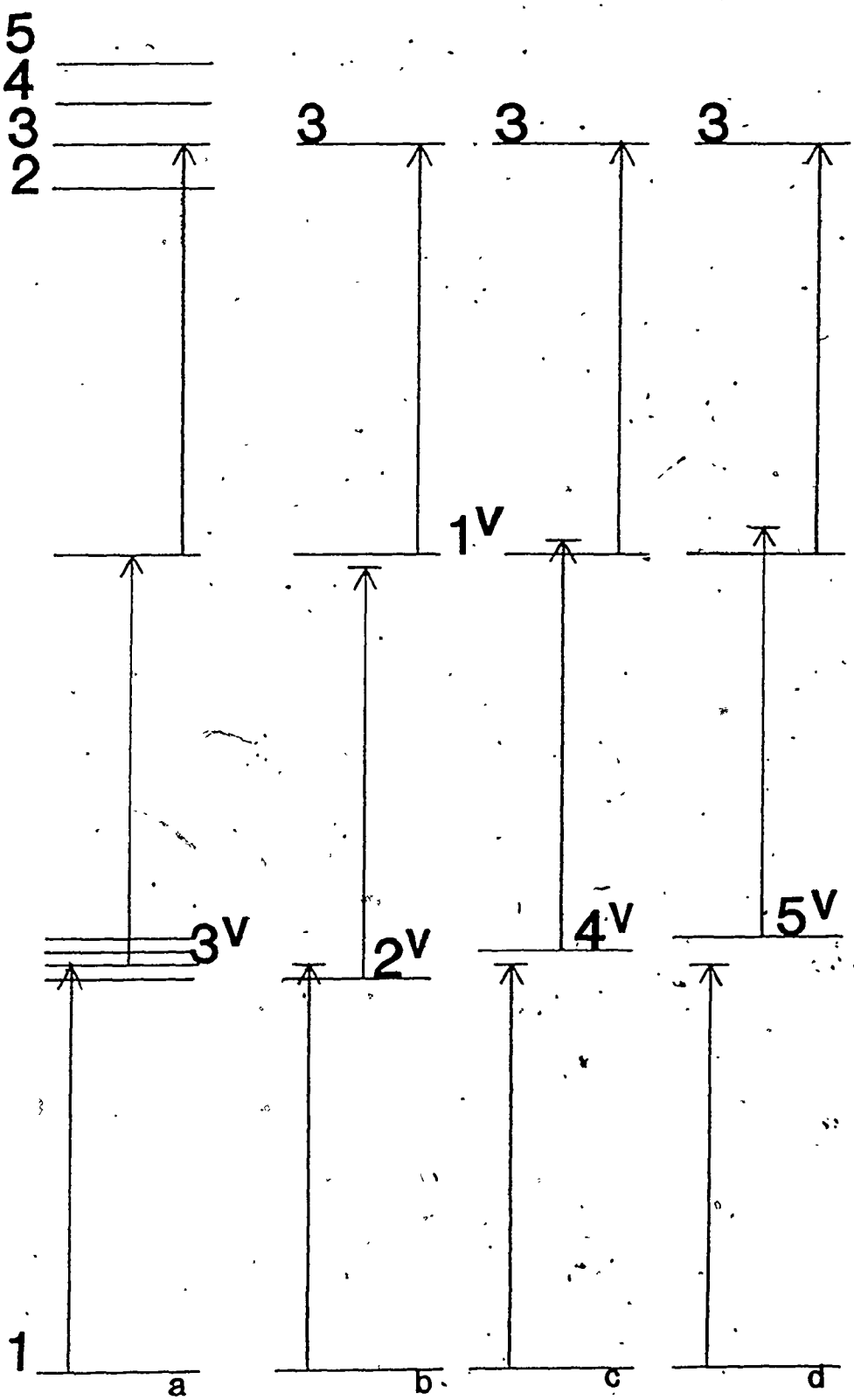
5
4
3
2
3
3
3
1V
3V
2V
4V
5V
1
a
b
c
d

appearing in figure (3-17) are small, since these other levels are not on resonance. Generally, the nearer the levels are to being on resonance and/or the greater the coupling strength, the larger the height of the secondary peak.

Upon closer inspection, figure (3-16) shows itself to be unusual both in the position of the peaks in the spectrum and in their widths. The peaks corresponding to the level 3 and level 4 resonances have shifted further from their zero-field predicted positions than have the peaks for levels 2 and 5, giving the spectrum a much less symmetric look than, say, figures (3-5) or (3-7). This difference in Bloch-Siegert shifts for the two different pairs of lines is expected, since the coupling strength term, $\beta_{1j} = \frac{|\mu\varepsilon|}{\omega_{1j}}$, on which the shift depends, is greater for the "inner" levels, 3 and 4. However, the actual changes in frequency from the zero-field predictions are also very different for level 3 versus level 4 and for level 2 versus level 5. As well, the widths of the peaks, expected intuitively to be approximately the same (see (2.3-14)) in pairs (2 and 5, 3 and 4), are far from being equal. These discrepancies are shown in table (3-1). This table lists the peak positions predicted by the two-level, three-photon equation (2.3-19), the RWA half-widths at half-maximum predicted by (2.3-14) and (2.3-11), and the observed frequencies, widths, and peak heights corresponding to figure (3-17). The differences in energy for pairs of levels produces small differences in the calculated shifts and widths, but these are much smaller than the observed discrepancies. The table illustrates that not only do the Bloch-Siegert shifts and half-widths at half-maximum differ from the two-level predictions of (2.3-19) and (2.3-14), but also that,

Table (3-1). The observed resonance peak positions, peak heights, and half-widths at half-maximum for figure (3-17), and the calculated peak positions (see (2.3-19)) and widths (see (2.3-11) and (2.3-14)).

Level, n	(a) Peak height	$\frac{\omega_{1n}}{3} \times 10^2$	(b) $\nu \times 10^2$, calc.	$\nu - \frac{\omega_{1n}}{3} = \delta\nu$, calc.	(a) $\nu \times 10^2$, obs.	$\nu - \frac{\omega_{1n}}{3} = \delta\nu$, obs.	(c) HWHM, calc.	HWHM, obs.
2	0.494	2.36776	2.36820	4.47×10^{-6}	2.37003	2.269×10^{-5}	2.892×10^{-8}	1.9×10^{-7}
3	0.463	2.37184	2.37350	1.664×10^{-5}	2.37457	2.730×10^{-5}	2.075×10^{-7}	4.0×10^{-7}
4	0.457	2.37483	2.37649	1.662×10^{-5}	2.37793	3.100×10^{-5}	2.070×10^{-7}	6.0×10^{-7}
5	0.484	2.37891	2.37936	4.45×10^{-6}	2.38134	2.423×10^{-5}	2.865×10^{-8}	3.8×10^{-7}

(a) Determined from figure (3-17) and the numerical data used to generate the figure.

(b) Calculated from (2.3-19).

(c) Calculated from (2.3-11) and (2.3-14).

as pointed out above, the levels that might be expected to show similar effects. (2 and 5, 3 and 4) differ significantly.

The use of two-level predictions in the interpretation of a five-level system apparently does not work as well in multi-photon spectra as it does for single-photon results. In order to test the validity of (2.3-11), (2.3-14), and (2.3-19) at the relevant values of the coupling strengths, two-level calculations were carried out using levels 1 and 2 alone ($\mu\varepsilon = 9.199 \times 10^{-4}$) and using levels 1 and 3 alone ($\mu\varepsilon = 1.777 \times 10^{-3}$). The results, $(1 - \overline{P}_{11})$, are shown in figure (3-19). In both cases, a maximum value of 0.5 for the peak heights is reached at the resonance frequencies predicted by (2.3-19) (see table (3-1)). Also, the HWHM in each case is correctly given by (2.3-11) and (2.3-14).

Since the shift and width predictions are borne out when the upper levels are considered in isolated two-level calculations, it is the presence of the other levels that is producing the unusual features pointed out in the discussion of figures (3-16) and (3-17) and table (3-1). Wong, Garrison, and Einwohner [46], Burrows and Salzman [83], Salzman [84], and Moloney and Meath [75] have all pointed out that extra non-resonant intermediate levels can effect the shift, and in some cases the shape, of the resonance peak in a multi-photon spectrum. These treatments describe very different level configurations and coupling schemes relative to the present system. Salzman did not do a steady-state calculation, but instead used the maximum values in the temporal plots at various frequencies to estimate linewidths for the transitions. He determined for the systems studied in his work that the time-dependent transition

Figure (3-19). Steady-state induced transition probabilities for two-level, three-photon calculations (a) Levels 1 and 2 of figure (3-2) with $\mu\varepsilon = 9.199 \times 10^{-4}$, resonance frequency $\sim 2.3682 \times 10^{-2}$, HWHM $\sim 2.9 \times 10^{-8}$ (b) Levels 1 and 3 of figure (3-2) with $\mu\varepsilon = 1.777 \times 10^{-3}$, resonance frequency $\sim 2.3735 \times 10^{-2}$, HWHM $\sim 2.1 \times 10^{-7}$. Approximate resonance frequencies and widths were predicted using (2.3 -19) and (2.3 - 14) and were verified with the numerical data used to generate the figures.

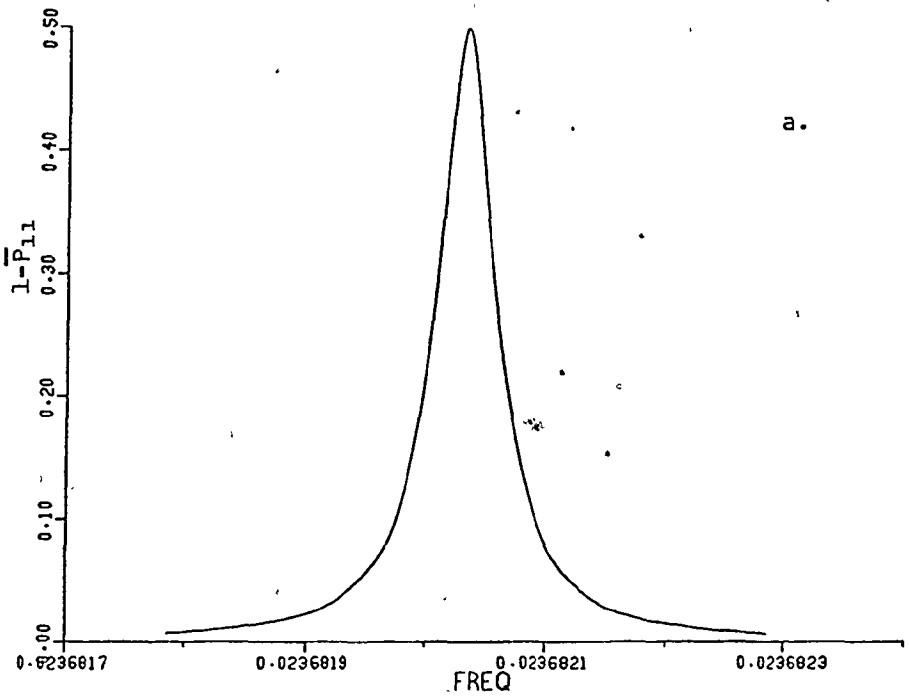
a.
$1-\bar{P}_{11}$
0.00
0.10
0.20
0.30
0.40
0.50
0.0236817
0.0236819
0.0236821
0.0236823
FREQ

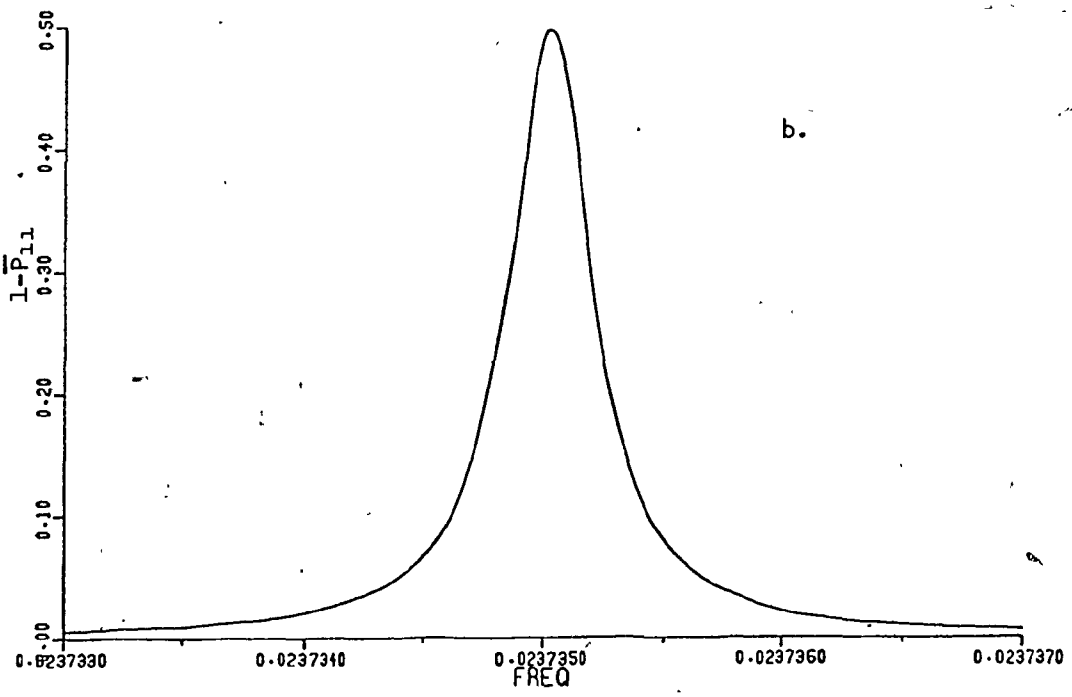
b.
$1-\bar{P}_{11}$
0.00
0.10
0.20
0.30
0.40
0.50
0.0237330
0.0237340
0.0237350
0.0237360
0.0237370
FREQ

probability for a multi-photon (n = 2,3,4) transition will have the "Rabi-like" form (see also (2.3-10)):

$$P_{22}(t) = \frac{\gamma^2}{(\omega_{12}^{\circ}+n\delta-n\nu)^2+\delta^2} \sin^2\{\frac{t}{2}\sqrt{(\omega_{12}^{\circ}+n\delta-n\nu)^2+\gamma^2}\} \qquad (3.3\text{-}1)$$

where δ is the Bloch-Siegert shift for the n-photon transition and γ^2 is a parameter analogous to $|u|^2$ in (2.3-10). The lineshape of the steady-state spectrum will be a Lorentzian with HWHM = $\frac{\gamma}{n}$, since the time-average of (3.3-1) will be

$$\overline{P}_{22} = \frac{\gamma^2}{2[(\omega_{12}^{\circ} + n\delta - n\nu)^2 + \gamma^2]} \qquad (3.3\text{-}2)$$

Since γ must be determined from the steady-state spectrum (or, as Salzman has done, from many temporal calculations), the utility of (3.3-1) and (3.3-2) is apparently restricted to the calculation of the "Rabi" period from the observed HWHM (see section 3.3.2), or vice-versa.

Figure (3-16) and table (3-1) illustrate how the neighbouring levels in the five-level calculation effect both the shift and the shape of lines in a three-photon spectrum. The effect of the neighbouring levels on the steady-state resonance peaks appears to depend upon the energy spacings between the observed resonance positions (ie. the shifted frequencies). The (isolated) two-level Bloch-Siegert shifts for resonances 3 and 4 are greater than those for 2 and 5 (see table (3-1) and figure (3-19)); this suggests that the resonance peaks for levels 3 and 4 will be shifted away from peak 2 and toward peak 5. As a first approximation, this would imply a greater

interaction between levels 4 and 5, as opposed to levels 2 and 3. When all of the excited levels are taken into account in the overall spectrum (see figure (3-16)), the greater resulting interaction between levels 4 and 5, as opposed to levels 2 and 3, apparently produces larger overall shifts in the peak positions and greater widths for these two resonances relative to their low frequency partners (see table (3-1)). That is, since the resonance peak for level 4 is shifted toward the level 5 peak, while the peak for level 3 is shifted away from the level 2 peak, the level 4 peak experiences a greater "neighbouring level effect" than level 3. Similarly, there is a greater neighbouring level effect on the level 5 peak, compared to the peak for level 2. (Since the coupling to levels 3 and 4 is very different from the coupling to levels 2 and 5, comparisons are made only between levels 3 and 4 or 2 and 5.)

The individual peak heights in figure (3-17) may also be analyzed according to the neighbouring level effect.. In both cases, the high frequency members of a pair show the greater deviation from 0.5, implying a greater contribution from neighbouring levels is needed in order to attain the peak height of 0.5 in the overall spectrum (see figure (3-16)). The secondary peak for level 4 at the level 5 resonance ($\sim$0.011) is much greater than the secondary peak for level 3 at the level 2 resonance ($\sim$0.004), again indicating the greater neighbouring level interaction for the high frequency partners in each pair.

3.3.2 Temporal results

As in the single-photon results of section 3.2, the three-photon

temporal results reinforce the ideas developed with respect to the steady-state spectra. Figure (3-20) shows the time-dependent behaviour of the phase-averaged transition probabilities for the four excited levels at each of the resonance frequencies (ν = 0.0237003, 0.0237457, 0.0237793, 0.0238134) of the three-photon spectrum of figure (3-16).

As might be expected, given the discussion in section 3.3.1, the "Rabi" periods (Δt) of oscillation for the four resonances differ from the simple two-level predictions of (2.3-12), as well as differing significantly from each other. This is summarized in table (3-2). In all four cases the period has decreased from the two-level prediction and the greater decrease within pairs of levels (3 vs. 4, 2 vs. 5) is for the level with the greater neighbouring level effect.

The two-level predictions of (2.3-12) can be checked by carrying out calculations on levels 1 and 2 alone ($\mu\varepsilon = 9.199 \times 10^{-4}$) and on levels 1 and 3 alone ($\mu\varepsilon = 1.777 \times 10^{-3}$). As in the case of the steady-state spectra (figure (3-19)), figure (3-21) illustrates the validity of the two-level equation for these coupling strengths ($\Delta t_2 \sim 7.2 \times 10^7$, $\Delta t_3 \sim 1.0 \times 10^7$).

Of note in the time-dependent plots of figure (3-20) are the periods of oscillation of the off-resonant levels. In the single-photon temporal results (section 3.2.2), the period of oscillation increased as the resonance frequency for the level was approached (see also (2.3-7)). In the three-photon results, all four levels share approximately the same overall period at each of the resonance frequencies. This further emphasizes the interactions that come about when all four upper levels are involved in a three-phton transition.

Figure (3-20). The phase-averaged temporal behaviour of the upper levels ($\overline{P}_{22}(t)$, $\overline{P}_{33}(t)$, $\overline{P}_{44}(t)$, $\overline{P}_{55}(t)$) of the five-level three-photon system of figures (3-16) and (3-17). Frequencies were chosen to be the three-photon resonance frequencies. "Rabi" periods were determined for the resonant level, although the secondary peaks showed approximately the same period (a) $\nu = 2.37003 \times 10^{-2}$, $\Delta t \sim 1.0 \times 10^{7}$ (b) $\nu = 2.37457 \times 10^{-2}$, $\Delta t \sim 5.5 \times 10^{6}$ (c) $\nu = 2.37793 \times 10^{-2}$, $\Delta t \sim 3.5 \times 10^{6}$ (d) $\nu = 2.38134 \times 10^{-2}$, $\Delta t \sim 5.3 \times 10^{6}$.

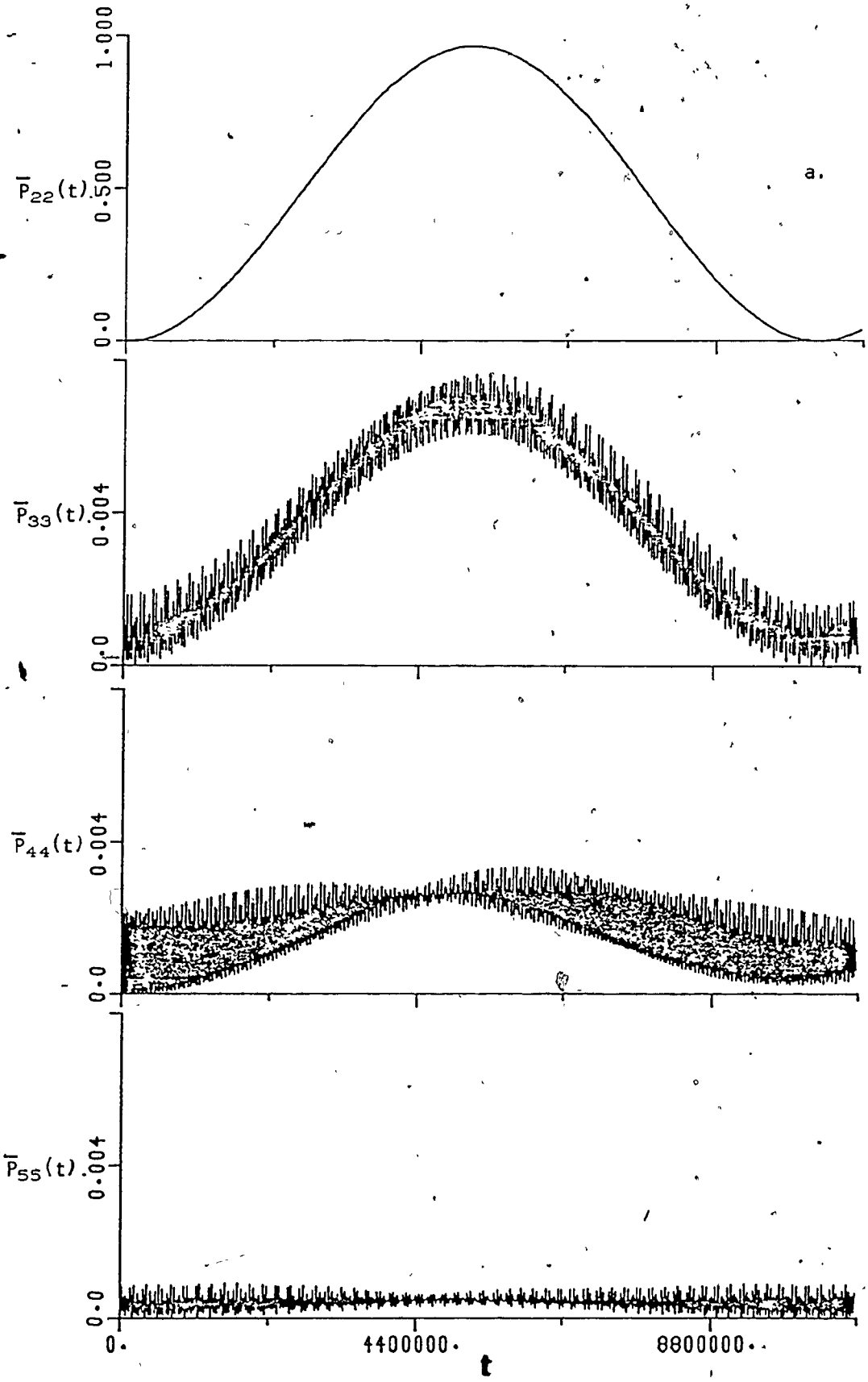
1.000
0.500
0.0
$\bar{P}_{22}(t)$
a.
0.004
0.0
$\bar{P}_{33}(t)$
0.004
0.0
$\bar{P}_{44}(t)$
0.004
0.0
$\bar{P}_{55}(t)$
0.
4400000.
8800000.
t

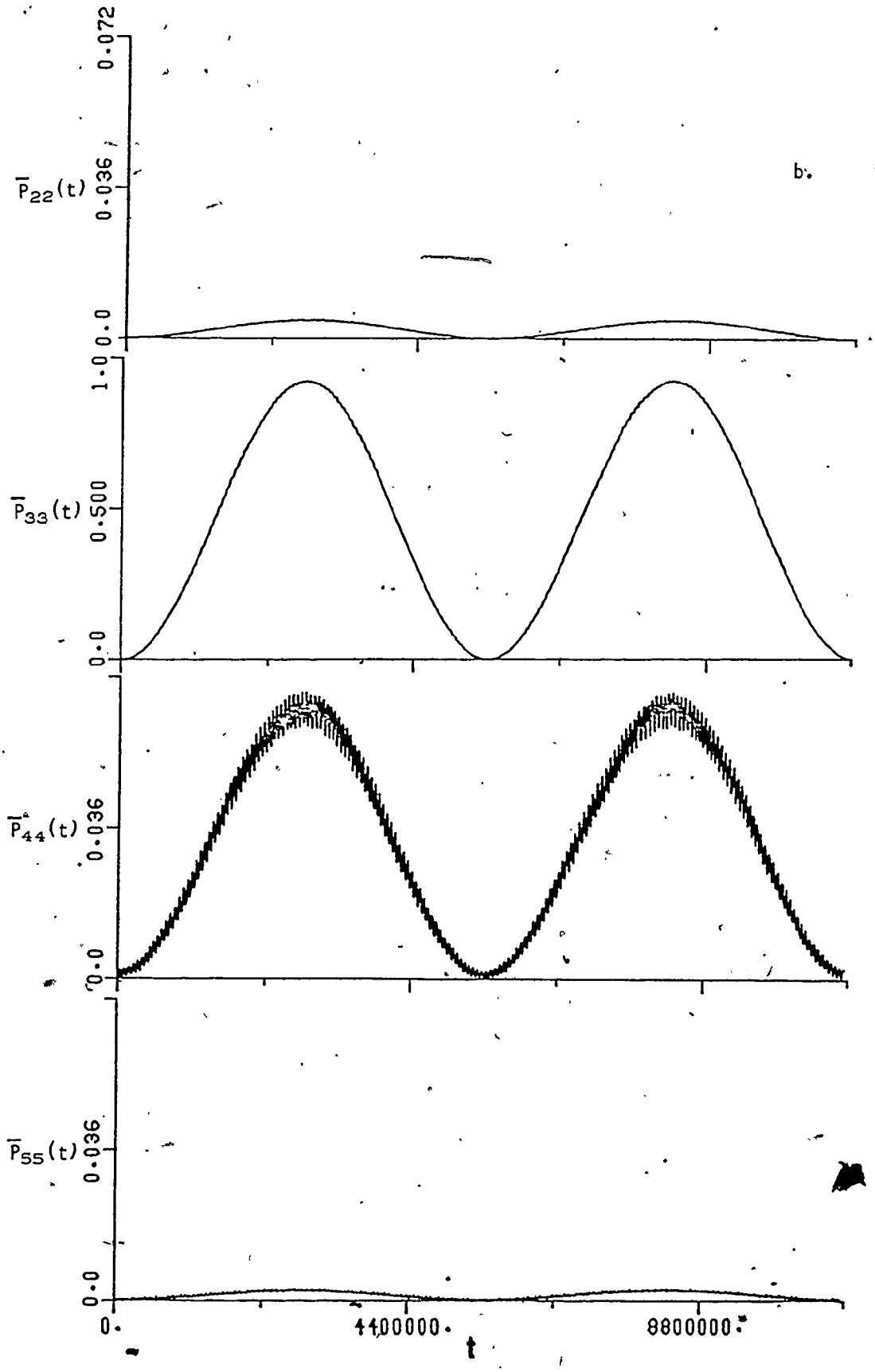
0.072
$\bar{P}_{22}(t)$
0.036
0.0
b.
1.0
$\bar{P}_{33}(t)$
0.500
0.0
$\bar{P}_{44}(t)$
0.036
0.0
$\bar{P}_{55}(t)$
0.036
0.0
0.
4400000.
8800000.
t

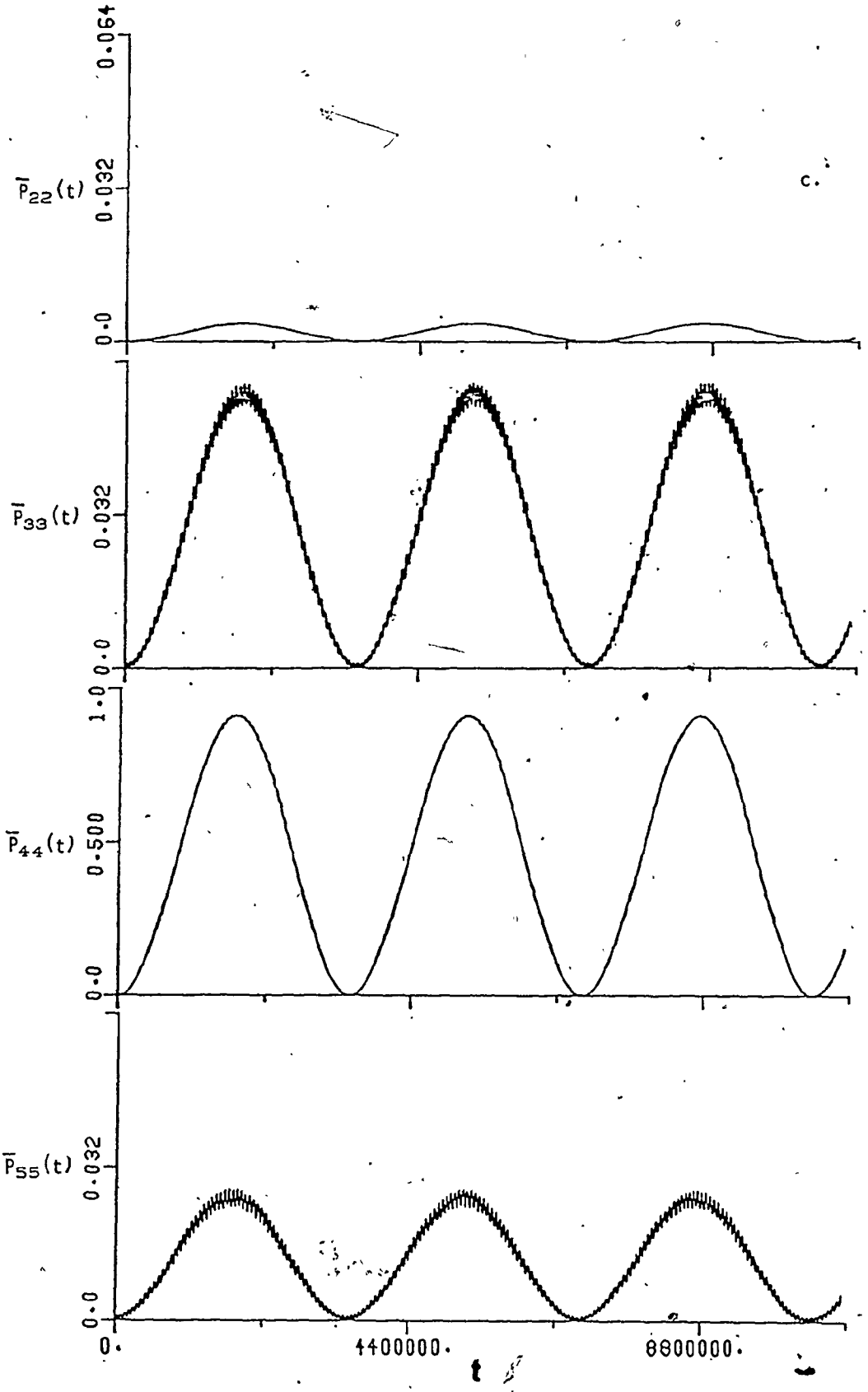
0.064
0.032
0.0
$\bar{P}_{22}(t)$
c.
0.032
0.0
$\bar{P}_{33}(t)$
1.0
0.500
0.0
$\bar{P}_{44}(t)$
0.032
0.0
$\bar{P}_{55}(t)$
0.
4400000.
8800000.
t

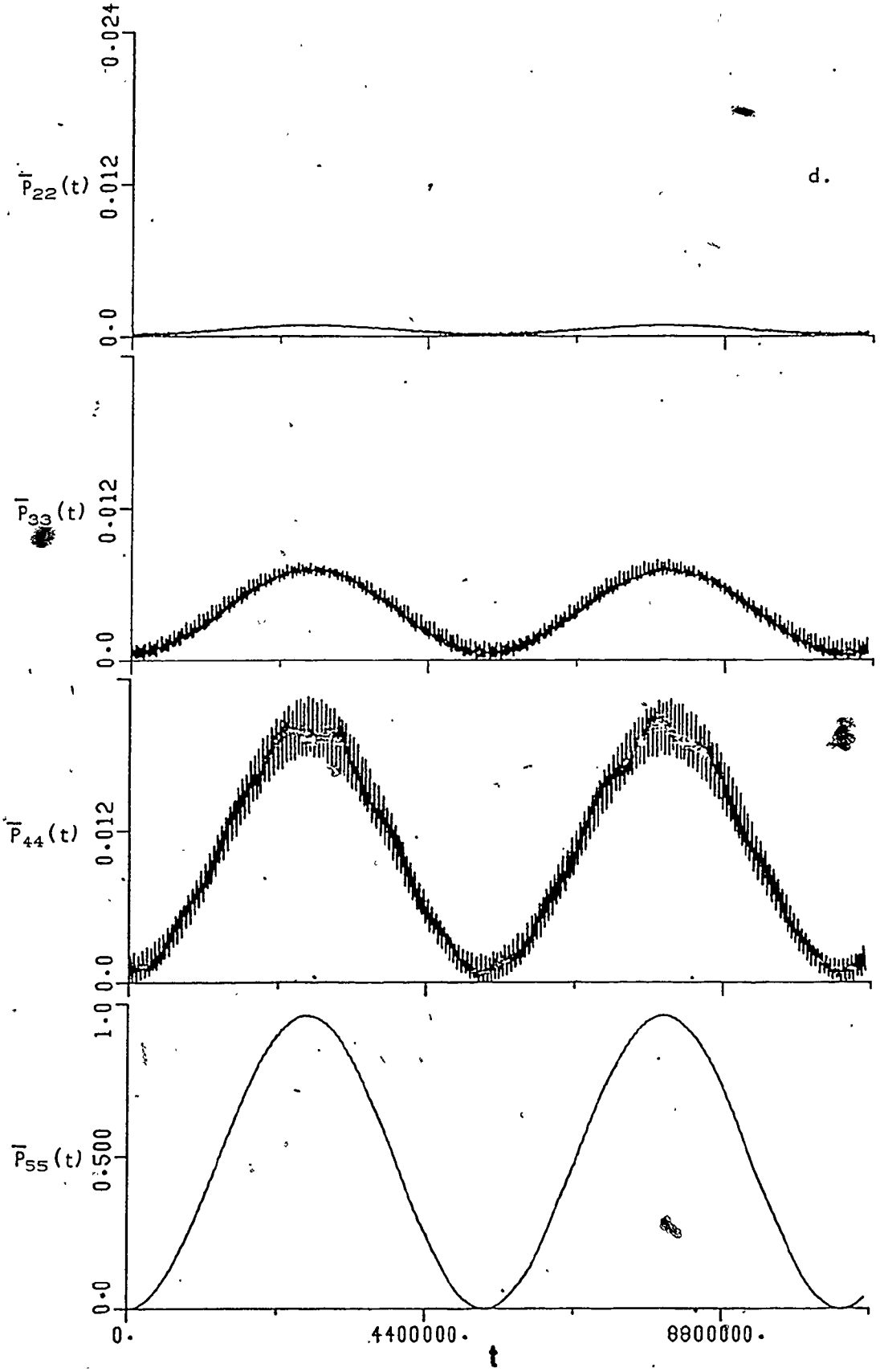
0.024
0.012
0.0
$\bar{P}_{22}(t)$
d.
$\bar{P}_{33}(t)$
$\bar{P}_{44}(t)$
1.0
0.500
$\bar{P}_{55}(t)$
0.
4400000.
8800000.
t

Table (3-2). Periods of oscillation, Δt, for the phase-averaged temporal results of figure (3-20) compared to the two-level predictions of (2.3-12) and the empirical formula given by (3.3-1) and (3.3-3). The HWHMs needed for the empirical result are the widths observed in figure (3-17) (see also table (3-1)).

Level, n	Resonance freq., $\nu \times 10^2$	Δt, obs (figure (3-20))	Δt^R, calc. (2.3-12)	Δt, calc. (3.3-3)
2	2.37003	$\sim 1.0 \times 10^7$	7.243×10^7	1.10×10^7
3	2.37457	$\sim 5.5 \times 10^6$	1.009×10^7	5.24×10^6
4	2.37793	$\sim 3.5 \times 10^6$	1.012×10^7	3.49×10^6
5	2.38134	$\sim 5.3 \times 10^6$	7.311×10^7	5.51×10^6

Figure (3-21). Phase-averaged temporal behaviour of two-level three-photon systems. Frequencies were chosen to be the three-photon resonance frequencies (see figure (3-19)). (a) Levels 1 and 2 of figure (3-2) with $\mu\varepsilon = 9.199 \times 10^{-4}$, $\nu = 2.3682 \times 10^{-2}$, $\Delta t \sim 7.2 \times 10^{7}$ (b) Levels 1 and 3 of figure (3-2) with $\mu\varepsilon = 1.777 \times 10^{-3}$, $\nu = 2.3735 \times 10^{-2}$, $\Delta t \sim 1.0 \times 10^{7}$.

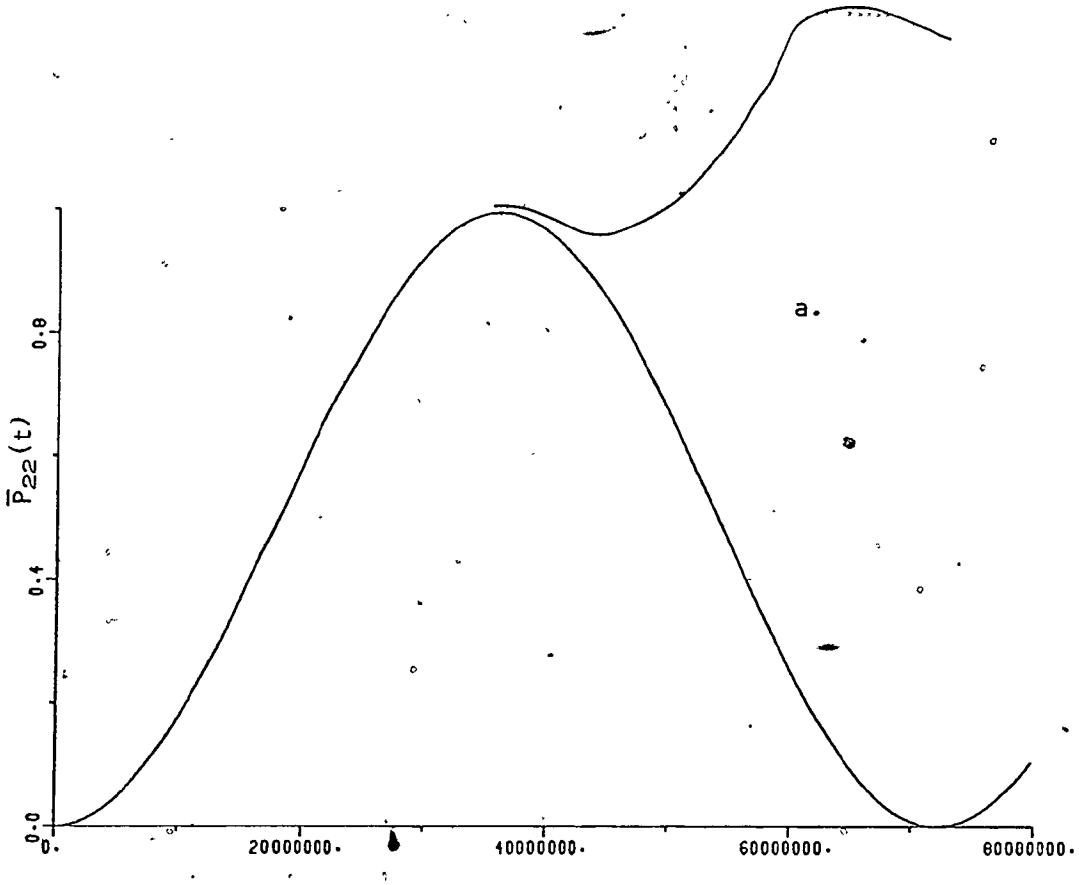
a.
$\bar{P}_{22}(t)$
0.0
0.4
0.8
0.
20000000.
40000000.
60000000.
80000000.

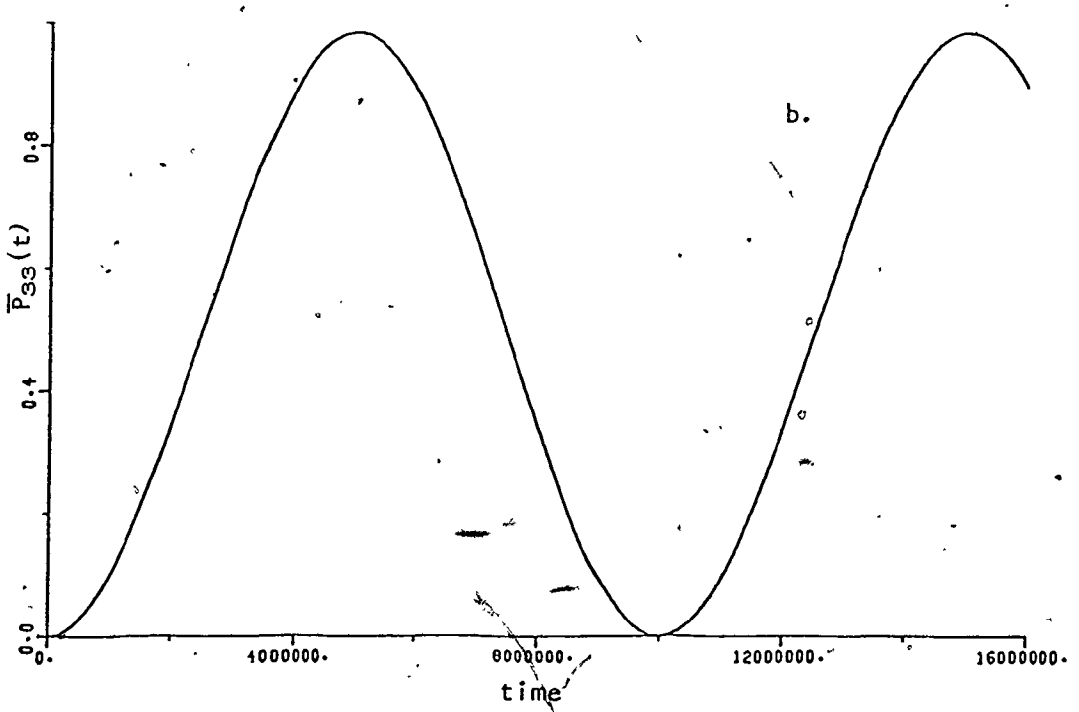
b.
$\bar{P}_{33}(t)$
0.0
0.4
0.8
0.
4000000.
8000000.
12000000.
16000000.
time

Table (3-2) also lists the "Rabi" periods predicted by (3.3-1) using the estimated observed HWHMs of table (3-1). According to (3.3-1), the period will be given by

$$\Delta t = \frac{2\pi}{\gamma} \qquad (3.3\text{-}3)$$

where

$$\gamma = (n)(\text{HWHM}) \qquad (3.3\text{-}4)$$

The agreement with the experimental results is much better than that for the two-level predictions of (2.3-12). Some of the discrepancy may be attributed to the very approximate values of the HWHM while some may also be attributed to the fact that the empirical equation (3.3-1) may not be completely valid for this system. It is in fact quite interesting that Salzman's results, (3.3-1), given originally for a much different energy level diagram [84], fits the present results so well. Since (3.3-1) is meant to apply in the region of a resonance, the periods corresponding to the secondary peaks, found in figure (3-20) to be approximately equal to the period for the corresponding resonance peak, would not have been predicted.

Figures (3-16), (3-17), and (3-20) and tables (3-1) and (3-2) illustrate the necessity of using an exact solution of the time-dependent Schroedinger equation to calculate the three-photon spectrum. The exact solution is able to take into account the effects of neighbouring levels on the shifts and widths of the resonance peaks and on the periods of oscillation of the temporal results. As noted above, these results could not be successfully predicted from simple two-level

calculations. Although the peaks in the spectrum are very narrow and appear to be well-separated, there is still significant interaction between levels. The use of separate two-level calcuations, successfully employed for the understanding of some of the single-photon results in section 3.2, cannot be used in the interpretation of the three-photon spectra given above.

CHAPTER 4

RELAXATION EFFECTS

In the studies of the five-level system carried out in the previous chapter, it has always been assumed implicitly that the decay of the energy levels has been negligible or non-existent. As pointed out in Chapter 2 (see (2.6-6)), the Floquet formalism can be used in a uniform damping model for the system, in which it is assumed that the molecules undergo "collisions" that will interrupt their interaction with the radiation field. While this model provides one useful way to examine the effect of relaxation on the steady-state spectrum, it is somewhat restricted in that the collisions act to terminate the interaction and the mechanism does not distinguish between the different levels.

In general, it would be expected that the excited energy levels in a molecule could have very different lifetimes (while the ground state would not be expected to decay), and that these lifetimes could effect the transition probabilities while the molecule-radiation interaction continued. To account for such behaviour, individual damping terms can be incorporated into the formalism (see Section 2.6) by replacing the energy terms, E_j, with the "damped energies", $E_j - \frac{i\Gamma_j}{2}$.

4.1 Damping of Individual Levels

It has been pointed out earlier (Section 2.6) that the introduction of individual pheomenological decay terms means that the Floquet formalism cannot be used to generate phase- and time-averaged spectra. However, the formalism of Section 2.4 can

still be used, with slight modifications, to calculate the temporal behaviour of a "damped" system. Examination of the form of (2.6-1) for the interaction representation would indicate that the time-dependent coefficients, $a_j(t)$, in the Schroedinger representation will satisfy the matrix equation (2.4-5) with the new definition of the matrix $\underline{\underline{E}}'$ given by

$$(\underline{\underline{E}}')_{ij} = (E_j - \frac{i\Gamma_j}{2})\delta_{ij} - \mu_{ij}\varepsilon^\circ \qquad (4.1\text{-}1)$$

Once the damping has been introduced in this manner, the use of the matrix equations of Section 2.4 to determine the temporal behaviour of a many-level system is straightforward. The effect of individual lifetimes on the time-dependent development of the transition probabilities will be treated explicitly for a two-level system below.

The time-dependent coefficients, $a_j(t)$, will satisfy (2.4-5) in its modified form (with $\mu\varepsilon^\circ = 0$ to correspond to a diagonalized representation)

$$\begin{aligned} i\frac{\partial}{\partial t}a_1(t) &= -\mu_{12}\varepsilon\cos(\nu t + \delta)a_2(t) + (E_1 - \frac{i\Gamma_1}{2})a_1(t) \\ i\frac{\partial}{\partial t}a_2(t) &= -\mu_{21}\varepsilon\cos(\nu t + \delta)a_1(t) + (E_2 - \frac{i\Gamma_2}{2})a_2(t) \end{aligned} \qquad (4.1\text{-}2)$$

When the damping terms are equal, $\Gamma_1 = \Gamma_2$, it can be shown that the temporal behaviour in the damped system will have a particularly simple form. Let α_1 and α_2 satisfy (4.1-2) with $\Gamma_1 = \Gamma_2 = 0$,

$$i\frac{\partial}{\partial t}\alpha_1(t) = -\mu_{12}\varepsilon\cos(\nu t + \delta)\,\alpha_2(t) + E_1\alpha_1(t)$$

$$i\frac{\partial}{\partial t}\alpha_2(t) = -\mu_{21}\varepsilon\cos(\nu t + \delta)\,\alpha_1(t) + E_2\alpha_2(t) \qquad (4.1\text{-}3)$$

and try a solution of (4.1-2) of the form

$$a_1 = \alpha_1 \exp(-\frac{\Gamma_1}{2} t)$$

$$a_2 = \alpha_2 \exp(-\frac{\Gamma_2}{2} t) \qquad (4.1\text{-}4)$$

Subsituting (4.1-4) into (4.1-2) leads to

$$i\frac{\partial}{\partial t}\,a_1(t) = i\frac{\partial}{\partial t}\,(\alpha_1 \exp(-\frac{\Gamma_1}{2} t)) \qquad (4.1\text{-}5)$$

$$= -\mu_{12}\varepsilon\cos(\nu t + \delta)\,\alpha_2 e^{-\Gamma_1 t/2} + (E_1 - i\Gamma_1\frac{1}{2})\alpha_1 e^{-\Gamma_1 t/2}$$

which will reduce to (4.1-2) if we write $\Gamma_1 = \Gamma_2$. When this is true, the transition probabilities are given by

$$P_{11}(t) = |a_1(t)|^2 = |\alpha_1(t)|^2 \exp(-\Gamma t)$$

$$P_{22}(t) = |a_2(t)|^2 = |\alpha_2(t)|^2 \exp(-\Gamma t) \qquad (4.1\text{-}6)$$

That is, the temporal behaviour of the damped system will simply be the temporal behaviour of the undamped system multiplied by an exponential decay term.

When the individual decay terms are not the same, no simple factoring in the solution of (4.1-2) occurs. The matrix formalism of Section 2.4 can still be used to calculate the temporal results, with the individual damping terms included in $\underline{\underline{E}}'$ in the power series solution. In order to see the effect of this damping, it is perhaps instructive to write out explicitly a few of the leading terms of the recurrence relation given by (2.4-11) for a simple two-level problem. The first term, $\underline{\underline{Q}}_0$, is defined by (2.4-12), $\underline{\underline{\mu}}$ is given by (2.4-6), and $\underline{\underline{E}}'$ is given by (4.1-1). In this example, $\underline{\underline{E}}'$, has the form ($\varepsilon^\circ = 0$)

$$\underline{\underline{E}}' = \begin{bmatrix} E_1 - \dfrac{i\Gamma_1}{2} & 0 \\ 0 & E_2 - \dfrac{i\Gamma_2}{2} \end{bmatrix} \tag{4.1-7}$$

Now the second term defined by (2.4-11), $\underline{\underline{Q}}_2$, for example, will be given by ($\mu_{12} = \mu_{21} = \mu$)

$$\begin{aligned}
(\underline{\underline{Q}}_2)_{11} &= \frac{1}{2(i\nu)^2}\left\{\left[E_1^2 + (\mu\varepsilon)^2\right] + \left[-iE_1\Gamma_1 - \frac{\Gamma_1^2}{4}\right]\right\} \\
(\underline{\underline{Q}}_2)_{12} &= (\underline{\underline{Q}}_2)_{21} = \frac{1}{2(i\nu)^2}\left\{\left[-(E_1 + E_2)\mu\varepsilon\right] + \left[\left(i\frac{\Gamma_1}{2} + i\frac{\Gamma_2}{2}\right)\mu\varepsilon\right]\right\} \\
(\underline{\underline{Q}}_2)_{22} &= \frac{1}{2(i\nu)^2}\left\{\left[E_2^2 + (\mu\varepsilon)^2\right] + \left[-iE_2\Gamma_2 - \frac{\Gamma_2^2}{4}\right]\right\}
\end{aligned} \tag{4.1-8}$$

The first term within the brace brackets corresponds to the terms that would be present in the undamped system, while the second term illustrates the effect of the added damping terms. The higher-order terms in the recurrence relation show an increasingly more complicated

form. For example, the next term in (2.4-11) includes the matrix elements:

$$(\underline{\underline{Q}}_3)_{21} = (\underline{\underline{Q}}_3)_{12} = \frac{1}{3!(i\nu)^3}\{[-(E_2(E_2+E_1)+\nu^2+E_1^2)\mu\varepsilon - (\mu\varepsilon)^3]$$

$$+ [\mu\varepsilon(iE_2\Gamma_2 + \frac{\Gamma_2^2}{4} + iE_1\Gamma_1 + \frac{\Gamma_1^2}{4} + i\frac{E_1\Gamma_2}{2} + i\frac{E_2\Gamma_1}{2} + \frac{\Gamma_1\Gamma_2}{4})]\} \quad (4.1\text{-}9)$$

where again the second term in the brace brackets shows the effect of adding the relaxation terms. When the various expressions for $\underline{\underline{Q}}_\ell$, with damping, are used in (2.4-10) to determine $\underline{\underline{F}}(\gamma)$, the complicated form of the added damping terms in the $\underline{\underline{Q}}_\ell$ will cause the matrix elements of $\underline{\underline{F}}$ to be similarly complicated. By correctly re-grouping terms, the effect of the damping on the originally undamped system can be seen more easily. For example, the matrix elements $(\underline{\underline{F}})_{21} = (\underline{\underline{F}})_{12}$ are given by

$$(\underline{\underline{F}})_{21} = (\underline{\underline{F}})_{12} = \{-\frac{\mu\varepsilon\gamma}{i\nu}\}\left[1-\frac{\gamma}{2\nu}\left(\frac{\Gamma_1+\Gamma_2}{2}\right) + \frac{\gamma^2}{2!\nu^2}\frac{1}{3}\left(\left[\frac{\Gamma_2}{2}\right]^2+\left[\frac{\Gamma_1}{2}\right]^2+\frac{\Gamma_1\Gamma_2}{4}\right)\ldots\right]$$

$$+ \{-\mu\varepsilon E_2\frac{\gamma^2}{2!(i\nu)^2}\}\left[1-\frac{\gamma}{2\nu}\left(\frac{2\Gamma_2+\Gamma_1}{3}\right) + \frac{\gamma^2}{2!\nu^2}\frac{1}{3}\left(\frac{3}{2}\left[\frac{\Gamma_2}{2}\right]^2+\frac{1}{2}\left[\frac{\Gamma_1}{2}\right]^2+\frac{\Gamma_1\Gamma_2}{4}\right)\ldots\right]$$

$$+ \{-\mu\varepsilon E_1\frac{\gamma^2}{2!(i\nu)^2}\}\left[1-\frac{\gamma}{2\nu}\left(\frac{2\Gamma_1+\Gamma_2}{3}\right) + \frac{\gamma^2}{2!\nu^2}\frac{1}{3}\left(\frac{3}{2}\left[\frac{\Gamma_1}{2}\right]^2+\frac{1}{2}\left[\frac{\Gamma_2}{2}\right]^2+\frac{\Gamma_1\Gamma_2}{4}\right)\ldots\right]$$

$$+ \ldots \quad (4.1\text{-}10)$$

In (4.1-10), the terms in brace brackets would normally be found in the explicit expansion of the matrix elements for an undamped system. Even for these few leading terms in the expansion, it can be seen

that the damping modifies each of the undamped terms differently. If the damping parameters are equal, $\Gamma_1 = \Gamma_2$, then (4.1-10) will be considerably simplified in that each term in the undamped expansion will be multiplied by the same power series expression for the exponential decay term (see (4.1-6) and recall that for $\delta = 0$, $\gamma = \nu t$). It should be reiterated that although the explicit results given above are for a simple two-level system, and are meant only to convey some idea of the complexity with which the damping terms combine to modify the undamped results, the general results in matrix form ensure that the treatment is valid for N-levels.

4.2 Numerical Examples for a Two-Level System

Before showing the effects of damping on the temporal behaviour of a more complicated five-level system, it is possible to illustrate some aspects of these effects using a simple two-level system. Figure (4-1) shows the energy level diagram for the two-level model to be studied, corresponding to levels 1 and 3 of figure (3-2). In the calculations that follow, the phase of the radiation field is given by $\delta = 0$. It has been pointed out [14] that the choice of phase can seriously effect the temporal behaviour of the transition probabilities, but the coupling strengths used here are small, so there will be little phase-dependence.

Figure (4-2) illustrates the temporal behaviour of the undamped system with $\mu_{12}\varepsilon = 1.777 \times 10^{-5}$ and $\nu = 7.1155 \times 10^{-2}$. This value of the coupling strength corresponds to the $\mu_{13}\varepsilon$ used to generate figures (3-5), (3-6), and (3-13) and the frequency corresponds to the predicted zero-field resonance. The transition probability in

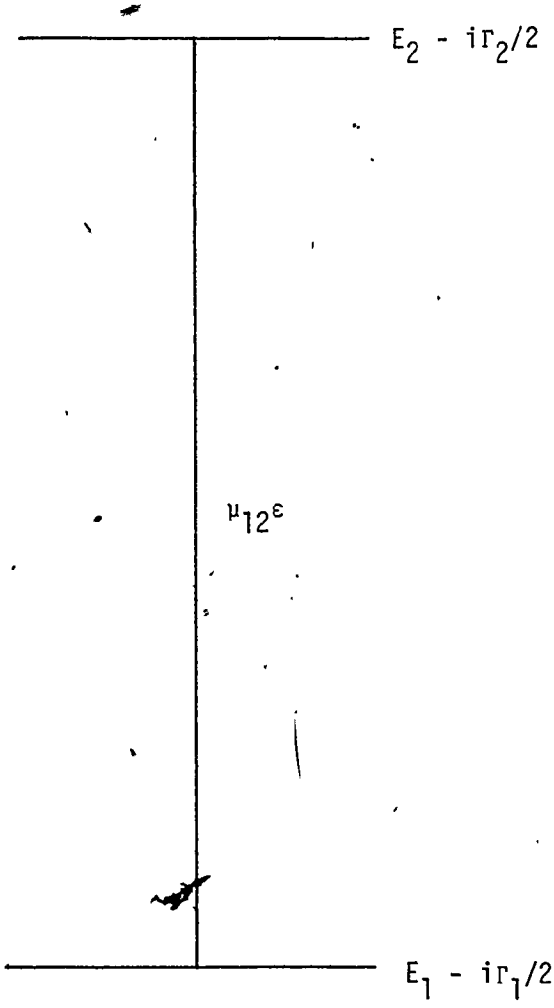

Figure (4-1). Energy level diagram for the two-level system used for model damping calculations. For the undamped case, $\Gamma_1 = \Gamma_2 = 0$, the energies are $E_1 = -7.12 \times 10^{-2}$ and $E_2 = -4.4829 \times 10^{-5}$. $\omega_{12}^{\circ} = E_2 - E_1 = 7.1155 \times 10^{-2}$.

Figure (4-2). The temporal behaviour of the two-level system of figure (4-1) with $\mu\varepsilon = 1.777 \times 10^{-5}$, $\Gamma_1 = \Gamma_2 = 0$, $\nu = 7.1155 \times 10^{-2}$. The period of oscillation is given by $\Delta t \sim 3.53 \times 10^{5}$. (a) $P_{11}(t)$, (b) $P_{22}(t)$, (c) $P_{11}(t) + P_{22}(t)$.

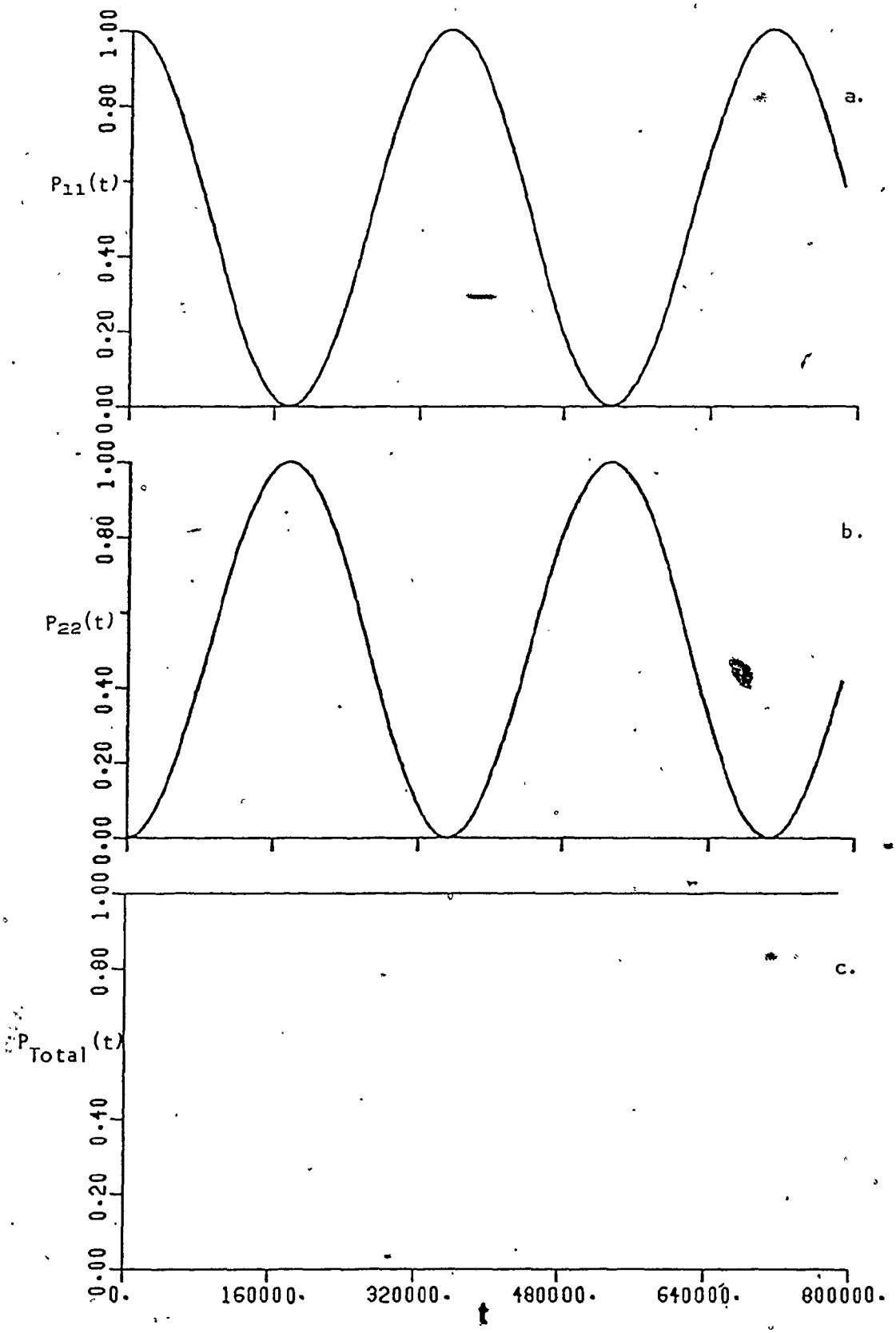
a.
$P_{11}(t)$
0.00
0.20
0.40
0.80
1.00
b.
$P_{22}(t)$
0.00
0.20
0.40
0.80
1.00
c.
$P_{Total}(t)$
0.00
0.20
0.40
0.80
1.00
0.
160000.
320000.
480000.
640000.
800000.
t

each state oscillates between 0 and 1 with the Rabi period given by $\frac{2\pi}{\mu\varepsilon}$ ($\frac{2\pi}{\mu\varepsilon} = 3.53 \times 10^{5} \sim \Delta t$).

When both levels of the system are equally damped, the temporal decay can be factored out of the temporal equations as an exponential decay term (see (4.1-6)). In figure (4-3), the temporal results are shown for the case in which both levels have the same relaxation term ($\Gamma_1 = \Gamma_2 = 4.0 \times 10^{-6}$). In an undamped system, the norm is conserved, so the sum of $P_{11}(t) + P_{22}(t)$ will always be unity. As figure (4-3) shows, in the equal damping case, the total transition probability shows an exponential decay with time.

Figure (4-4) shows the effect of damping only the excited level of the two-level system ($\Gamma_1 = 0$, $\Gamma_2 = 4.0 \times 10^{-6}$). In this case, the overall decay of $(P_{11}(t) + P_{22}(t))$ depends upon the transition probability in the decaying state as a function of time. The total transition probability shows a modulated decay curve that can be explained in terms of the temporal behaviour of the transition probabilities of the individual levels. The greater decay occurs when the majority of the remaining transition probability resides in state 2, since this is the damped level. Conversely, when the transition probability in the ground state is high, there is very little decay of the total transition probability. In this respect, the undamped results prove to be very useful in helping to predict the behaviour in the damped systems.

Figure (4-5) shows the overall decay $(P_{11}(t) + P_{22}(t))$ for a series of calculations in which the damping of the excited level is varied ($\mu_{12}\varepsilon = 1.777 \times 10^{-5}$, $\nu = 7.1155 \times 10^{-2}$, $\Gamma_1 = 0$, $\Gamma_2 = 1.5 \times 10^{-6} - 5.0 \times 10^{-4}$). As would be expected, as the Γ_2 value increases initially

Figure (4-3). Equal damping case. The temporal behaviour of the two-level system of figure (4-1) for the coupling strength and frequency of figure (4-2). The damping terms are given by $\Gamma_1 = \Gamma_2 = 4.0 \times 10^{-6}$. (a) $P_{11}(t)$, (b) $P_{22}(t)$, (c) $P_{11}(t) + P_{22}(t)$.

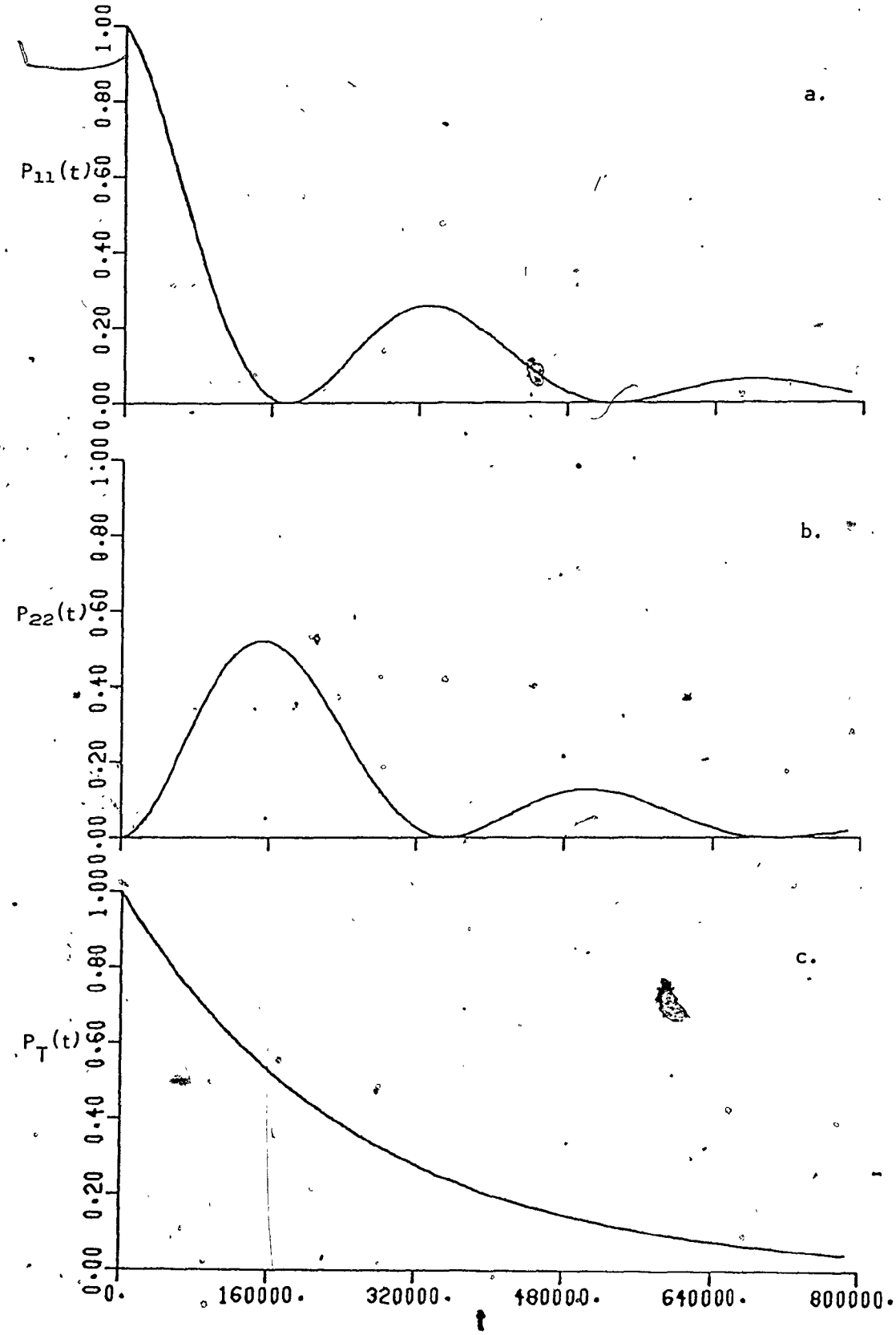
a.
$P_{11}(t)$
1.00
0.80
0.60
0.40
0.20
0.00
b.
$P_{22}(t)$
1.00
0.80
0.60
0.40
0.20
0.00
c.
$P_T(t)$
1.000
0.80
0.60
0.40
0.20
0.00
0.
160000.
320000.
480000.
640000.
800000.
t

Figure (4-4). The temporal behaviour of the damped two-level system of figure (4-1) for the coupling strength and frequency given in figure (4-2). The damping terms are given by $\Gamma_1 = 0$, $\Gamma_2 = 4.0 \times 10^{-6}$. (a) $P_{11}(t)$, (b) $P_{22}(t)$, (c) $P_{11}(t) + P_{22}(t)$.

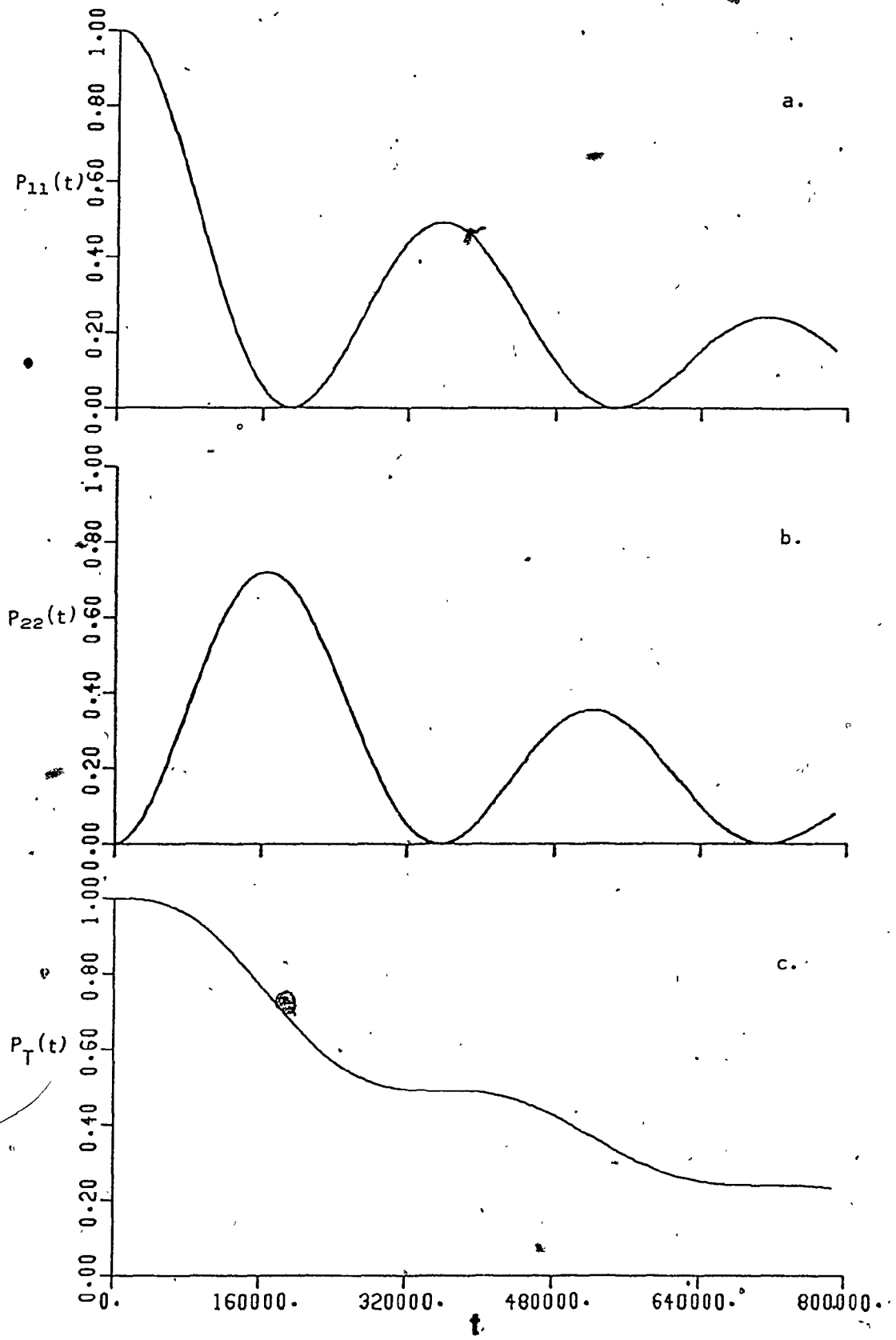
a.
$P_{11}(t)$
0.00
0.20
0.40
0.60
0.80
1.00
b.
$P_{22}(t)$
0.00
0.20
0.40
0.60
0.80
1.00
c.
$P_T(t)$
0.00
0.20
0.40
0.60
0.80
1.00
0.
160000.
320000.
480000.
640000.
800000.
t

Figure (4-5). The damped temporal behaviour of the total transition probability, $P_{11}(t) + P_{22}(t)$, for the two-level system of figure (4-1) for the coupling strength and frequency given in figure (4-2) for a series of different r_2 values, $r_1 = 0$. (a) $r_2 = 1.5 \times 10^{-6}$; (b) 5.0×10^{-6}, (c) 1.5×10^{-5}, (d) 2.8×10^{-5}, (e) 5.0×10^{-5}, (f) 1.5×10^{-4}, (g) 5.0×10^{-4}.

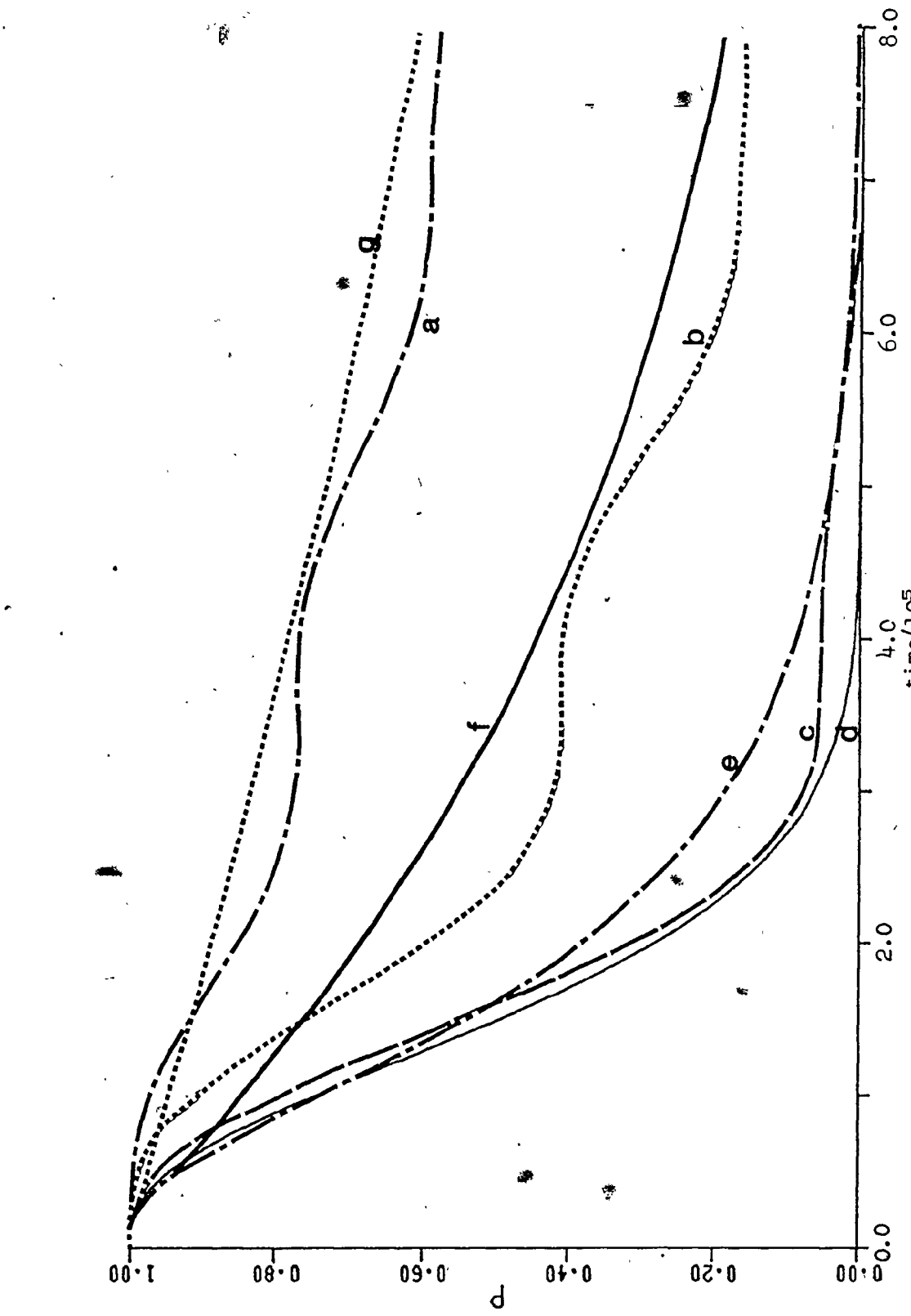
0.00
0.20
0.40
0.60
0.80
1.00
p
0.0
2.0
4.0
6.0
8.0
time/10⁵
a
b
c
d
e
f
g

from a value of 1.5×10^{-6}, the system is damped out more quickly. However, when the Γ_2 value gets too large ($>3.0 \times 10^{-5}$), the trend reverses itself and the overall decay actually proceeds more slowly. When $\Gamma_2 = 5.0 \times 10^{-4}$, for example, the two-level total transition probability decays at approximately the same rate as when $\Gamma_2 = 1.5 \times 10^{-6}$. Shore and Ackerhalt [85] have observed this same behaviour for the damping of the uppermost level of a three-level system in an RWA calculation. Apparently, there is an optimum Γ_2 value for maximum decay of the system. Figure (4-6) shows the temporal behaviour of the transition probabilities for the individual levels, $P_{11}(t)$ and $P_{22}(t)$, as well as the total, $P_{11}(t) + P_{22}(t)$, for one example of the large Γ_2 ($\Gamma_2 = 5.0 \times 10^{-4}$) cases. As this example illustrates, the strong damping arrests the build-up of the transition probability in the excited state before it can reach a significant value. This acts to effectively "shut off" the excited state so that the excitation from the ground state (and the subsequent decay from the strongly damped excited state) will proceed more slowly. If a "relaxation time" is defined as the inverse of Γ_2, then, in general, when the Rabi period given by $\frac{2\pi}{\mu\varepsilon}$ is more than ten times the value of the relaxation time, the anomalous "slow decay" will be observed. In the example above the Rabi period is given by $\Delta t^R \sim 3.5 \times 10^5$, so that for damping terms greater than $\Gamma_2 \sim 2.85 \times 10^{-5}$ ($\Gamma_2^{-1} \sim 3.5 \times 10^4$), the anomalous results are produced.

A complementary "experiment" to the series of calculations outlined above would be to vary the laser intensity for a constant value of the decay constant. This corresponds to varying ε in the calculation while keeping the same value of Γ_2. As $\mu\varepsilon$ varies, the

Figure (4-6). The temporal behaviour of the damped two-level system of figure (4-5g), $\Gamma_2 = 5.0 \times 10^{-4}$ (a) $P_{11}(t)$, (b) $P_{22}(t)$, (c) $P_{11}(t) + \overline{P_{22}(t)}$.

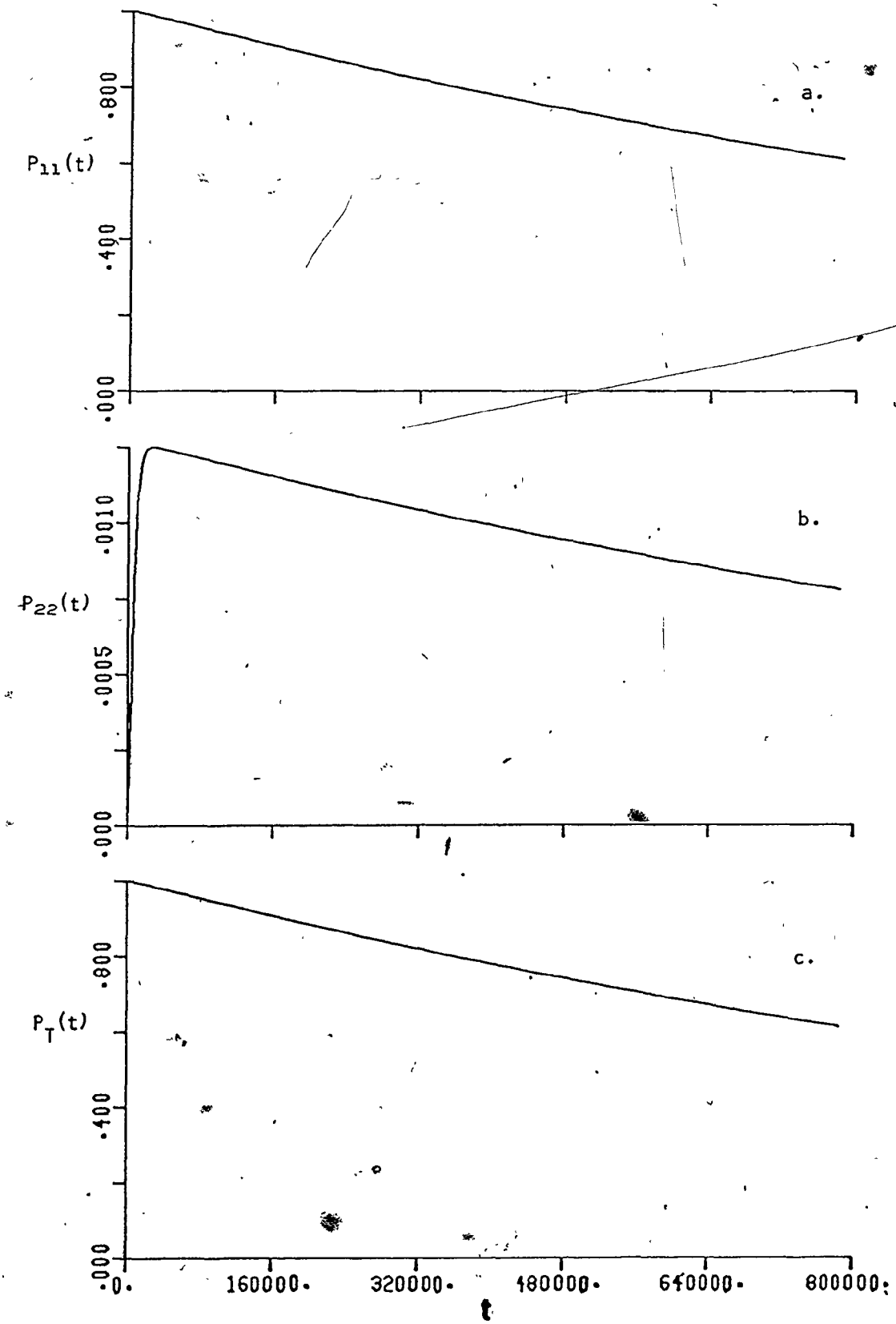
a.
$P_{11}(t)$
.800
.400
.000
b.
$P_{22}(t)$
.0010
.0005
.000
c.
$P_T(t)$
.800
.400
.000
0.
160000.
320000.
480000.
640000.
800000.
t

Rabi period will also vary, and the constant Γ_2 value can effect the decay of the system in different ways.

Figure (4-7) shows the overall decay, $(P_{11}(t) + P_{22}(t))$, for a series of calculations in which the value of $\mu\varepsilon$ is varied ($\nu = 7.1155 \times 10^{-2}$, $\Gamma_2 = 5.0 \times 10^{-6}$, $\mu\varepsilon = 1.0 \times 10^{-4} - 4.0 \times 10^{-7}$). When $\mu\varepsilon$ is large, the Rabi period is very short. Since the system will go through many periods before the damping term completely de-populates the system, the temporal behaviour will be analogous to that of a weak Γ_2 example in the previous series of results (see figure (4-5)). As the laser intensity decreases, the period increases, so that the system can be completely de-populated within a smaller number of Rabi cycles, just as would be true when Γ_2 is increased at constant ε. However, as figure (4-7) shows, although the total transition probability shows a greater decay per Rabi cycle, the period itself is increasing so that the overall decay with respect to time is approximately the same (see curves a, b, c of figure (4-7)). In other words, the "increasing Γ_2 effect" caused by decreasing the laser intensity is compensated for by the increased Rabi period to produce an overall decay that is approximately the same.

When the laser intensity is further weakened, the two-level system corresponds to the anomalous strong Γ_2 examples in the previous series of calculations. The Rabi period is now so large that, just as in the strong Γ_2 cases (see figure (4-6)), the damping prevents a significant transition probability from accumulating in the excited state. The result is that the decay of $P_{11}(t) + P_{22}(t)$ proceeds more slowly for the very weak laser intensity. Apparently, just as there is an optimum value of Γ_2 for maximum decay of the

Figure (4-7). The damped temporal behaviour of the total transition probability, $P_{11}(t) + P_{22}(t)$, for the two-level system of figure (4-1) for the frequency given in figure (4-2) for a series of different $\mu\varepsilon$ values, $\Gamma_1 = 0$, $\Gamma_2 = 5.0 \times 10^{-6}$. (a) $\mu\varepsilon = 1.0 \times 10^{-4}$, (b) 4.0×10^{-5}, (c) 1.777×10^{-5}, (d) 4.0×10^{-6}, (e) 1.0×10^{-6}, (f) 4.0×10^{-7}.

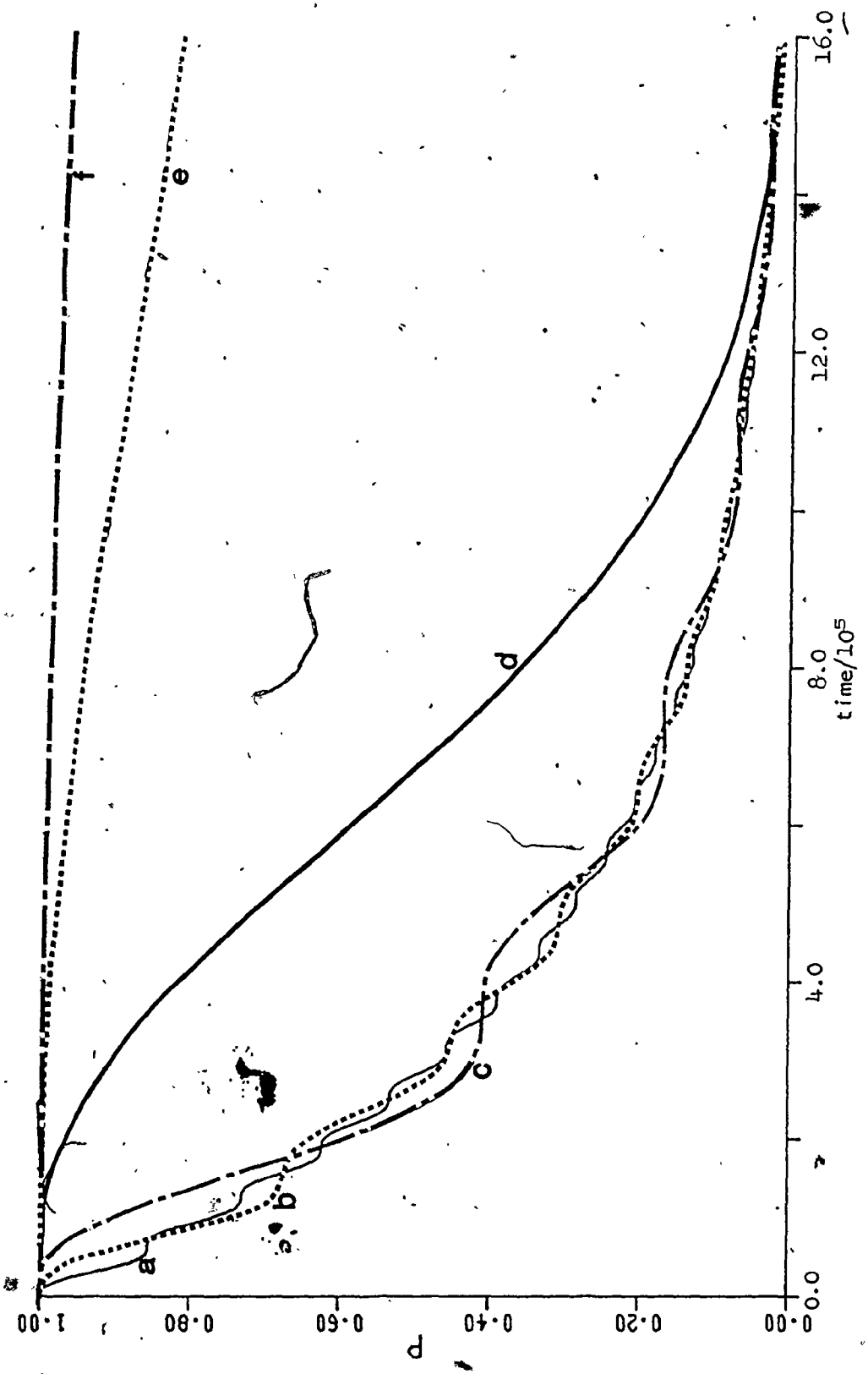
0.0
4.0
8.0
12.0
16.0
time/10^5
0.00
0.20
0.40
0.60
0.80
1.00
p
a
b
c
d
e
f

total transition probability for a fixed value of $\mu\varepsilon$, so, too, is there a laser intensity below which the two-level system will exhibit anomalously slow decay rates for a fixed Γ_2. Again, the general rule of thumb regarding the "relaxation time" given by Γ_2^{-1} and the Rabi period can be applied. In the example above, $\Gamma_2^{-1} \sim 2.0 \times 10^5$ so that for coupling strengths less than $\mu\varepsilon \sim 3.0 \times 10^{-6}$ the anomalous behaviour will be observed. Figure (4-8) shows the temporal behaviour of $P_{11}(t)$, $P_{22}(t)$, and $P_{11}(t) + P_{22}(t)$ for one of the weak laser calculations ($\mu\varepsilon = 4.0 \times 10^{-7}$).

4.3 Five-Level Systems

The results of the previous section can be used, along with the discussion of the temporal results of Section 3.2.2, to understand the time-dependent behaviour of the five-level system of figure (3-2) when the individual upper levels are damped. The effect of damping a single level is determined first, followed by calculations in which all four upper levels are damped. As with the two-level calculations, $\delta = 0$ in the results below.

Figure (4-9) shows the time-dependent results for the weak coupling single-photon case of figure (3-5) (see also figures (3-6) and (3-13)). In the two examples shown, $\mu_{12}\varepsilon = \mu_{15}\varepsilon = 9.199 \times 10^{-6}$, $\mu_{13}\varepsilon = \mu_{14}\varepsilon = -1.777 \times 10^{-5}$, and $\upsilon = 7.115517 \times 10^{-2}$, on resonance with the zero-field prediction for level 3. In figure (4-9a), only level 3 has been damped ($\Gamma_3 = 5.0 \times 10^{-6}$, $\Gamma_n = 0$, $n \neq 3$), while in figure (4-9b), only level 4 has been damped ($\Gamma_4 = 5.0 \times 10^{-6}$). As pointed out in the previous section, the time-dependent decay of a system will depend upon the transition probability in the damped

Figure (4-8). The temporal behaviour of the damped two-level system of figure (4-7f), $\mu\varepsilon = 4.0 \times 10^{-7}$, (a) $P_{11}(t)$, (b) $P_{22}(t)$, (c) $P_{11}(t) + P_{22}(t)$.

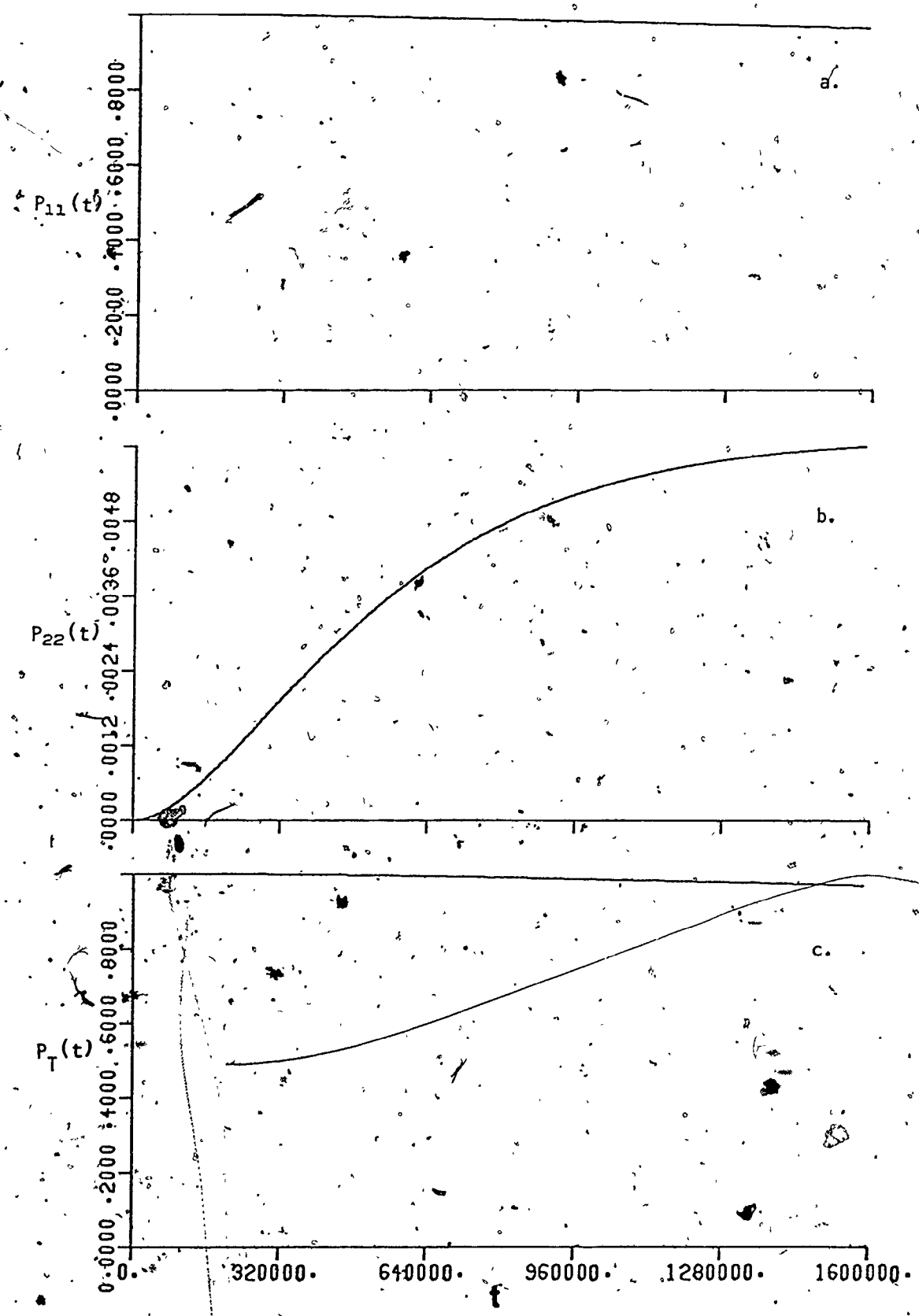
a.
$P_{11}(t)$
.0000
.2000
.4000
.6000
.8000
b.
$P_{22}(t)$
.0000
.0012
.0024
.0036
.0048
c.
$P_T(t)$
.0000
.2000
.4000
.6000
.8000
0.
320000.
640000.
960000.
1280000.
1600000.
t

Figure (4-9). The damped temporal behaviour of the five-level system given in figure (3-2) with $\mu_{12}\varepsilon_o = \mu_{15}\varepsilon = 9.199 \times 10^{-6}$, $\mu_{13}\varepsilon = \mu_{14}\varepsilon = -1.777 \times 10^{-5}$, $\nu = 7.115517 \times 10^{-2}$, (a) $\Gamma_n = 0$, $n \neq 3$, $\Gamma_3 = 5.0 \times 10^{-6}$, (b) $\Gamma_n = 0$, $n \neq 4$, $\Gamma_4 = 5.0 \times 10^{-6}$.

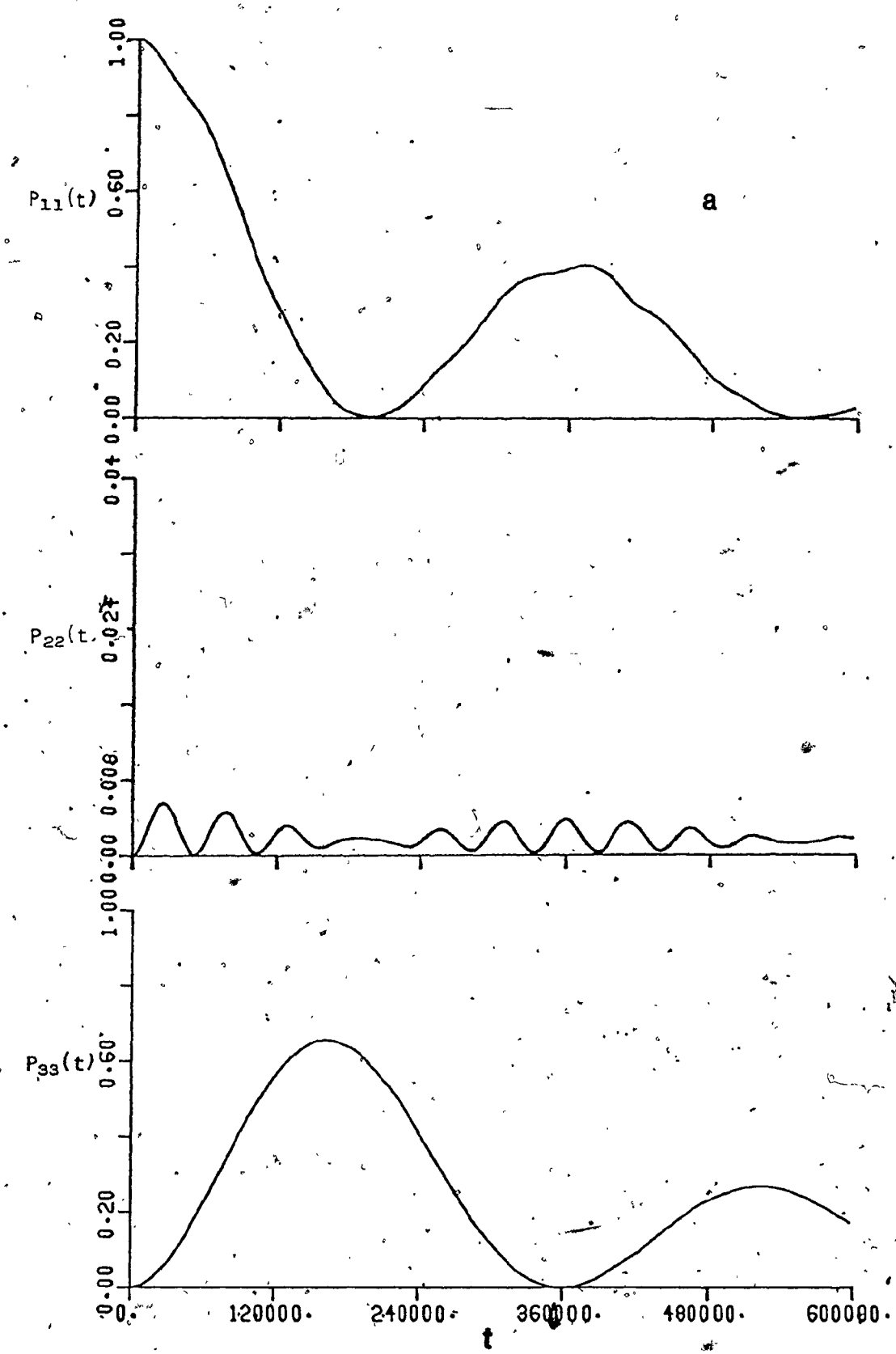
$P_{11}(t)$
1.00
0.60
0.20
0.00
a
$P_{22}(t$
0.04
0.02
0.008
0.00
$P_{33}(t)$
1.000
0.60
0.20
0.00
0.
120000.
240000.
360000.
480000.
600000.
t

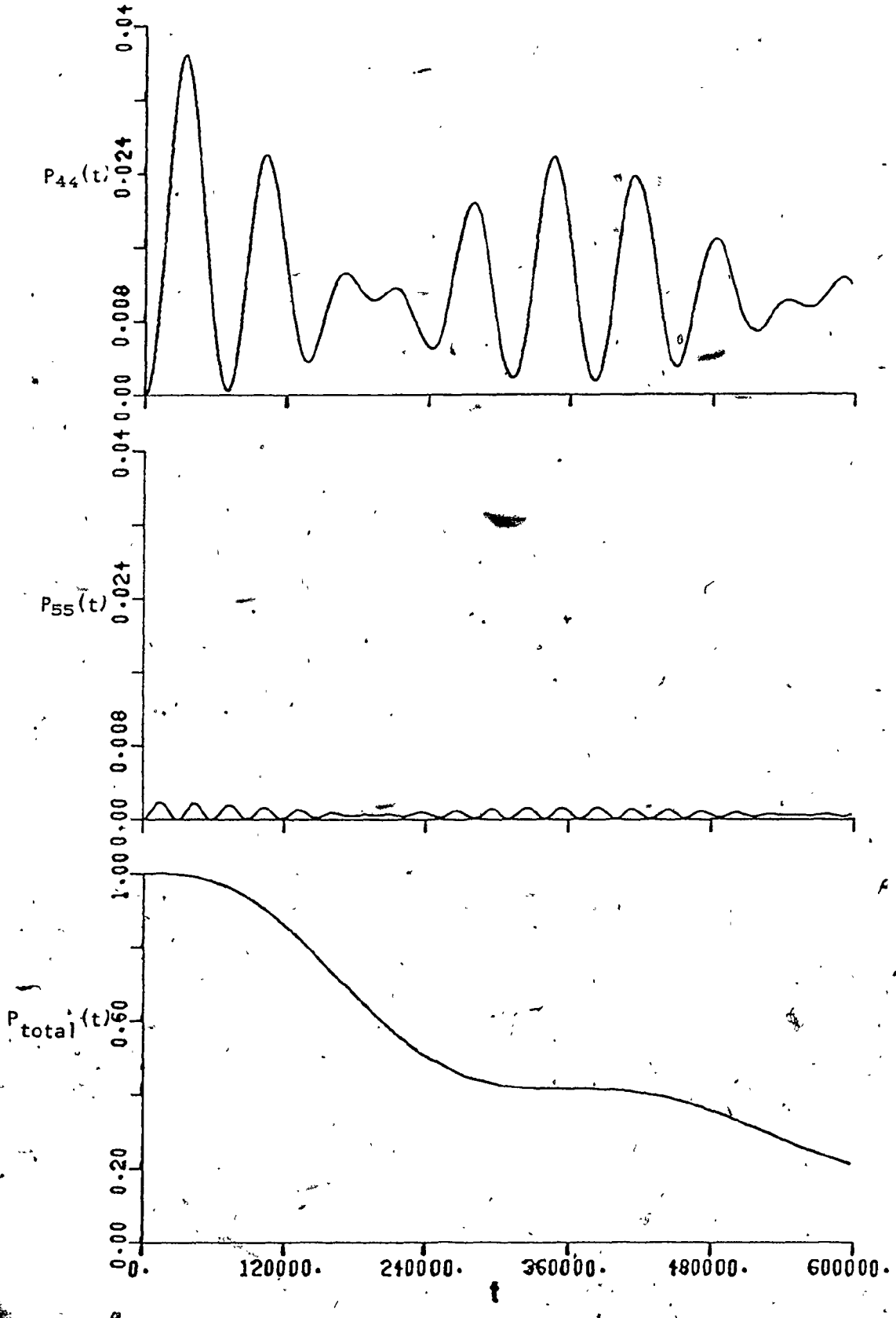
$P_{44}(t)$
0.04
0.024
0.008
0.00
$P_{55}(t)$
0.04
0.024
0.008
0.00
$P_{total}(t)$
1.00
0.60
0.20
0.00
0.
120000.
240000.
360000.
480000.
600000.
t

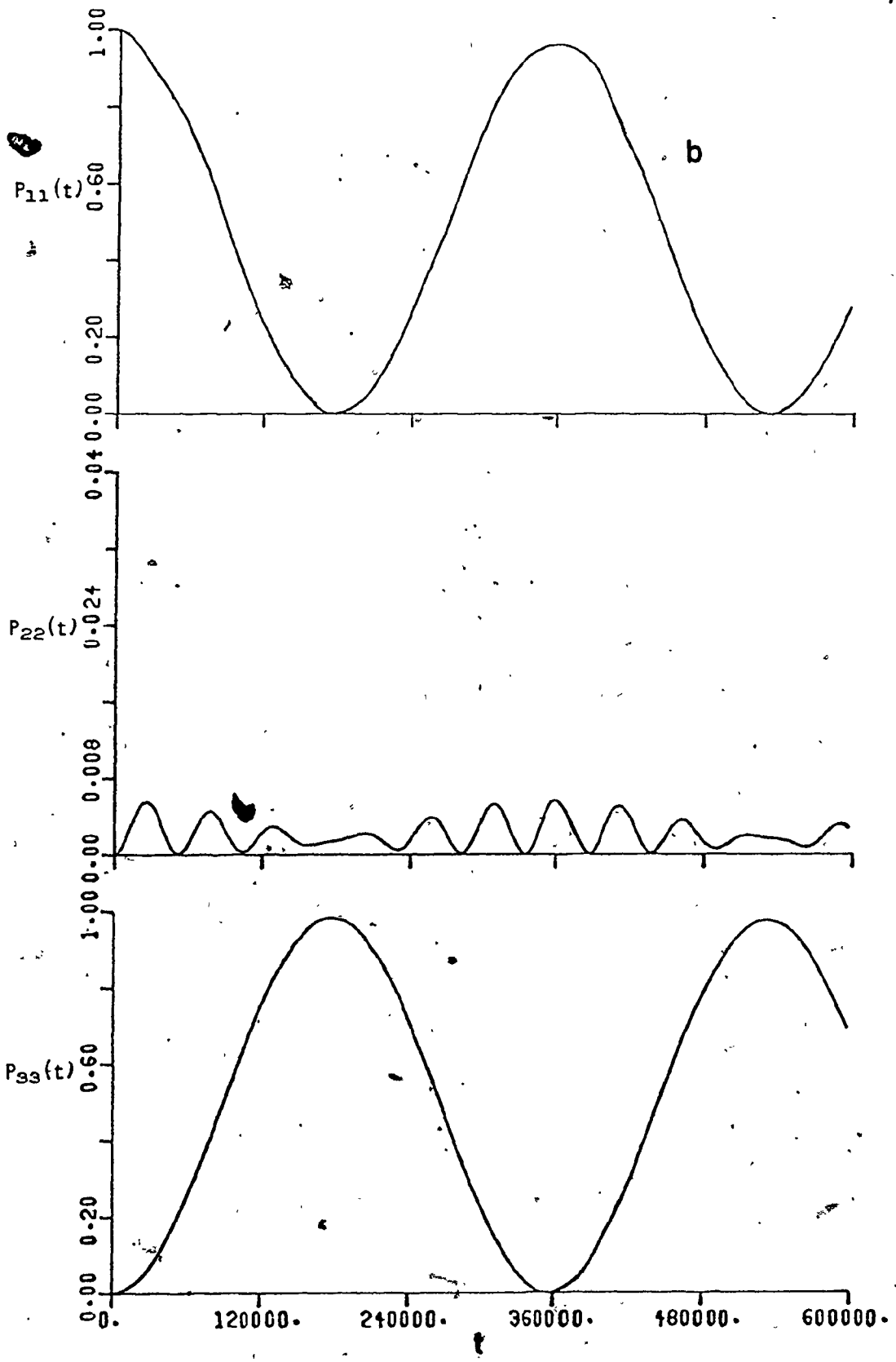
b
$P_{11}(t)$
1.00
0.60
0.20
0.00
0.04
$P_{22}(t)$
0.024
0.008
0.00
1.00
$P_{33}(t)$
0.60
0.20
0.00
0.
120000.
240000.
360000.
480000.
600000.
t

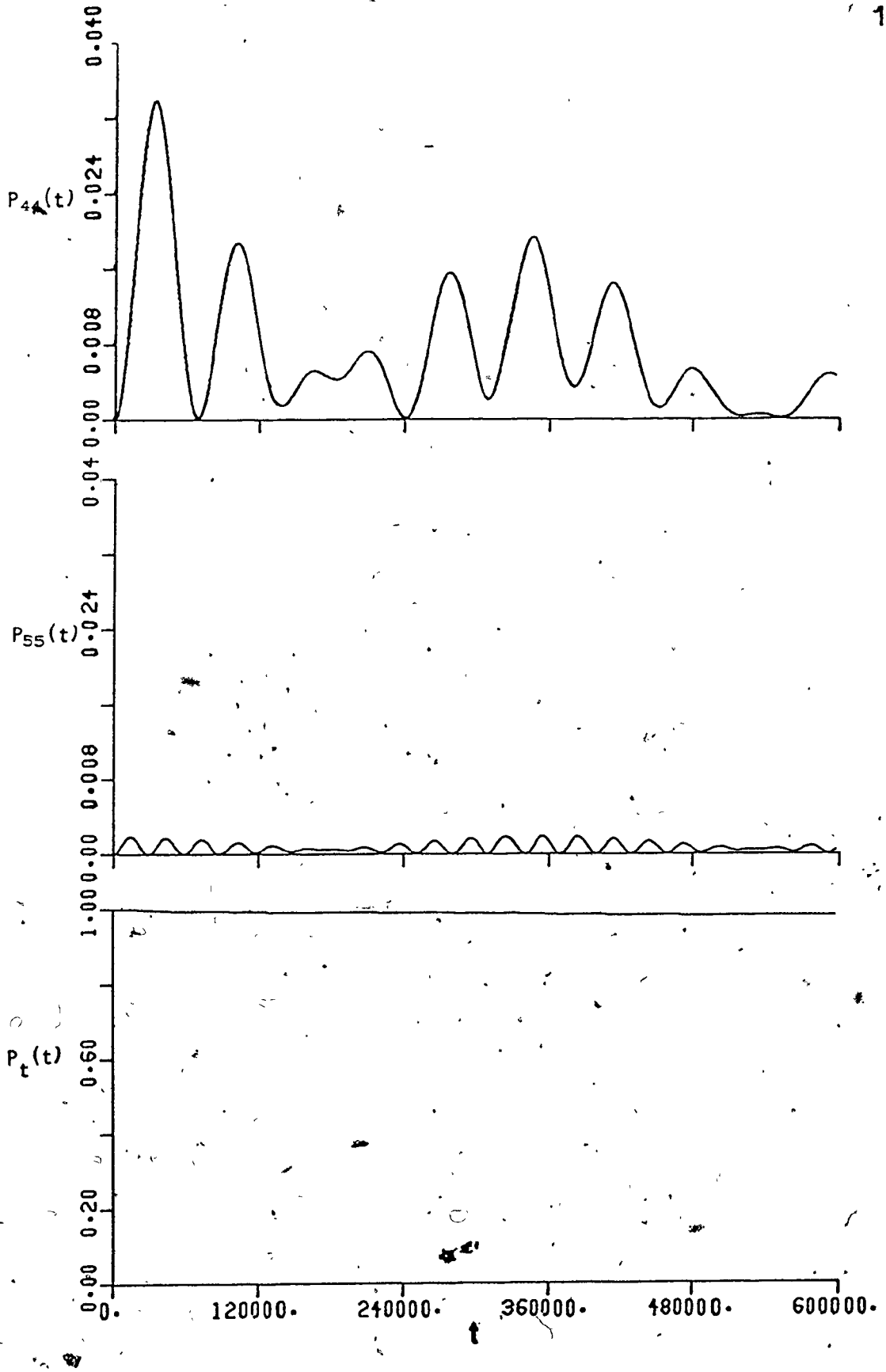
$P_{44}(t)$
0.040
0.024
0.008
0.00
$P_{55}(t)$
0.04
0.024
0.008
0.00
$P_t(t)$
1.00
0.60
0.20
0.00
0.
120000.
240000.
360000.
480000.
600000.
t

level (see figures (4-2) and (4-4)). Since level 3 is essentially on resonance, its transition probability is higher at this value of the frequency (see figure (3-13)) than are the transition probabilities for the other levels, so the overall decay is much greater in figure (4-9a) where the resonant level is damped. Figure (4-9b) illustrates that when the transition probability in the damped state is small, the system as a whole shows very little loss of total transition probability. Similarly, damping levels 2 and 5 has very little effect on the total transition probability, so the corresponding figures are not shown.

Transition probabilities as a function of time are shown in figure (4-10) for the strong coupling single-photon case of figure (3-3) (see also figures (3-4) and (3-11)). The coupling strengths are given by $\mu_{12}\varepsilon = \mu_{15}\varepsilon = 9.199 \times 10^{-4}$, $\mu_{13}\varepsilon = \mu_{14}\varepsilon = -1.777 \times 10^{-3}$, with the frequency again taken to be $\nu = 7.115517 \times 10^{-2}$. In each of figures (4-10a) - (4-10d) only one of the upper levels has the relaxation term, $\Gamma_n = 5.00 \times 10^{-4}$. In this example, all four excited levels can have significant populations at this frequency (see figure (3-11)), so damping any one of them causes a significant decrease of the total transition probability. Also, just as the transition probabilities reflect the magnitude of the coupling strength to the ground state, giving levels 2 and 5 and levels 3 and 4 similar appearances, it is also true that the decay of the total transition probabilities are similar when level 2 or 5 is damped and when level 3 or 4 is damped. Levels 3 and 4 have the greater coupling strengths to the ground state, so they have greater transition probabilities and, therefore, lead to greater overall decay than do levels 2 and 5.

Figure (4-10). The damped temporal behaviour of the five-level system given in figure (3-2) with $\mu_{12}\varepsilon = \mu_{15}\varepsilon = 9.199 \times 10^{-4}$, $\mu_{13}\varepsilon = \mu_{14}\varepsilon = -1.777 \times 10^{-3}$, $\nu = 7.115517 \times 10^{-2}$, $\Gamma_n = 0$ unless otherwise specified. (a) $\Gamma_2 = 5.0 \times 10^{-4}$, (b) $\Gamma_3 = 5.0 \times 10^{-4}$, (c) $\Gamma_4 = 5.0 \times 10^{-4}$, (d) $\Gamma_5 = 5.0 \times 10^{-4}$. The relaxation terms have been increased from those used in figure (4-9) in order to see the effect of the damping within a reasonable number of the much shorter Rabi periods observed here.

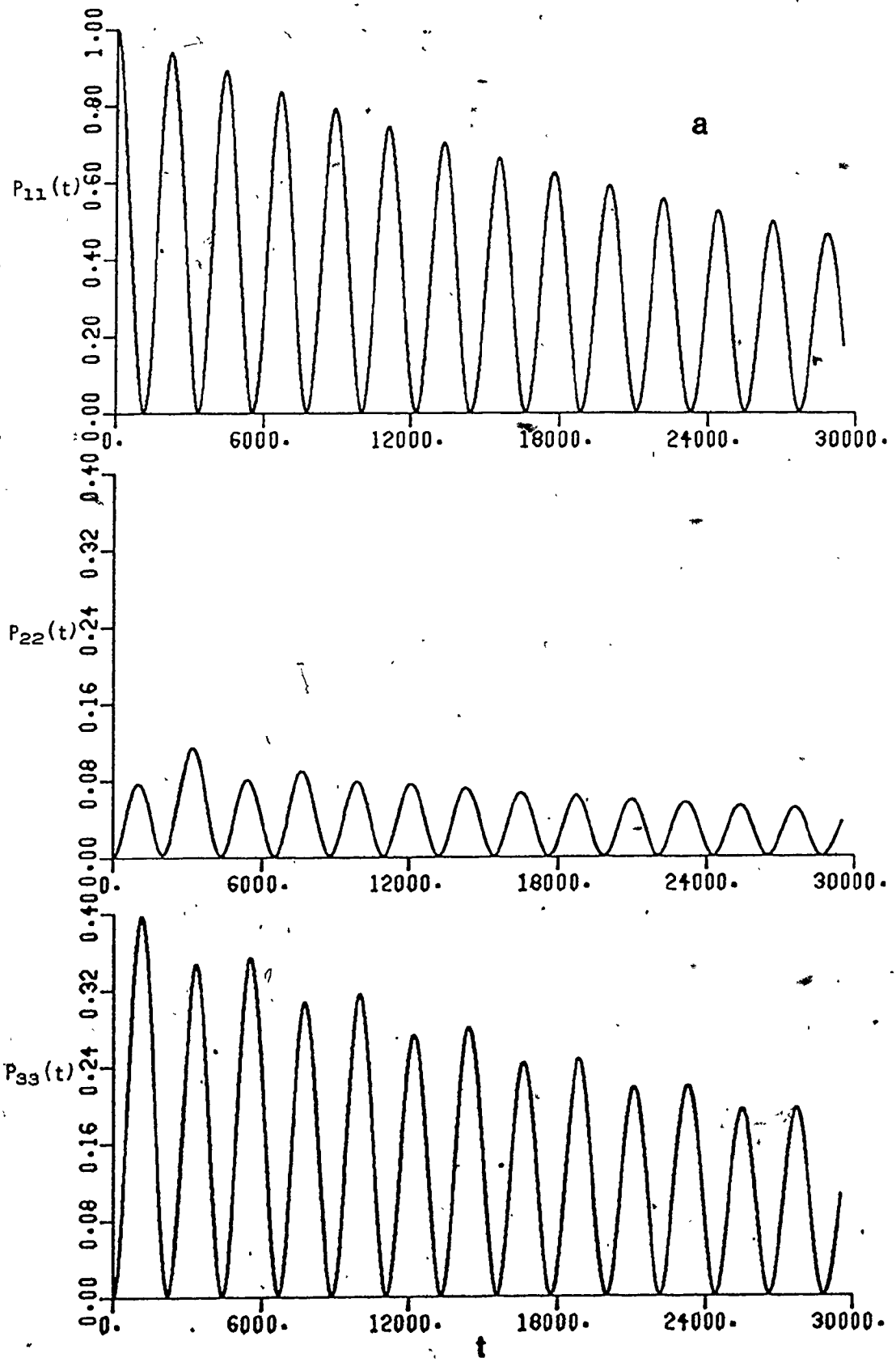
a
$P_{11}(t)$
0.00
0.20
0.40
0.60
0.80
1.00
0.
6000.
12000.
18000.
24000.
30000.
$P_{22}(t)$
0.00
0.08
0.16
0.24
0.32
0.40
$P_{33}(t)$
t

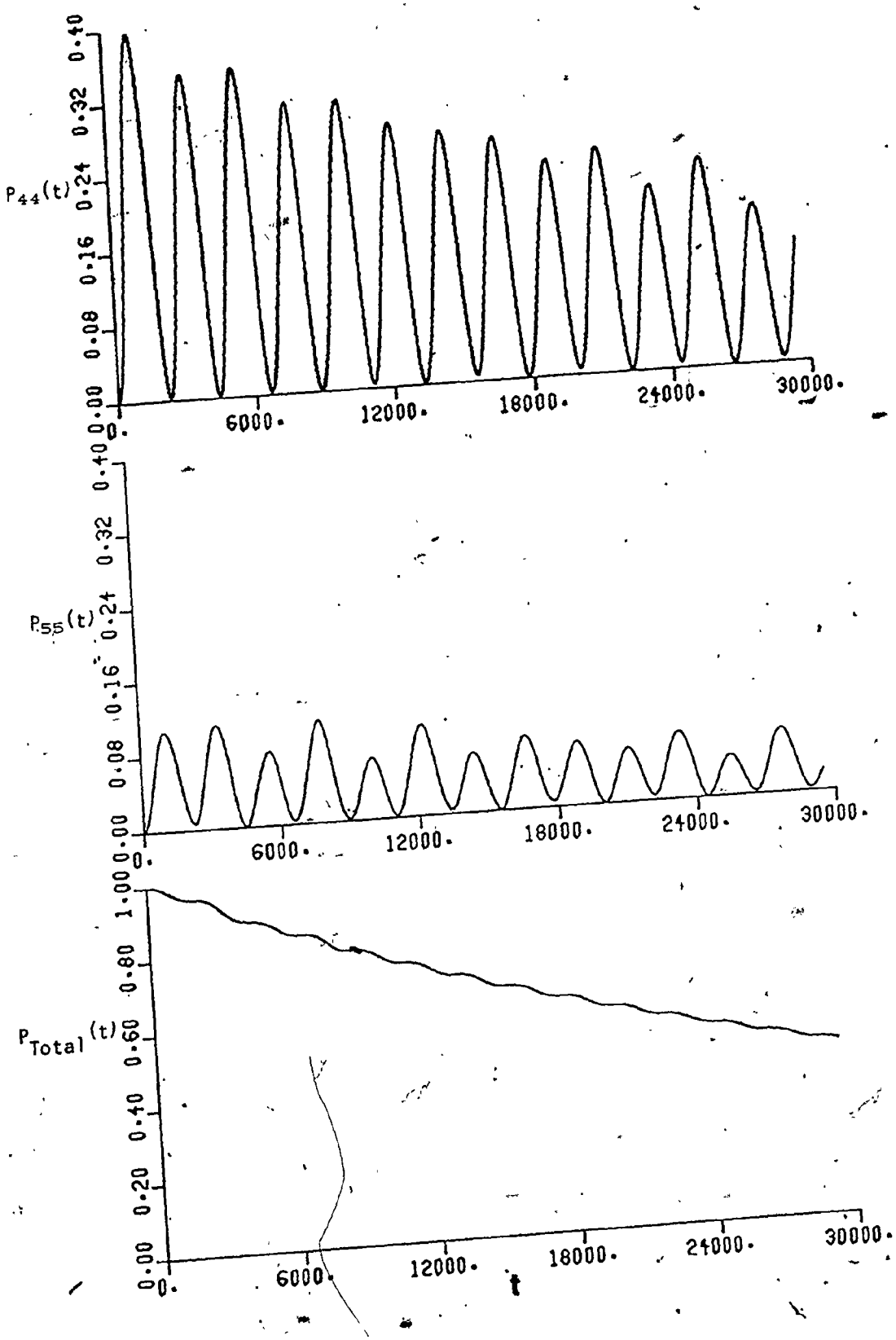
$P_{44}(t)$
0.00
0.08
0.16
0.24
0.32
0.40
0.
6000.
12000.
18000.
24000.
30000.
$P_{55}(t)$
0.00
0.08
0.16
0.24
0.32
0.40
0.
6000.
12000.
18000.
24000.
30000.
$P_{Total}(t)$
0.00
0.20
0.40
0.60
0.80
1.00
0.
6000.
12000.
18000.
24000.
30000.
t

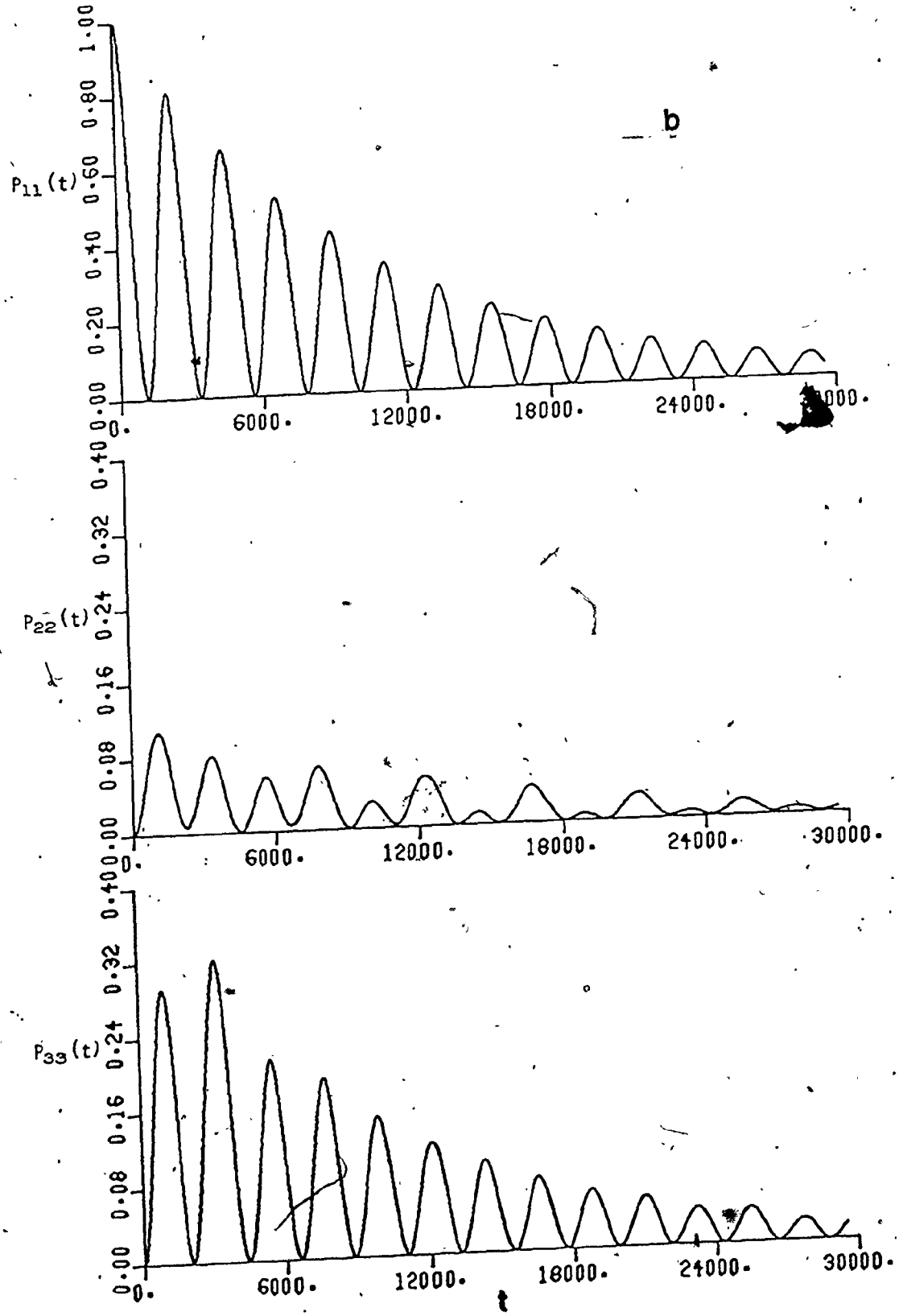
b
$P_{11}(t)$
0.00
0.20
0.40
0.60
0.80
1.00
0.
6000.
12000.
18000.
24000.
$P_{22}(t)$
0.00
0.08
0.16
0.24
0.32
0.40
30000.
$P_{33}(t)$
t

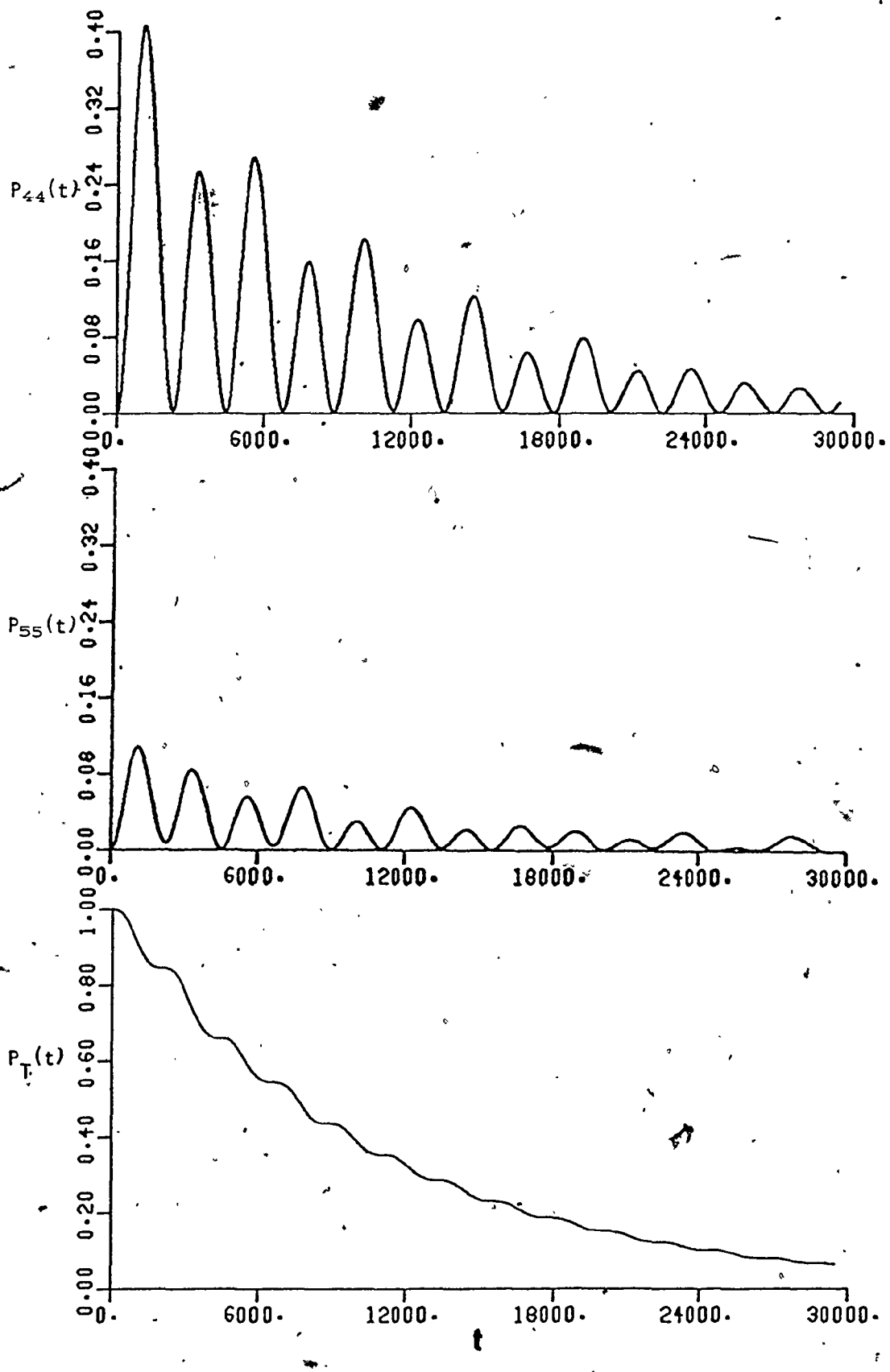
$P_{44}(t)$
0.00
0.08
0.16
0.24
0.32
0.40
0.
6000.
12000.
18000.
24000.
30000.
$P_{55}(t)$
0.00
0.08
0.16
0.24
0.32
0.40
0.
6000.
12000.
18000.
24000.
30000.
$P_T(t)$
0.00
0.20
0.40
0.60
0.80
1.00
0.
6000.
12000.
18000.
24000.
30000.
t

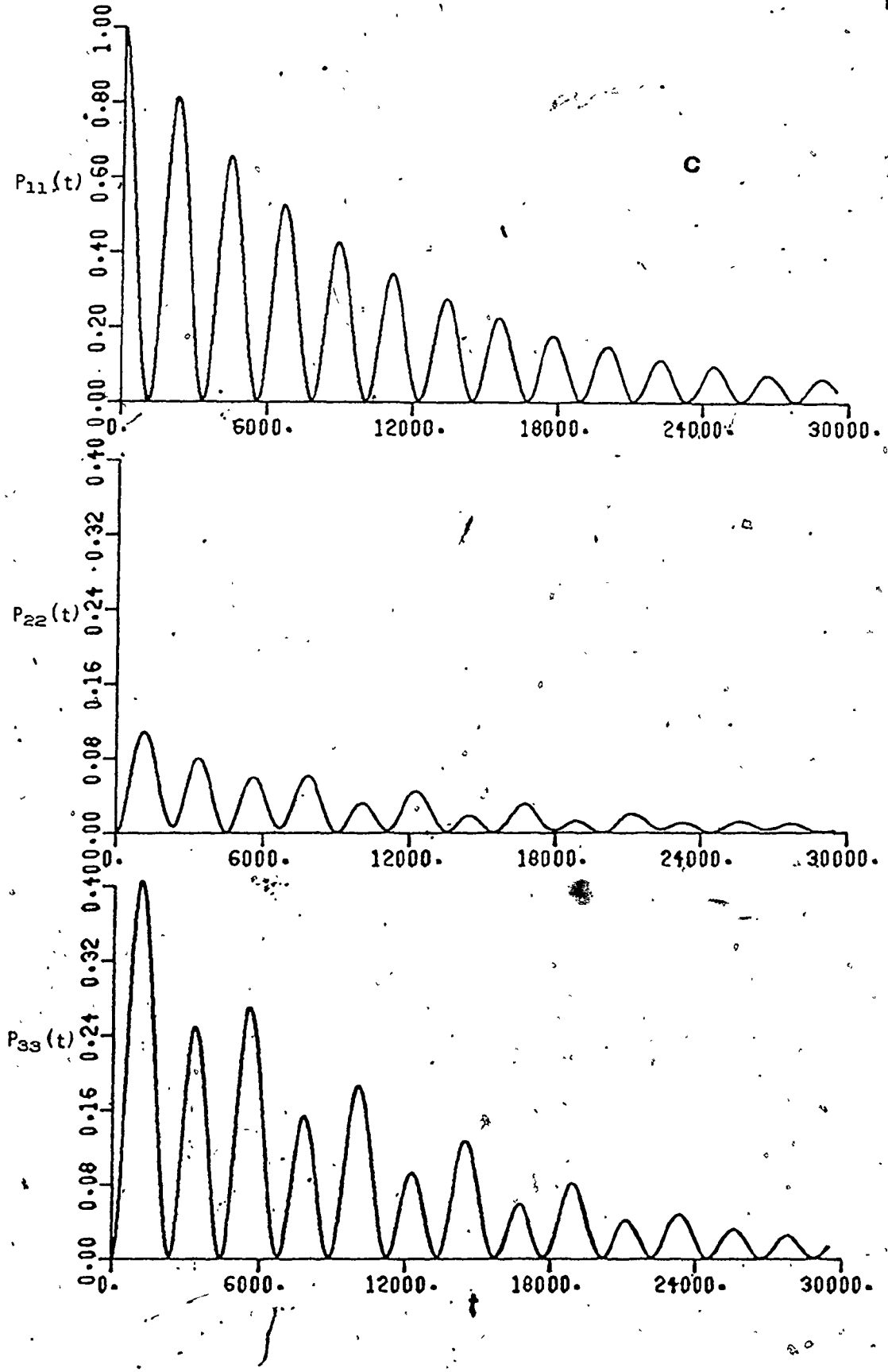
C
$P_{11}(t)$
0.00
0.20
0.40
0.60
0.80
1.00
0.
6000.
12000.
18000.
24000.
30000.
$P_{22}(t)$
0.00
0.08
0.16
0.24
0.32
0.40
0.
6000.
12000.
18000.
24000.
30000.
$P_{33}(t)$
0.00
0.08
0.16
0.24
0.32
0.40
0.
6000.
12000.
18000.
24000.
30000.

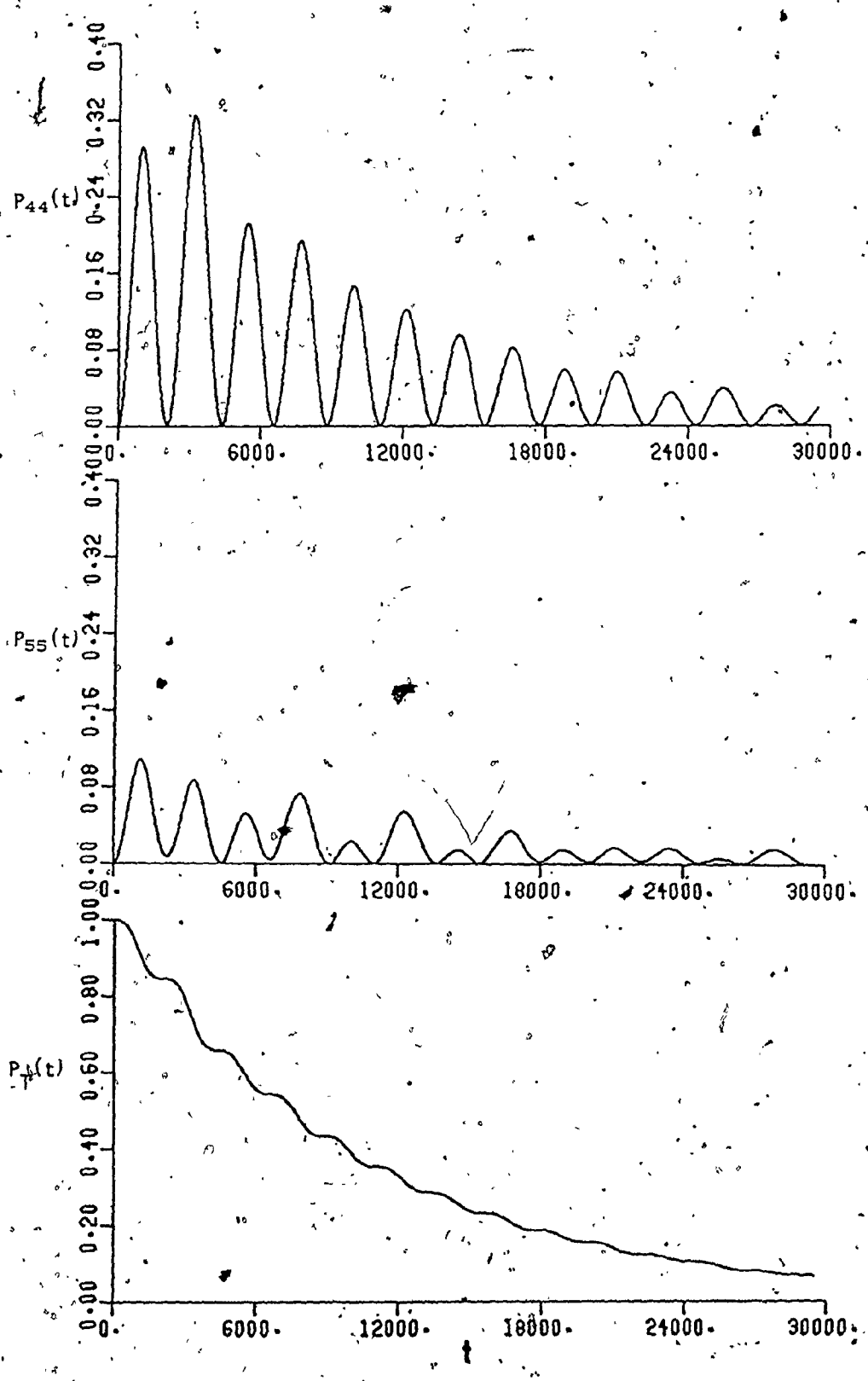
$P_{44}(t)$
0.00
0.08
0.16
0.24
0.32
0.40
0.
6000.
12000.
18000.
24000.
30000.
$P_{55}(t)$
0.00
0.08
0.16
0.24
0.32
0.40
0.
6000.
12000.
18000.
24000.
30000.
$P_{\frac{1}{2}}(t)$
0.00
0.20
0.40
0.60
0.80
1.00
0.
6000.
12000.
18000.
24000.
30000.
t

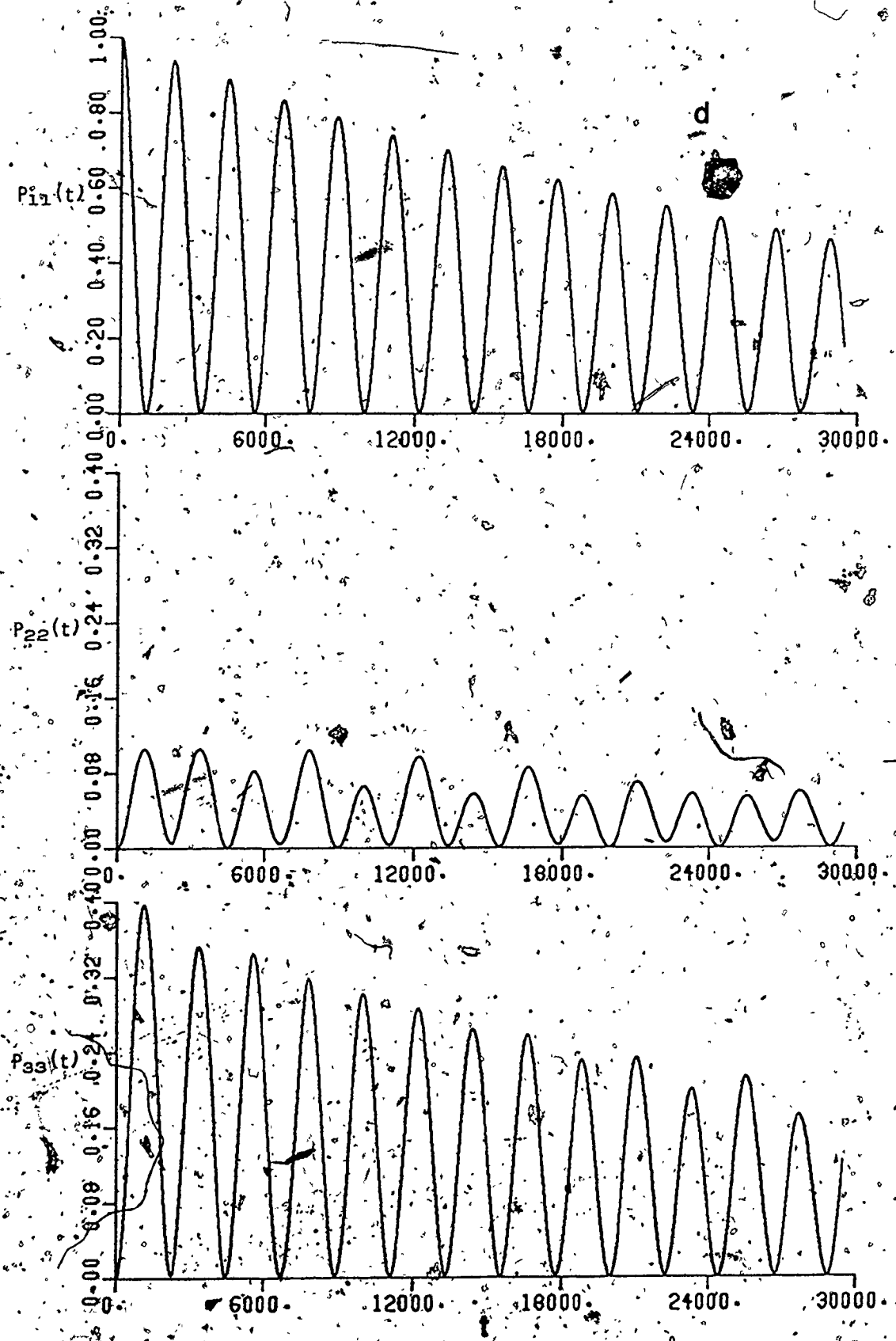
d
$P_{11}(t)$
1.00
0.80
0.60
0.40
0.20
0.00
0
6000
12000
18000
24000
30000
$P_{22}(t)$
0.40
0.32
0.24
0.16
0.08
0.00
$P_{33}(t)$

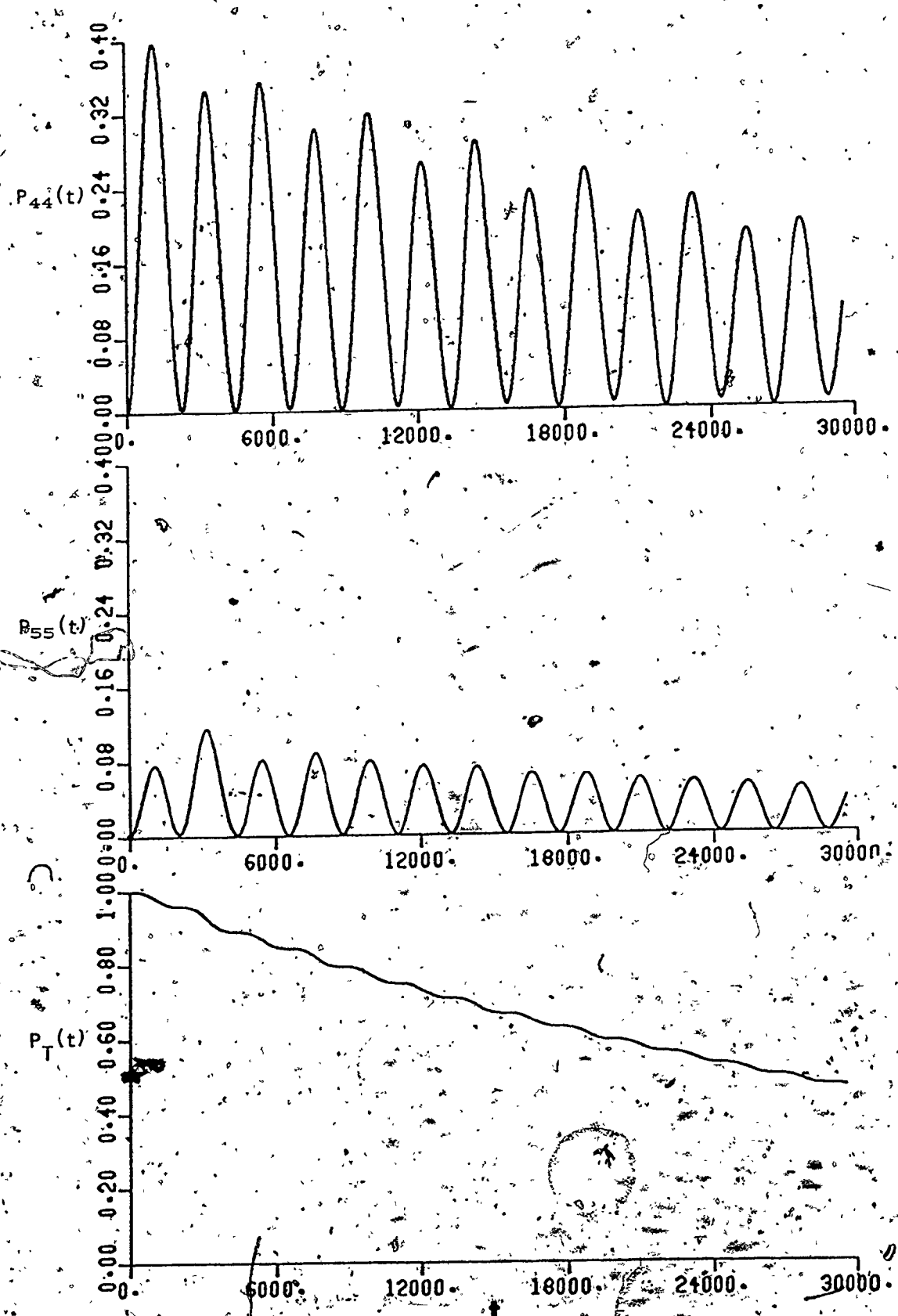
$P_{44}(t)$
0.00
0.08
0.16
0.24
0.32
0.40
0.
6000.
12000.
18000.
24000.
30000.
$P_{55}(t)$
0.00
0.08
0.16
0.24
0.32
0.40
0.
6000.
12000.
18000.
24000.
30000.
$P_T(t)$
0.00
0.20
0.40
0.60
0.80
1.00
0.
6000.
12000.
18000.
24000.
30000.
t

Since the total transition probability decays significantly, the transition probabilities in the undamped levels also decay. This was also true for the weak coupling cases of figure (4-9), but the effect is much more noticeable here.

When all four upper levels in the five-level system are individually damped, the overall decay of the total transition probability can be predicted from the single-damping results. Figure (4-11) shows the temporal behaviour of the strong coupling case when all four excited states are damped ($\Gamma_2=\Gamma_3=\Gamma_4=\Gamma_5 = 5.0 \times 10^{-4}$). As the total transition probability indicates, the system experiences an accumulative effect of the dampings in figure (4-10a) - (4-10d). Similarly, in the weak coupling case of figure (4-9), a cumulative effect is observed, although in this case, the contributions from all but the resonant level are small (see figure (4-12)).

The anomalous decay behaviour pointed out in the two-level calculations for large Γ values or small $\mu\varepsilon$ values has also been observed when single levels are damped in the five-level system. The additivity of the damping behaviour pointed out above implies the extension of the anomalous decay behaviour to cases in which all of the excited levels are damped.

4.4 Uniform Damping

In Section 2.6 a uniform damping model using the Floquet formalism was discussed. In this model, the atoms or molecules are characterized by a mean collision time, τ, that limits the time the sample interacts with the radiation. The treatment has been used previously to demonstrate how multi-photon peaks in a steady-state

Figure (4-11). The damped temporal behaviour of the five-level system given in figure (3-2) with the coupling strengths and frequency given in figure (4-10). The damping terms are given by $\Gamma_n = 5.0 \times 10^{-4}$, $n = 2,3,4,5$ (a) $P_{11}(t)$, (b) $P_{22}(t)$, (c) $P_{33}(t)$, (d) $P_{44}(t)$, (e) $P_{55}(t)$, (f) P_{Total}.

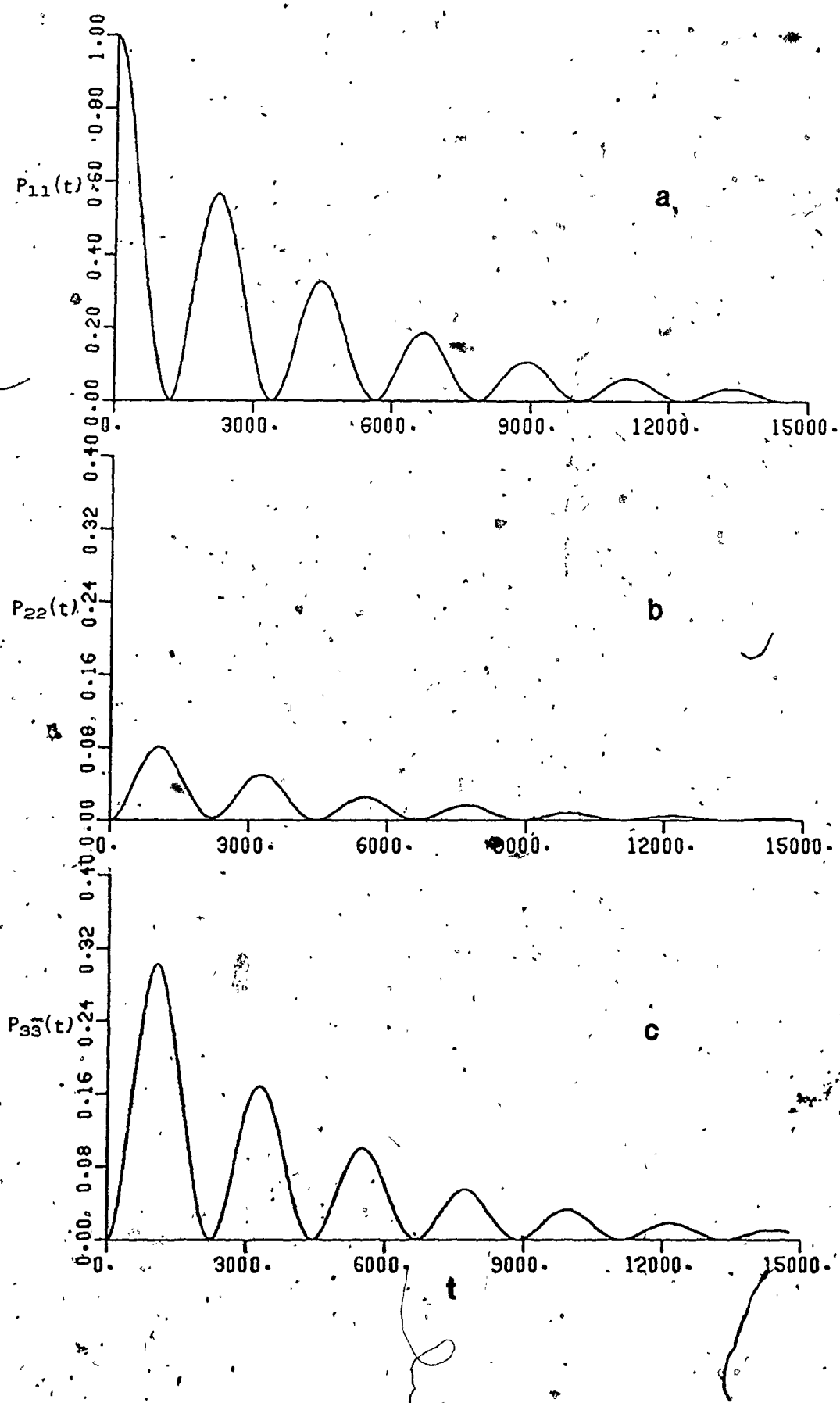
$P_{11}(t)$
a
0.00
0.20
0.40
0.60
0.80
1.00
0.
3000.
6000.
9000.
12000.
15000.
$P_{22}(t)$
b
0.00
0.08
0.16
0.24
0.32
0.40
$P_{33}(t)$
c
t

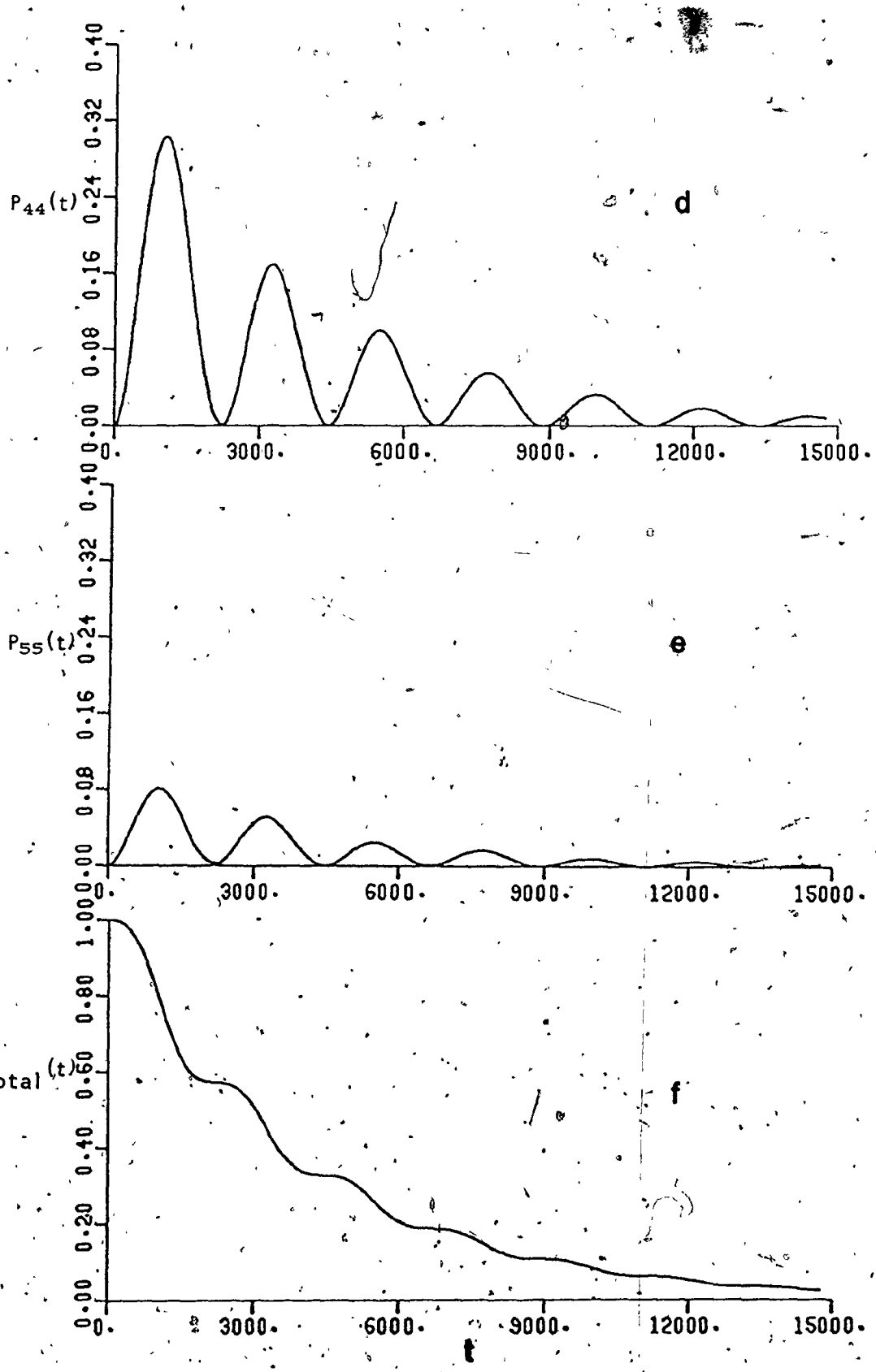
$P_{44}(t)$
0.00
0.08
0.16
0.24
0.32
0.40
0.
3000.
6000.
9000.
12000.
15000.
d
$P_{55}(t)$
e
$P_{Total}(t)$
0.00
0.20
0.40
0.60
0.80
1.000
f
t

Figure (4-12). The damped temporal behaviour of the five-level system given in figure (3-2) with the coupling strengths and frequency given in figure (4-9). The damping terms are given by $\Gamma_n = 5.0 \times 10^{-6}$, n = 2,3,4,5. (a) $P_{11}(t)$, (b) $P_{22}(t)$, (c) $P_{33}(t)$, (d) $P_{44}(t)$, (e) $P_{55}(t)$, (f) P_{Total}.

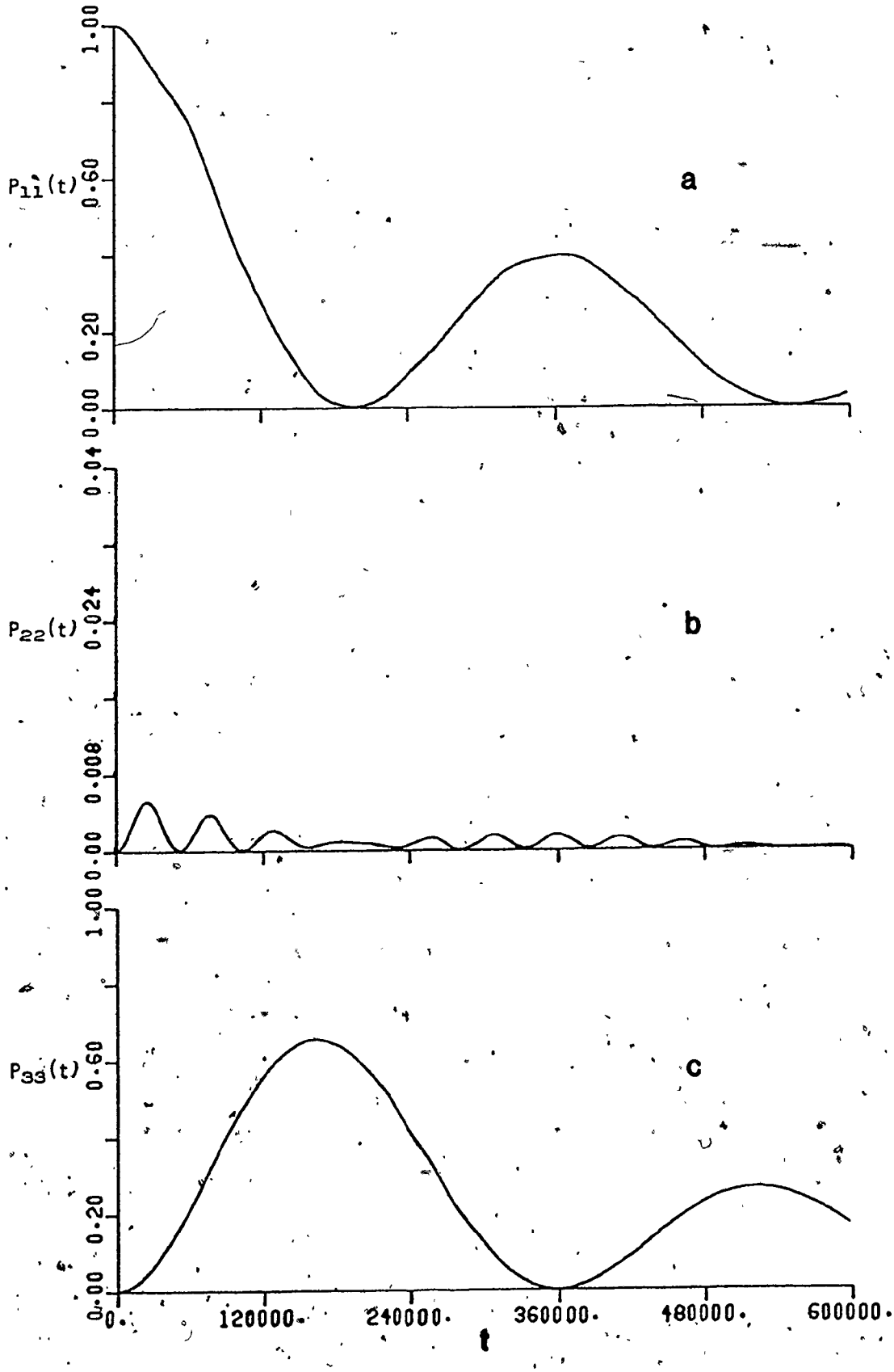
1.00
0.60
0.20
0.00
$P_{11}(t)$
a
0.04
0.024
0.008
0.00
$P_{22}(t)$
b
1.00
0.60
0.20
0.00
$P_{33}(t)$
c
0.
120000.
240000.
360000.
480000.
600000.
t

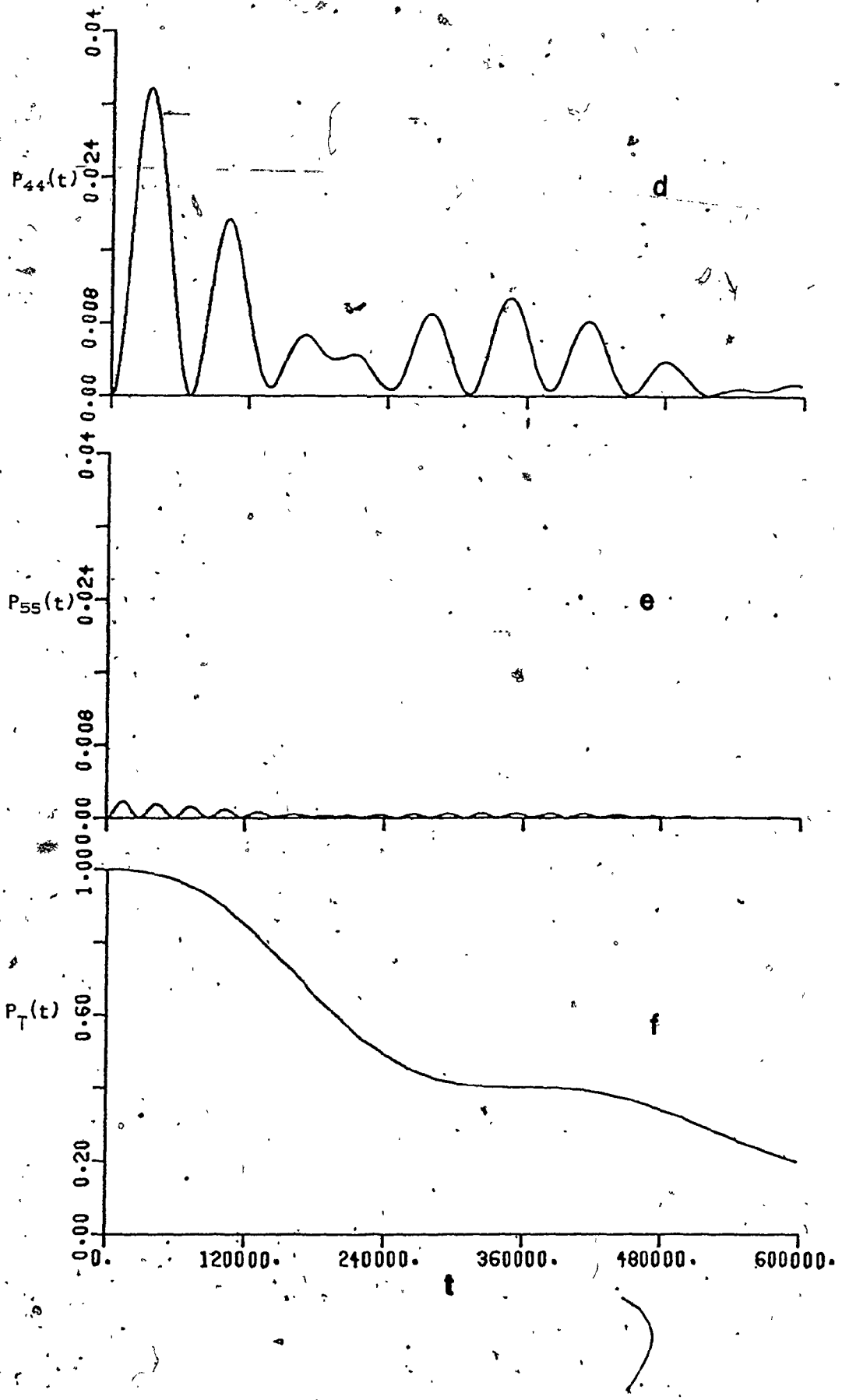
0.04
0.024
0.008
0.00
$P_{44}(t)$
d
0.04
0.024
0.008
0.00
$P_{55}(t)$
e
1.00
0.60
0.20
0.00
$P_T(t)$
f
0.
120000.
240000.
360000.
480000.
600000.
t

spectrum can be damped out relative to the single-photon peak. Because a multi-photon transition will have a much longer Rabi period than the corresponding single-photon transition, it is possible to choose the value of τ such that the multi-photon transition is interrupted before very much population gets into the excited state, while the single-photon transition can still reach the expected steady-state result.

In this section, it will be shown that the correct choice of τ can discriminate between the upper levels in the three-photon transitions of Section 3.3. Recall that in the temporal results of that section (see figure (3-20)) it was shown that the three-photon Rabi periods for the four upper levels differed significantly (see table (3-2)). Because of this, the value of τ can be picked to cause the level with the longest period to be damped considerably while the other levels approach more closely their steady-state values.

The phase- and long-time-averaged spectrum for the three-photon transitions of figures (3-16) and (3-17) is shown in figure (4-13) for a mean collision time given by $\tau = 1.0 \times 10^6$. The four peak heights have all been reduced from their undamped steady-state values of $\sim$0.5 (see figure (3-16)). However, the heights have all been reduced by varying amounts (Peak heights $\sim$0.134, $\sim$0.282, $\sim$0.383, $\sim$0.291). The damping of the different transitions, appearing as a reduction of peak heights in figure (4-13) relative to figure (3-16), can be related to the different periods for the transitions (see table (3-2)). Since the level 2 transition has the longest period ($\Delta t \sim 1.0 \times 10^7$), it exhibits the greatest decrease in peak height in the steady-state result. The level 4 transition has the shortest period ($\Delta t \sim 2.5 \times 10^6$),

Figure (4-13). Phase- and time-averaged transition probability for the five-level system of figure (3-2) with the coupling strengths given in figure (3-16). $\tau = 1.0 \times 10^6$ (a) The peak heights in the total spectrum ($1 - \overline{P}_{11}$) have been reduced from ~0.5 (see also figure (3-16)) to (l to r) ~0.134, 0.282, 0.383, 0.291, (b) $\overline{P}_{22}$; (c) $\overline{P}_{33}$, (d) $\overline{P}_{44}$, (e) $\overline{P}_{55}$.

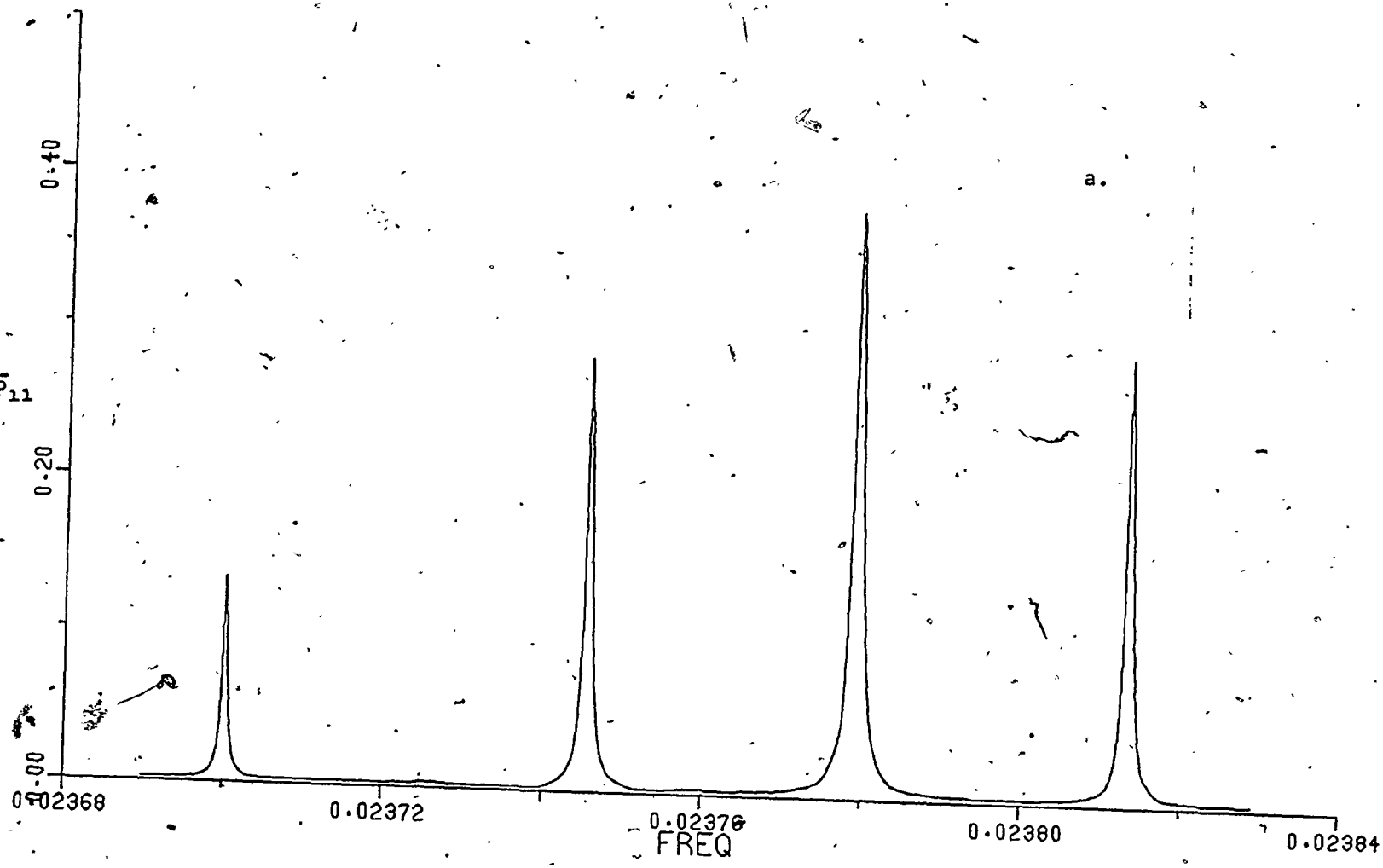
a.
0.40
0.20
0.00
$1-\bar{P}_{11}$
0.02368
0.02372
0.02376
0.02380
0.02384
FREQ

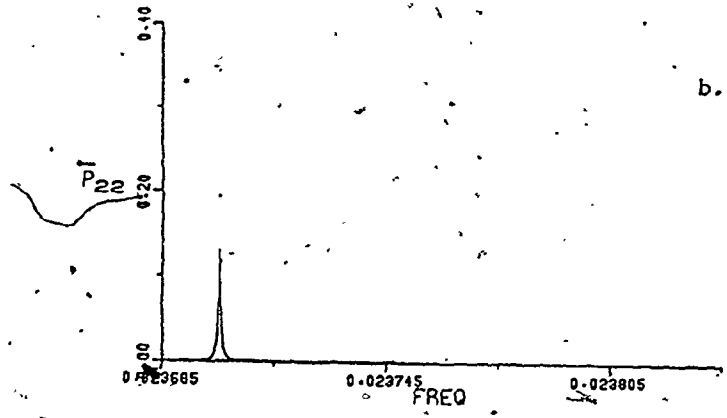
b.
$\bar{P}_{22}$
0.10
0.20
0.00
0.023685
0.023745
0.023805
FREQ

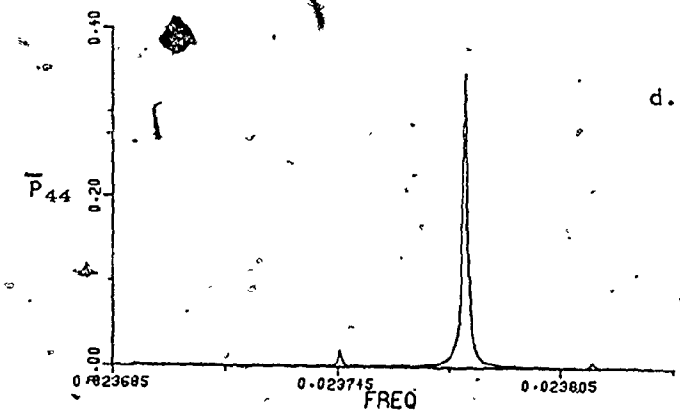
d.
$\bar{P}_{44}$
0.10
0.20
0.00
0.023685
0.023745
0.023805
FREQ

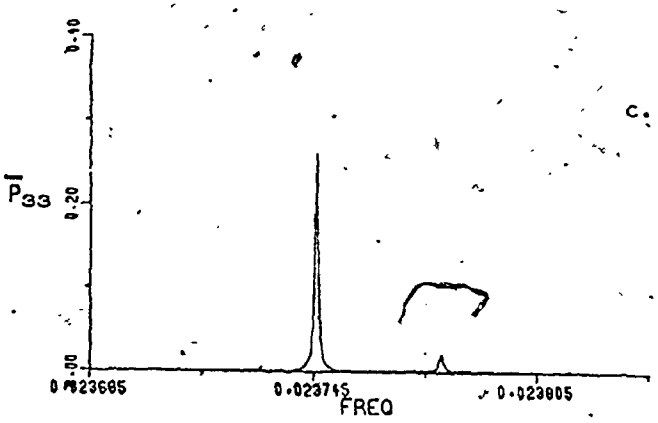
c.
$\bar{P}_{33}$
0.10
0.20
0.00
0.023685
0.023745
0.023805
FREQ

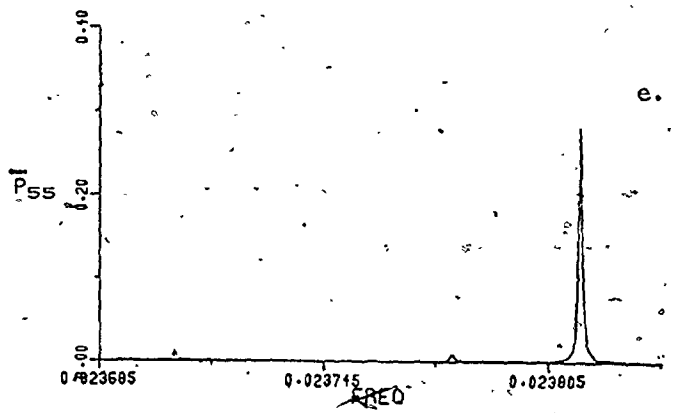
e.
$\bar{P}_{55}$
0.10
0.20
0.00
0.023685
0.023745
0.023805
FREQ

so that a greater transition probability is attained for the same value of the collision time. Table 4-1 shows the peak heights in the steady-state spectrum for the three-photon transitions for various values of τ. In every case, the level 2 transition shows the greatest decrease from 0.5 and the level 4 transition the least.

The effects discussed in this section for the three-photon transition would also be observed in the single-photon results although because the Rabi periods do not differ as greatly, the effect would be much less dramatic. In multi-level systems in which the individual coupling strengths differ significantly, the transition with the longest period can be damped appreciably relative to the other levels for single-photon transitions.

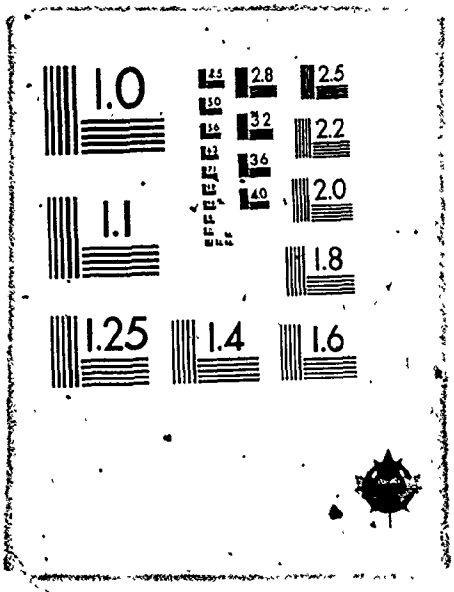

Table (4-1). Peak heights, $(1 - \bar{P}_{11})$, at the resonance frequencies for the three-photon transitions in the five-level system of figure (3-16) for various values of τ.

τ	$\nu = 2.37003 \times 10^{-2}$ $(\Delta t \sim 1.0 \times 10^{7})$	$\nu = 2.37457 \times 10^{-2}$ $(\Delta t \sim 5.5 \times 10^{6})$	$\nu = 2.37793 \times 10^{-2}$ $(\Delta t \sim 3.5 \times 10^{6})$	$\nu = 2.38134 \times 10^{-2}$ $(\Delta t \sim 5.3 \times 10^{6})$
1.0×10^{7}	0.4761	0.4938	0.4986	0.4923
5.0×10^{6}	0.4414	0.4827	0.4941	0.4822
2.5×10^{6}	0.3420	0.4432	0.4768	0.4455
1.0×10^{6}	0.1337	0.2821	0.3830	0.2910
7.5×10^{5}	0.08609	0.2113	0.3241	0.2205
5.0×10^{5}	0.04348	0.1237	0.2254	0.1309
1.0×10^{5}	0.004115	0.008784	0.01805	0.009283

CHAPTER 5

THE POLARIZATION LABELLING EXPERIMENT

The technique of polarization labelling spectroscopy, developed in the mid 1970's at Stanford University [20,22], has the capability to greatly simplify crowded molecular spectra. The basic principles of the technique may be easily understood with reference to the schematic diagram in figure (5-1). A relatively weak, broadband laser pulse passes through the sample cell located between linear polarizers with polarizations oriented perpendicular to one another. The crossing of the polarizers precludes the transmission of any conventional absorption spectroscopy signals. In order to produce a signal from the apparatus, the broadband pulse is preceded through the sample by a counterpropagating, intense, narrowband "pump" laser of circular polarization (although circular polarization was used almost exclusively in the following experiments, orientation of the pump laser polarization at 45° to that of the broadband laser is also possible). The pump laser "labels" the initial and final states of the transition to which it is tuned by exciting an asymmetric M_J population distribution. The resulting asymmetric distributions in the lower and upper levels of the pumped transition cause asymmetric absorption and transmission of the linearly polarized "probe" pulse at frequencies corresponding to transitions to or from these labelled levels (see figure (5-2)). The result is a rotation of the plane of polarization at these frequencies. The component at 90° will pass through the second polarizer and will be photographable at the spectrograph. Since only labelled transition frequencies pass

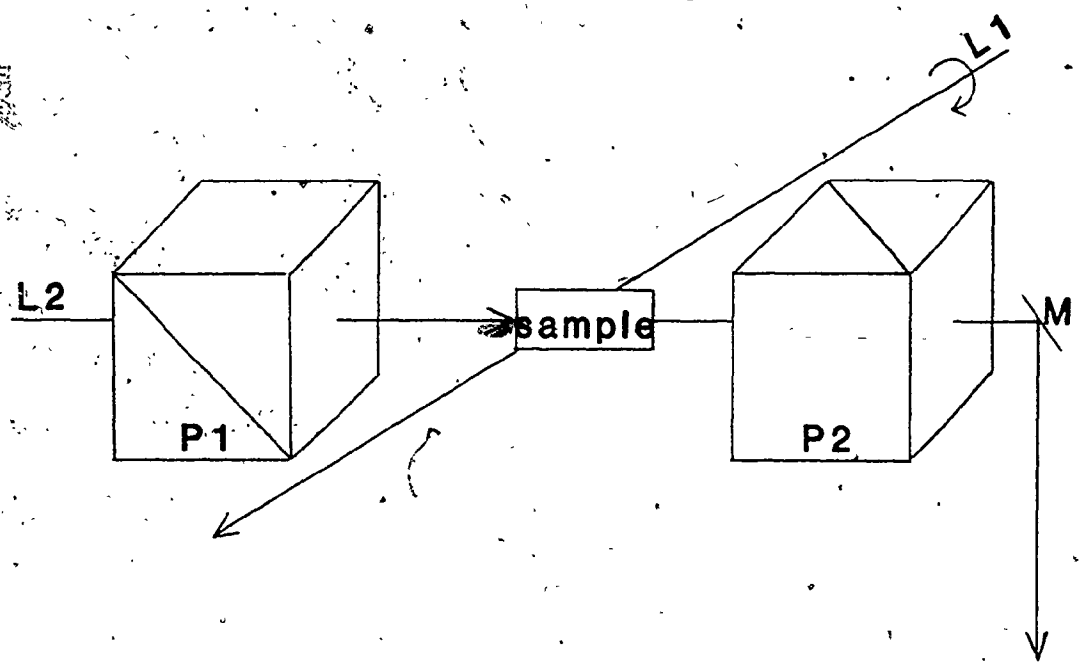

Figure (5-1). Schematic diagram of the polarization labelling experiment. An intense, narrowband "pump" L1, of circular polarization "labels" molecules in the sample cell. The broadband "probe" pulse, L2, passes through polarizer P1, the prepared sample, and polarizer P2. The polarizers are oriented with planes of polarization perpendicular to one another, so only polarization labelling signals are directed on to the spectrograph.

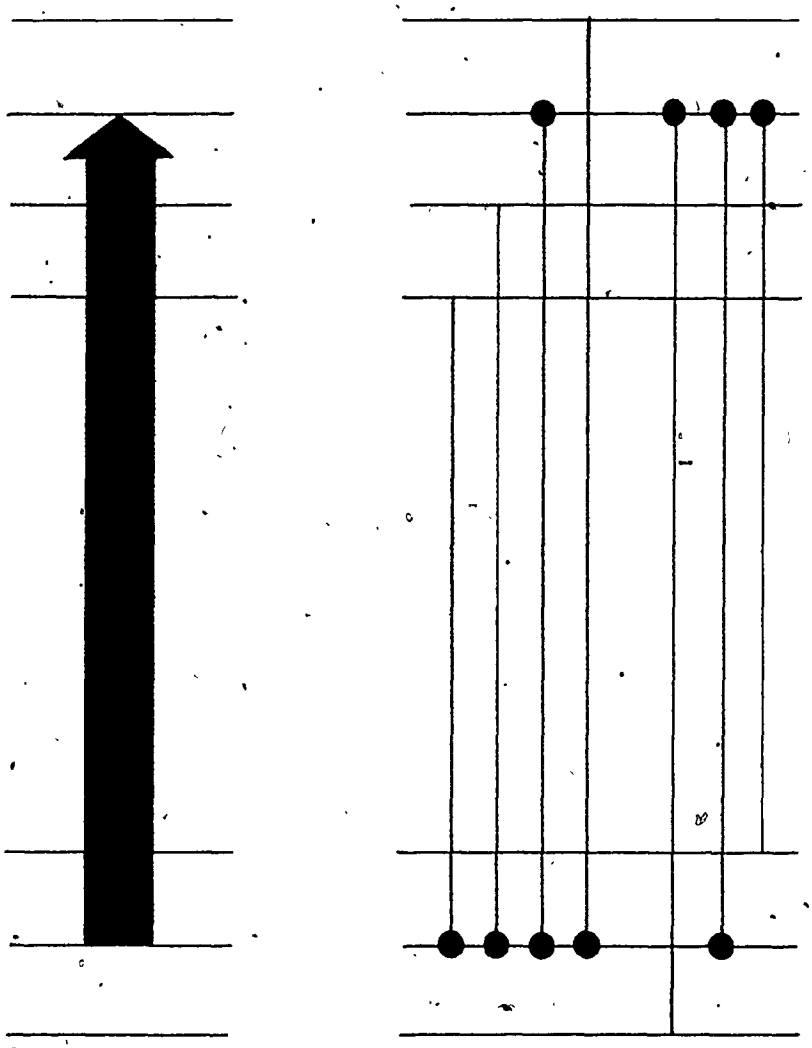

Figure (5-2). Energy level diagram for the polarization labelling experiment. (a) The pump laser labels only the ground and excited states of the transition to which it is tuned. (b) Only those transitions originating or terminating in a labelled level will appear in the spectrum. The dot (●) signifies the labelled level in the transition.

through the crossed polarizers arrangement, very few lines will appear in the spectrum. Their assignments will be further facilitated by the fact that the initial or final (or both) state(s) of the transition will generally be known from a correct assignment of the pumped transition.

Figure (5-3) illustrates some of the various pump and probe combinations that may be used in the experiment.

5.1 Theory

The theory of polarization labelling spectroscopy has been developed in detail elsewhere [22-24]; the abbreviated treatment given here relies heavily on these earlier results (to which the reader is directed for further detail). Two derivations will be outlined briefly below. The first of these, based mainly on [22], is the more physically intuitive approach, while the second is more exact mathematically.

In either case, the Maxwell's equation one is concerned with is given, in cgs units, by

$$\underline{\nabla} \times (\underline{\nabla} \times \underline{E}) + \frac{1}{c^2} \frac{\partial^2}{\partial t^2} \{ \underline{E} + 4\pi \underline{P} \} = 0 \qquad (5.1\text{-}1)$$

where $\underline{E}$ is the electric field, $\underline{P}$ is the polarization, and c is the speed of light in cm s^{-1}. To first order, a component of the polarization of the medium is related to the electric field by the complex first order susceptibility, χ_{ii}, through the equation

$$P_i = \chi_{ii} E_i \qquad (5.1\text{-}2)$$

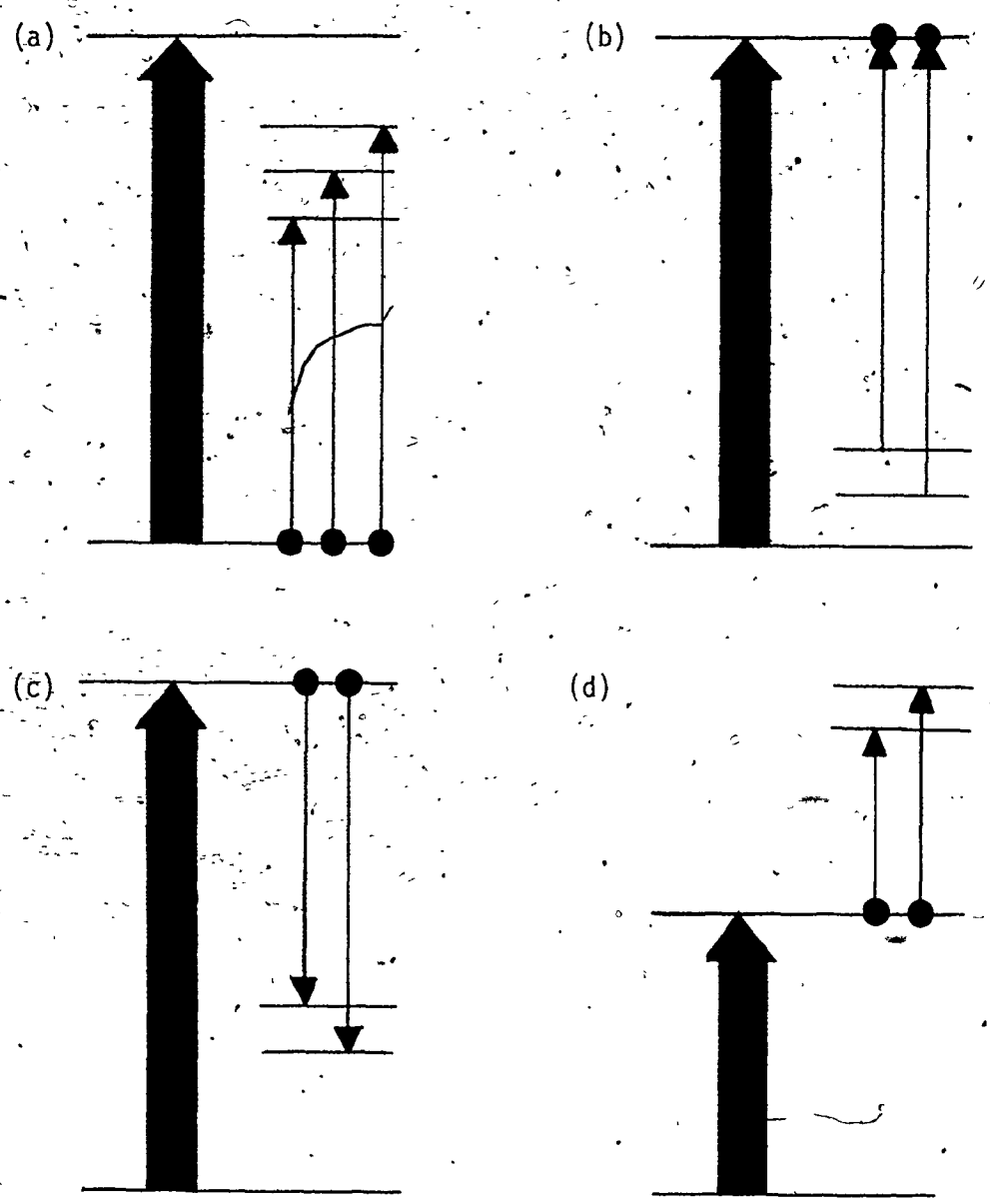

Figure (5-3). Typical polarization labelling experiments. The heavy arrow indicates the pumped transition. (a) Ground state labelling, (b) Upper state labelling, (c) Stimulated emission enhanced (SEEPOL) transitions [86], (d) Two-step polarization labelling of higher excited states.

The refractive index, n, and the absorption coefficient, α, can be written in terms of the real and imaginary parts of the first order susceptibility:

$$n_i = 1 + \frac{2\pi}{n_i} \mathrm{Re}\, \chi_{ii} \approx 1 + 2\pi\, \mathrm{Re}\chi_{ii} \qquad (5.1\text{-}3)$$

$$\alpha_i = -4\pi\left(\frac{\omega_i}{c}\right) \mathrm{Im}\chi_{ii} \qquad (5.1\text{-}4)$$

where ω is the angular frequency in radians s^{-1}.

For plane waves propagating along the z-axis, the expected solutions to (5.1-1) are of the form

$$E = A(z) \exp\{ i(kz - \omega t)\} \qquad (5.1\text{-}5)$$

where k is the wave number in radians cm^{-1} and A(z) is the amplitude of the wave. If (5.1-5) is substituted into (5.1-1), the first order result is

$$\frac{\partial A_i(z)}{\partial z} = 2\pi i\left(\frac{\omega_i}{c n_i}\right)\chi_{ii} A_i(z) \qquad (5.1\text{-}6)$$

This result can be used, along with (5.1-3) and (5.1-4), to re-write (5.1-5) as

$$E = A(0) \exp\{\left(\frac{i n_i \omega_i}{c} + \frac{\alpha_i}{2}\right)z\}\exp\{-i\omega t\} \qquad (5.1\text{-}7)$$

With a circularly polarized pump beam, the linear probe is best thought of as the sum of right (+) and left (-) circularly polarized

beams. The circular dichroism produced by the difference in absorption coefficients for the two halves of the probe ($\Delta\alpha = \alpha_+ - \alpha_-$) introduces some ellipticity into the probe polarization. The birefringence produced by the difference in refractive indices ($\Delta n = n_+ - n_-$) introduces a slight rotation of the probe polarization. Defining a polarization unit vector $\underline{p}_\pm$ by

$$\underline{p}_\pm = \frac{1}{\sqrt{2}}(\underline{x} \pm i\underline{y}) \qquad (5.1\text{-}8),$$

a probe beam polarized in the x-direction may be written

$$E = \frac{1}{\sqrt{2}} A(0)\{\underline{p}_+ \exp[(\frac{in_+\omega}{c} + \frac{\alpha_+}{2})z] + \underline{p}_- \exp[(\frac{in_-\omega}{c} + \frac{\alpha_-}{2})z]\}\exp\{-i\omega t\} \qquad (5.1\text{-}9)$$

This yields

$$E = A(0)\{\underline{x}(\cos B \cosh C - i \sin B \sinh C) + \underline{y}(-\sin B \cosh C - i \cos B \sinh C)\}\exp(\frac{-\alpha z}{2})\exp\{i\omega(\frac{nz}{c} - t)\} \qquad (5.1\text{-}10)$$

where

$$B = (n_+ - n_-)\frac{\omega z}{2c} \quad ; \quad C = (\alpha_+ - \alpha_-)\frac{z}{4} \qquad (5.1\text{-}11)$$

and

$$n = \frac{n_+ - n_-}{2} \quad ; \quad \alpha = \frac{\alpha_+ - \alpha_-}{2} \qquad (5.1\text{-}12)$$

Since the probe beam has been assumed to be polarized initially in the x-direction, the signal through the analyzing polarizer will be given by the y-terms of (5.1-10). Assuming all values are small, only lowest order terms will be retained. The result is

$$E_y = A(0)\{\theta - \frac{\omega z}{2c}(n_+ - n_-) - \frac{i}{4}(\alpha_+ - \alpha_-) + ib\} \qquad (5.1\text{-}13)$$

where the θ term has been added to account for any slight uncrossing of the polarizer and the ib term for any background dichroism. The intensity of the signal is given by

$$|E|^2 = I = I_0\{\xi + \theta^2 + b^2 - \theta(n_+ - n_-)\frac{\omega z}{c} - b(\alpha_+ - \alpha_-)\frac{z}{2}$$

$$+ [\frac{\omega z}{2c}(n_+ - n_-)]^2 + [\frac{z}{4}(\alpha_+ - \alpha_-)]^2\} \qquad (5.1\text{-}14)$$

where the term ξ has been added to take into account the imperfection of the polarizers. If the circular dichroism on resonance is defined as $\Delta\alpha$, and f is defined as a dimensionless frequency $\frac{\omega-\omega_0}{m}$, where m is the halfwidth and ω_0 is the resonant frequency, the Lorentzian lineshape for the dichroism can be written

$$\alpha_+ - \alpha_- = \frac{\Delta\alpha}{1+f^2} \qquad (5.1\text{-}15)$$

The birefringence can be re-written in terms of $\Delta\alpha$ as

$$n_+ - n_- = -\frac{\Delta\alpha c}{2\omega}\frac{f}{1+f^2} \qquad (5.1\text{-}16)$$

Equation (5.1-14) then becomes

$$\hat{I} = I_0 \{\xi + \theta^2 + b^2 - \theta \frac{\Delta\alpha z}{2} \frac{1}{1+f^2} - b \frac{\Delta\alpha z}{2} \frac{1}{1+f^2} + (\frac{\Delta\alpha z}{4})^2 \frac{1}{1+f^2}\} \quad (5.1\text{-}17)$$

an equation with only one term independent of "background" correction parameters. If the polarizer uncrossing (θ), background dichroism (b), and polarizer imperfection (ξ) terms are combined into a single background term, θ', the result becomes, on resonance,

$$I = I_0(\theta' + [\frac{\Delta\alpha}{4} z]^2) \quad (5.1\text{-}18)$$

According to this equation, an estimate of the signal intensity follows from the calculation of $\Delta\alpha$.

To this end, the M_J - dependence of the absorption cross-section for circularly polarized light must be examined. For right circularly polarized light, for example, the allowed transitions will be $(M_J + 1) \leftarrow M_J$. The square of the appropriate direction cosine matrix element factors [87], $\sigma^{+}_{J_a J_b M}$, have been evaluated for $J_a = 10$ for R- and Q- branch transitions. Here J_a and J_b refer to the lower and upper states of the transition, respectively. These absorption cross-sections are plotted in figure (5-4). This graph illustrates the strong M_J-dependence for R- (and P-) branch transitions for circularly polarized light. Q-branch transitions, on the other hand, are favoured by linear polarization. The total cross-section is given by averaging over M_J:

Figure (5-4). The M_J-dependence of $\sigma_{J_a J_b M}^{\pm}$. In this figure, $|\sigma_{J_a J_b M}^{+}|^2$ values are plotted against M_J for an R- and a Q-branch transition. The + sign indicates right circularly polarized light. $J_a = 10$.

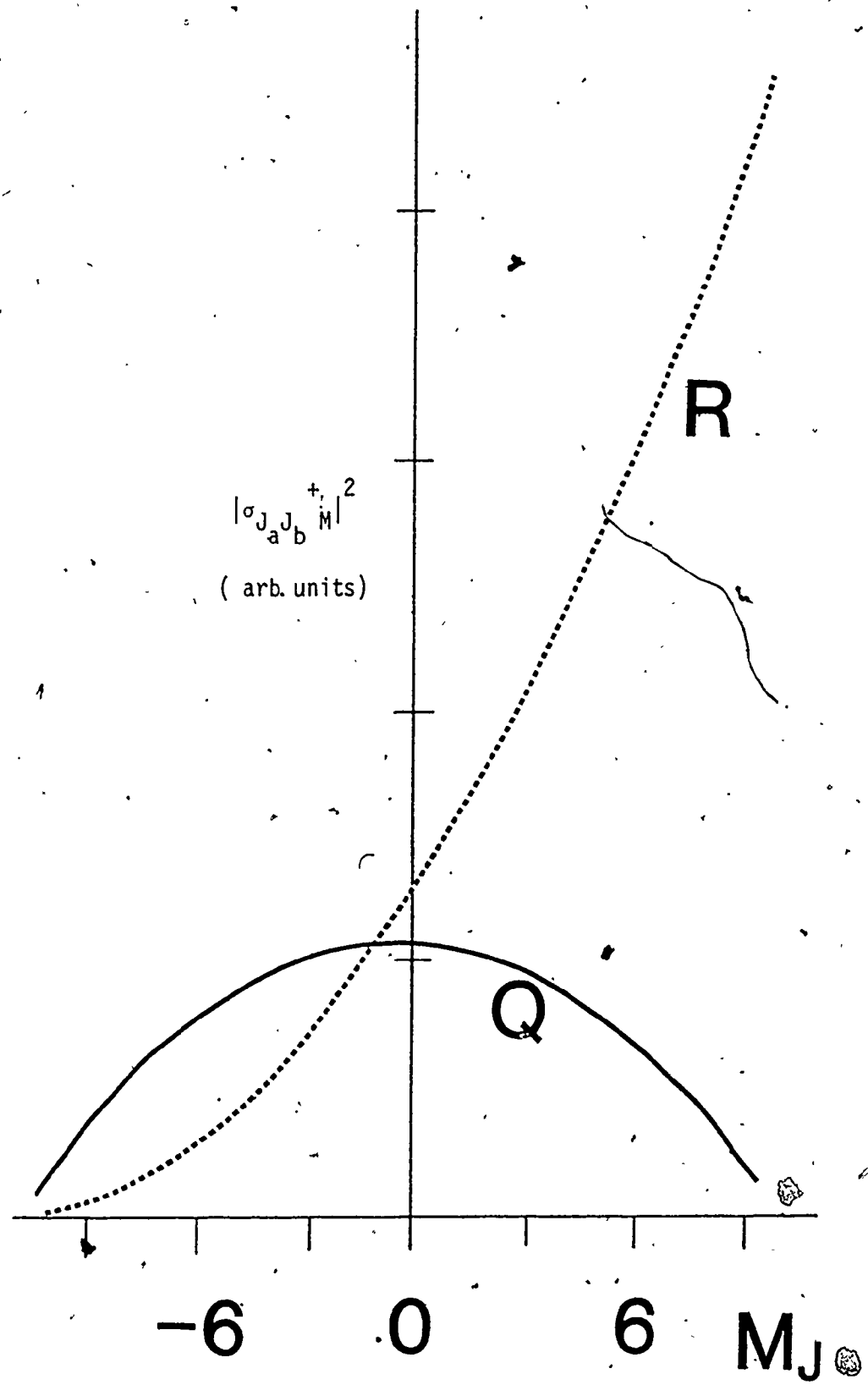
R
$|\sigma_{J_a J_b}^{+;M}|^2$
(arb. units)
Q
-6
0
6
M_J

$$\sigma_{J_a J_b} = \frac{1}{2J_a+1} \sum_M \sigma^{\pm}_{J_a J_b M} \qquad (5.1\text{-}19)$$

Examining first the pumped transition in the experiment, it is noted that the asymmetric population left in the ground state may be expressed as

$$n_M = \frac{1}{2J+1} N^\circ \{1 - \sigma^{+}_{J_a J_b M} \frac{I_1 t}{\hbar\omega}\} \qquad (5.1\text{-}20)$$

where N° is the total equilibrium number density in the lower state and n_M is the remaining number density in the M_Jth level after the circularly polarized pulse of intensity, I_1, duration, t, and frequency, ω, has passed through the sample. The dichroism will depend on the value of n_M and the cross-sections for the probed transition for the two oppositely circularly polarized beams making up the broadband pulse. This can be expressed as

$$\alpha_+ - \alpha_- = \sum_M n_M(\sigma^{+}_{J_a J_c M} - \sigma^{-}_{J_a J_c M}) \qquad (5.1\text{-}21)$$

where J_c is the angular momentum of the upper state of the probed transition. This equation further reduces to

$$\alpha_+ - \alpha_- = -(N^\circ \sigma_{J_a J_c} \sigma_{J_a J_b} \frac{I_1 t}{\hbar\omega}) \zeta_{J_a J_b J_c} \qquad (5.1\text{-}22)$$

where the numerical factor $\zeta_{J_a J_b J_c}$ can be defined by

$$\zeta_{J_a J_b J_c} = \sum_M \frac{\sigma^{+}_{J_a J_b M}(\sigma^{+}_{J_a J_c M} - \sigma^{-}_{J_a J_c M})}{\sigma_{J_a J_c} \sigma_{J_a J_b}} \qquad (5.1\text{-}23)$$

The table of values of $\zeta_{J_a J_b J_c}$ from [22] is reproduced here in table (5-1).

A more exact treatment of the experiment begins again with the Maxwell's equation given in (5.1-1), with the energy level diagram in figure (5-5) [23]. The polarization of the medium is expressed to higher order by

$$P_i = \sum_j \chi_{ij} E_j + \frac{1}{2} \sum_j \sum_k \chi_{ijk} E_j E_k + \frac{1}{6} \sum_j \sum_k \sum_l \chi_{ijkl} E_j E_k E_l \cdots \tag{5.1-24}$$

If (5.1-5) is again subsituted into (5.1-1) the result will now have higher order terms. In general [88], the result is

$$\frac{\partial A_i(z)}{\partial z} = 2\pi i \left(\frac{\omega_i}{cn_i}\right)\{\sum_j \chi_{ij} A_j + \frac{1}{6} \sum_j \sum_k \sum_l A_j A_k A_l \chi_{ijkl} \exp(i[\Delta k]z) + \frac{1}{6} \sum_{j=1}^{3} \chi_{iijj} A_i A_j A_j^* + \ldots\} \tag{5.1-25}$$

Conservation of energy dictates that

$$\omega_i = \omega_j + \omega_k + \omega_l \tag{5.1-26}$$

The "phase matching" requirement given by

$$\Delta k = k_j + k_k + k_l - k_i \cong 0 \tag{5.1-27}$$

is needed to keep the exponential term close to unity. With reference to the energy level diagram in figure (5-5), the equations for signal, probe, and pump amplitudes are

Table (5-1). Values of $\zeta_{J_a J_b J_c}$ for circularly polarized pump radiation.

Pump \ Probe	$J_c = J_a + 1$	$J_c = J_a$	$J_c = J_a + 1$
$J_b = J_a + 1$	$\frac{3J}{2(J+1)}$	$\frac{-3}{2(J+1)}$	$\frac{-3}{2}$
$J_b = J_a$	$\frac{-3}{2(J+1)}$	$\frac{3}{2J(J+1)}$	$\frac{3}{2J}$
$J_b = J_a - 1$	$\frac{-3}{2}$	$\frac{3}{2J}$	$\frac{3(2J^2+J-1)}{2J(2J-1)}$

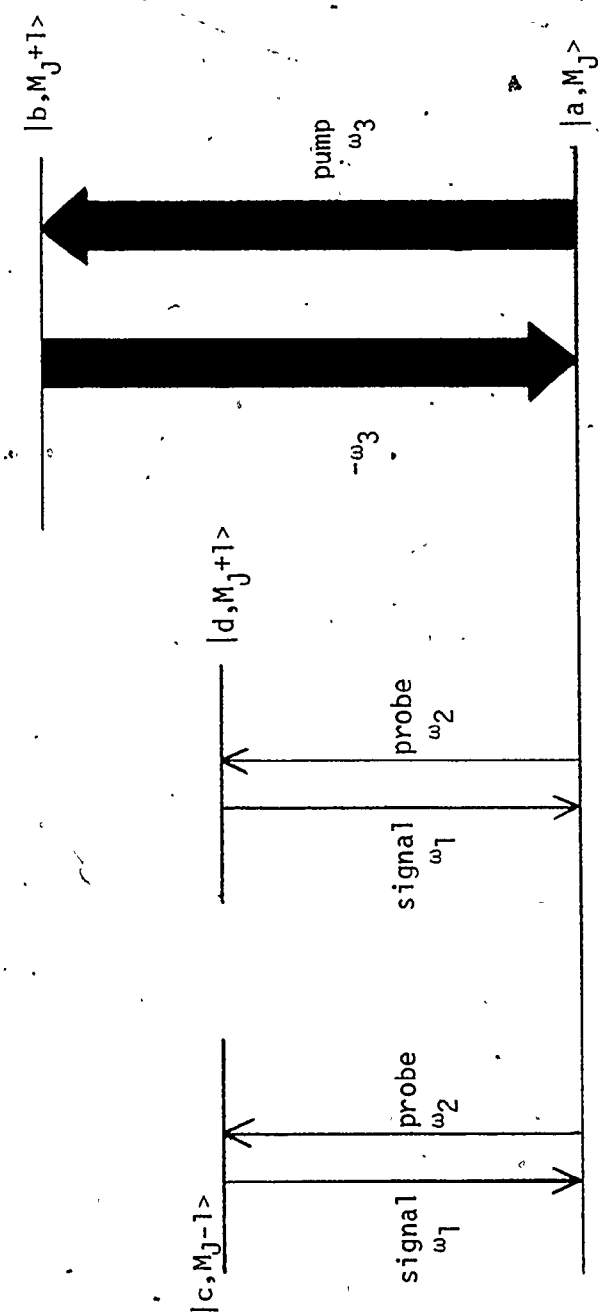

Figure (5-5). Schematic energy level diagram for the theoretical treatment of the polarization labelling experiment given in [23]. The heavy lines indicate the pumped transition.

$$\frac{\partial A_1}{\partial z} = 2\pi i \left(\frac{\omega_1}{cn_1}\right)\{\chi_{11}A_1 + \frac{2}{3}\chi_{1233}A_2A_3A_3^*\} \quad (5.1\text{-}28)$$

$$\frac{\partial A_2}{\partial z} = 2\pi i \left(\frac{\omega_2}{cn_2}\right)\{\chi_{22}A_2 + \frac{2}{3}\chi_{2133}A_1A_3A_3^*\} \quad (5.1\text{-}29)$$

$$\frac{\partial A_3}{\partial z} = 2\pi i \left(\frac{\omega_3}{cn_3}\right)\chi_{33}A_3 \quad (5.1\text{-}30)$$

respectively. Assuming solutions to (5.1-28) and (5.1-29) of the form

$$A_1(z) = M_1(z)A_2(0)\exp\{2\pi i \left(\frac{\omega_1}{cn_1}\right)\chi_{11}z\} \quad (5.1\text{-}31)$$

$$A_2(z) = M_2(z)A_2(0)\exp\{2\pi i \left(\frac{\omega_2}{cn_2}\right)\chi_{22}z\} \quad (5.1\text{-}32)$$

yields

$$M_1(l) = \sin\{2\pi\left(\frac{\omega_1}{cn_1}\right)\frac{2|\chi_{1233}|}{3}|A_3|^2\,l\} \quad (5.1\text{-}33)$$

where l is the interaction length for pump and probe beams. Substituting (5.1-33) into (5.1-31) and squaring the result gives the intensity of the signal wave. If the argument of the sine function is small, the argument itself can be used in place of the sine. The final result would indicate that the signal intensity depends on the square of the pump laser intensity, the square of the interaction length, and the first power of the probe laser intensity. This is the same general dependence as that of (5.1-18).

In order to determine the required third order susceptibility, χ_{1233}, density matrix theory may be used. The 4 x 4 matrix needed to describe the energy level diagram of figure (5-5) is of the form

$$\underline{\rho} = \begin{bmatrix} \rho_{aa} & \rho_{ba} & \rho_{ca} & \rho_{da} \\ \rho_{ab} & \rho_{bb} & 0 & 0 \\ \rho_{ac} & 0 & \rho_{cc} & 0 \\ \rho_{ad} & 0 & 0 & \rho_{dd} \end{bmatrix} \tag{5.1-34}$$

The diagonal elements represent the populations of the different levels; the off-diagonal elements are related to the dipole moments connecting different levels. The equations describing the behaviour of the individual matrix elements are given by

$$\left[\frac{\partial}{\partial t} + V\frac{\partial}{\partial z}\right]\rho_{aa} = \lambda_a - \gamma_a\rho_{aa} + \frac{i\mu_{ba}A_3}{2\hbar}(\rho_{ba}\exp\{i(\omega_3 t - k_3 z)\} - \rho_{ab}\exp\{-i(\omega_3 t - k_3 z)\})$$
$$+ \frac{i\mu_{ca}A_2}{2\hbar}(\rho_{ca}\exp\{i(\omega_2 t + k_2 z)\} - \rho_{ac}\exp\{-i(\omega_2 t + k_2 z)\})$$
$$+ \frac{i\mu_{da}A_2}{2\hbar}(\rho_{da}\exp\{i(\omega_2 t + k_2 z)\} - \rho_{ad}\exp\{-i(\omega_2 t + k_2 z)\}) \tag{5.1-35}$$

$$\left[\frac{\partial}{\partial t} + V\frac{\partial}{\partial z}\right]\rho_{bb} = \lambda_b - \gamma_b\rho_{bb} - \frac{i\mu_{ba}A_3}{2\hbar}(\rho_{ba}\exp\{i(\omega_3 t - k_3 z)\} - \rho_{ab}\exp\{-i(\omega_3 t - k_3 z)\}) \tag{5.1-36}$$

$$\left[\frac{\partial}{\partial t} + V\frac{\partial}{\partial z}\right]\rho_{cc} = \lambda_c - \gamma_c\rho_{cc} - \frac{i\mu_{ca}A_2}{2\hbar}(\rho_{ca}\exp\{i(\omega_2 t + k_2 z)\} - \rho_{ac}\exp\{-i(\omega_2 t + k_2 z)\}) \tag{5.1-37}$$

$$\left[\frac{\partial}{\partial t} + V\frac{\partial}{\partial z}\right]\rho_{ba} = -(\gamma_{ba} + i\omega_{ba})\rho_{ba} - \frac{i\mu_{ba}A_3}{2\hbar}(\rho_{bb} - \rho_{aa})\exp\{-i(\omega_3 t - k_3 z)\} \tag{5.1-38}$$

$$\left[\frac{\partial}{\partial t} + V\frac{\partial}{\partial z}\right]\rho_{ca} = -(\gamma_{ca} + i\omega_{ca})\rho_{ca} - \frac{i\mu_{ca}A_2}{2\hbar}(\rho_{cc} - \rho_{aa})\exp\{-i(\omega_2 t + k_2 z)\} \tag{5.1-39}$$

where the equations for ρ_{dd} and ρ_{da} are analogous to (5.1-37) and (5.1-39), respectively. The λ_i term expresses the rate at which level i is populated and the γ_i term described the rate at which level i decays. μ_{ij} is the dipole moment connecting states i and j, and γ_{ij} is the rate of decay of the dipole moment.

The introduction of λ and γ terms may be cause for some consternation, so it is perhaps appropriate that a few words be said at this juncture to justify the existence of these phenomenological constants. The decay of a level through a γ term does not explicitly terminate in another of the levels in the calculation. Similarly, the λ terms describe the populating of a level, but fail to specify the origins of the population. However, a real molecule, it must be remembered, will have many more energy levels than the four used here. Decay of an excited state will be to a large manifold of levels, only a few of which are specified in the calculation. Similarly, the re-distribution of population necessary for a return to equilibrium distributions involves all levels, not just those few examined in the density matrix formalism. The λ values, often introduced in laser theory treatments to account for the incoherent pumping of the lasing medium, can be used here to describe the re-distribution of population from other levels into the specific levels of the calculation. To maintain a Maxwell-Boltmann distribution, λ_i will be of the form

$$\lambda_i = \Lambda_i W(v) \qquad (5.1\text{-}40)$$

where the Boltzmann weighting factor, $W(v)$, is given by

$$W(v) = (\pi^{1/2} v_m)^{-1/2} \exp\left\{\frac{-v^2}{v_m^2}\right\} \qquad (5.1\text{-}41)$$

In this equation, v_m is the most probable velocity at the temperature, T:

$$v_m = \left(\frac{2kT}{M}\right)^{1/2} \qquad (5.1\text{-}42)$$

where M is the molecular weight.

Steady-state solutions for the density matrix elements are sought. First, examining the pump transition alone, the desired solutions will be of the form

$$\rho_{ii}(z,t,v) = \rho_{ii}(v) \quad , \quad i = a,b \qquad (5.1\text{-}43)$$

and

$$\rho_{ab}^*(z,t,v) = \rho_{ba}(z,t,v) = S(v) \exp\{-i(\omega_3 t - k_3 z)\} \qquad (5.1\text{-}44)$$

The solution (5.1-35) yields

$$\rho_{aa} = \frac{\lambda_a}{\gamma_a} + \frac{1}{2}\left[\frac{\mu_{ab}^2 |A_3|^2}{\hbar^2 \gamma_{ba} \gamma_a}\right] \gamma_{ba}^2 (\rho_{bb} - \rho_{aa}) \{(\omega_{ba} - \omega_3 + k_3 v)^2 + \gamma_{ab}^2\}^{-1} \qquad (5.1\text{-}45)$$

A similar result for ρ_{bb} produces the difference

$$(\rho_{bb} - \rho_{aa}) = NW(v)\left[1 - \frac{R^2 \gamma_{ba}^2}{\gamma_{ba}^2 + (\omega_{ba} - \omega_3 + k_3 v)^2 + R^2 \gamma_{ba}^2}\right] \qquad (5.1\text{-}46)$$

where N is defined by the field-free equation

$$(\rho_{bb} - \rho_{aa})A_3 = NW(v) \qquad (5.1\text{-}47)$$

R^2 is defined by

$$R^2 = \frac{\mu_{ba}^2 |A_3|^2}{\hbar^2 \mu_{ba} \gamma_-} \qquad (5.1\text{-}48)$$

and

$$2\gamma^{-1} = \gamma_a^{-1} + \gamma_b^{-1} \qquad (5.1\text{-}49)$$

The molecular transition dipole moment is given by the value of S(v) used in the above equations:

$$S(v) = -i\frac{\mu_{ba}A_3}{2\hbar} NW(v) \frac{\gamma_{ba} - i(\omega_{ba} - \omega_3 + k_3 v)}{(\omega_{ba} - \omega_3 + k_3 v)^2 + \gamma_{ba}^2(1+R^2)} \qquad (5.1\text{-}50)$$

The probed transitions may be treated in an analogous manner. The off-diagonal elements, ρ_{ca} and ρ_{da}, will be assumed to be of the form

$$\rho_{ca}(z,t,v) = T(v) \exp\{-i(\omega_2 t + k_2 z)\} \qquad (5.1\text{-}51)$$

$$\rho_{da}(z,t,v) = U(v) \exp\{-i(\omega_2 t + k_2 z)\} \qquad (5.1\text{-}52)$$

The difference in induced dipole moments, $(\overline{P_d - P_c})$, may be expressed in terms of the solutions to (5.1-51) and (5.1-52). Retention of terms dependent on the a state population yields

$$(\overline{P_d - P_c})_a = \frac{iA_2}{2\hbar} \rho_{aa} \frac{|\mu_{ca}|^2 - |\mu_{da}|^2}{\{i(\omega_{da} - \omega_2 - k_2 v) + \gamma_{da}\}} \exp\{-i(\omega_2 t + k_2 z)\} \qquad (5.1\text{-}53)$$

The desired susceptibility can be calculated from this equation after substituting (5.1-45) for ρ_{aa}, integrating over molecular velocities, and summing over the M_J levels of the a state. The final expression is

$$\chi_{1233} = \sum_{M_J} \frac{N^\circ}{14\hbar^3\gamma_a}\left(\frac{\pi}{v_m}\right)^{1/2} \exp\left\{\frac{-(\omega_{ba}-\omega_3)^2}{k_3^2 v_m^2}\right\}\left[\frac{(1+R^2)^{-1/2}}{k_3}\right]\left[\frac{\omega + i\Gamma}{\omega^2+\Gamma^2}\right]$$

$$\times \quad |\mu_{ba}|^2\{|\mu_{da}|^2 - |\mu_{ca}|^2\} \qquad (5.1\text{-}54)$$

where

$$\Gamma = \gamma_{ca} + \left|\frac{k_2}{k_3}\right|\sqrt{1+R^2}\ \gamma_{ba} \qquad (5.1\text{-}55)$$

$$\omega = (\omega_{ca} - \omega_2) + \left|\frac{k_2}{k_3}\right|(\omega_{ba}-\omega_3). \qquad (5.1\text{-}56)$$

It has been pointed out that (5.1-18) and (5.1-31) will agree in their predictions of the signal intensity dependence on the interaction length of the two lasers in the sample cell and on the pump probe laser intensities. What should also be pointed out here is that the approximations used in both derivations necessarily mean that the final results will only qualitatively describe the experimentally observed signal intensities. One of the major drawbacks of the solutions so far is the as-yet-unanswered question of the effect of the laser pulse profiles on the calculated intensities; this is further exacerbated by the inability to guarantee that the pump laser pulse will be exactly on resonance with a particular transition. Steady-state solutions, with the short pulse durations used in the experiment, may not be reasonable in some cases. Further, the

parameters describing an individual rovibronic level of the sample molecule may be unknown or inadequately determined. All of these misgivings must be borne in mind when assessing any calculation based on the derivations outlined above.

5.2 Experimental

The experimental arrangements are illustrated schematically in figure (5-6). A Lumonics Model TE-261 laser was operated as a XeCl excimer laser, delivering a pulse of approximately 12 ns. duration and 5MW peak power at 308 nm. Part of this beam (~15%) was used to excite the oscillator and amplifier stages of a Molectron DL-14P dye laser. The remainder of the excimer laser pulse was further split to excite both a second amplifier cell in the pump line and the broadband probe dye laser.

The Molectron laser was operated with an intracavity etalon that reduced the laser linewidth to $<0.05\ cm^{-1}$ FWHM. The second amplifier in the pump laser line consisted of a 10 mm flowing dye cell set at Brewster's angle and pumped longitudinally by the excimer laser pulse so as to blend with and amplify the laser line from the Molectron. The pump laser light was circularly polarized by passing it through a Fresnel rhomb or a stressed quartz block. The probe laser consisted of a 20 mm. long flowing dye cell pumped transversely by the excimer laser in a Hansch-type arrangement [89].

The pump and probe laser pulses, each of approximately 8 ns. duration, counterpropagated through a 50 cm. sample cell outfitted with flat quartz windows. The spatially-produced delay between pulses, varied by moving the cell along the optical axis, was 2-4 ns.

Figure (5-6). Schematic diagram of the experimental set-up used in the polarization labelling experiment. L1, pump laser; L2, probe laser; A, amplifier cell; B, beam splitter; M, mirror; P, polarizer; S, spectrometer; SC, sample cell; CP, circular polarizer.

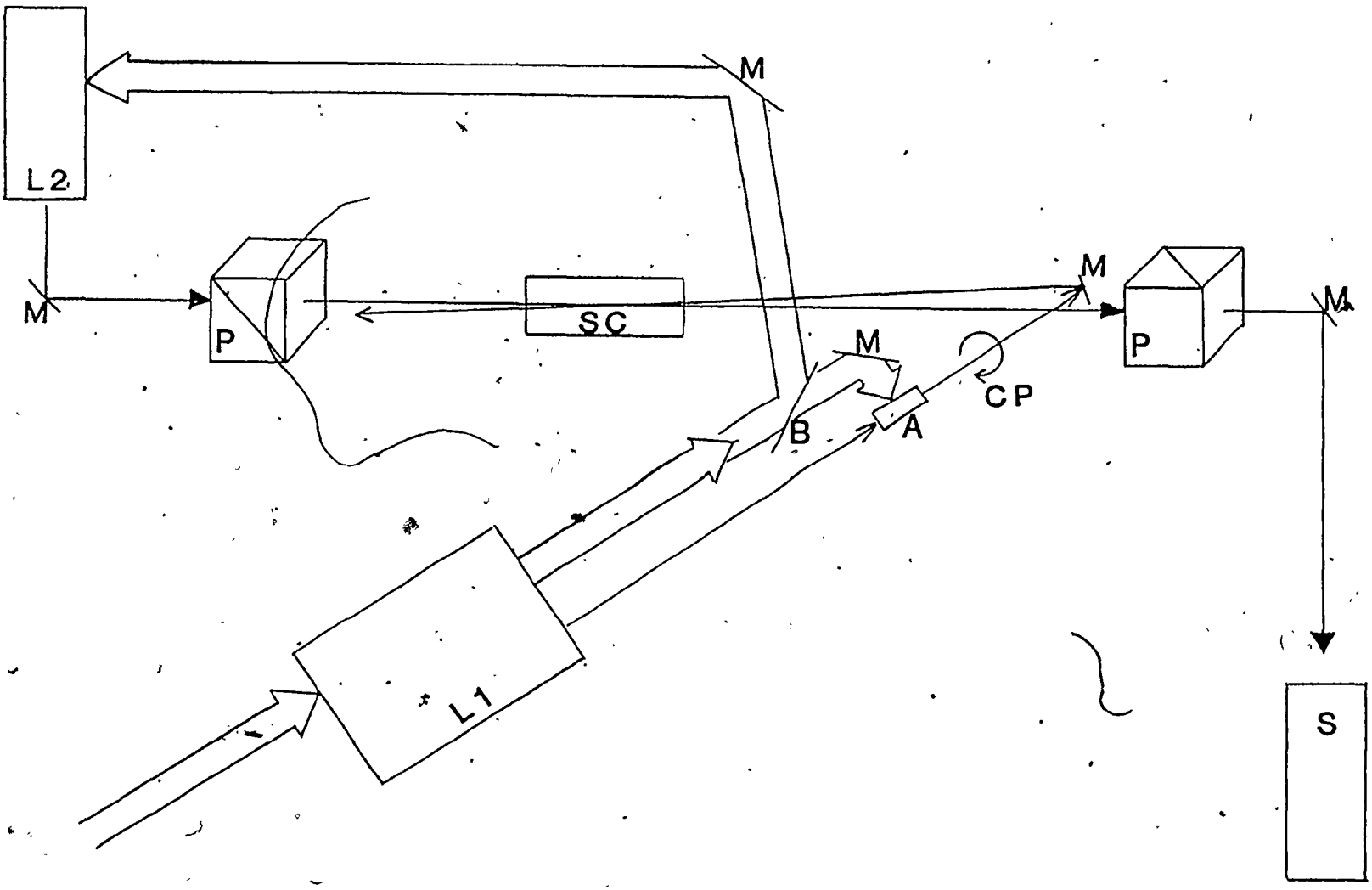

200

at the cell centre. The signal emerging from the analyzing polarizer was directed through a cylindrical lens onto the slit of a 3.4 m. f/35 Ebert-mounted Jarrell-Ash spectrograph. Spectra were recorded on a 20 inch camera loaded with either Kodak 2475 or SA-1 film. Calibration lines from an Fe/Ne hollow cathode lamp were recorded on the same film immediately before or immediately after each spectrum was taken. The signal intensities were strong enough, in some cases, to be photographed in a single pump-probe sequence. In general, however, real time exposures on the order of 25-50 μs were used in order to bring up weaker lines.

For the polarization labelling experiments described in Chapter 7, the sample cell was filled with iodine vapour at its room temperature vapour pressure of ∿250 mTorr. The three-stage pump laser arrangement produced powers on the order of 60 kW per pulse (∿0.5 mJ per pulse) with Coumarin 540A (Exciton) or Coumarin 500 (Exciton) dye in ethanol solution. With C540A in the dye laser, the light was circularly polarized by passing it through a Fresnel rhomb. With C500 in the laser, the light was circularly polarized by passing it through a quartz block which, when stressed, acted as a $\lambda/4$ plate. The dyes used in the probe laser were bis-MSB (Exciton) in a 50:50 mixture of ethanol and toluene, and Coumarin 440 (Exciton) in ethanol. Powers in the probe beam, measured after the initial linear polarization, were on the order of 25 kW per pulse. Spectra were recorded in the 13th order of the spectrograph with a dispersion at the camera of ∿2.2 cm^{-1}/mm.

5.3 Examples

The initial polarization labelling experiments were performed with nitrogen dioxide [22,26] and the sodium dimer [21,22,25]. The work done in this laboratory has not only expanded both the theoretical understanding of the experiment [23,24] and the treatment of NO_2 [24,27], but has also successfully extended the technique to other molecules [28,90-92].

Plate (5-1) shows a portion of a polarization labelling spectrum of room temperature vapour pressure of iodine, produced with Coumarin 540A dye in both pump and probe dye lasers. Since P- and R-branch transitions in the B-X system were pumped and probed, circular polarization was preferred. The real time exposure for this film was approximately 400 ns.

The spectrum shows the tremendous simplification that the polarization labelling technique introduces. The usually crowded spectrum of iodine has been reduced to a few easily-measured, easily-assigned P- and R-lines. As well, the spectrum illustrates both ground state and upper state labelling (see figure (5-3a,b)). The pump laser, tuned to 18499.17 cm^{-1} excites the P60 (28-0) transition in the B ← X system. The probe laser excites P- and R-branch transitions from the labelled J" = 60 level of the ground state to a vibrational progression, V' = 20-31 (not all shown in plate (5-1)). in the B state. Upper state labelling in the v' = 28, J' = 59 level results in a series of P60 and R58 transitions from v" = 0, 1, and 3 (again, not all shown).

Propynal, HCCCHO, is the largest molecule to be studied to date by polarization labelling [90]. In undertaking the study, it was

Plate (5-1). A portion of a polarization labelling spectrum in the iodine B ← X system taken with C540A dye in both pump and probe lasers. The pumped transition, P60, $v' = 28 \leftarrow v'' = 0$ (18499.17 cm^{-1}), and the labelled levels are indicated by heavy lines. The analysis of the total spectrum (not shown) includes the vibrational progression $v = 20 - 31$ (P60, R60 from $v_X = 0$ in the B state (ground state labelling) and $v = 0, 1, 3$ (P60, R58 to $v_B = 28$) in the X state (upper state labelling).

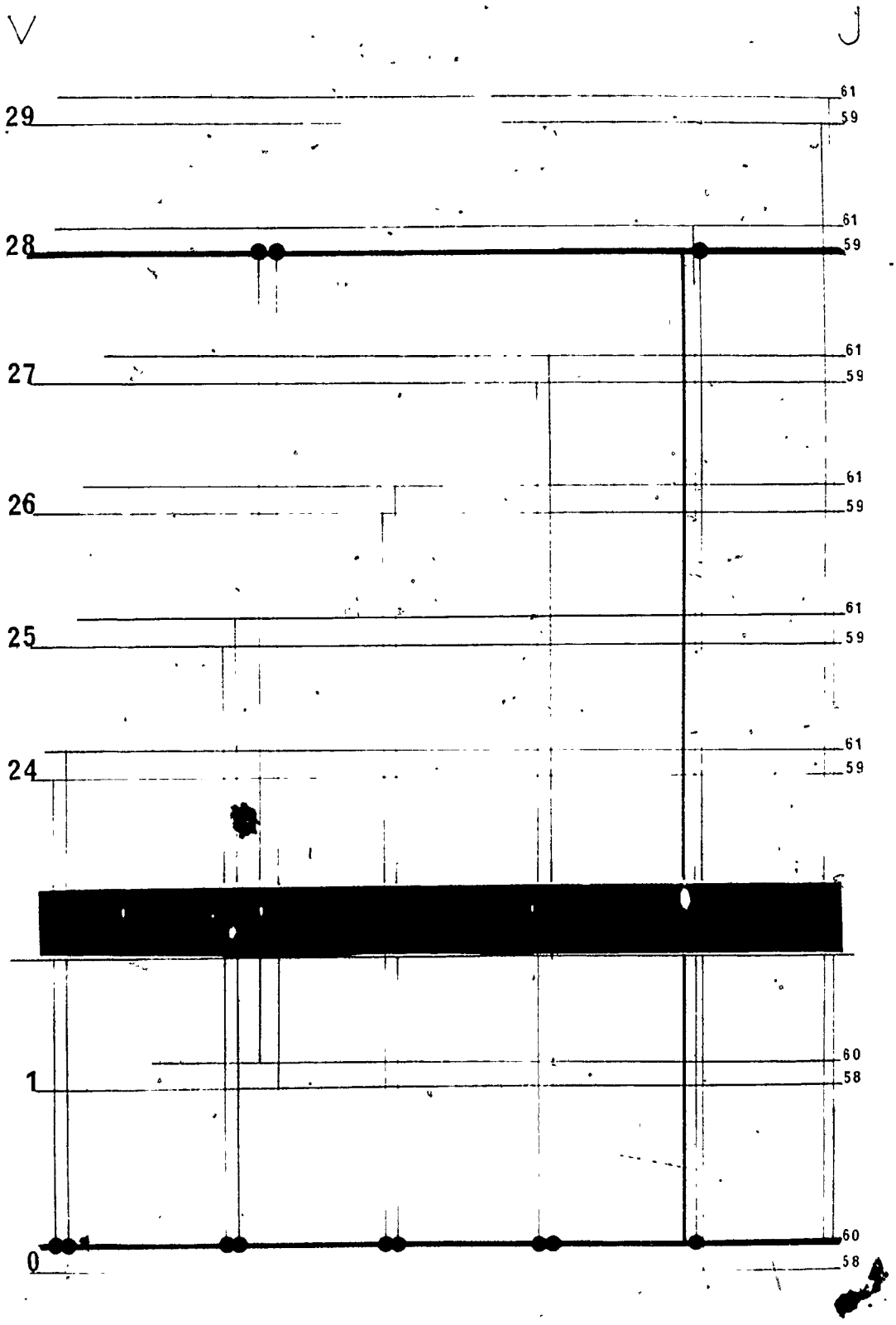
V
J
29
28
27
26
25
24
1
0
61
59
61
59
61
59
61
59
61
59
61
59
60
58
60
58

hoped to obtain simplified, high resolution spectra of propynal, while at the same time demonstrating the applicability of the polarization technique to a more complex molecule. Of particular interest in this series of experiments was the strong progression in the ν_4 vibration, the C = O stretch, seen in emission from both the singlet and triplet excited states.

Propynal was prepared using a slight modification of the technique outlined in [93]. The pump laser, containing BBQ (New England Nuclear) dissolved in a 50:50 mixture of ethanol and toluene, was tuned to the strong absorption feature in the 3820 Å region. Since the absorption is assigned to the overlap of several transitions in two Q-branches ($^rQ_0, ^pQ_1$) [94], the pump laser was linearly polarized at 45° to the plane of polarization of the probe laser. The large number of transitions simultaneously pumped means, of course, that the individual transitions are much weaker than if only one transition were involved. Since the signal depends on the square of the absorption coefficient (see, for example, (5.1-18) and (5.1-22)), the polarization labelling effect will be weaker still.

The spectrum reproduced in plate (5-2) was taken with Coumarin 440 in the probe dye laser, and a vapour pressure of ~2.4 Torr of propynal in the sample cell. The real time exposure was approximately 60 μs. The observed signal corresponds to the upper state labelled transition from the excited singlet state to the level two quanta in ν_4 above the ground state, denoted in shorthand notation as 4_2^0. The measured position of the line (22791.09 cm^{-1}) corresponds with that seen in emission by Lin and Moule. The single broad line is in reality produced by the overlap of a number of polarization signals

Plate (5-2). The polarization labelling spectrum of propynal, H—C≡C—COH. The heavy line corresponds to the pumped transition (BBQ dye in the pump laser), the dotted lines correspond to transitions that have not been observed, and the solid line corresponds to the transition that has been observed (C440 dye in the probe laser) in the spectrum.

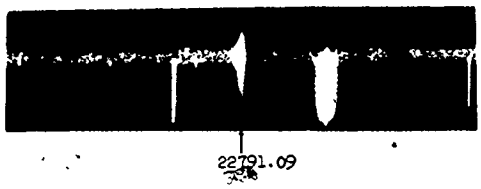
22791.09

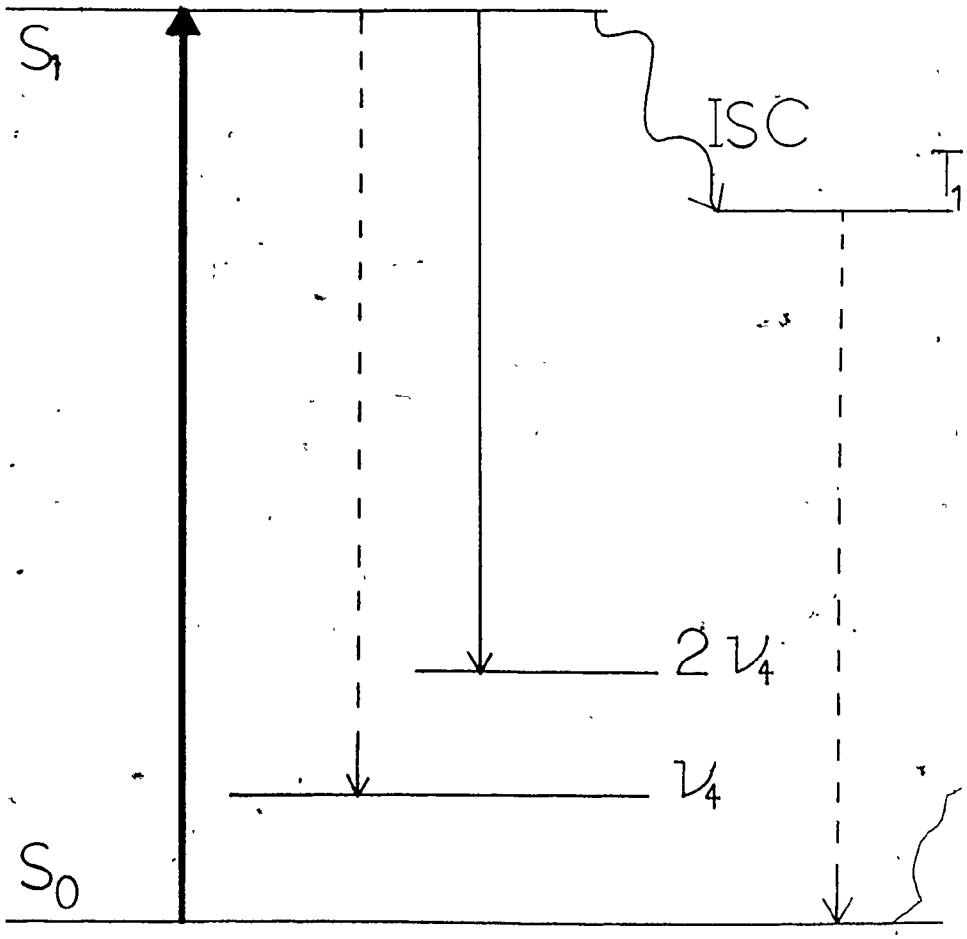
S1
ISC
T1
2ν4
ν4
S0

corresponding to the many pumped transitions. Obviously, the concentration of Q-branch transitions seen in the excited state is present in the $2\nu_4$ level as-well.

Attempts to photograph other transitions from the excited singlet state were generally frustrated by the low powers generated by the probe laser when other dyes were used. The fact that the very strong emission bands from the triplet state, including the triplet origin band, were not observed is due to the relative slowness of the intersystem crossing [96] compared to the timescale of the experiment. In fact, the intersystem crossing rate can be investigated, in theory, by varying the pump-probe delay, thereby observing the system through differing "windows" in time. A foreign gas may be added to the sample in an attempt to collisionally destroy or transfer the polarization label. Collision cross-section experiments done with iodine pressured with oxygen have been reported [97]. However, although collisionally-induced polarization labelling signals have been observed, the intersystem crossing in propynal would likely distribute the "label" over a very wide range of rotational levels, so that transitions from the triplet state would be too weak to be detected.

The experiments done here on propynal demonstrate the possibility of using polarization labelling spectroscopy on large molecules, but further experiments with more efficient laser systems are necessary before the overall usefulness or feasibility of the technique in these types of applications can be evaluated.

CHAPTER 6

MOLECULAR STATES OF IODINE

The potential energy curves for the valence shell states of iodine have been given exhaustive treatment by Mulliken [29]. Although relatively few of these states have been observed spectroscopically, a great many are predicted to exist.

The electronic states of a molecule may all be determined from a careful consideration of the possible couplings of the electron spin and orbital angular momentum. For free atoms, diatomics, and linear polyatomics, a simple vector coupling picture can adequately serve to illustrate how various states arise from different coupling cases. A more general method, necessary for more complicated molecules, is based on group-theoretical considerations [98].

6.1 Vector Coupling Model

Hund's case (a) refers to the situation in which the spin and orbital angular momentum are not strongly coupled [99]. For this (Λ,S) coupling case (analogous to Russell-Saunders coupling in atoms), the vector model takes into account the projections along the internuclear axis of the spin and orbital angular momentum vectors of the molecule. The orbital angular momentum vector, $\underline{L}$, formed from vector additions of the atomic orbital angular momenta, precesses about the internuclear axis with components along the axis of magnitude $M_L\hbar$, where M_L can take on all integer values from L to -L. The angular momentum vector, $\underline{\Lambda}$, defined as the component of the electronic angular momentum along the internuclear axis, is equated with the

absolute value of M_L:

$$\Lambda = |M_L| = 0,1,2,\ldots,L \qquad (6.1\text{-}1)$$

where the corresponding molecular states are denoted Σ, π, Δ, ... in an analogous manner to the labelling of electron orbitals in an atom. For states with $\Lambda \neq 0$, the precession of the spin, $\underline{S}$ (determined from vector additions of atomic spins), has components along the internuclear axis of magnitude $M_S\hbar$. M_S can take on all values from S to -S. Σ (not to be confused with the molecular state with $\Lambda = 0$) is defined as being equal to M_S:

$$\Sigma = -S, -S+1, \ldots, S-1, S \qquad (6.1\text{-}2)$$

The total electronic angular momentum about the internuclear axis is then given by the addition of $\underline{\Lambda}$ and $\underline{\Sigma}$:

$$\underline{\Omega} = |\underline{\Lambda} + \underline{\Sigma}| \qquad (6.1\text{-}3)$$

The molecular state is labelled with the Greek letter corresponding to the Λ value; a preceding superscript corresponding to the value of the multiplicity, 2S+1, and a following subscript corresponding to the value of Ω.

If the coupling $\underline{L}$ and $\underline{S}$ is strong, Λ and Σ will no longer be good quantum numbers. Instead, L and S will couple to form a vector, $\underline{J}_x$, which will precess about the internuclear axis. The projection of $\underline{J}_x$ on to the axis will give $\underline{\Omega}$ directly. In this case, Hund's case

(c), the molecular state is identified only by the numerical value of $\underline{\Omega}$.

The symmetry properties of the electronic wave functions are also important. States are labelled "u" ("ungerade", odd) or "g" ("gerade", even) depending upon whether or not the wave function changes sign upon inversion. Σ states and states with $\Omega = 0$, $\Lambda \neq 0$ are further labelled "-" or "+" depending upon whether or not the wave function changes sign upon reflection through a plane containing the internuclear axis.

6.2 Building-up Principles

As pointed out earlier, the molecular states of iodine may also be determined from the group-theoretical "building-up principles" outlined by Herzberg [100]. The atoms forming the diatomic molecule are brought together to form the molecular states predicted by the direct product of the orbital angular momenta (case (a)) or the total electronic angular momenta (case (c)) of the atoms. The results for a number of different point groups have been determined and tabulated [100,101]. The valence states of iodine, for example, formed from the union of neutral iodine atoms, can be determined, for case (a) coupling, from the direct products $\pi \otimes \pi$, $\pi \otimes \Sigma$, and $\Sigma \otimes \Sigma$ in the $D_{\infty h}$ point group. The spin functions for various multiplicities have also been determined for many different point groups. Multiplying the state label by the appropriate spin functions produces values for the total angular momentum, the values of which appear as subscripts on the molecular state labels. In this manner, all of the state labels listed by Mulliken [29] can be derived. As

well, the appearance of both + and - labelling on the same state, for example $^3\Sigma^-_{g(0^+)}$, can now be explained. The Σ^-_g state, when multiplied by the triplet spin functions, Σ^-_g and π_g, produces the results Σ^+_g and π_g. The complete molecular state labels are then $^3\Sigma^-_{g(0^+)}$ and $^3\Sigma^-_{1g}$. The valence states of iodine are listed in table (6-1).

For case (c) coupling, the spin and orbital angular momentum must first be multiplied together. In iodine, recourse to the "double groups" including half-integer entries becomes necessary. The direct product for the $^2P_{3/2} + {}^2P_{3/2}$ states yields the same ten values predicted by the case (c) vector coupling of $J_1 = J_2 = \frac{3}{2}$. Table (6-1) lists the case (c) molecular states for the valence states of iodine.

The molecular states of iodine may also be determined from the molecular orbitals. The iodine molecule has ten 5p electrons occupying four molecular orbitals (σ_g, π_u, π_g, σ_u) in various configurations in the valence shell states. Mulliken differentiates the various electron configurations by using the number of electrons in each MO, in order, as a shorthand notation [29]. For example, the ground state of iodine has the configuration ... $\sigma_g^2\,\pi_u^4\,\pi_g^4\,\sigma_u^0$, or 2440 in Mulliken's notation.

The molecular states belonging to each configuration can be determined from the direct products of the unfilled molecular orbitals. The states corresponding to the 2431 configuration, for example, can be determined from the product $\pi_g \otimes \sigma_u$. A few examples of molecular states of iodine arising from various electron configurations are listed in table (6-2).

Table (6-1). Molecular states of iodine for case (a) and case (c) coupling.

case (a)			case (c)		
Orbital function	Spin function	Molecular state	Double group entry	Double group entry	Molecular state
$^3\Delta_u$	π_g	$^3\Delta_{3u}$	$E_{3/2} + E_{1/2}$	$E_{3/2} + E_{1/2}$	3_u
		$^3\Delta_{1u}$			2_u
	Σ_g^-	$^3\Delta_{2u}$			1_u
$^1\Sigma_u^-$	Σ_g^+	$^1\Sigma_u^-(0^-)$			0_u^-
$^1\Delta_g$		$^1\Delta_{2g}$			2_g
$^3\Sigma_g^-$	π_g	$^3\Sigma_g^-(1)$			1_g
	Σ_g^-	$^3\Sigma_g^-(0^+)$			0_g^+
$^3\Sigma_u^+$	π_g	$^3\Sigma_u^-(1)$			1_u
	Σ_g^-	$^3\Sigma_u^+(0^-)$			0_u^-
$^1\Sigma_g^+$	Σ_g^+	$^1\Sigma_g^+(0^+)$			0_g^+
$^3\pi_g$	π_g	$^3\pi_{2g}$	$E_{3/2} + E_{1/2}$	$E_{1/2}$	2_g
		$^3\pi_{0_g^+}$			1_g
		$^3\pi_{0_g^-}$			0_g^+
	Σ_g^-	$^3\pi_{1g}$			0_g^-

(continued)

Table (6-1). (Continued)

case (a)			case (c)		
Orbital function	Spin function	Molecular state	Double group entry	Double group entry	Molecular state
$^3\pi_u$	π_g	$^3\pi_{2u}$			^2_u
		$^3\pi 0_u^+$			^1_u
		$^3\pi 0_u^-$			0_u^+
	Σ_g^-	$^3\pi_{1u}$			0_u^-
$^1\pi_g$	Σ_g^+	$^1\pi_{1g}$			^1_g
		$^1\pi_{1u}$			^1_u
$^3\Sigma_u^+$	π_g	$^3\Sigma_u^+(1)$	$E_{1/2}$	$E_{1/2}$	^1_u
	Σ_g^-	$^3\Sigma_u^+(0_\odot^-)$			0_u^-
$^1\Sigma_g^+$	Σ_g^+	$^1\Sigma_g^+(0^+)$			0_g^+

Table (6-2). Molecular states from direct products of molecular orbitals.

Electron configuration	Direct product	Molecular states
1441	$\sigma_g \otimes \sigma_u$	$^1\Sigma_u^+$, $^3\Sigma_{1u}^+$, $^3\Sigma_{0u}^+$
2422	$\pi_g \otimes \pi_g$	$^1\Sigma_g^+$, $^1\Delta_g$, $^3\Sigma_{1g}^-$, $^3\Sigma_{0g}^-$
2341	$\pi_u \otimes \sigma_u$	$^1\pi_g$, $^3\pi_{2g}$, $^3\pi_{1g}$, $^3\pi_{0_g^+}$, $^3\pi_{0_g^-}$
2431	$\pi_g \otimes \sigma_u$	$^1\pi_u$, $^3\pi_{2u}$, $^3\pi_{1u}$, $^3\pi_{0_u^+}$, $^3\pi_{0_u^-}$

Both case (a) and case (c) labels are determined for iodine, since the molecule has intermediate coupling. Case (c) coupling predominates in heavy molecules and at large internuclear distances, but labels derived from either coupling case are found in the literature. Many authors retain both labels, so the B state of iodine, for example, is often written as $^3\pi_{0_u^+}$ or $0_u^+(^3\pi)$.

Some confusion results from the intermediate nature of the coupling in iodine, especially in that different sets of selection rules should be observed in the two different domains. The absolute assignments of the higher lying excited states and the ability to explain transition intensities are compromised somewhat by the ambiguity associated with the choice of coupling case. If case (c) labels are used exclusively, for example, the electric dipole selection rules in iodine are [102]:

$$\pm \not\longleftrightarrow \pm \qquad \mp \not\longleftrightarrow \pm \qquad (6.2\text{-}1)$$

$$g(u) \not\longleftrightarrow g(u) \qquad u(g) \longleftrightarrow g(u) \qquad (6.2\text{-}2)$$

$$\Delta\Omega = 0, \pm 1 \qquad (6.2\text{-}3)$$

$$\Delta J = 0, \pm 1 \qquad (6.2\text{-}4)$$

where $\Delta J = 0$ is forbidden for any $\Omega = 0 \longleftrightarrow \Omega = 0$ transition. In this regime, the E ← B ← X system of iodine to be presented later is simply $0_g^+ \leftarrow 0_u^+ \leftarrow 0_g^+$. With case (a) coupling, on the other hand, spin-forbidden transitions are assigned to this system, so the observed intensities must be postulated to arise from the presence of admixtures of different multiplicities in the states [29,103].

6.3 Molecular States of Iodine

The valence-shell states of iodine correlate upon dissociation either with neutral iodine atoms (valence states) or with iodine ions (ion-pair states). The states arising from the different electron configurations can be deduced group-theoretically, and the atoms and ions of the dissociation products are well-known; the difficulty lies in determining the exact positions of the potential curves and correctly assigning them to both the corresponding electronic states and dissociation products. The situation is further cloudied by the large number of states predicted to exist and the facility with which these states are expected to interact and perturb one another.

Of the states correlated with neutral atoms upon dissociation, the best-known are the 2440 X 0_g^+ ($^1\Sigma^+$) and 2431 B 0_u^+($^3\pi$) states. The X state is characterized by a large vibrational frequency ($\omega_e \sim 214.5$ cm^{-1} [104-106]) and a small equilibrium bond distance ($r_e = 2.6663$Å [105]), as would be expected for the ground state of the molecule. It is correlated with two ground state iodine atoms ($^2P_{3/2}$) with a resulting dissociation energy of 12547.4 cm^{-1} [105]. The B state has a somewhat larger internuclear separation ($r_e = 3.0248$ Å [105]) and smaller vibrational frequency ($\omega_e = 126.1650$ cm^{-1} [106]). It is correlated, not with the ground state atoms, but with one ground state and one excited state atom, $^2P_{1/2}$. The potential curve is rather shallow, extending from a minimum at $T_e = 15769.0$ cm^{-1} [76,105] to an asymptote at $D_e = 20150.47$ cm^{-1} [105], relative to the X state minimum.

The intensity of the B-X system, formally spin-forbidden by case (a) selection rules, has been attributed by Mulliken [29] to

case (c) configuration interactions. The X state acquires some triplet character from interaction with the 2431 $0_g^+(^3\pi)$ state. In the B state region, the 1342 $0_u^+(^3\pi)$ state interacts with both the 1441 $0_u^+(^1\Sigma^+)$ and the 2431 $0_u^+(^3\pi)$ states; this introduces some singlet character from the $^1\Sigma^+$ state into the B $0_u^+(^3\pi)$ state. Das and Wahl [103], using multiconfiguration self-consistent field (MCSCF) techniques, put forth similar interactions in the B-X system, with the admixture coefficients for the states involved varying with internuclear separation.

Of the other states predicted to dissociate to atomic iodine, both the A 1_u and A' 2_u states are fairly well-established. The A state has been observed in absorption [107] and emission [108,109] and has been assigned to be 2431 $1_u(^3\pi)$ correlating with ground state atoms. The A' state has shown up prominently as the terminus for the D' → A' emission in iodine pressured with a foreign gas. The assignment of this state is still a bit uncertain; early treatments [109] favoured an assignment of 2431 $2_u(^3\pi)$, but more recent studies [110,111] indicate that the state may, in fact, be 2332 $2_u(^3\Delta)$ correlating with an excited iodine atom.

Two further states of 0_g^+ and 1_g symmetry have recently been observed in emission from the B state [112]. These states, labelled a' and a, respectively, are also seen to perturb the X state in the region of high vibrational levels. The a' 0_g^+ and a 1_g states are very weakly bound, have large internuclear separation, and correlate, with the X state, to two ground state iodine atoms.

The ion-pair states of iodine, states formally correlated with dissociation to iodine ions, begin in the 40,000 cm^{-1} region, well

above the dissociation limits of the valence states.

The D $0_u^+(^1\Sigma^+)$ state of iodine has been observed in absorption from, and emission to, the ground state. Recalling the Mulliken notation, the 1441 ← 2440 transition in iodine is analogous to the $H^+H^- \leftarrow H_2$ transition in which an electron is excited from a σ bonding molecular orbital to a σ anti-bonding orbital [113]. The transition is predicted to be strong [113,114]. Other ion-pair states are similarly expected to have strong charge-transfer spectra with transitions to low-lying valence states.

The other known ion-pair states of iodine in the 5-6 eV energy region are similar to the D state in having large internuclear separations, relatively low vibrational frequencies ($\omega_e \approx 100$ cm^{-1}), and very high dissociation energies (the separated ions are on the order of at least 9 eV above X). The F → X, D' → A', and E → B series have all been observed [36,109] in emission from iodine pressured with a foreign gas. Guy et al. [111], in fact, claim to have observed emission from 12-14 of the 18 ion-pair states predicted to arise from correlations to $I^-(^1S) + I^+(^3P,^1D)$. Unfortunately, the assignment of these higher-lying states remains controversial. Mulliken [29], for example, assigned the D state to 1441 $0_u^+(^1\Sigma^+)$ and the E state to possibly 2242 $0_g^+(^1\Sigma^+)$ or probably 1432 $0_g^+(^3\pi)$, all dissociating to $I^+(^3P_0)$. Das and Wahl [103] agree with the $^3P_0$ assignment, but determine the E state to be largely $^1\Sigma_g^+$ in character. Guy et al. [111], in contrast, favour the association of the D, D', and E states all with $I^-(^1S) + I^+(^3P_2)$.

Table (6-3) lists the known valence-shell states of iodine along with a few molecular constants and references to their recent determinations.

Table (6-3). Molecular states of iodine.

State	T_e/cm^{-1}	$r_e/Å$	ω_e/cm^{-1}	Dissociation Products (b)	Reference
X $0_g^+(^1\Sigma^+)$	0	2.6663	214.5016(140)	$^2P_{3/2}+^2P_{3/2}$	105
			214.5186		76
A' 2_u	~10200		106.29(54)	$^2P_{3/2}+^2P_{3/2}$	109
A $1_u(^3\pi)$	10907	3.06	95	$^2P_{3/2}+^2P_{3/2}$	108
	10846.35(a)				107
a 1_g	12141.1775(39)	4.311	23.6233(55)	$^2P_{3/2}+^2P_{3/2}$	112
a' 0_g^+	12303.4023(11)	4.641	17.6868(19)	$^2P_{3/2}+^2P_{3/2}$	112
B $0_u^+(^3\pi)$	15769.01	3.0248		$^2P_{3/2}+^2P_{1/2}$	105
	15769.0485		125.6724		76
D' 2_g	~40540		103.97(5)	$^1S + ^3P_2$	109,111
β 1_g	41029.74(56)	3.669(82)	104.19(14)	$^1S + ^3P_2$	40
	41031.82(13)		103.807(13)		32
D $0_u^+(^1\Sigma^+)$	~41200			$^1S + ^3P_2$	111
E 0_g^+	41411.8	~3.7	101.59	$^1S + ^3P_2$	36
	41410.27(15)	3.6342(18)	101.907(41)		40
f 0_g^+	47027.63(18)	3.576	103.904(18)	$^1S + ^3P_{1,0}$	33
	47032(6)		98(2)		34
	47024.6(25)		104.2(10)		35
F 0_u^+	47217.8	~3.6	95.955	$^1S + ^3P_{1,0}$	36
1_g	47559.1	3.53	106.60	$^1S + ^3P_{1,0}$	108
0_u^+	51720			$^1S + ^1D$	111

(a) T_0 value.

(b) Dissociation products for ion-pair states remain uncertain.

It should be pointed out that the assignment of dissociation energies and dissociation products is a formal exercise for the ion-pair states. The lowest energy ion pairings ($I^-('S) + I^+(^3P_2)$) lie 8.93 eV above the X state potential minimum. There are two Rydberg states ($5p^5$, $^2P_{3/2}$ + $5p^4 6s$, $^4P_{5/2}$; $5p^5$, $^2P_{3/2}$ + $5p^4 6s$, $^2P_{3/2}$) lying below this in energy (8.32 eV; 8.50 eV). The adiabatic correlation would have ion-pair states "short-cutting" at large internuclear distances to the Rydberg state dissociation products [29]. Recently, de Vries et al [115] suggested that the Rydberg states might predissociate through a repulsive state and correlate finally with the atomic products at 3.43 eV and 2.49 eV. Table (6-4) gives a partial list of dissociation products along with their energy above the ground state minimum.

Table (6-4). Dissociation products and dissociation energies of iodine [105,116,117].

Configuration	Dissociation products		Energy[(a)]
$5p^5$	$^2P_{3/2}$	I	1.54 eV
$5p^5$	$^2P_{3/2}$	I	
$5p^5$	$^2P_{3/2}$	I	2.49 eV
$5p^5$	$^2P_{1/2}$	I	
$5p^5$	$^2P_{1/2}$	I	3.43 eV
$5p^5$	$^2P_{1/2}$	I	
$5p^5$	$^2P_{3/2}$	I	8.22 eV
$5p^4 6s$	$^4P_{5/2}$	I*	
$5p^5$	$^2P_{3/2}$	I	8.50 eV
$5p^4 6s$	$^2P_{3/2}$	I*	
$5p^6$	^1S	I^-	8.93 eV
$5p^4$	$^3P_0$	I^+	
$5p^6$	^1S	I^-	9.73 eV
$5p^4$	$^3P_2$	I^+	
$5p^6$	^1S	I^-	9.81 eV
$5p^4$	$^3P_1$	I^+	
$5p^6$	^1S	I^-	10.64 eV
$5p^4$	$^1D_2$	I^+	

(a) Relative to the ground-state minimum potential.

CHAPTER 7

POLARIZATION SPECTROSCOPY OF THE E STATE OF IODINE

The iodine molecule is well-known to possess a strong absorption spectrum at visible wavelengths. The B ← X system has been extensively studied, so much so that detailed atlases of the spectral lines are available [118,119]. The strong absorption and wealth of available information make the molecule a popular choice for initial studies with any new laser technique using visible radiation. Indeed, the initial polarization labelling experiments performed in this laboratory were done with iodine vapour [28].

While the B state of iodine has been well-characterized almost to its dissociation limit [76,105,120,121], much less is known about higher-lying states. According to Mulliken [29], several states are predicted to exist in the 5 eV region. The E-B system has been studied in the 400-440 nm. emission spectrum of iodine in an inert gas [36], and as the second leg in resonant two-photon excitation spectra [37-40,122]. The analyses of these results produce vibrational constants for the E state which are in reasonably good agreement. The rotational constants, on the other hand, are either not determined or are determined with significant uncertainty and disagreement between studies.

With this in mind, polarization labelling spectroscopy was used in an optical-optical double resonance (OODR) experiment, E ← B ← X, to obtain high resolution spectra for the E state. Analysis of the results yields improved determinations for the vibrational and rotational constants of the E state of iodine. Two-step polarization

labelling has been used previously [25,123] in the study of the excited states of the sodium dimer.

7.1 Polarization Labelling

The schematic energy level diagram in figure (7-1) illustrates the typical pump and probe combination used in the experiment. A circularly polarized pump laser pulse excites iodine from its ground state to the B state. The linearly polarized probe laser pulse then excites molecules from the labelled level in the B state to the higher-lying E state.

The use of circular polarization was based on the assumption that only P- and R- branch transitions are involved in both pump and probe stages. Q-branch transitions are enhanced if the pump laser is polarized at 45° to the plane of the polarization of the probe laser. Experiments done with a 45° arrangement showed the expected decrease in intensity of P- and R-branch transitions, but no evidence of any Q-branch lines. This absence of Q-branch transitions would confirm the assignment of the E ← B transition as $0_g^+ \leftarrow 0_u^+$.

The serendipitous energy level separations in the iodine molecule make the identification of the two resonant transitions unambiguous. That is, the green dyes used to excite iodine to the B state are too low in frequency to bring about the second transition, E ← B. Conversely, the dyes used in the probe laser are too high in frequency to initiate any interfering B-X transitions; ground state labelled transitions would be well into the B state continuum above the dissociation limit, while upper state labelled transitions could

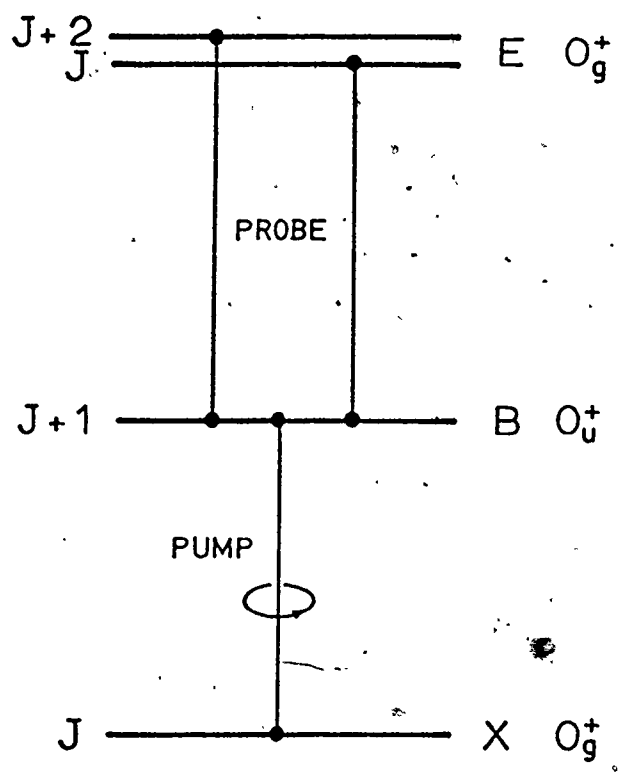

Figure (7-1). Schematic energy level diagram showing the pump-probe sequence used in the two-step polarization labelling experiment in iodine. The circularly polarized pump beam excites a B $O_u^+ \leftarrow$ X O_g^+ transition (an R-branch transition is shown), and the linearly polarized broadband laser probes the E $O_g^+ \leftarrow$ B O_u^+ system.

not be resonant with any ground state levels.

Plates (7-1) and (7-2) show one of the first E ← B ← X spectra recorded in this study. Typically, the pump laser overlapped more than one transition, but this was generally easy to disentangle. Plate (7-2) shows more clearly the vibrational progressions in the E state resulting from the two labelled B ← X transitions, R75 26-0 (18327.02 cm^{-1}) and P76 29-1 (18326.87 cm^{-1}) (A third series arising from the V = 26, J = 93 level of the B state, excited by a weak, extra laser mode off the main line, was also assigned, but has not been explicitly labelled on these plates.)

The use of Coumarin 500 in the pump laser made it possible to excite iodine close to the B state dissociation limit. Unfortunately, at the very high frequency end, the dye laser gain profile begins to drop off so that v_B = 66 was the highest vibrational level for which signals were observed. A portion of a spectrum taken with C500 in the pump laser is shown in plate (7-3).

The pump laser, as has already been intimated, produced a weak "ghost" mode very far from the principal laser line. These extra lines, thought to originate from a stray reflection from one face of the etalon, were extremely weak, but were often sufficiently strong to pump B ← X transitions in iodine. Once this problem was recognized, it was a relatively simple matter to assign the additional E ← B lines so produced. However, as the B state dissociation limit was approached, the C500 dye was operating in a very unfavourable region of its gain profile. A significant amount of "off-resonant" superradiant pumping occurred, especially in the region of the peak in the dye laser gain profile. This resulted in a complicated mix of

Plate (7-1). A typical polarization labelling spectrum of the $E \leftarrow B \leftarrow X$ system of iodine. The vibrational progressions in the E state corresponding to two different pumped transitions are indicated.

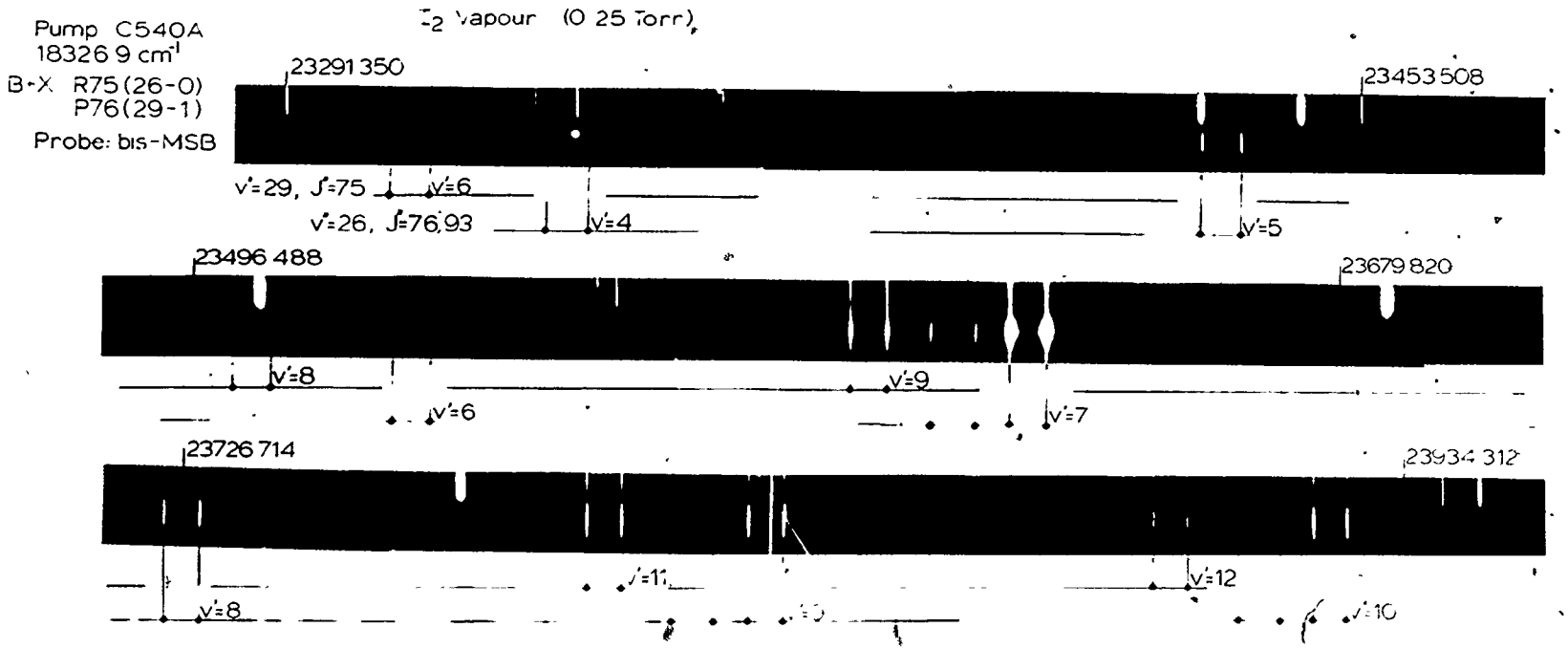
Pump C540A
18326 9 cm⁻¹
B-X R75(26-0)
P76(29-1)
Probe: bis-MSB
I2 Vapour (0 25 Torr)
23291 350
23453 508
v'=29, J'=75
v'=6
v'=26, J'=76,93
v'=4
v'=5
23496 488
23679 820
v'=8
v'=9
v'=6
v'=7
23726 714
23934 312
v'=11
v'=12
v'=8
v'=10

Plate (7-2). The spectrum of plate (7-1) decomposed to illustrate more clearly the vibrational progressions in v_E for the two pumped transitions. The single line marked with an asterisk denotes the pump laser line recorded in another order of the spectrometer.

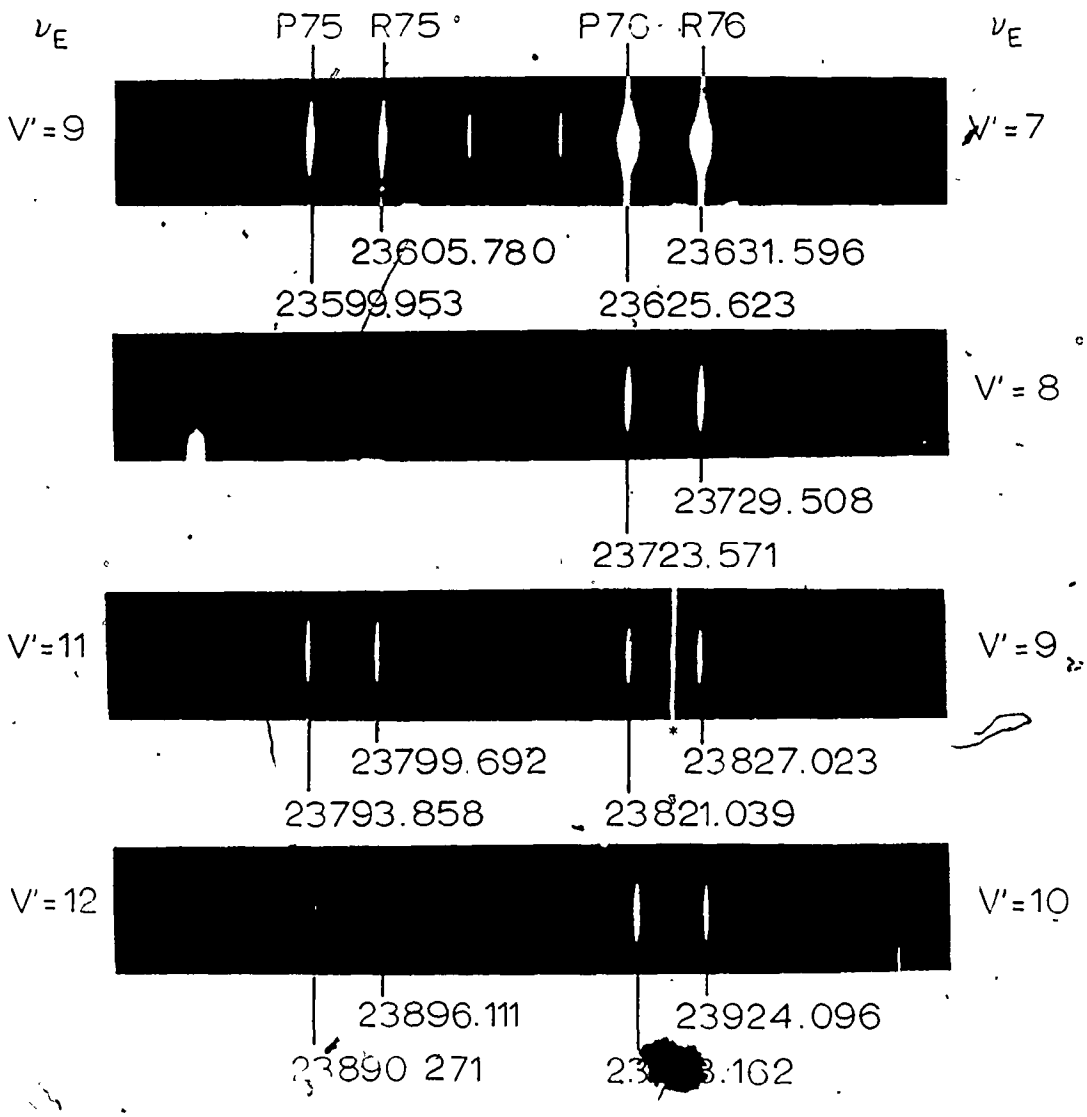
ν_E
P75
R75
P76
ν_E
V'=9
V'=7
23605.780
23631.596
23599.953
23625.623
V'=8
23729.508
23723.571
V'=11
V'=9
23799.692
23827.023
23793.858
23821.039
V'=12
V'=10
23896.111
23924.096
23890 271

Plate (7-3). Vibrational progressions in the E state for the two pumped B ← X transition, P28 (59-0) and R29 (59-0). The pump laser (C500), tuned to 19878.4 cm^{-1}, is again recorded in another order of the spectrometer and is denoted by an asterisk. C440 is the probe laser dye.

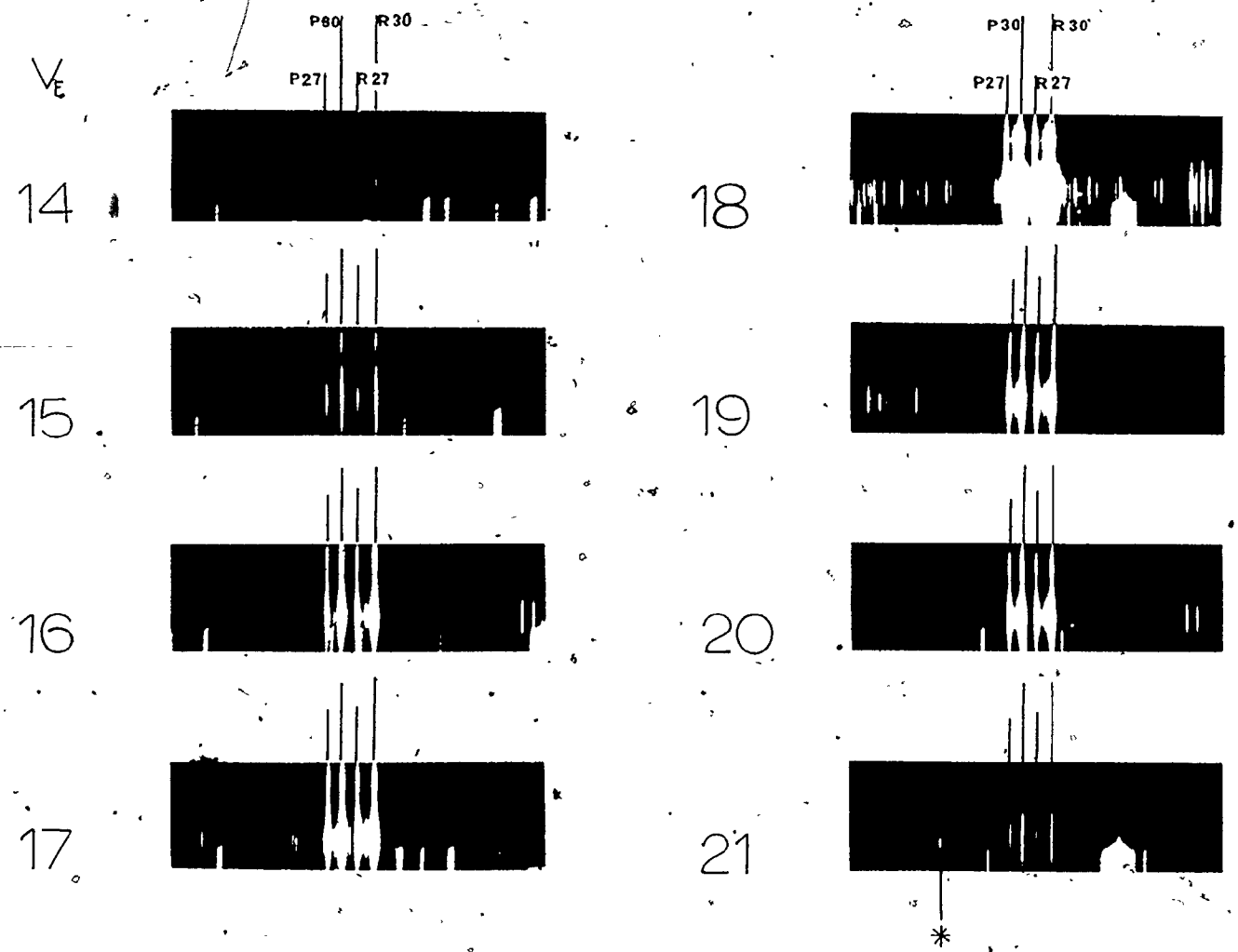
P80
R30
P27
R27
V_ξ
14
15
16
17
P30
R30'
P27
R27
18
19
20
21

the expected E ← B signals and, in contrast to the "ghost" mode situation, numerous weaker lines associated with the extra pumped transitions (see plate (7-3)). When the number of these lines became excessive, their assignment became increasingly more difficult. In effect, the Molectron laser was acting almost like a broadband source, exciting literally hundreds of transitions in the B ← X system. Plate (7-4) shows an assigned portion of a spectrum along with the corresponding microdensitometer trace that was used to help elucidate the assignment.

7.2 Results and Discussion

The initial assignments of the pumped and probed transitions were done using the B-X atlas of Simmons and Hougen [118] and the E state constants of Williamson [38]. The measurements and assignments were run through a linear least-squares computer program to get the best fit to the standard equation

$$T = T_e + \omega_e(v+\tfrac{1}{2}) - \omega_e x_e(v+\tfrac{1}{2})^2 + \omega_e y_e(v+\tfrac{1}{2})^3 + \ldots$$

$$+ \{B_e - \alpha_e(v+\tfrac{1}{2}) + \gamma_e(v+\tfrac{1}{2})^2 + \ldots\}\, J(J+1)$$

$$- \{D_e - \beta_e(v+\tfrac{1}{2}) + \ldots\}\, J^2(J+1)^2 \qquad (7.2\text{-}1)$$

where the electronic term value (T_e), the vibrational constants ($\omega_e, \omega_e x_e, \omega_e y_e, \ldots$), and the rotational constants ($B_e, \alpha_e, \gamma_e, D_e, \beta_e \ldots$) were allowed to vary. Later assignments were made based on the latest E state constants determined by (7.2-1) and the B-X data of references

Plate (7-4). A small portion of a polarization labelling spectrum excited by a "broadband" pump laser. The microdensitometer trace of the spectrum was used to help assign the lines in the spectrum. In this example, the transitions shown are $v_E = 14 \leftarrow v_B = 48$.

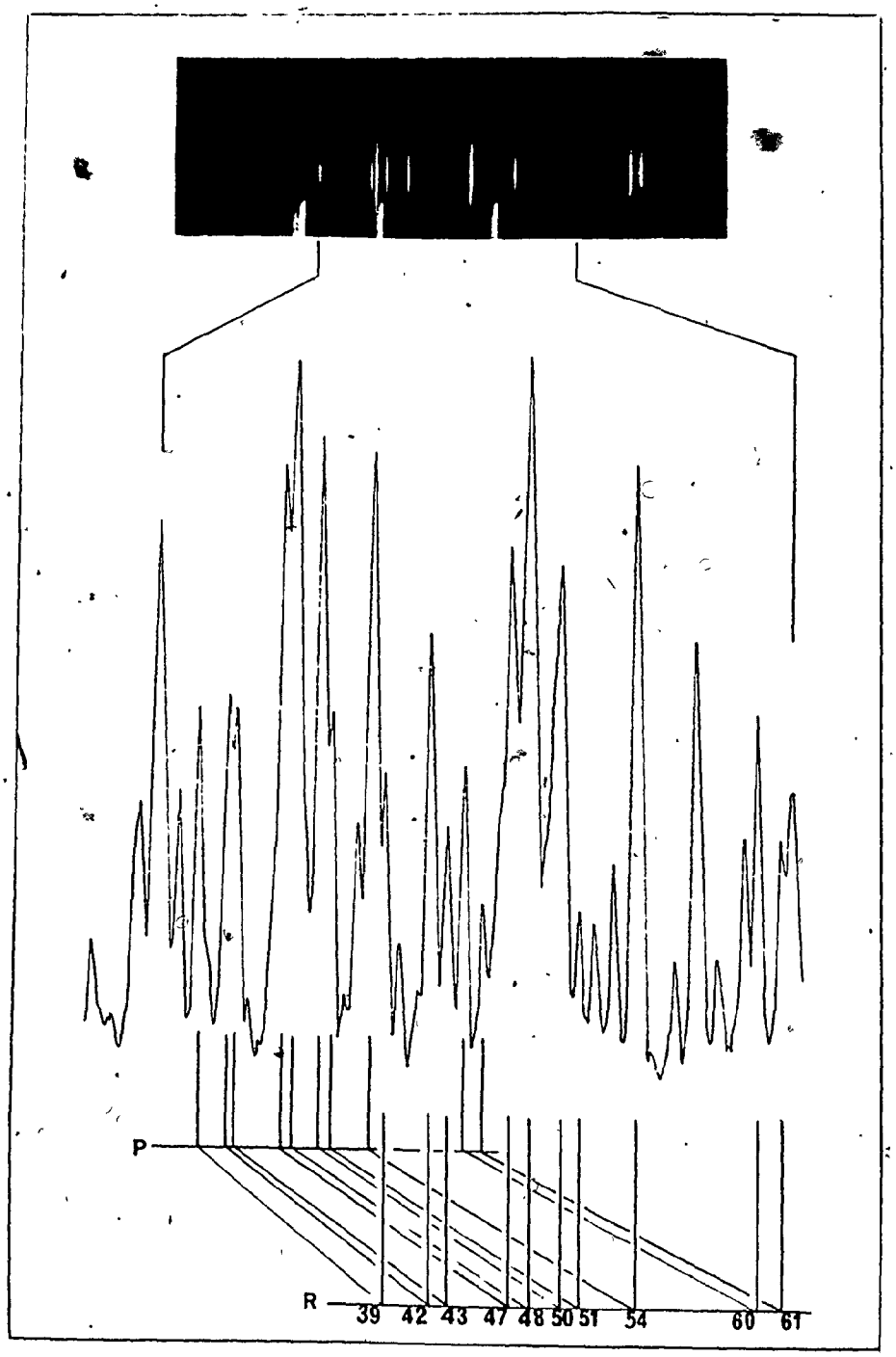
P
R
39 42 43 47 48 50 51 54 60 61

76 and 105.

Figure (7-2) illustrates the various v_E and v_B combinations used in these experiments. The observed transitions will be dependent, in part, on the choice of dyes used in the lasers, but, overall, the transitions shown in figure (7-2) agree with those predicted by Franck-Condon calculations on the E ← B system.

Figure (7-3) shows the various J values observed for the E state vibrational levels in these experiments. While a reasonable range of rotational levels has been observed, J values of 60-80 tend to predominate. As figure (7-3) illustrates, a number of rotational values are underrepresented. However, the vibrational-rotational distribution considered here is, it is safe to say, more comprehensive than any other previous study.

Table (7-1) lists the E state constants determined by other authors [36,38-40] along with the results of the present set of experiments. The point that bears reiteration in examining the other authors' results in table (7-1) is that the vibrational constants are in qualitative agreement but the rotational constants are either not determined or determined with significant disagreement.

The early work of Wieland et al. [36] was a vibrational study only of the E → B emission spectrum of iodine pressured with a foreign gas. Williamson [38] used two-photon spectroscopy to study a relatively small range of v_B (11-17) and v_E (0-11) values and included very few different J values in his rotational analysis. Cunha et al. [39] performed a similar experiment, studying an even smaller range of v_B (25-28) values in only three different B ← X transitions. In neither of the two-photon studies was the E-B probe laser wavelength determined to better than ± 0.5 cm^{-1}.

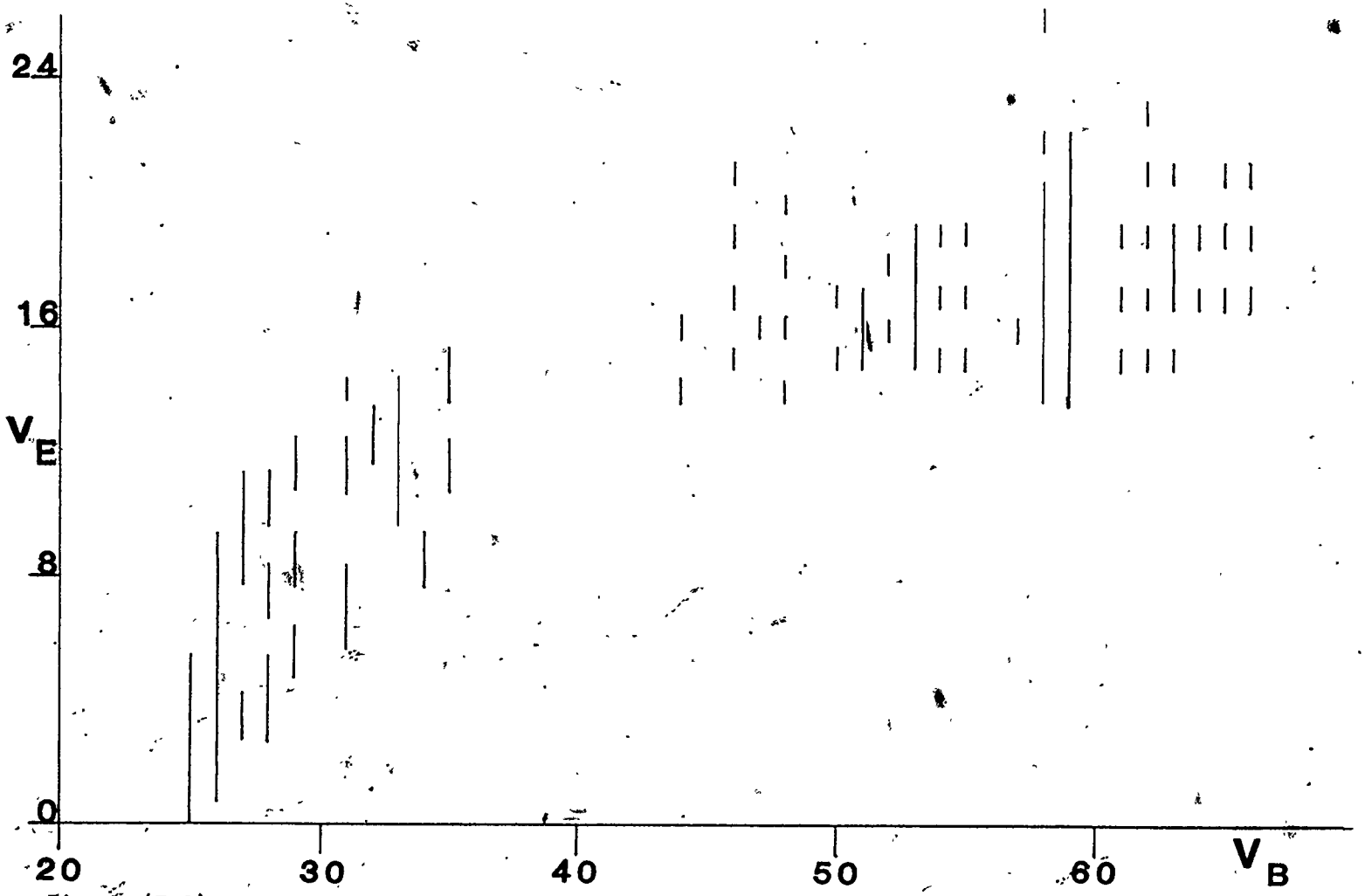

Figure (7-2). A plot of v_E vs. v_B showing the various combinations used in this study.

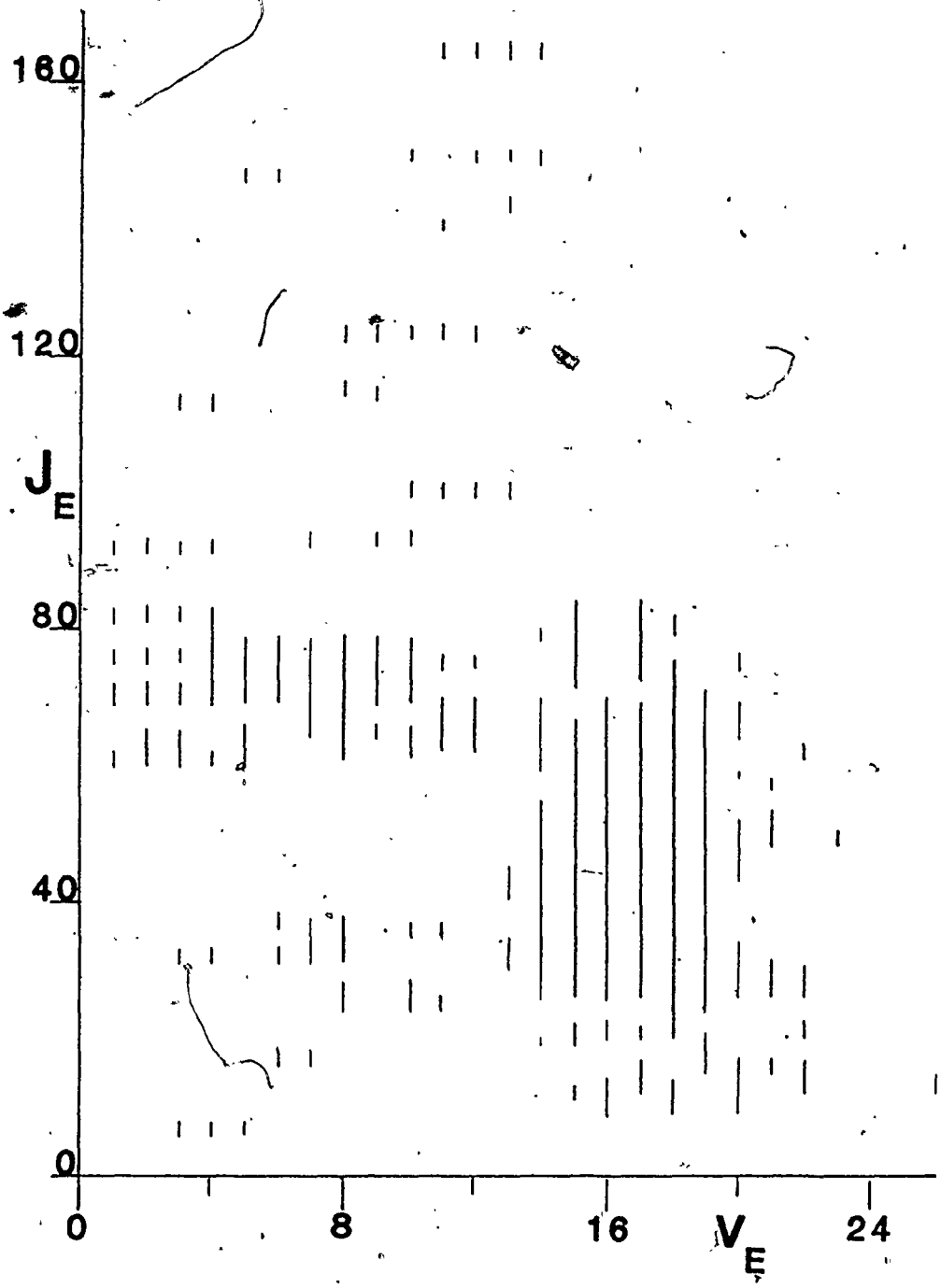

Figure (7-3). A plot of J_E vs. v_E illustrating the range of J-values covered in this study.

Table (7-1). Molecular constants/cm^{-1} for the E state of the iodine molecule.

Parameter	Wieland et al. [36]	Williamson [38]	Cunha et al. [39]	King et al. [40]	Present Work[a]
T_e	41411.8	41411.43	41412.1	41410.27 (15)	41411.779 (22)
ω_e	101.59	101.59	101.56	101.907 (41)	101.3761 (55)
$\omega_e x_e$	0.2380	0.205	0.19	0.2373 (32)	0.20088 (40)
$10^3 \omega_e y_e$				0.905 (70)	0.2347 (90)
$10^3 B_e$		20.255	20.52	20.116 (20)	19.9699 (31)
$10^5 \alpha_e$		8.34	16.0	8.76 (44)	5.503 (59)
$10^7 \gamma_e$				18.6 (23)	0.51 (25)
$10^9 D_e$				(b)	3.037 (47)
r_e(Å)	3.65 (2)[c]		3.6	3.6342 (18)	3.64736 (37)

(a) Value in parentheses is 1σ (Statistical error only)
(b) Calculated value used
(c) From Tellinghuisen, reference 124.

The detailed rotational analysis of King et al. [40] was the continuation of earlier two-photon studies of iodine done in the same laboratory [37]. Over 850 lines covering a wide range of v_B (21-78), v_E (0-29), and J (0-158) values were measured and assigned. The confessed preponderance of low J values in these experiments means, however, that the rotational constants reported are still open to question. Indeed, the rotational distribution was such that the centrifugal distortion constant was not determined by the data. As in the experiments of Williamson and Cunha and co-workers, the iodine emission was monitored as a function of the probe laser frequency. Again, the line positions could only be determined to $\pm$ 0.5 cm^{-1} [40].

The present set of E state constants were determined with over 1000 weighted values fit simultaneously to (7.2-1). With the spectra recorded on film and measured on a comparator, line positions could easily be determined to $\pm$ 0.02 cm^{-1}. The 1σ values quoted in table (7-1) should be regarded with some caution, however, since, as stated earlier, the J distribution was not ideal.

The E state constants determined here can be extrapolated to examine the results of Rousseau and Williams [122]. These authors, using a fixed frequency krypton-ion laser for the E $\leftarrow$ B transition, pumped iodine molecules into the v $\approx$ 50 region of the E state. The strongest transitions they observed have now been assigned as P38 $v_E - v_B$ = 45-11, P15 51-16, and P87 53-17 using the constants produced by this study. Tellinghuisen [124] had earlier proposed a v_E = 52 assignment for the P15 transition, based on the E state constants of [36], combined with an analysis of the Franck-Condon

profile of the bound and continuum fluorescence from the final state. Tellinghuisen's simulation of the dispersed emission spectrum shown in [122] has been re-evaluated using the RKR potential curve derived from the present set of E state constants. The B state potential curve giving the best fit for the emission spectrum is in striking agreement with Tellinghuisen's early calculations. Rousseau and Williams's term values agree with those predicted from the present set of E state constants to within 4 cm^{-1} and indicate that the E state is extremely regular even as one goes higher in energy. A rough estimate for $\omega_e z_e$ of 5 x 10^{-7} cm^{-1} is predicted.

Further experiments on the higher vibrational levels confirm the regularity of the E state and the validity of the molecular constants determined here [125]. Transitions in the range v_E = 45-100 have been observed and their assignment requires ~~little~~ modification of the E state constants reported in the present study.

The molecular constants determined by the present experiments are consistent with the assignment of the E state as an ion-pair state of iodine. The internuclear separation is quite large, the vibrational frequency is relatively low (for comparison, ω_e for the ground state is 214.5016 cm^{-1} [105]), and the dissociation energy is high.

One of the main problems among investigators in this area is their failure to come to agreement on the assignment of the E state. Mulliken's oft-quoted examination of the molecular states of iodine [29] provides two possible assignments. If the E state is 2242 $0_g^+(^1\Sigma^+)$, then the E-B system is argued to derive intensity from case (c) mixing of 1432 $0_g^+(^3\pi)$ into the 2242 0_g^+ state to produce some triplet character in the E state. On the other hand, the E state may be

assigned as 1432 $0_g^+(^3\pi)$, in which case no admixture needs to be assumed to account for the then-allowed $^3\pi_g - {}^3\pi_u$ transitions. Mulliken favours an admixture that varies with internuclear separation, with 2242 predominating at small r values, and 1432 predominating at large separations. The E state has been assigned to correlate with $I^-(^1S) + I^+(^3P_0)$ ions upon dissociation. Wieland et al. [36], and subsequent authors [38,39], have adopted the $0_g^+(^3\pi)$ assignment. Das and Wahl [103], while agreeing with Mulliken's choice of dissociation products, claim that the E state admixture is predominantly $^1\Sigma_g^+$. The intensity of the E-B transitions is then proposed to be generated as a result of singlet character mixed into the B state.

The present set of experiments can only establish the fact that the E ← B transition in iodine is a case (c) allowed $0_g^+ \leftarrow 0_u^+$ transition. The $^1\Sigma$ or $^3\pi$ case (a) designations cannot be confirmed, especially if complicated admixtures in both B and E states are allowed. Again, the case (a) - case (c) ambiguity serves only to confuse the situation.

The question of the dissociation of the E state remains a matter for discussion. If the dissociation of the state to the $I^+(^3P_0)$ ion mentioned above is accepted, then another 0_g^+ state of lower energy, correlating with the $^3P_2$ ion, should be predicted to exist. Though no indication of such a state has been found in any polarization labelling experiments of iodine, Tai et al. [126] report the observation of a 0_g^+ state with $T_e \sim 36{,}000\ cm^{-1}$ as an intermediate level in a multi-photon experiment. Transitions to this state should be allowed in the two-step polarization labelling experiments described here with, for example, Coumarin 540 A in both pump and probe lasers (see plate (5-1)). A possible explanation for the failure

of these lines to appear in earlier iodine work is that the signals would be too weak to be recorded by the technique used here. The other possibility is that the assumption that only resonant transitions are involved in the multi-photon process may be incorrect, and the results of Tai et al. require re-interpretation.

Guy et al. [111] dispute the existence of ion-pair states below the $D'2_g$ state. When iodine is pressured with an inert gas, the emission spectrum undergoes a profound change. The strong $D \rightarrow X$ emission signals decrease, while other bands, most notably the $F \rightarrow X$, $E \rightarrow B$, and $D' \rightarrow A'$ systems, come up in intensity [36]. This has been interpreted to mean that while the original excitation is into the D state, the addition of a foreign gas causes collisional transfer into other, nearby ion-pair states of the molecule. If the foreign gas pressure increases considerably, the $D' \rightarrow A'$ transition accounts for by far the greatest fraction of the emission intensity. The fact that the molecules seem to "pool" in the D' state suggested to Guy et al. [111] that it was the lowest-lying of the ion-pair states. The analogous spectrum in bromine has also been assigned to a $D'\ 2_g \rightarrow A'\ 2_u$ transition [127] with a similar conclusion that the D' state is the lowest, or one of the lowest, ion-pair states of the molecule.

If D' is the lowest of the ion-pair states of iodine, correlation should be to the $I^-(^1S) + I^+(^3P_2)$ ions, the lowest energy pair. The D and E states, lying in the same 40,000 cm^{-1} energy region, are also ascribed to these same dissociation products by Guy et al. [111]. They argue further that states correlating with the higher energy ion-pairs should lie correspondingly higher in energy at the potential curve

minima, thus eliminating the assignment of the E state to the $I^+(^3P_0)$ ion. King et al. [40] suggest that such an argument is too restrictive, but the fact remains that other known higher-lying ion-pair states do lie in the 47,000 cm^{-1} region (see table (6-3)) or higher.

The idea that the ion-pair states exist in "families" according to their dissociation products is an attractive method for at least partially disentangling the ion-pair states. The fact that a number of states do seem to occur in clusters with their potential minima separated approximately by the energy separations of the different ion pairings lends some credence to the hypothesis. Mulliken has shown this same apparent behaviour in the potential curves drawn in [29]. However, the curves themselves, in light of these more recent assignments, would all have to be raised, with the D, D', and E states belonging to the group correlated with the lowest energy dissociation products. Given this, and the results in table (6-4), the present experiments would predict the dissociation energy of the E state, for $I^-(^1S) + I^+(^3P_2)$ ions, to be ~30,600 cm^{-1}.

King and co-workers [31,37,40] have also reported the observation of four other electronic states in the E state region. Their α, β, and δ states were accessible only from levels near the B state dissociation limit ($v_B \geq 69$) with very low values of J. The γ state was observed for lower vibrational levels in the B state, but was preferentially probed from the same high v_B - low J levels as the other states. No evidence of any transitions to these states has been observed in the present set of experiments. However, no E ← B transitions from $v_B < 66$ have been successfully recorded. As well, the weakness of the transitions observed by King et al. would be

further discriminated against by the characteristics of the polarization technique itself, especially for low J values, and by the method used here to record signals. Recently, Chevaleyre et al. [32] have observed transitions to the β state and have assigned it as ^1g.

The fact that the molecular constants for the α, β, γ, and δ states are similar to those of the E state, while the observed transitions from the B state are very dissimilar, is somewhat disquieting. It would seem more logical to expect that if the potential curves are similar, the Franck-Condon factors for the "E" ← B transitions would also be similar for all five states. Guy et al. [111] take exception to the assignment of the transitions as being from the B state to states of 0_g^+ and ^1g symmetry, because their grouping of levels with the same dissociation products does not provide for enough states of correct symmetry in the E state region. Instead, they propose that, since the transitions seem to depend on excitation to near the B state dissociation limit, that perturbations at large internuclear distances can mix some ^1u character into the B state. Similar perturbations of the ground state of the molecule by the a ^1g and a' 0_g^+ states have been observed [112]. The observations of King et al. might then involve $^1g \leftarrow {}^1u$ and $^2g \leftarrow {}^1u$ transitions. However, Guy et al. still fail to account for all of the extra states seen by King et al. without dismantling their "family of states" argument. Chevaleyre et al. [32] propose that a u-g perturbation of the B state near its dissociation limit will give the B state some g character. Some of the transitions observed by King et al. [31,37,40] would then be to states of u symmetry in the E state energy region.

Evidently, more work must be done in the area before this intriguing problem can be solved.

CHAPTER 8

SUMMARY AND CONCLUSIONS

In this work two different aspects of laser spectroscopy have been examined. In the first part, an exact solution to the time-dependent Schroedinger equation has been used in a number of theoretical model calculations; in the second part, the technique of polarization labelling has been applied successfully to a study of the iodine molecule.

The results in Chapter 3 illustrate how a previously-derived exact solution to the Schroedinger equation for the interaction of a sinusoidal radiation field with a molecular system can be used to obtain steady-state and temporal spectra in the study of a five-level system consisting of a ground state and four "nearly degenerate" excited states. The steady-state and time-dependent results complement one another in the interpretation of the behaviour of the five-level system. Section 3.2 shows the trend produced for single-photon transitions as the laser intensity is varied. When the laser intensity is strong, the four excited states behave like a single band, with the width of the single peak in the steady-state spectrum being much greater than the individual level separations. At weak laser intensities, the upper states interact with the ground state almost independently of one another, so an interpretation in terms of four two-level systems is possible. Intermediate results show that complicated behaviour begins to occur as the "four two-level systems" begin to overlap and interact.

The three-photon transitions studied in Section 3.3 illustrate the narrowness of peaks observed in multi-photon steady-state results. However, despite the appearance of well-separated peaks, an examination of the transition probabilities for the individual levels shows that there is still considerable interaction among the levels. This unexpected result shows how the off-resonant levels in a multi-photon transition can contribute in a subtle way to the total spectrum.

These results can be extrapolated, with caution, to systems with more levels, or to transitions of higher "photonicity". The results of Section 3.2 imply that the appearance of the steady-state spectrum of a multi-level system will depend upon the relationship between the energy level spacings and the predicted "widths" of the individual transitions. When the coupling strengths are large enough that the individual widths are predicted to be much greater than the energy level spacings, a single broad band will appear in the steady state result. When the coupling strengths are small, individual peaks due to the individual levels will be observed. In higher-order transitions, the peaks in the steady-state spectrum will be relatively very narrow, but the underlying interaction between levels will be expected to persist.

In Chapter 4, the previously-derived formalism [9,11] was modified to include individual decay terms for the excited states. The results for the temporal behaviour of the system indicate that the contribution of a single damped level to the overall decay can usually be predicted from its behaviour in the undamped system. Generally, the multi-level system will be damped more efficiently when the transition probability for the decaying state is high. For the uniform damping model, the

undamped temporal behaviour again proves useful for the interpretation of the results. When the "Rabi" period for a transition is long, it takes more time for the spectrum to reach its steady-state value. The peak in the phase- and time-averaged damped spectrum corresponding to this "slow" transition will be smaller relative to those for the "faster" transitions. This has been used in Chapter 4 to differentially damp transitions with significantly different temporal behaviour in the three-photon transitions in the five-level model system.

The high-lying ion-pair states of iodine have recently been the subject of a great deal of spectroscopic research. Detailed analyses of the E state of the molecule have resulted from two-photon excitation experiments. Renewed interest in the ion-pair region in general has led to new states of the molecule being observed, identified, and characterized [31-35,40].

Polarization labelling spectroscopy, as described in Chapter 5, is a very good candidate for use in analyzing the ion-pair states of the iodine molecule. The spectra that are recorded have very few lines, and these lines are easily assigned and easily measured with a resolution surpassing that for the excitation experiment.

In Chapter 7, the least-squares analysis of the assigned lines in the E state of iodine produces a better determination of the molecular constants describing the state. A comparison with other authors' results [36,38-40] in table (7-1) shows the often significant improvement the present study provides.

REFERENCES

1. M.J. Beesley, Lasers and their applications, Taylor and Francis, Ltd., London (1976).

   S. Kimmel and S. Speiser, Chem. Rev., 77, 437 (1977).

   J.L. Hall and J.L. Carlsten, editors, Laser Spectroscopy III, Springer-Verlag, Berlin (1977).

   J.C. Wright and M.J. Wirth, Anal. Chem., 52, 988A (1980).

2. R.G. Brewer, Science, 178, 247 (1972).

   Y.R. Shen, Rev. Mod. Phys., 48, 1 (1976).

3. L.I. Schiff, Quantum Mechanics, second edition, McGraw-Hill Book Company, Inc., New York (1955), Chapter 8.

4. A. Dalgarno, Perturbation Theory and its Applications in Quantum Mechanics (C.H. Wilcox, ed.), John Wiley and Sons, Inc., New York (1966), pp. 145-183 .

5. P.W. Langhoff, S.T. Epstein, and M. Karplus, Rev. Mod. Phys., 44, 602 (1972).

6. I.I. Rabi, Phys. Rev., 51, 652 (1937).

7. M. Sargent III, M.O. Scully, and W.E. Lamb, Jr., Laser Physics, Addison-Wesley Publishing Company, Reading, Massachusetts (1974), chapter 2.

8. L. Allen and J.H. Eberly, Optical Resonance and Two-Level Atoms, John Wiley and Sons, New York (1975), chapter 2.

9. J.V. Moloney, M.K. Ali, and W.J. Meath, Phys. Letters, 49A, 207 (1974).

10. W.R. Salzman, Phys. Rev. A, 10, 461 (1974).

11. J.V. Moloney and W.J. Meath, Molec. Phys., 30, 171 (1975).

12. J.V. Moloney, Ph.D. Thesis, The University of Western Ontario, London, Ontario (1976).

13. J.H. Shirley, Phys. Rev., 138, B979 (1965).

14. J.V. Moloney and W.J. Meath, Molec. Phys., 31, 1537 (1976).

15. D.R. Dion and J.O. Hirschfelder, Adv. Chem. Phys., 35, 265 (1976), and references therein.

16. R.G. Breene, Jr., The Shift and Shape of Spectral Lines, Pergamon Press, Frankfurt (1961), chapter 1.

17. J.V. Moloney and W.J. Meath, Molec. Phys., 35, 1163 (1978).

18. W. Rhodes, J. Phys. Chem., 86, 2657 (1982).

19. B.W. Shore, Am. J. Phys., 47, 262 (1979).

20. C. Wieman and T.W. Hänsch, Phys. Rev. Letters, 36, 1170 (1976).

21. R. Teets, R. Feinberg, T.W. Hänsch, and A.L. Schawlow, Phys. Rev. Letters, 37, 683 (1976).

22. R.E. Teets, Ph.D. Thesis, Stanford University, Palo Alto, California (1978).

23. K.J. Cross, Ph.D. Thesis, The University of Western Ontario, London, Ontario (1980).

24. J.C.D. Brand, K.J. Cross, and N.P. Ernsting, Chem. Phys., 59, 405 (1981).

25. N.W. Carlson, F.V. Kowalski, R.E. Teets, and A.L. Schawlow, Opt. Commun., 29, 302 (1979).

26. R.E. Teets, N.W. Carlson, and A.L. Schawlow, J. Mol. Spectrosc., 78, 415 (1979).

27. J.C.D. Brand and N.P. Ernsting, J. Mol. Spectrosc., 91, 389 (1982).

28. J.C.D. Brand, K.J. Cross, and R.J. Hayward, Can. J. Phys., 57, 1455 (1979).

29. R.S. Mulliken, J. Chem. Phys., 55, 288 (1971).

30. J. Tellinghuisen, J. Mol. Spectrosc., 94, 231 (1982).

31. G.W. King, I.M. Littlewood, and J.R. Robins, Chem. Phys., 68, 129 (1982).

32. J. Chevaleyre, J.P. Perrot, J.M. Chastan, S. Valignat, and M. Broyer, Chem. Phys., 67, 59 (1982).

33. J.C.D. Brand and A.R. Hoy, Can. J. Phys., 60, 1209 (1982).

34. H.P. Grieneisen and R.E. Francke, Chem. Phys. Letters, 88, 585 (1982).

35. U. Heeman, H. Knockel, and E. Tiemann, Chem. Phys. Letters, 90, 17 (1982).

36. K. Wieland, J.B. Tellinghuisen, and A. Nobs, J. Mol. Spectrosc., 41, 69 (1972).

37. a. M.D. Danyluk and G.W. King, Chem. Phys. Letters, 44, 440 (1976).
b. M.D. Danyluk and G.W. King, Chem. Phys., 22, 59 (1977).

38. A.D. Williamson, Chem. Phys. Letters, 60, 451 (1979).

39. S.L. Cunha, J.A. Lisboa, R.E. Francke, H.P. Grieneisen, and B.P. Chakraborty, Opt. Commun., 28, 321 (1979).

40. G.W. King, I.M. Littlewood, and J.R. Robins, Chem. Phys., 56, 145 (1981).

41. E.R. Cohen and B.N. Taylor, J. Phys. Chem. Ref. Data, 2, 663 (1973).

42. A. Messiah, Quantum Mechanics, Volume 2, John Wiley and Sons, Inc., New York (1961), chapter 17.

43. L.I. Schiff, op. cit., chapter 7.

44. Equation (2.1-5) is written in the Dirac or interaction representation, as opposed to the result in the Schroedinger representation, namely

$$\Psi(r,t) = \sum_k a_k(t)\, \phi_k(r).$$

The two representations are related simply by the equation

$$a_k(t) = b_k(t) \exp\{-iE_k t\} .$$

45. L. Pauling and E.B. Wilson, Introduction to Quantum Mechanics, McGraw-Hill Book Company, Inc., New York (1935), chapter 11.

46. J. Wong, J.C. Garrison, and T.H. Einwohner, Phys. Rev. A, 13, 674 (1976).

47. J.H. Shirley, Ph.D. Thesis, California Institute of Technology, Pasadena, California (1963).

48. J.H. Shirley, J. Appl. Phys., 34, 783 (1963).

49. M. Quack, J. Chem. Phys., 69, 1282 (1978).

50. T.H. Einwohner, J. Wong, and J.C. Garrison, Phys. Rev. A, 14, 1452 (1976).

51. F. Bloch and A. Siegert, Phys. Rev., 57, 522 (1940).

52. a. S. Stenholm, J. Phys. B, 5, 878 (1972).

    b. S. Stenholm, J. Phys. B, 5, 890 (1972).

53. D.T. Pegg, J. Phys. B, 6, 246 (1973).

54. a. C. Cohen-Tannoudji, J. Dupont-Roc, and C. Fabre, J. Phys. B, 6, L214 (1973).

    b. C. Cohen-Tannoudji, J. Dupont-Roc, and C. Fabre, J. Phys. B, 6, L218 (1973).

55. P. Hannaford, D.T. Pegg, and G.W. Series, J. Phys. B., 6, L222 (1973).

56. S. Stenholm, J. Phys. B, 6, L240 (1973).

57. F. Ahmad and R.K. Bullough, J. Phys. B, 7, L147 (1974).

58. a. F.T. Hioe and J.H. Eberly, Phys. Rev. A, 11, 1358 (1975).

b. F.T. Hioe, private communication.

59. R.I. Jackson and S. Swain, J. Phys. B, 15, 575 (1982).

60. J.H. Eberly, B.W. Shore, Z. Bialynicka-Birula, I. Bialynicki-Birula, Phys. Rev. A, 16, 2038 (1977).

61. a. F.H.M. Faisal, J. Phys. B, 9, 3009 (1976).

b. J.V. Moloney and F.H.M. Faisal, Opt. Commun., 29, 62 (1979).

62. G.F. Thomas and W.J. Meath, Molec. Phys., 46, 743 (1982).

63. M.H. Protter and C.B. Morrey, Jr., Modern Mathematical Analysis, Addison-Wesley Publishing Company, Inc., Reading, Massachusetts (1964), chapter 8.

64. B.T. Smith, J.M. Boyle, J.J. Dongarra, B.S. Garbow, Y. Ikebe, V.C. Klema, and C.B. Moler, Matrix Eigensystem Routines - EISPACK Guide, second edition, Springer-Verlag, Berlin (1976).

65. A. Javan, Phys. Rev., 107, 1579 (1957).

66. J.K. Hale, Ordinary Differential Equations, John Wiley and Sons, Inc., New York (1969), chapter 3.

67. H. Margenau and G.M. Murphy, The Mathematics of Physics and Chemistry, second edition, D. Van Nostrand Company, Inc., Princeton, New Jersey (1956), chapter 2.

68. V.A. Yakubovich and V.M. Starzhinskii, Linear Differential Equations with Periodic Coefficients, Volume 1 (translated by D. Louvish), John Wiley and Sons, Inc., New York (1975), chapter 2.

69. Equation (2.5-5) can be written more generally as

$$(2\Delta_j + m)\pi = \tan^{-1}(^{\text{Im}}\lambda_j/\text{Re}\ \lambda_j)$$

where m is an arbitrary integer [63]. For convenience, m may

be taken to be zero without affecting the physically meaningful results of the calculation.

70. C. Besset, J. Horowitz, A. Messiah, and J. Winter, J. Phys. Radium, 15, 251 (1954).

71. J.V. Moloney and W.J. Meath, Phys. Rev. A, 17, 1550 (1978).

72. R.W. Daniels, An Introduction to Numerical Methods and Optimization Techniques, Elsevier North-Holland, New York (1978), chapter 6.

73. Ibid., chapter 4.

74. International Mathematical and Statistical Libraries, Inc., The IMSL Library, Houston (1980), routine ICSICU.

75. J.V. Moloney and W.J. Meath, J. Phys. B, 11, 2641 (1978).

76. P. Luc, J. Mol. Spectrosc., 80, 4 (1980).

77. G.P. Gillispie and E.C. Lim, Chem. Phys. Letters, 70, 532 (1980). J.C.D. Brand and A.R. Hoy, J. Mol. Spectrosc., 65, 75 (1977).

78. H. Margenau and G.M. Murphy, op. cit., chapter 11.

79. J.I. Steinfeld, Molecules and Radiation, Harper and Row, New York (1974), chapter 13.

80. The ratio of the maximum values of the averaged transition probabilities for levels 2 and 3 in the steady-state spectra of figure (3-4) is approximately equal to the ratio of the coefficients of the original state 2' in each level (see figure (3-2)), squared.

81. Even-photon transitions are allowed if the levels are of "mixed parity" [62] or if an external static field induces a mixing [17].

82. S. Leasure and R.E. Wyatt, Chem. Phys. Letters, 61, 625 (1979).

83. M.D. Burrows and W.R. Salzman, Phys. Rev. A, 15, 1636 (1977).

84. W.R. Salzman, Phys. Rev. A, 16, 1552 (1977).
W.R. Salzman, Phys. Rev. A, 17, 1240 (1978).

85. B.W. Shore and J. Ackerhalt, Phys. Rev. A, 15, 1640 (1977).

86. J.C.D. Brand, K.J. Cross, N.P. Ernsting, and A.B. Yamashita, Opt. Commun., 37, 178 (1981).

87. C.H. Townes and A.L. Schawlow, Microwave Spectroscopy, McGraw-Hill Book Company, New York (1955), p. 96.

88. N. Bloembergen, Am. J. Phys., 35, 989 (1967).

89. T.W. Hänsch, Appl. Opt., 11, 895 (1972).

90. J.C.D. Brand, N.P. Ernsting, A.K. Kalkar, and A.B. Yamashita, unpublished results.

91. J.C.D. Brand, U.D. Deshpande, A.R. Hoy, and E.J. Woods, Can. J. Chem., in press.

92. J.C.D. Brand, U.D. Deshpande, A.R. Hoy, and S.M. Jaywant, to be published.

93. J. Sauer, Organic Synthesis, 36, 66 (1956).

94. J.C.D. Brand, J.H. Callomon, and J.K.G. Watson, Disc. Farad. Soc., 35, 175 (1963).

95. C.T. Lin and C.D. Moule, J. Mol. Spectrosc., 37, 280 (1971).

96. C.A. Thayer, A.V. Pocius, and J.T. Yardley, J. Chem. Phys., 62, 3712 (1975).

97. J.C.D. Brand and R.J. Hayward, Chem. Phys. Letters, 68, 369 (1979).

98. G. Herzberg, Molecular Structure and Molecular Spectra, Volume III, Electronic Spectra of Polyatomic Molecules, Van Nostrand Reinhold Company, New York (1966) pp. 9-20.

99. G. Herzberg, Molecular Structure and Molecular Spectra, Volume I, Spectra of Diatomic Molecules, Van Nostrand Reinhold Company, New York (1950) pp. 212-225.

100. G. Herzberg, op. cit. (1966) chapter 3.

101. Ibid., Appendices.

102. G. Herzberg, op. cit. (1950) pp 240-244.

103. G. Das and A.C. Wahl, J. Chem. Phys., 69, 53 (1978).

104. R.J. LeRoy, J. Chem. Phys., 52, 2683 (1970).

105. R.F. Barrow and K.K. Yee, J.C.S. Faraday II, 69, 684 (1973).

106. J. Wei and J. Tellinghuisen, J. Mol. Spectrosc., 50, 317 (1974).

107. S. Gerstenkorn, P. Luc, and J. Vergès, J. Phys. B, 14, L193 (1981).

108. K.S. Viswanathan, A. Sur, and J. Tellinghuisen, J. Mol. Spectrosc., 86, 393 (1981).

109. J. Tellinghuisen, Chem. Phys. Letters, 49, 485 (1977).

110. H. Hemmati and G.J. Collins, Chem. Phys. Letters, 67, 5 (1979).

111. A.L. Guy, K.S. Viswanathan, A. Sur, and J. Tellinghuisen, Chem. Phys. Letters, 73, 582 (1980).

112. a. R. Bacis, S. Churassy, R.W. Field, J.B. Koffend, and J. Vergès, J. Chem. Phys., 72, 34 (1980).

b. R. Bacis, M. Broyer, S. Churassy, J. Vergès, and J. Vigué, J. Chem. Phys., 73, 2641 (1980).

c. S. Churassy, F. Martin, R. Bacis, J. Vergès, and R.W. Field, J. Chem. Phys., 75, 4863 (1981).

113. R.S. Mulliken, J. Chem. Phys., 7, 20 (1939).

114. G. Herzberg, op. cit. (1950) pp. 384-385.

115. M.S. de Vries, N.J.A. Van Veen, T. Baller, and A.E. de Vries, Chem. Phys., 56, 157 (1981).

116. Charlotte E. Moore, Atomic Energy Levels, Volume III, National Bureau of Standards, Washington, D.C. (1957) pp. 106-108.

117. Handbook of Chemistry and Physics, 51st edition, CRC Press, Cleveland, Ohio (1970) p. E-73.

118. J.D. Simmons and J.T. Hougen, J. Res. Natl. Bur. Stand., Sect. A, 81, 25 (1977).

119. S. Gerstenkorn and P. Luc, Atlas du spectre d'Absorption de la Molecule d'Iode, CNRS, Paris (1978).

120. M.D. Danyluk and G.W. King, Chem. Phys., 25, 343 (1977).

121. a. K.K. Yee, J.C.S. Faraday II, 72, 2113 (1976).

b. P. Luc, 36th Symposium on Molecular Spectroscopy, Columbus, Ohio (1981) Abstract WA3.

122. D.L. Rousseau and P.F. Williams, Phys. Rev. Letters, 33, 1368 (1974).

123. a. N.W. Carlson, A.J. Taylor, and A.L. Schawlow, Phys. Rev. Letters, 45, 18 (1980).

b. N.W. Carlson, A.J. Taylor, K.M. Jones, and A.L. Schawlow, Phys. Rev. A, 24, 822 (1981).

124. J. Tellinghuisen, Phys. Rev. Letters, 18, 1137 (1975).

125. J.C.D. Brand, A.R. Hoy, A.K. Kalkar, and A.B. Yamashita, J. Mol. Spectrosc., 95, 350 (1982).

126. C. Tai, F.W. Dalby, and G.L. Giles, Phys. Rev. A, 20, 233 (1979).

127. A. Sur and J. Tellinghuisen, J. Mol. Spectrosc., 88, 323 (1981).

END

20.09.83

FIN